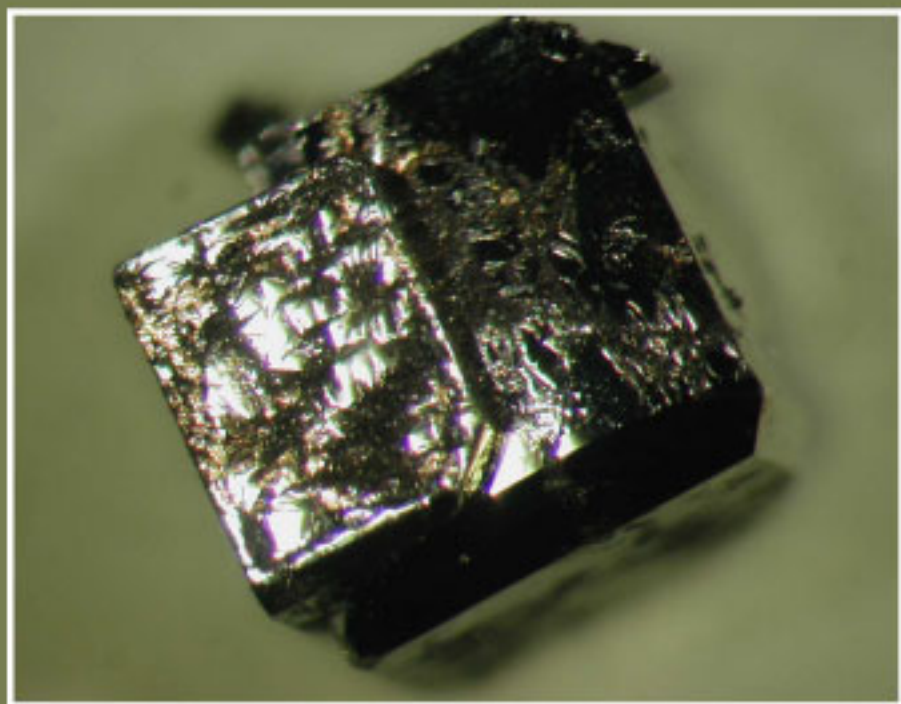


Julia Ferstl

**New Yb-based systems: From an  
intermediate-valent to a magnetically  
ordered state**



Cuvillier Verlag Göttingen

**New Yb-based systems: From an  
intermediate-valent to a magnetically  
ordered state**

DISSERTATION

zur Erlangung des akademischen Grades

**Doctor rerum naturalium**

(Dr. rer. nat.)

vorgelegt

der Fakultät Mathematik und Naturwissenschaften  
der Technischen Universität Dresden

von

**Julia Ferstl**

geboren am 27. Februar 1975 in Leipzig

MAX-PLANCK-INSTITUT FÜR CHEMISCHE PHYSIK FESTER STOFFE,  
DRESDEN 2006

## **Bibliografische Information Der Deutschen Bibliothek**

Die Deutsche Bibliothek verzeichnet diese Publikation in der Deutschen Nationalbibliografie; detaillierte bibliografische Daten sind im Internet über <http://dnb.ddb.de> abrufbar.

1. Aufl. - Göttingen : Cuvillier, 2007

Zugl.: (TU) Dresden, Univ., Diss., 2006

978-3-86727-375-6

*Gutachter:*

Prof. Dr. F. Steglich

Prof. Dr. J. Wosnitza

Prof. Dr. E. Bauer

*Eingereicht am: 15. Dezember 2006*

*Tag der Verteidigung: 04. April 2007*

© CUVILLIER VERLAG, Göttingen 2007

Nonnenstieg 8, 37075 Göttingen

Telefon: 0551-54724-0

Telefax: 0551-54724-21

[www.cuvillier.de](http://www.cuvillier.de)

Alle Rechte vorbehalten. Ohne ausdrückliche Genehmigung des Verlages ist es nicht gestattet, das Buch oder Teile daraus auf fotomechanischem Weg (Fotokopie, Mikrokopie) zu vervielfältigen.

1. Auflage, 2007

Gedruckt auf säurefreiem Papier

978-3-86727-375-6

*Imagination is more important than knowledge.*

– Albert Einstein –



# Contents

<b>1</b>	<b>Introduction</b>	<b>1</b>
<b>2</b>	<b>Introduction to 4f-based heavy Fermions</b>	<b>5</b>
<b>3</b>	<b>YbFe<sub>2</sub>Ge<sub>2</sub> and its ‘reference’ compound LuFe<sub>2</sub>Ge<sub>2</sub>: paramagnetic Fe moment</b>	<b>21</b>
3.1	Introduction.....	21
3.2	YbFe <sub>2</sub> Ge <sub>2</sub> .....	23
3.2.1	Crystal growth.....	23
3.2.2	Physical properties of YbFe <sub>2</sub> Ge <sub>2</sub> .....	30
3.2.2.1	Resistivity.....	30
3.2.2.2	Specific heat.....	35
3.2.2.3	Magnetic properties.....	39
3.2.2.3.1	Susceptibility.....	39
3.2.2.3.2	Magnetisation.....	43
3.3	LuFe <sub>2</sub> Ge <sub>2</sub> .....	45
3.3.1	Crystal growth.....	45
3.3.2	Physical properties of LuFe <sub>2</sub> Ge <sub>2</sub> .....	50
3.3.2.1	Resistivity.....	50
3.3.2.2	Specific heat.....	52
3.3.2.3	Magnetic properties.....	56
3.3.2.3.1	Susceptibility.....	56
3.3.2.3.2	Magnetisation.....	65
3.4	Neutron scattering.....	68
3.5	LDA calculations.....	73

3.6	Final discussion of $\text{YbFe}_2\text{Ge}_2$ and $\text{LuFe}_2\text{Ge}_2$ .....	76
3.6.1	Paramagnetic Fe moment.....	76
3.6.2	Spin fluctuations and magnetic order in $\text{LuFe}_2\text{Ge}_2$ .....	77
3.6.3	Intermediate valency and heavy-fermion behaviour in $\text{YbFe}_2\text{Ge}_2$ .....	78
3.7	Summary.....	82
<b>4</b>	<b>Pure and doped <math>\text{YbRh}_2\text{Si}_2</math>: Crossing the QCP</b>	<b>83</b>
4.1	Introduction.....	83
4.1.1	Review.....	83
4.1.2	Aim of this work.....	89
4.2	Crystal growth.....	90
4.2.1	Introduction .....	90
4.2.2	Crystal growth of pure $\text{YbRh}_2\text{Si}_2$ .....	92
4.2.3	Crystal growth of doped $\text{YbRh}_2\text{Si}_2$ .....	96
4.2.3.1	Crystal growth of $\text{YbRh}_2(\text{Si}_{1-x}\text{Ge}_x)_2$ .....	96
4.2.3.2	Crystal growth of $\text{Yb}_{1-x}\text{La}_x\text{Rh}_2\text{Si}_2$ and $\text{Yb}_{0.95}\text{Y}_{0.05}\text{Rh}_2\text{Si}_2$ ...	102
4.3	Lattice constants.....	105
4.4	Physical properties.....	108
4.4.1	Resistivity.....	108
4.4.1.1	Resistivity of pure $\text{YbRh}_2\text{Si}_2$ .....	108
4.4.1.2	Resistivity of $\text{Yb}_{1-x}\text{La}_x\text{Rh}_2\text{Si}_2$ .....	111
4.4.2	Specific heat.....	116
4.4.2.1	Specific heat of pure $\text{YbRh}_2\text{Si}_2$ .....	116
4.4.2.2	Specific heat of $\text{Yb}_{1-x}\text{La}_x\text{Rh}_2\text{Si}_2$ .....	126
4.5	Magnetic properties.....	130
4.5.1	Susceptibility.....	131
4.5.1.1	Susceptibility of pure $\text{YbRh}_2\text{Si}_2$ in both directions.....	131
4.5.1.2	Comparison of susceptibility of all La-doped $\text{YbRh}_2\text{Si}_2$ .....	135
4.5.2	Magnetisation.....	137
4.6	Neutron scattering.....	138

---

4.7	ESR.....	145
4.7.1	ESR signal in pure $\text{YbRh}_2\text{Si}_2$ .....	146
4.7.2	ESR signal in $\text{Yb}_{1-x}\text{La}_x\text{Rh}_2\text{Si}_2$ .....	148
4.8	Muon spin relaxations in $\text{Yb}_{0.95}\text{La}_{0.05}\text{Rh}_2\text{Si}_2$ .....	150
4.9	Summary.....	151
<b>5</b>	<b>Magnetic order of well localised <math>\text{Yb}^{3+}</math> moments in <math>\text{Yb}_4\text{Rh}_7\text{Ge}_6</math></b>	<b>155</b>
5.1	Crystal growth.....	155
5.2	Physical properties.....	160
5.2.1	Magnetic properties: susceptibility and magnetisation.....	161
5.2.2	Resistivity.....	163
5.2.3	Anomalous specific heat and entropy.....	166
5.3	Discussion and comparison with other Yb-based compounds..	169
5.4	Summary.....	170
<b>6</b>	<b>Summary</b>	<b>171</b>
	<b>Bibliography</b>	<b>175</b>



## Contents

---

# 1 Introduction

Heavy fermion (HF) systems belong to the group of strongly correlated electron systems and have attracted considerable attention because of their unusual physical behaviour at low temperatures. Only a few ytterbium-based heavy-fermion compounds were discovered in the past twenty years in comparison to Ce-based ones, because of the difficulty in synthesising Yb compounds due to its high vapour pressure. Thus the aim of this thesis was to synthesise and investigate new Yb-based heavy-fermion systems.

Only very little is known e.g. about  $RT_2X_2$  compounds with  $X = \text{Ge}$  and a transition metal  $T$  from the Fe or Co columns. A few compounds like  $\text{YbNi}_2\text{Ge}_2$  and  $\text{YbCo}_2\text{Ge}_2$  have been investigated and both show a weakly intermediate-valent Yb state, at the border to the Kondo regime. Therefore, we looked for new  $RT_2\text{Ge}_2$  systems, which are close to a quantum critical point (QCP), where the magnetic ordering temperature goes continuously to 0 K. Close to such a QCP, one often observes in these compounds unusual transport and thermodynamic properties, which differ from Landau-Fermi-liquid behaviour. These compounds are therefore called non-Fermi-liquid (NFL) systems. We grew polycrystalline and single crystalline  $\text{YbFe}_2\text{Ge}_2$  and investigated its physical properties (chapter 3). Previously only the structure, but no physical properties of  $\text{YbFe}_2\text{Ge}_2$  had been reported. Our results show a weakly intermediate-valent Yb state with a low characteristic  $4f$  energy, at the border to the Kondo regime. The susceptibility shows an anomalous behavior and can be fitted at high temperatures ( $T > 100$  K) with a Curie-Weiss law with a surprisingly high effective moment of  $\mu_{\text{eff}} = 6.2 \mu_{\text{B}}$  and a very large Curie-Weiss temperature. The results on  $\text{YbFe}_2\text{Ge}_2$  will be discussed in comparison with the reference compound  $\text{LuFe}_2\text{Ge}_2$ , which shows an additional phase transition at  $T_0 \approx 9$  K.

The HF system  $\text{YbRh}_2\text{Si}_2$ , has attracted strong attention because it is located very close to a QCP connected with the transition from a magnetically ordered ground state to a non-magnetic one. At ambient pressure it orders antiferromagnetically at a very low temperature,  $T_{\text{N}} = 70$  mK. Upon

applying a small magnetic field (60 mT) or a slight negative chemical pressure using Ge doping,  $T_N$  disappears at a QCP where the effective mass of the quasiparticles diverges. The proximity to the QCP leads to pronounced NFL behaviour in the resistivity  $\rho(T)$  and the specific heat  $C(T)$ . The low-temperature physics of this system can be explained within the local QCP scenario. The aim of this work was to reach and to cross the quantum critical point by using negative chemical pressure in doped  $\text{YbRh}_2\text{Si}_2$ . Already slight negative chemical pressure using 5 % nominal Ge doping leads to the extension of the NFL behaviour to the lowest investigated temperature  $T \approx (10 - 20)$  mK. But this Ge content was not enough to cross the QCP. Since crystals with a higher Ge-content could not be obtained, we tried to replace Yb by the larger lanthanum, which should also lead to an increase of the unit-cell volume. Single crystals of pure and doped  $\text{YbRh}_2\text{Si}_2$  were grown using a flux technique in closed Ta crucibles. We succeeded with the single-crystal growth of  $\text{Yb}_{1-x}\text{La}_x\text{Rh}_2\text{Si}_2$  with  $0 < x < 0.3$ , which allowed us to study the behaviour upon crossing the QCP (chapter 4).

The second reason to investigate more intensively  $\text{YbRh}_2\text{Si}_2$  was the missing detailed analysis of the high-temperature properties, like e.g. the crystal electric field, which was not settled. We therefore analyzed the high-temperature specific heat to fix the energy of the first excited crystal electric field (CEF) level. From the analysis of the temperature dependence of the entropy we deduce the Kondo temperature of pure and La-doped  $\text{YbRh}_2\text{Si}_2$ . The samples obtained from the reproducible crystal growth were used for many other investigations, like e.g. neutron-scattering experiments to study the magnetic excitations i.e., the higher excited CEF levels and magnetic fluctuations. Additionally ESR experiments were performed on pure and La-doped  $\text{YbRh}_2\text{Si}_2$ , which shows a very surprising result, because for the first time the ESR signal of the Kondo ion was found in a dense Kondo system.

Attempts to prepare the pure isoelectronic compound  $\text{YbRh}_2\text{Ge}_2$  failed, instead single crystals of  $\text{Yb}_4\text{Rh}_7\text{Ge}_6$  were obtained and studied (chapter 5).

The results evidence a stable  $\text{Yb}^{3+}$  state, which orders presumably antiferromagnetically at 0.49 K.

The main results of this thesis are summarised at the end in chapter 6.



## 2 Introduction to 4f-based heavy fermions

This chapter will give a short introduction into heavy-fermion systems, especially Yb-based ones. In comparison with Ce-based compounds, only a few Yb-based heavy fermions were discovered in the past twenty years. The main reason for this is the difficulty in synthesising Yb compounds because of the high vapour pressure of Yb.

Heavy-fermion systems belong to the group of strongly correlated electron systems and have attracted considerable attention because of their unusual physical behaviour at low temperatures. These systems are intermetallic compounds with elements from the group of lanthanides or actinides. Especially systems with elements having an instable f shell like cerium, ytterbium or europium are of interest, because of the transition from a magnetic to a non-magnetic ground state.

The following text will give a short introduction into intermetallic 4f-based systems with an instable 4f shell. First, a very general approach and phase diagrams for the transition from a magnetic to a non-magnetic state shall be presented, followed by a more detailed discussion of the difference between Ce-, Eu- and Yb-based compounds. Finally, two theoretical models, the localised-moment scenario and the spin-density-wave scenario, will be discussed at the end of this chapter.

The origin for the interesting physical properties is the hybridisation of the atomic 4f or 5f states (of the cerium, ytterbium or uranium atoms) with the valence-band states. Different ground states are occurring in dependence of the hybridisation between the 4f or 5f electrons and the valence electrons. Two types of interactions are important: the Ruderman-Kittel-Kasuya-Yoshida (RKKY) exchange and the Kondo [Kondo 1964] effect. The first one (RKKY) describes the indirect interaction between neighbouring magnetic moments through the conducting electrons and favours magnetic order. The second mechanism describes the interaction between a single

magnetic ion in the lattice with its metallic surrounding. The simplest description of the competition between a non-magnetic Kondo-state and a magnetically ordered state is given by the Doniach model [Doniach 1977], where only one parameter, the coupling parameter  $g$  is used (fig. 2.1).

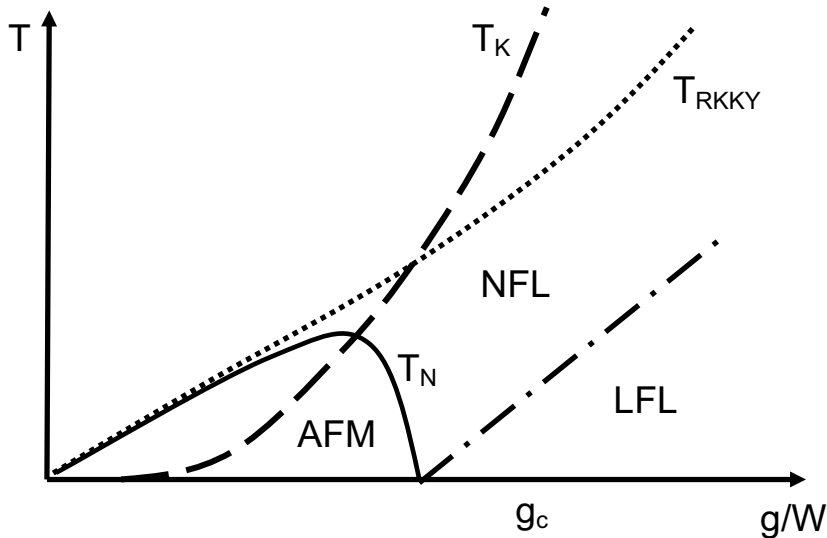


**Figure 2.1:** This schematic phase diagram shows the effect of the competition between Kondo effect,  $T_K$ , and RKKY exchange,  $T_{RKKY}$ , in dependence of the hybridisation strength  $g$ . Antiferromagnetism occurs in the region, where  $T_{RKKY} > T_K$ . For  $T_K > T_{RKKY}$  the non-magnetic ground state with enhanced effective mass of the quasiparticles is formed. This modified Doniach diagram [Doniach 1977] shows a QCP, where  $T_N$  goes to zero temperature at a critical value  $g_c$ . The area close to this point is dominated by non-Fermi-liquid behaviour. The blue line indicates the crossover temperature below which Landau-Fermi-liquid (LFL) behaviour is expected.

This parameter  $g$  is determined by the exchange  $J$  between the 4f level and the conduction electrons and by the density of states at the Fermi edge  $N(E_F)$ :  $g = |J| \cdot N(E_F)$ . Large  $g$  values favour a nonmagnetic ground state and small  $g$  values a magnetically ordered ground state. The exchange strength  $J$

can be tuned experimentally by applying pressure or by chemical doping. Upon increasing  $g$  beyond a critical value  $g_c$ , one observes the transition from a magnetically ordered to a paramagnetic state. Systems very close to the critical  $g_c$  are of special interest, because there the competition between Kondo and RKKY interaction results in very unusual low temperature properties.

The point, where the magnetic ordering temperature goes continuously to 0 K is called a quantum critical point (QCP). Systems, which are very close to such a QCP present properties which often differ from those expected for a Landau-Fermi liquid (LFL) and show abnormal transport and thermodynamic properties, so called non-Fermi-liquid (NFL) behaviour.

Landau-Fermi-liquid theory is very essential for solid-state physics and was originally developed to explain the behaviour of liquid  $^3\text{He}$ . In comparison with the model of the free electron gas the Landau-Fermi-liquid theory includes the interaction between the fermions among each other. A short overview is given in [Landau 1957] and [Ashcroft 1976]. The electrons are colliding with each other and one expects a high scattering rate, but this is reduced because of the Pauli principle. Landau's theory describes the excitation states of single particles in a system of interacting particles. Those excitation states are called quasiparticles and one can visualise them as single particles surrounded by a distortion cloud, when moving inside the electron gas. Each quasiparticle (like electrons with spin  $\frac{1}{2}\hbar$  and charge  $\pm e$ ) corresponds to one excitation state in the free electron gas and obeys Fermi statistic. The effective mass of the electrons changes drastically, because of the interaction between the electrons. The specific heat of Fermi liquids is given by:

$$C(T) = \gamma T, \quad \text{with } \gamma = \gamma_0 m^*/m, \quad (1)$$

$\gamma_0$  being the Sommerfeld coefficient in the absence of interactions.

This is equivalent to the equation of a free electron gas, but with a renormalized electron mass  $m^*/m_0$ . In the special case of heavy-fermion systems, the effective mass of the quasiparticles  $m^*$  is about 100 to 1000



times larger than in normal Fermi-liquid systems. The electronic contribution of the resistivity follows

$$\rho = \rho_0 + AT^2, \quad (2)$$

where the residual resistivity  $\rho_0$  comes from the scattering of the quasiparticles with lattice defects and  $A^2$  scales with  $\gamma$ .

In the last years a lot of systems have been discussed showing characteristic deviations from typical Landau-Fermi-liquid systems. Such compounds are so called non-Fermi liquids and show for example a resistivity dependence  $\rho \propto T^n$  with  $1 \leq n \leq 1.5$ , like CeCu<sub>2</sub>Si<sub>2</sub> with  $n = 3/2$  [Steglich 1996] or CePd<sub>2</sub>Si<sub>2</sub> close to its critical pressure of  $p_c \approx 2.8 \text{ GPa}$  with  $n = 1.2$  [Julian 1996]. The specific heat  $C(T)/T$  towards low temperatures is not constant anymore, but shows different behaviours, such as a logarithmic increase,  $C(T)/T \propto \ln(T_0/T)$ , for CeCu<sub>5.9</sub>Au<sub>0.1</sub> [Löhneysen 1996], [Löhneysen 1999] and for YbRh<sub>2</sub>Si<sub>2</sub> [Trovarelli 2000a, b, c] or a square-root-like increase of the form  $C(T)/T = \gamma_0 - cT^{0.5}$  in CeNi<sub>2</sub>Ge<sub>2</sub> [Steglich 1996].

Since this work is more focused on the experimental investigation and crystal growth of such compounds it is not the appropriate place for a detailed presentation of the theoretical aspects. A more detailed overview about non-Fermi-liquid behaviour is given in the proceedings of the ‘International Conference on Non-Fermi-liquid Behaviour in Metals’ [Santa Barbara 1996] or [Stewart 2001].

Before giving an overview on the different chapters in this work a comparison between Ce, Yb and Eu systems is necessary to underline the difference between heavy-fermion compounds based on those elements. The character of the 4f electrons determines the ground state properties of intermetallic rare-earth compounds. The 4f electrons have a very small radial extension and are therefore located within the Xe-core electrons. The influence of ligand atoms is very small and 4f electrons in solids have atomic-like character. Looking at the periodic table of elements within the row of the lanthanides and considering the trivalent state usually taken by the lanthanides in a metallic compound, Ce is sitting on the left side (just after La) with a configuration  $4f^1 5d6s^2$ , while Yb is on the right side (before

Lu) with  $4f^{13}5d6s^2$ . Both La and Lu are non-magnetic, because of their empty and full shell, respectively. Ytterbium is considered as the hole analogue of cerium. For the complete filling of the 4f shell one electron is missing in the magnetic  $\text{Yb}^{3+}$  state, while  $\text{Ce}^{3+}$  has one electron too much for an empty 4f shell. Both configurations are unstable and the Ce ion can become non-magnetic with a  $4f^05d6s^2$  ( $\text{Ce}^{4+}$ ) configuration and the Yb ion can take the divalent configuration of  $4f^{14}5d6s^2$  ( $\text{Yb}^{2+}$ ). Another element which is frequently observed in a non-trivalent state is Eu. Its magnetic divalent  $\text{Eu}^{2+}$  state presents an exactly half filled 4f shell ( $4f^76s^2$ ) which can easily be stabilised compared to the non-magnetic  $\text{Eu}^{3+}$  state which has one hole in the f shell ( $4f^65d^16s^2$ ).

The magnetic  $\text{Yb}^{3+}$  ion has an effective magnetic moment of  $\mu_{\text{eff}} = 4.54 \mu_{\text{B}}$  with the following quantum numbers:  $S = 1/2$  (spin quantum number),  $L = 3$  (orbital quantum number) and  $J = 7/2$  (total angular quantum number), while the non-magnetic  $\text{Yb}^{2+}$  ion has 14 electrons with  $S = L = J = 0$ . The magnetic  $\text{Ce}^{3+}$  with  $S = 1/2$ ,  $L = 3$ ,  $J = 5/2$  has a smaller effective moment  $\mu_{\text{eff}} = 2.54 \mu_{\text{B}}$ . Therefore,  $\text{Yb}^{3+}$  (13 electrons) and  $\text{Ce}^{3+}$  (one 4f electron) are electron-hole analogues and they are frequently treated in theories accordingly. In contrast, the  $\text{Eu}^{3+}$  is non-magnetic ( $4f^6$ ) because  $S = 3$  and  $L = 3$  exactly cancel to  $J = 0$ , while the divalent Eu is magnetic ( $4f^7$ ) with  $S = 7/2$ ,  $L = 0$ ,  $J = 7/2$ , resulting in a very large effective moment of  $\mu_{\text{eff}} = 7.94 \mu_{\text{B}}$ .

Additional to those integer 4f occupations also non-integer occupations are possible, which lead to mixed, intermediated or fluctuating valence. Systems where different (integer) valence states, e.g.  $\text{Eu}^{3+}$  and  $\text{Eu}^{2+}$  are sitting on different crystallographic sites, are called mixed valent. One example for a mixed-valent Yb compound with the mean valence of 2.25 is  $\text{Yb}_4\text{As}_3$ , which is also a heavy-fermion system (with a large linear specific-heat coefficient of  $\gamma \approx 200 \text{ mJ}/(\text{mol K}^2)$  with a low carrier density. The Yb ions occupy four sets of parallel chains oriented along the space diagonals of a cube in the anti- $\text{Th}_3\text{P}_4$  structure. There is one 4f hole per formula unit. The eight Yb sites forming the crystallographic bases are all equivalent by symmetry at high temperatures. Therefore, a homogeneous mixed-valent state with

75 %  $\text{Yb}^{2+}$  and 25 %  $\text{Yb}^{3+}$  states exists, with an equal distribution among the chains. But a structural phase transition into the trigonal R3c structure at room temperature changes the homogeneous mixed-valent state into a charge-ordered state at low temperatures, where the trivalent Yb-ions are arranged along one of the four chain systems (e.g. along a  $\langle 111 \rangle$  direction) [Ochiai 1987], [Rams 1997], [Kimura 1997], [Fulde 1997], [Schmidt 1997]. In contrast, intermediate-valent systems are systems with a quantum mechanically mixture of e.g.  $4f^{13}$  and  $4f^{14}$  contributions. In such a case all lanthanide atoms are equivalent and the valence can take any non-integer value, e.g. 2.88.

Coming back to the comparison of Yb-, Ce- and Eu-based systems, it is necessary to look at the volumes of the ions. The magnetic  $\text{Ce}^{3+}$  has a larger volume than the non-magnetic  $\text{Ce}^{4+}$  ion. This is inverse to the Yb case, where the magnetic  $\text{Yb}^{3+}$  ion has a smaller volume than the non-magnetic  $\text{Yb}^{2+}$ . The trivalent  $\text{Eu}^{3+}$  has, analogue to  $\text{Yb}^{3+}$ , a smaller volume than  $\text{Eu}^{2+}$ , but here  $\text{Eu}^{3+}$  is non-magnetic and the divalent Eu is magnetic. Thus applying pressure shall drive a magnetic  $\text{Ce}^{3+}$  or a magnetic  $\text{Eu}^{2+}$  into the non-magnetic  $\text{Ce}^{4+}$  or  $\text{Eu}^{3+}$  state, but in Yb it shall drive the non-magnetic  $\text{Yb}^{2+}$  state into the magnetic  $\text{Yb}^{3+}$  state.

One of the possible origins for an unequal behaviour in Yb, Ce and U compounds is the different mechanism for delocalisation of f electrons. The  $5f$  electrons in U compounds have a much larger spatial extension than the  $4f$  electrons in lanthanides. Therefore, the direct hybridisation between  $5f$  and ligand electrons can be quite significant and can induce a delocalisation of the  $5f$  electrons without a change of the number of  $5f$  electrons. This mechanism might be relevant for Ce, in which, because it is at the beginning of the Lanthanide row, the ratio between the  $4f$  radius and the  $6s - 5d$  radius is comparatively large. In contrast, for Yb, being at the end of the Lanthanide row, this ratio is much smaller, and thus this direct hybridisation is very likely not relevant. In Yb compounds, the origin of the instability of the  $4f$  shell is that two different valence states can be almost degenerated. Therefore valence fluctuations should play a more important role. As a result

the scenario for transitions from a magnetic to a non-magnetic ground state might be different for Ce, Eu and Yb compounds. Until now a lot of Ce-based compounds have been investigated. Most of them show a smooth and continuous evolution. As an example, Fig. 2.2 shows the phase diagram found for  $\text{CePd}_2\text{Si}_2$  under pressure [Mathur 1998]. At ambient pressure  $\text{CePd}_2\text{Si}_2$  orders antiferromagnetically below a Néel temperature of about 10 K [Dhar 1987]. The Néel temperature was found to decrease slowly and monotonically with increasing pressure and to extrapolate to zero at a critical pressure  $p_c \sim 26$  kbar. At temperatures below 1 K superconductivity appears in a narrow window around  $p_c$ , where  $T_N$  tends to absolute zero. The Ce valence is still almost trivalent at the disappearance of the magnetically ordered state. Thus, the phase diagram from a magnetically ordered ground state into a non-magnetic one for Ce compounds shows a continuous decrease of i) the ordering temperature  $T_N$  down to lowest temperature, ii) the value of the ordered moment, and iii) the free energy of the magnetically ordered state. Up to now, there is no Ce compound where charge ordering leads to a mixed-valent state. There are still many open questions concerning the phase transitions close to the quantum critical point. It is not clear whether this phase transition is of first or second order. And what is the mechanism of the transition from the magnetic state to the non-magnetic one? How can one describe the delocalisation of the f electrons?

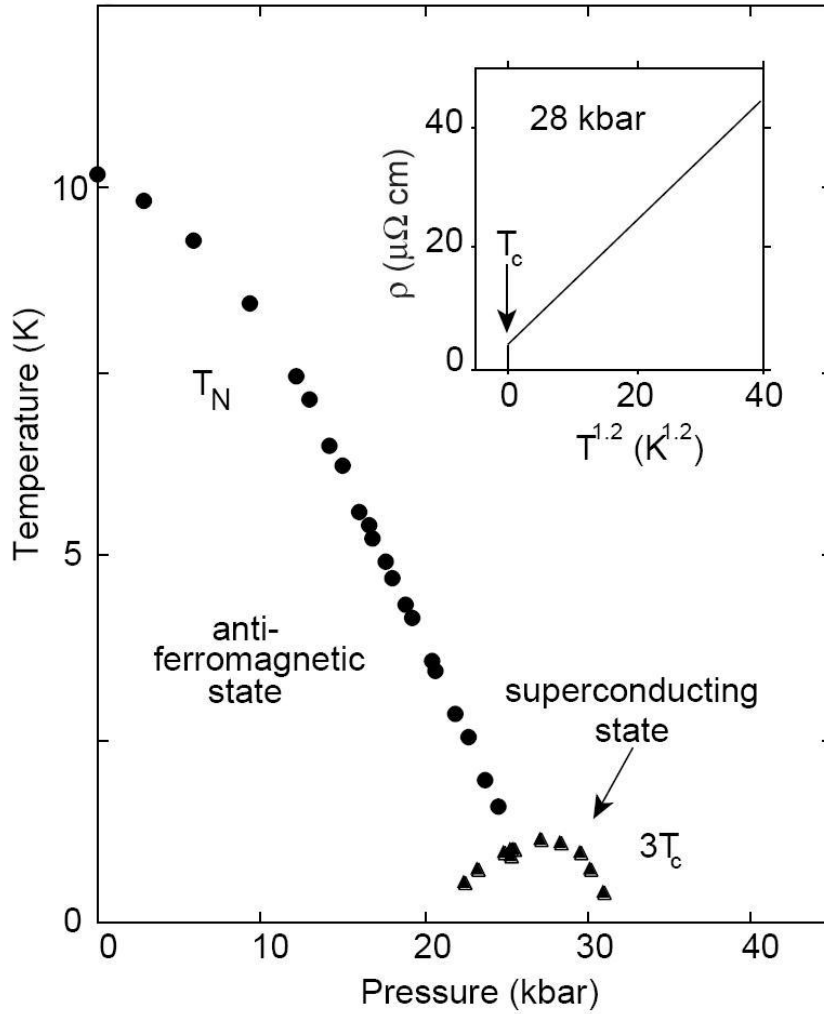


**Figure 2.2:** *The temperature-pressure phase diagram of  $CePd_2Si_2$  shows a continuous decrease of  $T_N$  with increasing pressure (Fig. taken from [Mathur 1998]). Superconductivity appears in a small region around the critical pressure  $p_c$  where  $T_N$  tends to absolute zero.*

Eu systems have a different phase diagram, where no decrease of  $T_N$  and also no decrease of the size of anomalies at  $T_N$  is seen. As an example, the phase diagram for  $EuNi_2(Ge_{1-x}Si_x)_2$  is shown in fig. 2.3. At ambient pressure  $EuNi_2Ge_2$  is antiferromagnetic because of a stable  $Eu^{2+}$  moment. Upon

applying pressure or replacing Ge by Si,  $T_N$  first slightly increases and then the system shows a (chemical) pressure-induced valence transition.

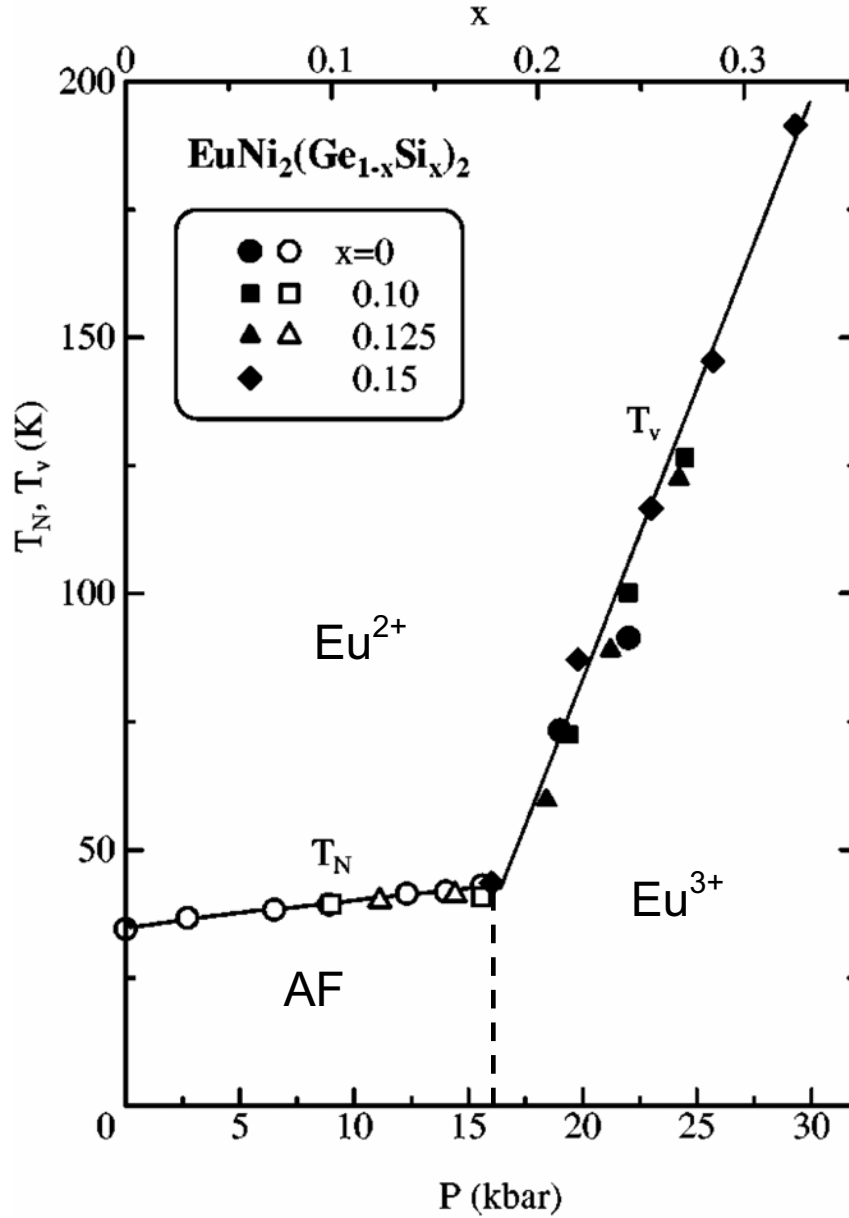


**Figure 2.3:** The generalized pressure/composition-temperature phase diagram of  $\text{EuNi}_2(\text{Ge}_{1-x}\text{Si}_x)_2$  showing the slight increase of  $T_N$  with  $p$  or  $x$  at low pressures or concentrations and the pronounced valence transition at higher  $p$  or  $x$ , where  $T_V$  strongly increases with  $p$  or  $x$  (modified from [Wada 1999]).

The compound undergoes a first-order valence transition from a divalent to an almost trivalent Eu state above the critical pressure or the critical concentration. The first-order valence-transition temperature increases strongly with further increasing pressure or Si concentration before disappearing at a classical end point [Wada 1999]. As a consequence of the pronounced first-order valence transition, Eu systems presenting heavy-fermion or Kondo behaviour are extremely scarce, because in the paramagnetic state the f-fluctuation energy is too large. In many Eu compounds one observes a charge ordering, which leads to a mixed-valent state.

The phase diagrams of Ce systems was explored quite well, a lot of compounds were measured and analysed in the last decades. A well-defined general phase diagram emerged from these studies. In contrast to Ce compounds only a few Yb-based systems were explored and no general phase diagram was yet established. It seems to be much more complicated, because the nature of the phase transition (first or second order) is not clear. The following examples will show this problem in more details.  $\text{YbCu}_2\text{Si}_2$  is an intermediate-valent compound reflecting the strong hybridisation between the 4f localised electrons and the conduction-band electrons [Sales 1976]. It is non-magnetic down to 0.05 mK [Bonville 1985] with a large Sommerfeld constant  $\gamma = 210 \text{ mJ}/(\text{mol K}^2)$  [Thompson 1987]. Applying isostatic pressure larger than  $\sim 8 \text{ GPa}$  induces a magnetically ordered state, but the transition from the non-magnetic to the magnetic state seems to be first order, in contrast to the general behaviour observed in Ce compounds [Alami-Yadri 1997]. However, in the compound  $\text{YbNi}_2\text{Ge}_2$ , which at ambient pressure is quite similar to  $\text{YbCu}_2\text{Si}_2$ , the transition from the non-magnetic to the magnetic state under pressure seems to be second order [Knebel 2001]. Finally, in  $\text{YbRh}_2\text{Si}_2$ , one observes a second-order transition at small negative pressure followed by a first-order transition from a low-moment magnetic state to a high-moment magnetic state at around 8 GPa [Plessel 2003, Dionicio 2005].

$\text{YbInCu}_4$  is the only stoichiometric compound, which undergoes a first-order temperature-induced isostructural valence phase transition at ambient pressure. Yb is in the trivalent state above the critical temperature of  $T_v = 42$  K where the valence drops in a first-order transition by  $\Delta \sim 0.1$  [Felner 1986], [Kojima 1990], [Sarrao 1998], [Nowik 1988], [Mushnikov 2003], [Sarrao 1999], [Aviani 1997]. Such transitions are very rare. The prototypical example is usually the  $\gamma$ - $\alpha$  transition of elementary Cerium. Some Yb compounds show charge ordering leading to a mixed-valence state, like  $\text{Yb}_4\text{As}_3$ . Thus Yb-systems display very different scenarios.

### Theoretical scenarios to describe the QCP

Actually two different models for the description of the non-Fermi-liquid behaviour near quantum critical points are in discussion. The first model, known as spin-density-wave scenario (fig. 2.4), assumes the formation of magnetic ordering due to a spin-density wave instability [Hertz 1976, Moriya 1979, Millis 1993, Moriya 1995, Moriya 2000].

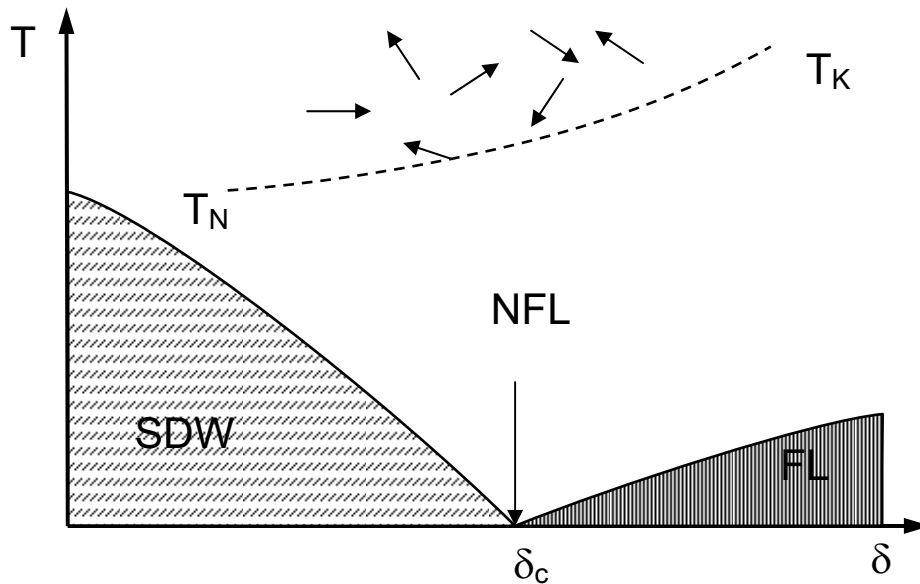


**Figure 2.4:** *Itinerant scenario for a QCP. It shows the phase diagram for a 2D quantum phase transition from an (antiferromagnetic) to a non-magnetic state.*



The local moments are screened on both sides of the quantum critical point below a characteristic temperature  $T_K$  and, therefore, the heavy quasiparticles are formed out of the local  $4f$  electrons and conduction electrons and do not change at the QCP, they are the same on both sides of the QCP. But the Fermi surface of these heavy quasiparticles gets unstable against the formation of a SDW at the QCP. Here magnetic ordering occurs among the heavy quasiparticles. The critical behaviour in this scenario is the same as that of a spin-density-wave transition in a 3d-compound.

For the SDW scenario the scaling theory [Millis 1993] predicts for the two-dimensional antiferromagnetic and three-dimensional ferromagnetic system a logarithmical temperature dependence of  $C(T)/T$ .

$$C(T)/T = a \ln(T_0/T) \quad (3)$$

While for a three dimensional antiferromagnetic system a square-root behaviour is expected.

$$C(T)/T = \gamma_0 - b \cdot \sqrt{T} \quad (4)$$

The spin-fluctuating theory of [Moriya 1995] predicts for a three-dimensional antiferromagnetic system at lowest temperature the following temperature dependence of the specific heat, susceptibility and resistivity:

$$C(T)/T = \gamma_0 - a \cdot \sqrt{T}, \quad (5)$$

$$\chi(T) = 1/(A + B \cdot T^{3/2}), \quad (6)$$

$$\rho(T) = \rho_0 + b \cdot T^{3/2}. \quad (7)$$

The low-temperature region is followed by a crossover area over one decade in temperature, where the dependence of the electronic part of the specific heat and resistivity behave like:

$$C(T)/T \propto \ln(T_0/T), \quad (8)$$

$$\rho(T) \propto T. \quad (9)$$

Here  $T_0$  is the characteristic temperature of the system and can be taken as a measure for the dispersion of the low energy spin fluctuations.

The evolution of the magnetic-ordering temperature was calculated for a three-dimensional ferromagnetic, a three-dimensional antiferromagnetic and a two-dimensional antiferromagnetic system as following:

$$T_{FM} \propto (\delta_C - \delta)^{3/4}, \quad (10)$$

$$T_N \propto (\delta_C - \delta)^{2/3}, \quad (11)$$

$$T_N \propto (\delta_C - \delta). \quad (12)$$

According to the model of Hlubina and Rice [Hlubina 1995] in the SDW scenario so called ‘hot lines’ (2D) or ‘hot spots’ (3D) are formed on the Fermi surface, where strong inelastic scattering occurs, which influence the physical properties of the system. Those ‘hot lines’ or ‘hot spots’ are connected by the magnetic-ordering wave vector  $Q$ . All other areas of the Fermi surface are not much influenced by the inelastic scattering. To clarify the transport properties at low temperatures the scattering on defects has to be taken into account [Rosch 2000]. Therefore, the temperature dependence of the resistivity is different for samples in the clean limit (equation 13) and for samples with defects (equation 14).

$$\rho(T) - \rho_0 \propto T \quad (13)$$

$$\rho(T) - \rho_0 \propto T^{3/2} \quad (14)$$

This model of Rosch describes quite well for example the resistivity behaviour of  $\text{CePd}_2\text{Si}_2$  at the critical pressure of  $p_c \approx 2.8$  GPa under the assumption of weak impurity-scattering.

The alternative model is called the localised scenario [Coleman 1999, Schröder 2000, Coleman 2002, Si 2001, Si 2004] and describes the heavy quasiparticles as a composite bound state formed between the local magnetic moments and the conduction electrons under the influence of the Kondo effect.

In contrast to the itinerant scenario, the local moments play an important role for the QCP in the scenario for a local quantum critical point. Above an effective screening temperature  $T_{loc}^*$  local moments are existing here (fig. 2.5).  $T_{loc}^*$  decreases (coming from the side, where no magnetic order occurs) continuously and reaches zero exactly at the QCP. One can imagine this as the breakdown of the Kondo effect at the QCP due to the competition between the Kondo energy scale and the RKKY interaction. Here magnetic order occurs within the local-moment subsystem. The local-moment scenario was first proposed for  $\text{CeCu}_{6-x}\text{Au}_x$  because of the observation of a

$Q$ -independent  $\omega/T$  scaling in the generalised  $\chi(Q, \omega)$  susceptibility. In the local-moment scenario, one expects a different behaviour of many properties compared to the SDW scenario, although the theory of the local QCP is far less developed than that of the SDW scenario.

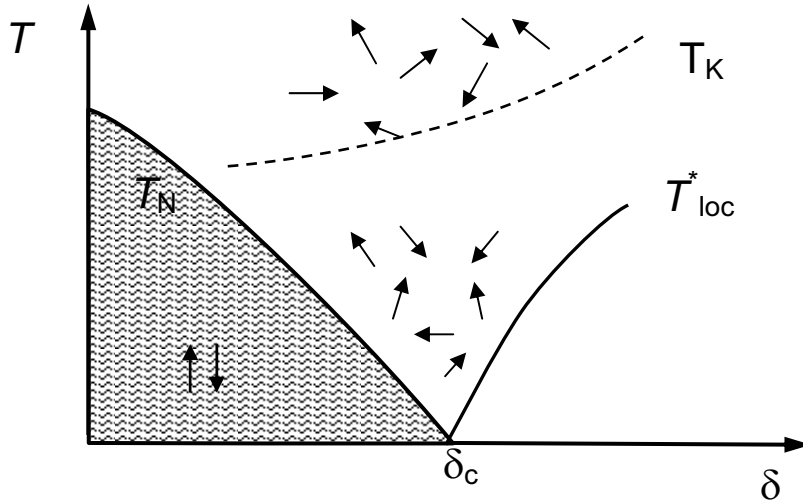


**Figure 2.5:** Local-moment scenario of the QCP. At  $\delta = \delta_c$  the local moments exist down to lowest temperatures and strongly influence the physical properties.

## Content of thesis

Up to now only a few Ytterbium-based heavy fermions were discovered, because of the difficulty in synthesising Yb systems. Ytterbium has a very high vapour pressure and the crystal growth in open systems is often impossible.

A lot of  $RT_2Si_2$  compounds are known, but only very little is known e.g. about Yb compounds with Ge and a transition metal from the Fe or Co columns. Only a few compounds like  $YbNi_2Ge_2$  and  $YbCo_2Ge_2$  have been investigated and both show an intermediate-valent Yb. Therefore, we looked for new  $RT_2Ge_2$  systems, which are close to a QCP. We grew polycrystalline and single-crystalline  $YbFe_2Ge_2$  and investigated their physical properties

(chapter 3). Previously, only the structure of  $\text{YbFe}_2\text{Ge}_2$  had been reported. Our results show an intermediate-valent Yb state with a low characteristic 4f energy. The anomalous behavior of the susceptibility can be fitted at high temperatures ( $T > 100$  K) with a Curie-Weiss law with a surprisingly high effective moment of  $\mu_{\text{eff}} = 6.2 \mu_{\text{B}}$  and a very large Curie-Weiss temperature. These results will be discussed in comparison with the reference compound  $\text{LuFe}_2\text{Ge}_2$ .

The HF system  $\text{YbRh}_2\text{Si}_2$  has attracted strong attention because it is located very close to a QCP connected with the transition from a magnetically ordered ground state to a non-magnetic one. At ambient pressure it orders antiferromagnetically at a very low temperature,  $T_{\text{N}} = 70$  mK. Upon applying a small magnetic field (60 mT) or a slight negative chemical pressure using Ge doping,  $T_{\text{N}}$  disappears at a QCP where the effective mass of the quasiparticles diverges. The proximity to the QCP leads to pronounced non-Fermi-liquid (NFL) behaviour in the resistivity  $\rho(T)$  and the specific heat  $C(T)$  even in pure  $\text{YbRh}_2\text{Si}_2$  in zero field. The low-temperature physics of this system can be explained within the local QCP scenario. Chapter 4 of this work addresses the crystal growth and physical properties of pure and doped  $\text{YbRh}_2\text{Si}_2$  single crystals. Single crystals were grown using a flux technique in closed Ta-crucible. The physical properties, like resistivity and specific heat were measured from room temperature down to 350 mK and susceptibility down to 2 K to get a deeper inside into this system. To cross the quantum critical point by applying negative chemical pressure using Ge doping turns out to be very hard, because of difficulties in the crystal growth. Another possibility to push the system closer to its QCP is La doping on the Yb site. We succeeded with the single-crystal growth of  $\text{Yb}_{1-x}\text{La}_x\text{Rh}_2\text{Si}_2$  with  $0 < x < 0.3$ , which allowed us to study the behaviour upon crossing the QCP.

Attempts to prepare the pure isoelectronic compound  $\text{YbRh}_2\text{Ge}_2$  failed, instead single crystals of  $\text{Yb}_4\text{Rh}_7\text{Ge}_6$  were obtained and investigated (chapter 5). The results evidence a stable  $\text{Yb}^{3+}$  state, which orders presumably antiferromagnetically at 0.49 K. The CEF-ground-state doublet is well

separated from the excited states. The stable  $\text{Yb}^{3+}$  state likely results from the very short Ytterbium-Rhodium and Ytterbium-Germanium nearest-neighbour distances in the  $\text{Yb}_4\text{Rh}_7\text{Ge}_6$ -structure.

The main results of this thesis are summarised at the end in chapter 6.

# 3 YbFe<sub>2</sub>Ge<sub>2</sub> and its ‘reference’ compound LuFe<sub>2</sub>Ge<sub>2</sub>: paramagnetic Fe moment

## 3.1 Introduction

The magnetism in rare-earth (R) transition-metal (T) metalloid (X) compounds with composition RT<sub>2</sub>X<sub>2</sub> and crystallizing in the ThCr<sub>2</sub>Si<sub>2</sub> or related structure types has been the subject of intensive research in the past 30 years [Szytula1989]. While most of the research focuses on the magnetism of the R element, some work has been devoted to the magnetism of 3d-T elements. It is meanwhile generally believed that in these compounds Fe, Co and Ni are non magnetic for X = Si, Ge, while they can become magnetic for X = P and As depending on the valence of the R element. For T = Fe (and X = Si, Ge) early experiments claimed a spontaneous magnetization of the Fe sublattice [Felner1975], but later experiments gave conclusive evidence for a non-magnetic Fe state in those compounds which were investigated more carefully [Szytula1989 and Avila2004]. However investigations of the germanides are rather scarce.

Until now only the structure of YbFe<sub>2</sub>Ge<sub>2</sub> has been reported [Rossi 1978] and the only physical investigation was Mößbauer spectroscopy [Bara1990], which shows no ordering at 300 K. In the course of our study of YbT<sub>2</sub>X<sub>2</sub> compounds, we, therefore, started a detailed investigation of YbFe<sub>2</sub>Ge<sub>2</sub>, and found to our surprise a much larger value of the effective moment at high temperature than expected for Yb<sup>3+</sup>, which pointed to a fluctuating Fe moment of the order of 3.0 μ<sub>B</sub> [Ferstl2003]. During the course of our investigation, Avila et al. [Avila2004] reported an extensive investigation of the series RFe<sub>2</sub>Ge<sub>2</sub> for many rare-earth with the exception of La, Ce, Pm, Eu and Yb. While they notice an enhanced Sommerfeld coefficient and an

enhanced temperature-independent susceptibility in YFe<sub>2</sub>Ge<sub>2</sub> and LuFe<sub>2</sub>Ge<sub>2</sub>, they apparently did not consider the possibility of fluctuating Fe moments. We, therefore, decided to perform our own investigation of LuFe<sub>2</sub>Ge<sub>2</sub> in order to have a reliable basis for the analysis and interpretation of our YbFe<sub>2</sub>Ge<sub>2</sub> results.

Preliminary results on a first polycrystalline YbFe<sub>2</sub>Ge<sub>2</sub> sample already evidence interesting properties. The next step thus was the growth of pure single-crystalline YbFe<sub>2</sub>Ge<sub>2</sub> and LuFe<sub>2</sub>Ge<sub>2</sub> samples allowing a more detailed investigation of their physical properties. We shall report and discuss here measurements of the resistivity, susceptibility and specific heat. Additionally neutron scattering experiments were performed. Our results on YbFe<sub>2</sub>Ge<sub>2</sub> evidence an intermediate-valent (IV) Yb state with a low characteristic energy. The temperature  $T = 16$  K of the well-defined maximum in  $\chi(T)$ , a hallmark for an IV system, is the lowest among all intermediate-valent Yb systems. The susceptibility can be fitted at high temperatures ( $T > 100$ K) with a Curie-Weiss law with an effective moment of  $\mu_{\text{eff}} = 6.2 \mu_{\text{B}}$ , exceeding by far the expected value  $4.54 \mu_{\text{B}}$  for Yb<sup>3+</sup>, and a very large Curie-Weiss temperature. These results will be discussed in comparison with related RT<sub>2</sub>X<sub>2</sub> compounds and their magnetic properties. We propose that the main origin for the anomalous behavior of the susceptibility in YbFe<sub>2</sub>Ge<sub>2</sub> and LuFe<sub>2</sub>Ge<sub>2</sub> is due to fluctuating Fe moments.

## 3.2 YbFe<sub>2</sub>Ge<sub>2</sub>

### 3.2.1 Crystal growth

Investigations of the germanides are rather scarce. Until now only the chemical properties (like crystal structure, lattice parameters and chemical bonds) [Rossi 1978, Bara 1990, Venturini 1996] and melting temperatures [Morozkin 1997, Morozkin 1998] have been successfully established for the RFe<sub>2</sub>Ge<sub>2</sub> series. Compared to other systems such as RCu<sub>2</sub>Si<sub>2</sub> or RNi<sub>2</sub>Ge<sub>2</sub>, the physical properties of the RFe<sub>2</sub>Ge<sub>2</sub> series have not been studied intensively. The main reason is that, while Fe in these compounds is in its non-magnetic spin-paired  $3d^6$  state [Bara 1990], many of the Fe-based impurity phases are strongly magnetic and, even in small quantities, influence the determination of the physical properties of the main phase. Further on, it turned out that the preparation of pure RFe<sub>2</sub>Ge<sub>2</sub> samples is very difficult [Avila 2004].

Several crystal-growth techniques were tried to get YbFe<sub>2</sub>Ge<sub>2</sub> samples. The first attempts were performed using In flux. A stoichiometric amount of the elements Yb, Fe, Ge and an excess of In were weighted in the ratio 4 mol % YbFe<sub>2</sub>Ge<sub>2</sub> : 96 mol % In and placed in an Al<sub>2</sub>O<sub>3</sub> crucible. This crucible was then put into a Ta crucible and sealed. After covering it with zirconium foil it was placed into a GERO furnace. After heating the furnace to a temperature of 1350°C in order to dissolve all elements, a Bridgman technique was used to start the growth process. This crystal growth failed completely, only black needles and powder were obtained after etching the indium. A second attempt using the same technique, but starting at 1400 °C and replacing Fe and Ge by the appropriate amount of binary FeGe also failed. No crystals did form, only a lump containing 50% Yb, 30% Ge and 20% In could be identified.

Neither changing the flux ratio to 2 mol % YbFe<sub>2</sub>Ge<sub>2</sub> : 98 mol % In, nor replacing the In flux by Sn flux (4 mol % YbFe<sub>2</sub>Ge<sub>2</sub> : 96 mol% Sn) were successful. Thus flux methods do not seem very promising for this compound.



In the case of In flux one can invoke the very low solubility of Fe in In, e.g. only 6 at % at 1350°C. In Sn the solubility of Fe is much higher, but still smaller than the solubility of Ge. This might prevent the formation of the YbFe<sub>2</sub>Ge<sub>2</sub> phase, since Fe-rich phases shall form more easily. A general problem for the synthesis and crystal growth of YbFe<sub>2</sub>Ge<sub>2</sub> is very likely the poor miscibility of Yb and Fe. According to the phase diagram of Fe-Yb (Fig. 3.1) a miscibility gap opens in the liquid phase between ~ 25 % Fe and ~ 90 % Fe. In this concentration range the liquid will separate into an Yb-rich liquid and a Fe-rich liquid. Unfortunately the Yb:Fe ratio in YbFe<sub>2</sub>Ge<sub>2</sub>, 1:2, falls within this miscibility gap. However, no phase diagram is available for the Yb-Fe-Ge ternary phase diagram. Thus it is not known how far this miscibility gap extends with increasing Ge content.

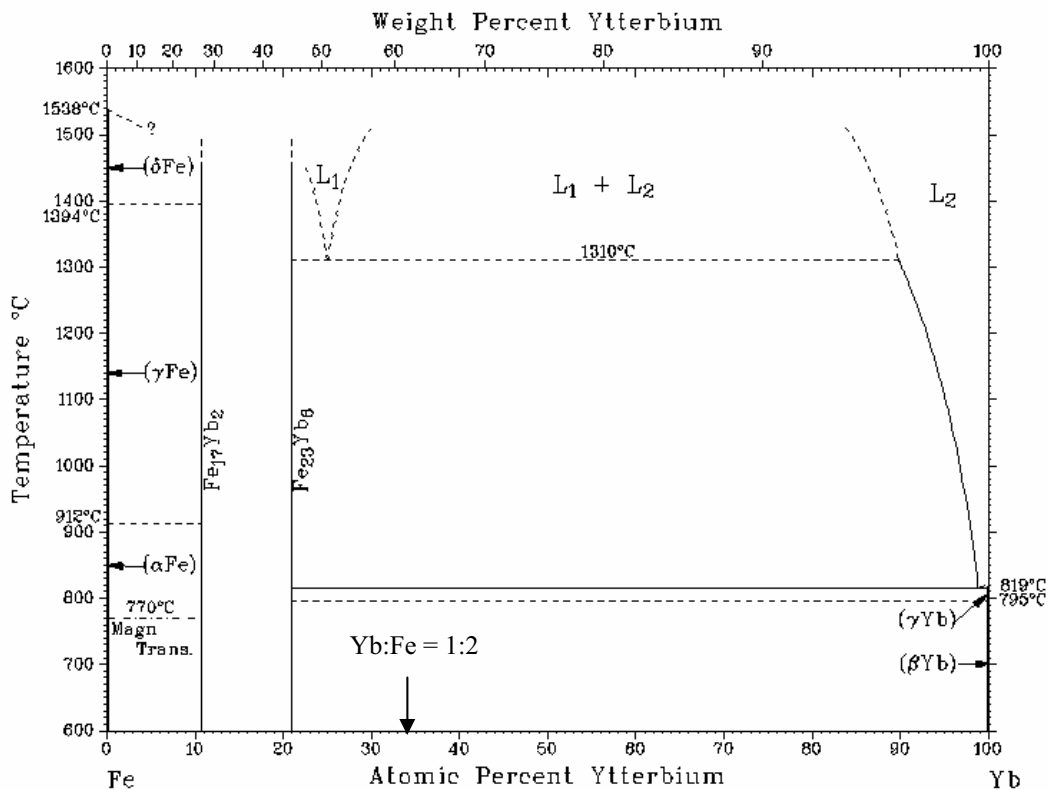


**Figure 3.1:** Phase diagram of Fe-Yb [Massalski 1986c]. Yb : Fe in the ratio 1 : 2 (marked by the arrow) lies within the miscibility gap in the liquid state.

Successful growths of  $\text{YbFe}_2\text{Ge}_2$  were achieved by cooling a nearly stoichiometric melt, without using any flux. We successfully performed several growths with this technique and improved the sample quality by small changes from one batch to the next.

The  $\text{YbFe}_2\text{Ge}_2$  samples were prepared in two steps. In order to avoid the immiscibility between Yb and Fe, we first prepared FeGe by arc-melting a stoichiometric amount of the pure elements. Then a mixture of Yb and the appropriate amount of FeGe was sealed in a tantalum crucible. A few percent of Yb excess were added to account for the evaporation of Yb. Then the single crystals were grown either by pulling down the crucible (Bridgman technique) or by reducing the furnace temperature without moving the crucible (furnace cooling). Typical temperature versus time profiles are shown in Fig. 3.2.

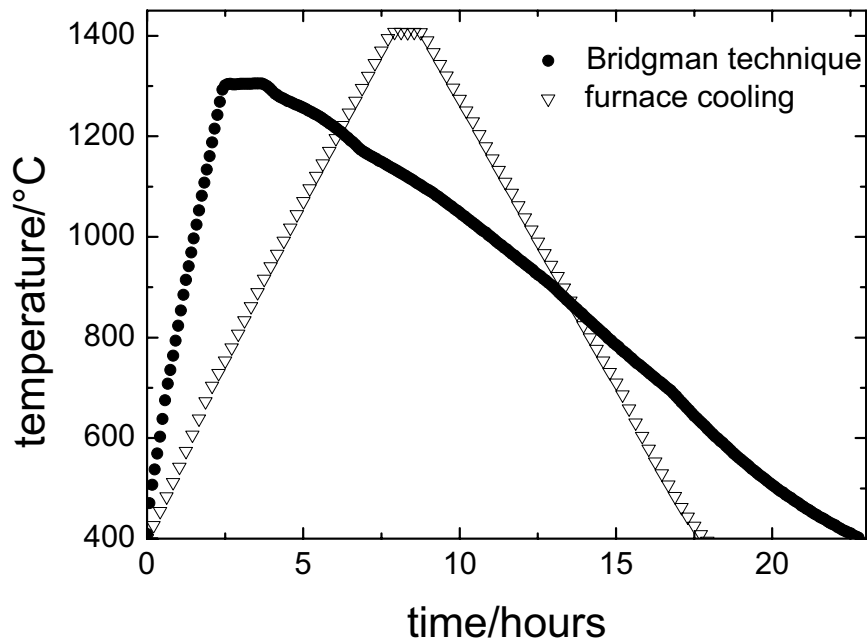


**Figure 3.2:** *Temperature versus time profiles during crystal growth for both growth methods.*

After the crystal growth the surrounding tantalum crucible was cut like an orange to peel out the batch. The first characterisation of the batch was always performed by X-ray analysis. The powder-diffraction pattern (Fig. 3.3) shows the ThCr<sub>2</sub>Si<sub>2</sub> crystal structure (Fig. 3.4) with the lattice constants  $a = 3.936(1) \text{ \AA}$  and  $c = 10.455(3) \text{ \AA}$ , which are slightly different from those of [Rossi 1978]. A small amount of a foreign phase is also present, as evidenced by a few additional lines with very low intensity. Single crystals, embedded in polycrystalline material (Fig. 3.5), were separated by cutting with a diamond saw and polishing the polycrystals off with diamond paste of 6  $\mu\text{m}$  and 1  $\mu\text{m}$ . The quality of the single crystals, with a size of 3 mm x 2 mm x 0.5 mm, was proved by Laue-technique. Most platelets grew perpendicular to the c axis.

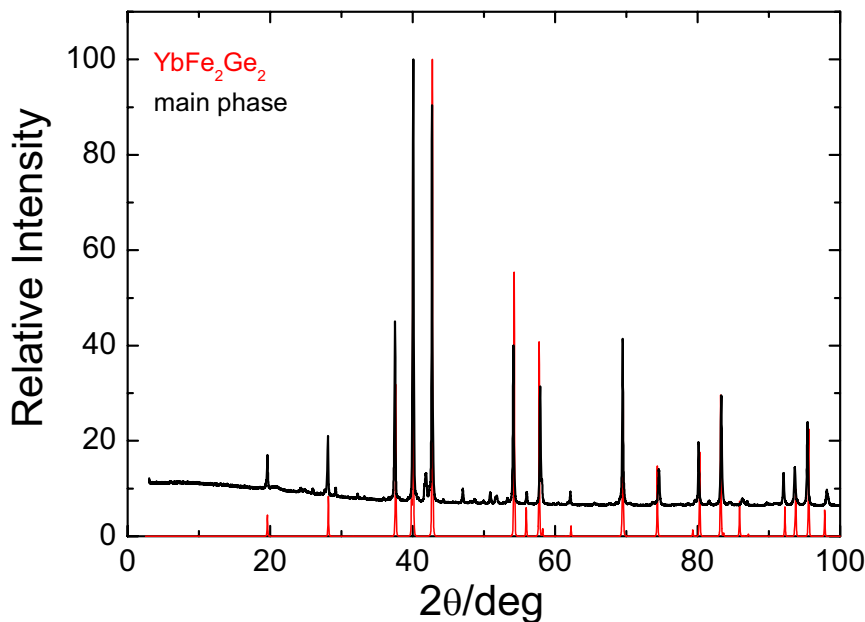


**Figure 3.3:** The powder-diffraction pattern of polycrystalline YbFe<sub>2</sub>Ge<sub>2</sub> (black) shows the peaks of the main phase (red) in the ThCr<sub>2</sub>Si<sub>2</sub> crystal structure and weak additional lines due to a small amount of foreign phases.

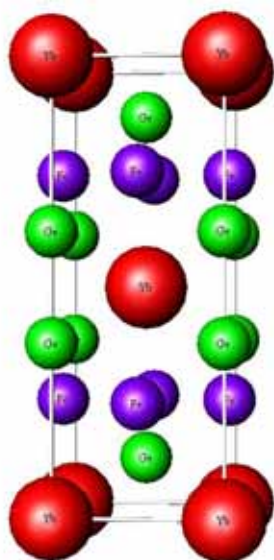


**Figure 3.4:** *The tetragonal unit cell of  $\text{YbFe}_2\text{Ge}_2$  belongs to space group  $I4/mmm$ . The samples crystallise in the  $\text{ThCr}_2\text{Si}_2$  structure with the lattice constants  $a = 3.936(1) \text{ \AA}$  and  $c = 10.455(3) \text{ \AA}$ .*



**Figure 3.5:** *Single crystals of  $\text{YbFe}_2\text{Ge}_2$  embedded in polycrystalline material.*

The best crystals were grown using temperature profiles as displayed in Fig. 3.2, where the highest temperature reached were around 1300°C and 1400°C. Some of the batches were heated up to higher temperature up to 1500°C, but these batches (55027 and 55023) contain crystals with some Yb oxides as foreign phases. Another try to get single crystals using the Yb-self-flux method, with 33% Yb excess did not result in a higher quality. The crystals of this batch (55033) were grown in an Al<sub>2</sub>O<sub>3</sub> crucible inside a sealed Ta crucible using the Bridgman technique. This batch contained only one single crystal of YbFe<sub>2</sub>Ge<sub>2</sub> and a lot of polycrystalline material after the growth process. The quality of the crystals is quite good and comparable with the quality of the crystals grown without any flux. The other try with the self-flux method using a Ta crucible and running a temperature profile was not very successful. The material resulted in polycrystalline YbFe<sub>2</sub>Ge<sub>2</sub> with a lot of foreign phases. Both growths did not improve the crystal quality and, therefore, we used a standard method with the temperature profiles from Fig. 3.2 for the next crystal growths (e.g. to get enough material for the neutron-scattering experiment). The difference between the mentioned crystal growths is best seen in the X-ray powder diffraction patterns (Fig. 3.6). The amount of foreign phases in the polycrystalline material varies from batch to batch. EDAX analysis showed mainly two foreign phases, one Yb-poor phase and the other an Yb-rich phase (both ternary Yb-Fe-Ge phases).

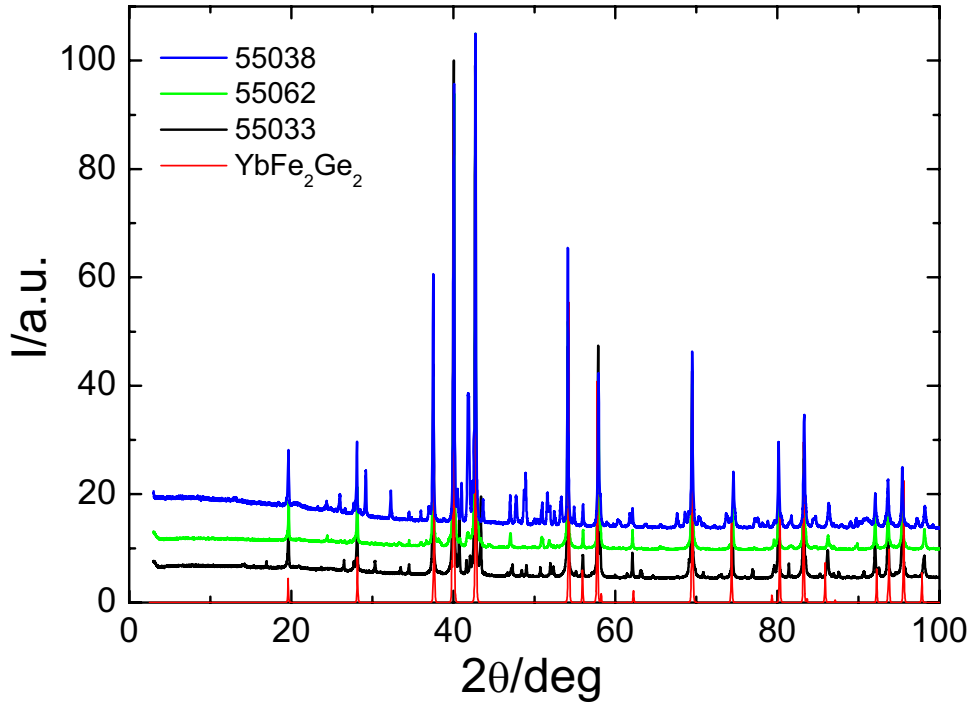


**Figure 3.6:** A comparison of the powder-diffraction patterns of different batches of  $\text{YbFe}_2\text{Ge}_2$ . The blue curve corresponds to the batch with Yb flux using a sealed Ta-crucible (55038). The black data are from the batch with Yb flux using an  $\text{Al}_2\text{O}_3$  crucible inside a sealed Ta crucible (55033). The data of the growth 55062 (green data) was included in order to compare the two previous ones with an optimised crystal growth using Bridgman technique. The successive curves were shifted by +3% for sake of clarity. Additionally, the calculated pattern of  $\text{YbFe}_2\text{Ge}_2$  was included (red) for comparison.

## 3.2.2 Physical properties of YbFe<sub>2</sub>Ge<sub>2</sub>

The resistivity and specific heat were measured with a commercial PPMS equipment using an ac four-contact technique and a relaxation method, respectively. The magnetisation measurements were performed using a MPMS-SQUID magnetometer. Additional resistivity data down to 20 mK were obtained in a dilution refrigerator.

### 3.2.2.1 Resistivity

The resistivity  $\rho(T)$  was measured on two polycrystals and on several annealed and non-annealed single crystals of YbFe<sub>2</sub>Ge<sub>2</sub>.

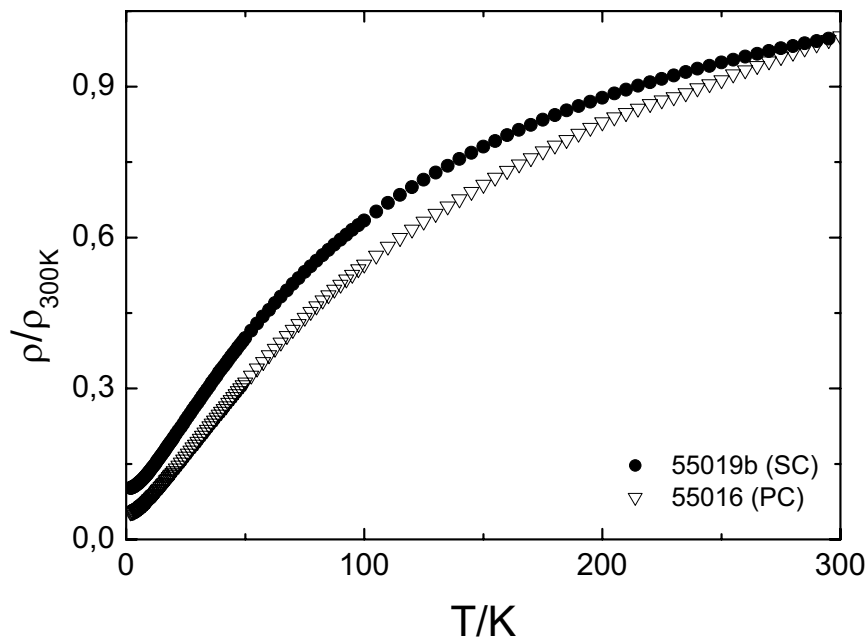


**Figure 3.7:** Comparison of the resistivity of an YbFe<sub>2</sub>Ge<sub>2</sub> single crystal and a polycrystal from different batches in the temperature region from 2 K to 300 K.

For the single crystals the resistivity measurements were done on platelets with the current  $j$  flowing in the plane. Measurements with  $j \parallel c$  could not be performed because of the too small thickness of the single crystals.

The comparison of  $\rho(T)$  of selected crystals is shown in Fig. 3.7. The temperature dependence is reproducible. Only the residual resistivity varies slightly. An absolute value of  $\rho_{2K} = 32 \mu\Omega\text{cm}$  at a temperature of 2 K was calculated for sample 55019a, where it was easy to determine the geometrical factor. The resistivity of YbFe<sub>2</sub>Ge<sub>2</sub> decreases with cooling from room temperature down to low temperatures with a broad curvature, typical for intermediate-valent systems.

No large difference between polycrystalline and single-crystalline material is visible in the temperature dependence of  $\rho(T)$ . A comparison of the resistivity ratio at 2 K of different samples is listed in table 3.1. There is no evidence for a big quality difference between single crystals and polycrystals. Some parts of batch 55019 and 55023 were annealed at a temperature of 850 °C for 310 hours, which improved the sample quality for both batches.

**Table 3.1:** Comparison of the resistivity ratio of different samples from various batches. 55016 is polycrystalline material, whereas all the other samples are single crystals. The letter “G” indicates annealed samples.

sample	RR at 2 K
55016d	$RR_{2K} = 18.5$
55016b	$RR_{2K} = 14$
55019a	$RR_{2K} = 10$
55019b	$RR_{2K} = 10$
55019G	$RR_{2K} = 27$
55023a	$RR_{2K} = 6$
55023Gb	$RR_{2K} = 15.5$
55027a	$RR_{2K} = 16.6$
55027d	$RR_{2K} = 13.4$
55033a	$RR_{2K} = 13.4$



The low-temperature region between 2 and 40 K is shown in Fig. 3.8. Also here all samples show a similar temperature dependence. No anomaly or peak is visible around the temperature of the maximum in  $\chi(T)$  (see chapter 3.2.2.3 magnetic). Between 15 and 40 K the temperature dependence of the resistivity seems to show a linear behaviour. Below 12 K the data show a curvature towards a power law  $\rho = \rho_0 + AT^\varepsilon$  with  $\varepsilon$  approaching 2, the value expected for a Fermi liquid.

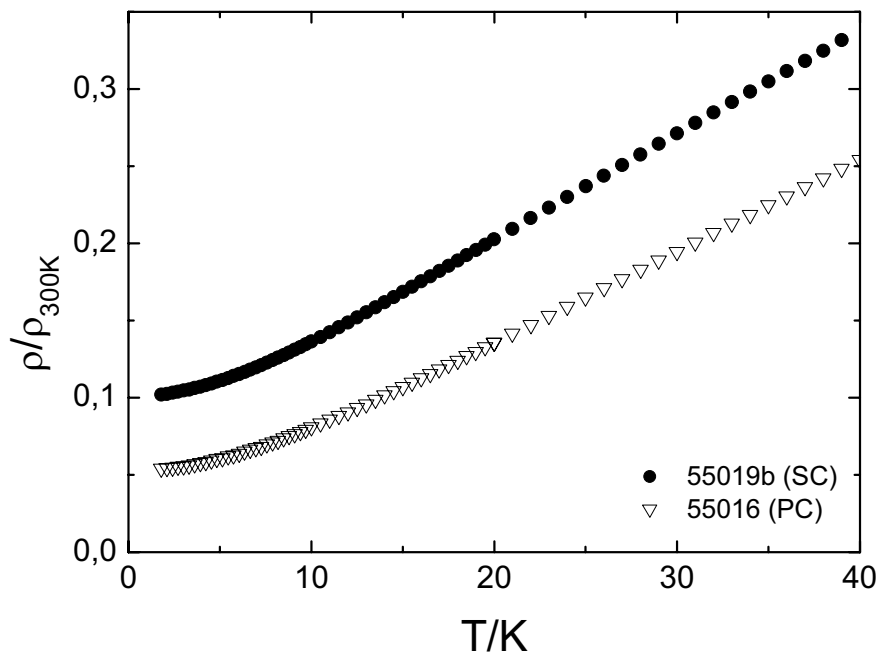


**Figure 3.8:** *Temperature dependence of the resistivity at low temperatures ( $2\text{ K} < T < 40\text{ K}$ )*

Applying a magnetic field leads to an increase of the resistivity below 25 K (Fig. 3.9). This positive magnetoresistance increases with magnetic field and with decreasing temperature. This field dependence shall be discussed below in the context of the presentation of the data taken below 2 K.

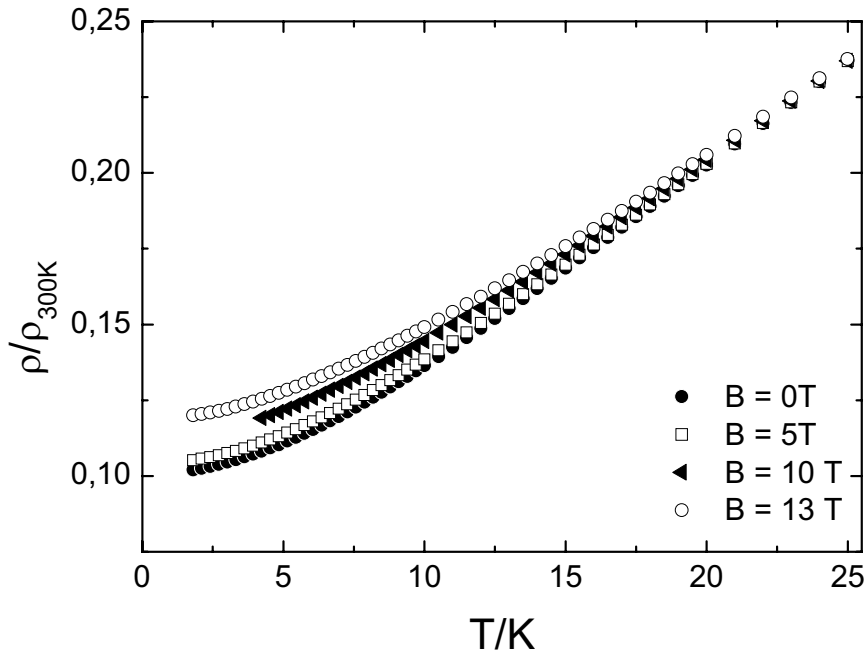


**Figure 3.9:** Influence of a magnetic field on the resistivity below 25 K.

Low-temperature measurements were performed by J. Custers in a dilution refrigerator down to 16 mK and in magnetic fields up to 16 T (Fig. 3.10). In zero field the slope of  $\rho(T)$  seems to decrease only very weakly with decreasing temperature below 1.5 K, resulting in an exponent  $\varepsilon \approx 1.5$  [Custers 2003]. A magnetic field leads to the recovery of a Fermi-liquid  $T^2$  power law in a rather large T range. This has been confirmed by more detailed measurements and more detailed analysis in [Weickert 2006]. The coefficient A of the  $AT^2$  increment is about  $0.16 \mu\Omega\text{cmK}^{-2}$  and does not depend very strongly on the magnetic field. The main uncertainty originates from the unreliable value of the absolute resistivity. The origin of the small exponent in zero field is not clear. A field-induced Fermi-liquid state is commonly observed in systems close to a quantum critical point, There the field suppress critical fluctuation and thus lead to the recovery of a  $T^2$  behaviour. However, we have presently no evidence that YbFe<sub>2</sub>Ge<sub>2</sub> is close to a QCP.

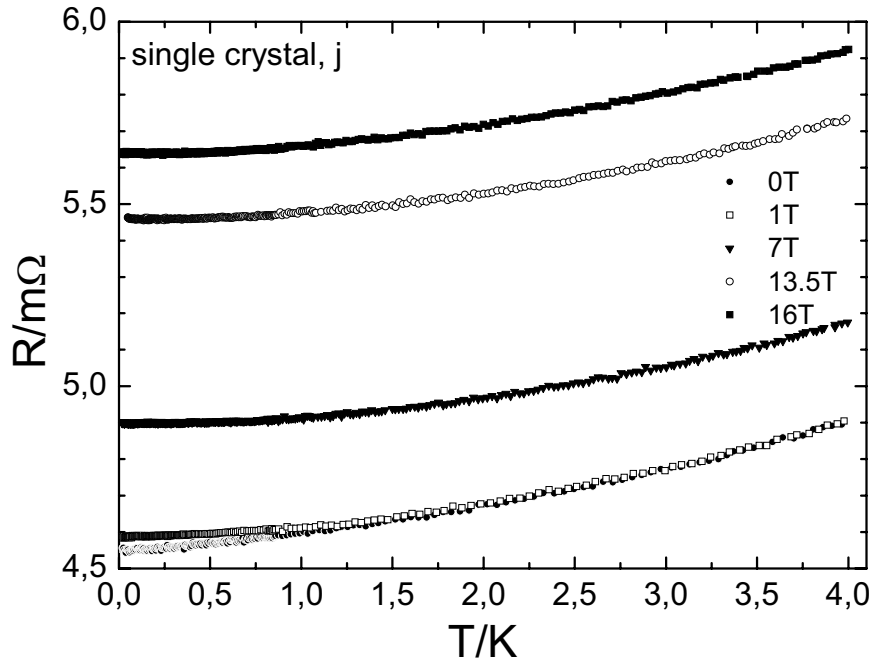


**Figure 3.10:** Low-temperature resistance of YbFe<sub>2</sub>Ge<sub>2</sub> down to 16 mK with applied magnetic field up to 16 T.

Magnetoresistivity measurements were performed at the constant temperature of  $T = 200$  mK up to a magnetic field of 16 T (Fig. 3.11). At low fields ( $B < 10$  T),  $\rho(B)$  increases with a power law ( $\rho(B) = \rho_0 + b B^n$ ) in between linear and quadratic ( $n = 1.5$ ), likely indicating the influence of both closed and open orbits. Around 12 T, the curvature in  $\rho(B)$  changes sign. This is likely related to the broader metamagnetic transition observed in  $M(B)$  measurements.

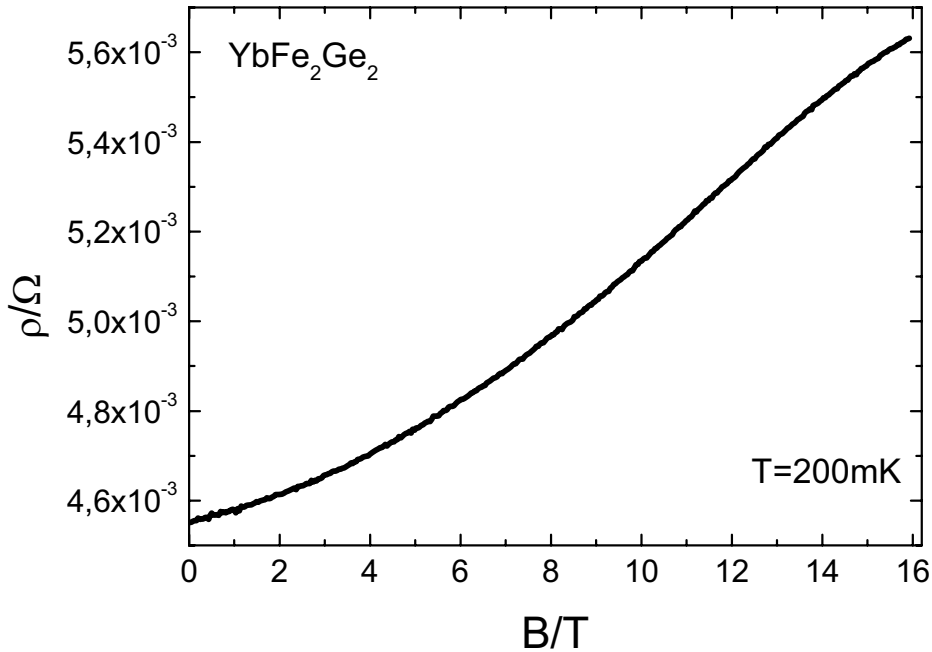


**Figure 3.11:** *The field dependence of the resistance of YbFe<sub>2</sub>Ge<sub>2</sub> at a constant temperature of  $T = 200$  mK shows a positive magnetoresistance.*

### 3.2.2.2 Specific heat

The specific heat of YbFe<sub>2</sub>Ge<sub>2</sub> was measured first on polycrystalline samples and then on single-crystalline material. The single crystals were cut out of the polycrystalline material and polished with the method described earlier. The platelets were oriented perpendicular to the c-axis. After this procedure the single crystals were placed on the ceramic platform of a specific-heat sample holder. All the measured samples produce quite similar results. A typical temperature dependence of  $C(T)$  is shown in Fig. 3.12. It shows the behaviour expected due to the phonon contribution which strongly increases with temperature in this temperature range. All data sets show the same temperature dependence, no matter whether the material is single-crystalline or polycrystalline. Even the annealed sample (55019Ga) does not show a significant difference from the average curve.

A more precise look at the data evidences some difference between the samples, which are best seen in a plot  $C/T$  versus  $T$  (main part of Fig. 3.12). Here we show two extreme curves and the measurement of sample no. 55027a which we believe is the more reliable. While the temperature dependence is identical for all measurements, the absolute values differ by  $\sim 60 \text{ mJmol}^{-1}\text{K}^{-2}$  in the whole temperature range. Below 20 K, this difference is larger than the accuracy expected from the PPMS. We suspect this difference to originate from some amount of foreign phases in the different single crystals.

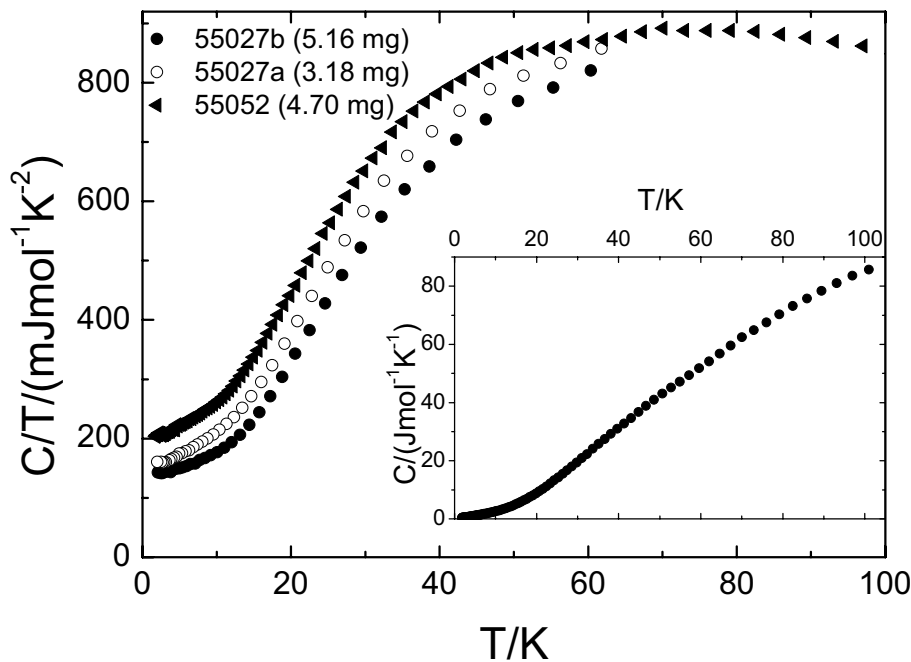


**Figure 3.12:** *The inset shows the specific heat of single-crystalline YbFe<sub>2</sub>Ge<sub>2</sub> (batch 55052) on a linear temperature scale. Main part: The difference between the specific heat of different samples is better seen in a plot of  $C/T$  versus temperature. The temperature dependence of all data sets is quite similar, but the absolute values differ by  $\sim 60 \text{ mJmol}^{-1}\text{K}^{-2}$ .*

Below 25 K, a plot  $C/T$  versus  $T^2$  (Fig. 3.13) shows almost a straight line demonstrating that the specific heat of  $\text{YbFe}_2\text{Ge}_2$  at these temperatures is described quite well by the sum of a linear-in- $T$  electronic contribution  $\gamma T$  and a  $\beta T^3$  phonon contribution. From  $\beta$  one can calculate a Debye temperature of  $\Theta = 253$  K while the Sommerfeld coefficient  $\gamma$  varies between  $150 \text{ mJmol}^{-1}\text{K}^{-2} < \gamma < 210 \text{ mJmol}^{-1}\text{K}^{-2}$ .

It is important to point out, that there is no anomaly visible around  $T = 15$  K, the temperature of the maximum in  $\chi(T)$ . Since the curves reveal below  $T = 10$  K a small hump we performed on a few samples additional measurements in the  $\text{He}^3$  inset down to 350 mK.

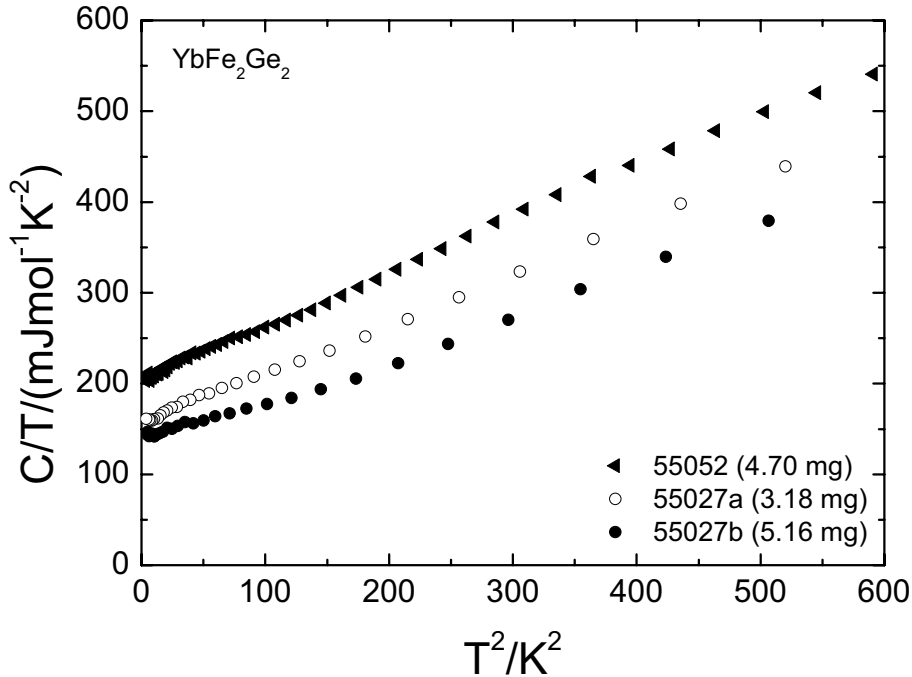


**Figure 3.13:** A plot of  $C/T$  versus  $T^2$  for different  $\text{YbFe}_2\text{Ge}_2$  samples evidencing the  $T$ -linear electronic contribution and the  $T^3$  lattice contribution.

The data of two different samples (with a similar mass) and their overlap with the  $\text{He}^4$  data set of a sample with a comparable mass are shown in Fig.

3.14. The data are plotted as  $C/T$  versus  $T$  with a strongly enlarged  $C/T$  scale, while the inset shows  $C$  versus  $T$ . Both plots demonstrate again that at low temperatures  $C(T)$  is dominated by the linear electronic contribution with a Sommerfeld coefficient  $\gamma \approx 195 \text{ mJmol}^{-1}\text{K}^{-2}$ . However both data sets evidence below 2 K a contribution which increases with decreasing temperature. We suspect that this contribution is related to weak disorder or foreign phases in the sample. The value of the Sommerfeld coefficient ( $\gamma = 195 \text{ mJmol}^{-1}\text{K}^{-2}$ ) is quite large and evidences heavy-fermion behaviour.

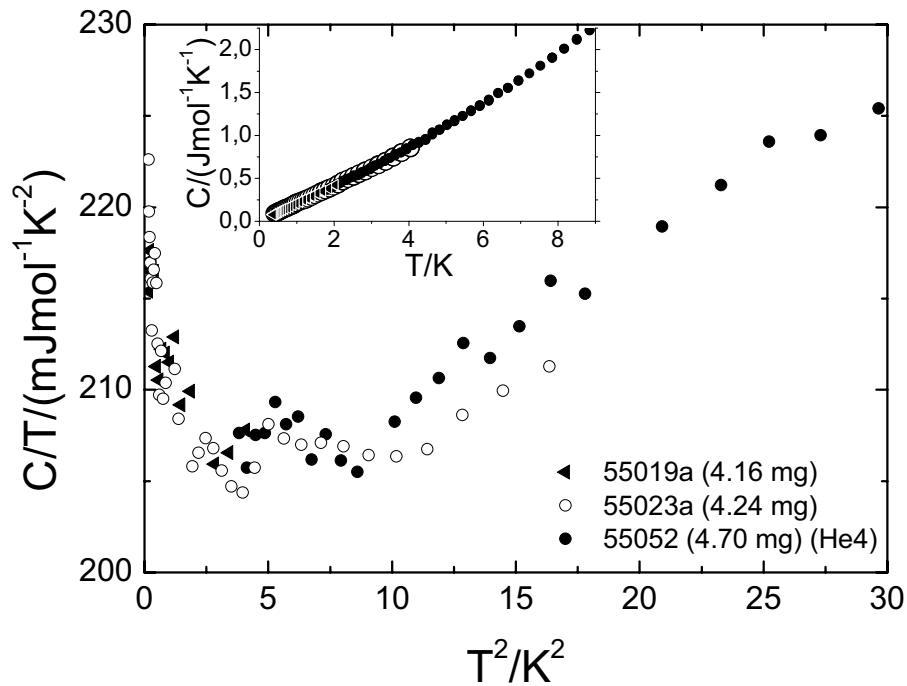


**Figure 3.14:** The low-temperature specific heat of YbFe<sub>2</sub>Ge<sub>2</sub> for different samples with a comparable mass on a plot  $C/T$  versus  $T^2$ . The inset shows  $C$  versus  $T$  and demonstrates that at low temperatures  $C(T)$  is dominated by the linear electronic contribution. The green dots correspond to the result obtained in the He<sup>4</sup> measurement.

### 3.2.2.3 Magnetic properties

All susceptibility and magnetisation measurements were performed using a commercial SQUID magnetometer. Depending on the shape and size of the samples either capsules (for powder or large polycrystals) or special plastic arrangement (for single crystals) were used to fix the sample in the sample holder (which is either a plastic straw or a thin glass tube). The background signal of the plastic straw is negligible compared to the sample signal. For measurements at higher temperatures a thin glass tube is used to hold the sample. The background of this glass tube is not negligible and was subtracted from the whole signal to get the magnetisation of the sample only.

#### 3.2.2.3.1 Susceptibility

The susceptibility of YbFe<sub>2</sub>Ge<sub>2</sub> (Fig. 3.15) was measured first on polycrystalline samples (batch 55016) and then on single crystals (batch 55019). The magnetic field (0.1 T in Fig. 3.15) was applied parallel or perpendicular to the *c* axis of the single-crystalline platelet. All three curves are rather close to each other. Thus these data evidence only a weak anisotropy of the susceptibility. The result of the measurement for the polycrystalline sample lies in between the single crystal data for  $B \parallel c$  and  $B \parallel a$ , but not exactly at  $2/3 \chi_{BIIa} + 1/3 \chi_{BIIc}$ . This indicates some minor difference between the properties of single and polycrystals. Nevertheless the temperature dependence of  $\chi$  is very similar. With decreasing temperature  $\chi$  is increasing below 400 K and presents a broad maximum around 15 K. This behaviour is typical for intermediate-valent Yb systems, although the temperature of the maximum is comparatively low. This indicates a rather low *4f* fluctuation energy and an Yb valence of the order of  $\sim 2.9$ , not far from the trivalent Yb<sup>3+</sup> (see for example [Schlottmann 1993]).



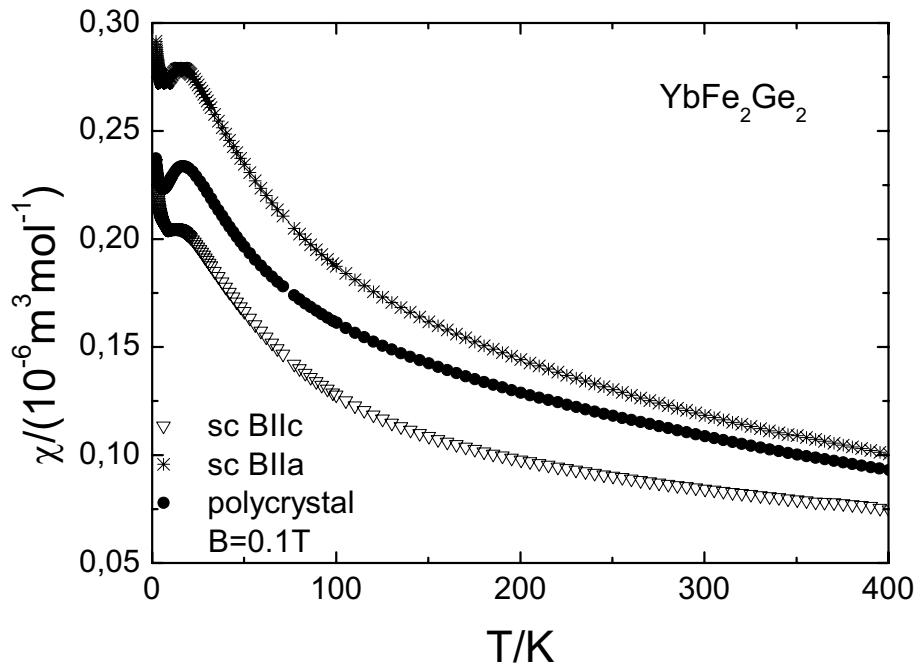


**Figure 3.15:** Comparison of susceptibility data of polycrystalline (55016p) and single-crystalline (55019a) YbFe<sub>2</sub>Ge<sub>2</sub>.

We did not observe a significant field dependence of the susceptibility. The data for the single crystal 55019a (with a mass of  $m = 8.47 \text{ mg}$ ) for  $\mu_0 H = 0.1 \text{ T}$ ,  $1 \text{ T}$  and  $5 \text{ T}$  applied along the  $c$  direction are shown in Fig. 3.16. The most pronounced differences are found at low temperatures, where the low-field data show a Curie-like increase, while the high-field data show saturation. This can be attributed to a small amount of paramagnetic impurities.

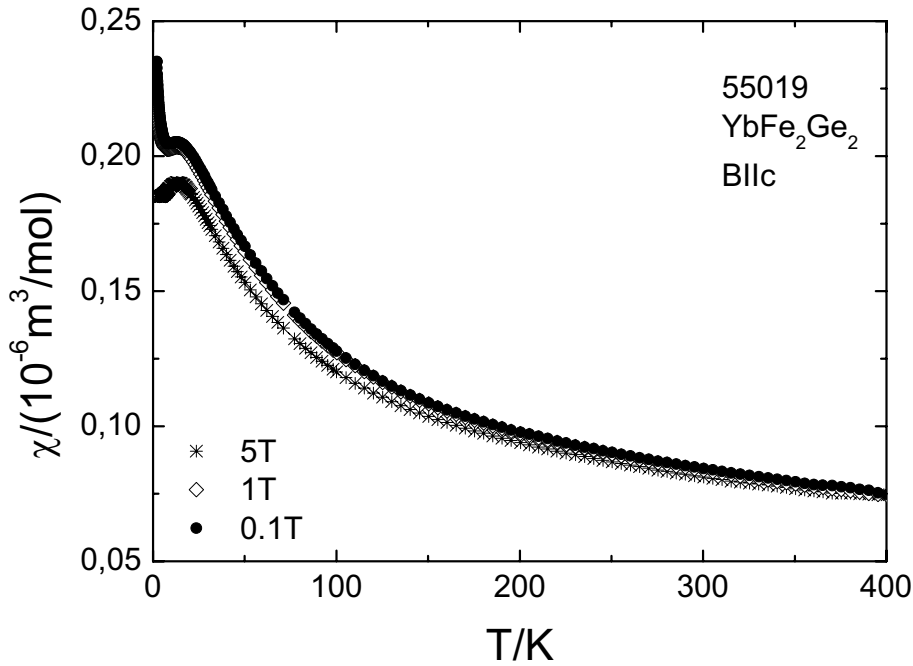


**Figure 3.16:** Susceptibility data for the single crystal 55019a for three different fields along the *c* direction.

The surprise came when we fit the data above 100 K to a Curie-Weiss law. We got an effective moment  $\mu_{\text{eff}} \approx 6 \mu_{\text{B}}$ , much larger than the value  $4.54 \mu_{\text{B}}$  expected for the free Yb<sup>3+</sup> ion. In order to study this anomalous behaviour in more detail, we performed measurements up to 800 K using the special oven for the SQUID (Fig. 3.17).

This measurement demonstrated that the Curie-Weiss law is valid from 100 K up to the upper limit of the measurement and confirmed the large value of  $\mu_{\text{eff}}$  which could now be precisely determined to  $\mu_{\text{eff}} \approx 6.2 \mu_{\text{B}}$ . The observation of such a high moment is very surprising. The only possibility to account for such a large moment seems to be a paramagnetic Fe moment. Because of the low *4f* fluctuation energy and an Yb valence close to trivalent, we can assume that at high temperatures Yb shall have an effective moment close to that of the free Yb<sup>3+</sup> ion. Then the paramagnetic moment on

the Fe can be calculated to  $\mu_{\text{eff(Fe)}} \approx 3.0 \mu_B$  using the formula  $\mu_{\text{total}}^2 = \mu_{\text{eff(Yb)}}^2 + 2 \mu_{\text{eff(Fe)}}^2$ .

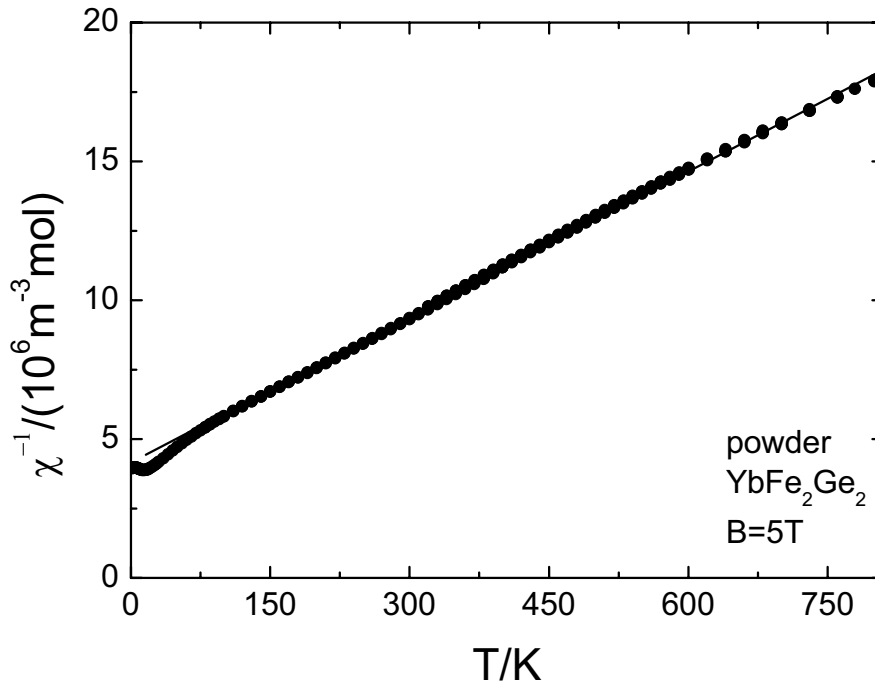


**Figure 3.17:** *The temperature dependence of the inverse susceptibility of powdered single crystals of YbFe<sub>2</sub>Ge<sub>2</sub> up to 800 K evidences a Curie-Weiss behaviour above 100 K. The slope gives the large effective moment of  $\mu_{\text{eff}} = 6.2 \mu_B$ , which is much larger than the expected moment for trivalent Yb ( $4.54\mu_B$ ) and indicates the presence of paramagnetic Fe moments.*

The paramagnetic Weiss temperature is also quite large,  $\theta = -250$  K. Assuming that at high temperatures  $\chi$  is the sum of two independent Curie-Weiss contributions, one due to Yb and one due to Fe, and taking into account that the Curie constants are very similar, one can show that  $\theta$  corresponds roughly to the mean value of the two individual Curie-Weiss temperatures. One can suspect the  $\theta$  value of Yb to be smaller than 250 K, while that of Fe is likely higher.

To my knowledge only manganese is holding a moment in RT<sub>2</sub>X<sub>2</sub> (X = Si, Ge) systems with trivalent rare-earth ions [Szytula 1989]. As stated in the introduction, the magnetism of Ni, Co and Fe in these compounds have been studied quite intensively and the general believe was that they are nonmagnetic. For X = P and T = Co, a change from a divalent R (Eu<sup>2+</sup>) to a trivalent R (Eu<sup>3+</sup>) leads to a transition from a nonmagnetic to a magnetic Co [Chefki 1998]. Our surprising result raised the question whether this fluctuating Fe moment is a consequence of Yb being non-trivalent. In order to settle this question we decided to investigate the homologue LuFe<sub>2</sub>Ge<sub>2</sub> with a stable trivalent Lu (see paragraph 3.3).

### 3.2.2.3.2 Magnetisation

The magnetisation measurements up to 5 T were performed using the SQUID magnetometer. Fig. 3.18 shows the linear field dependence of the magnetisation up to 5 T at the constant temperatures of 2 K, 15 K and 25 K.

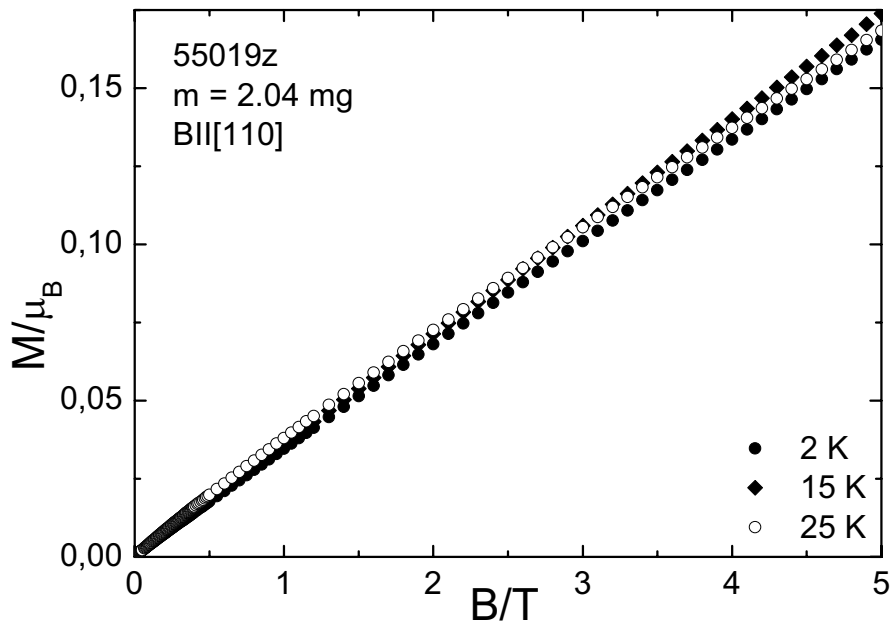


**Figure 3.18:** Magnetisation up to 5 T at four temperatures measured on a commercial SQUID magnetometer.

There is a very small curvature at low fields, which can be attributed to a tiny amount of impurities. All three curves almost overlap in this field region and don't show any anomaly or phase transition. Additional magnetisation data of YbFe<sub>2</sub>Ge<sub>2</sub> (Fig. 3.19) were measured by P. Gegenwart up to 60 T, using the pulsed-field facilities at the High Magnetic Field Laboratory of Los Alamos. The data show no saturation even up to high fields. However there is a clear S-type anomaly in the slope around 16 T for all temperatures, which indicate a weak metamagnetic like behaviour. The broadness of the anomaly suggests that it is rather a crossover than a true cooperative transition.

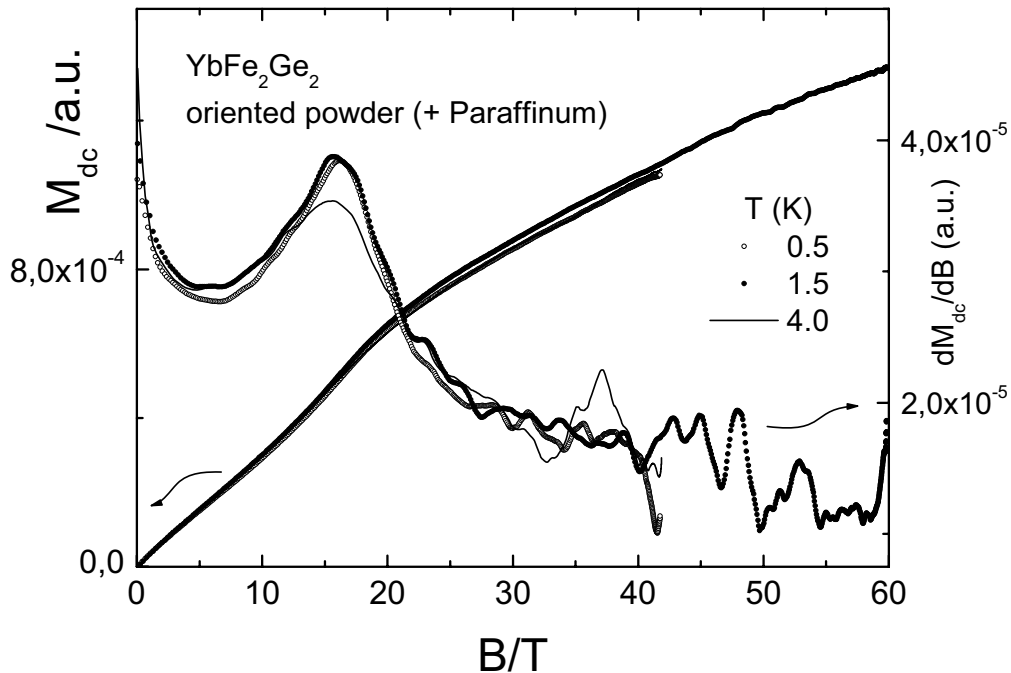


**Figure 3.19:** DC magnetisation up to 60 T, using the pulsed field at the High Magnetic Field Laboratory of Los Alamos. A metamagnetic like anomaly is visible around 16 T.

### 3.3 LuFe<sub>2</sub>Ge<sub>2</sub>

As already stated in the introduction to this chapter, within the RT<sub>2</sub>X<sub>2</sub> family of compounds for X = Si, Ge no moment was yet observed on the transition metals T = Ni, Co and Fe. The only exception is the magnetic moment on manganese [Nowik 1997, Nowik 1995]. In YbFe<sub>2</sub>Ge<sub>2</sub> the Yb atom is intermediate valent and therefore a change in the rare-earth valence might induce a change of the magnetic character of the transition-metal atom. An example for this consideration is EuCo<sub>2</sub>P<sub>2</sub>. At ambient pressure the europium is divalent and orders antiferromagnetically below T<sub>N</sub> = 66.5 K. The cobalt sublattice is nonmagnetic and does not participate in the magnetic ordering. Applying pressure leads to a first-order structural phase transition around p<sub>c</sub> = 3.1 GPa, which changes the P-P distances along the c axis from the nonbonding to the bonding P-P state [Huhnt 1998]. This transition results in a trivalent europium and the cobalt becomes ferromagnetic [Chefki 1998]. The valence change of the Eu from Eu<sup>2+</sup> towards Eu<sup>3+</sup> (which is nonmagnetic) leads to a cobalt sublattice with the magnetic moment of μ<sub>Co</sub> ≈ 0.6 μ<sub>B</sub>. In EuCo<sub>2</sub>P<sub>2</sub> it is the change in the P-P distances along the c axis which leads to this surprising result. Therefore, we started to investigate the compound LuFe<sub>2</sub>Ge<sub>2</sub> with the non-magnetic Lu on the Yb site.

Surprisingly LuFe<sub>2</sub>Ge<sub>2</sub> is not an ordinary, i.e. non-magnetic reference compound. It has an enhanced Sommerfeld constant of γ = 60 mJmol<sup>-1</sup>K<sup>-2</sup> and the results evidence a Curie Weiss behaviour of the susceptibility, which also indicate the presence of a fluctuating Fe moment with μ<sub>eff</sub> = 2.9 μ<sub>B</sub> at high temperatures, as already proposed for YbFe<sub>2</sub>Ge<sub>2</sub>.

#### 3.3.1 Crystal growth

For LuFe<sub>2</sub>Ge<sub>2</sub>, we first prepared polycrystalline samples and then, in a second step, grew single crystals. The polycrystalline LuFe<sub>2</sub>Ge<sub>2</sub> samples were synthesised in an arc furnace. An appropriate amount of the elements

were mixed and put into the cooper heart of an arc furnace. After evacuating and flooding the sample chamber with argon several times a voltage was applied to flash the arc. Melting and mixing of the elements by the high temperature of the arc was achieved. The resulting batch had the shape of a sphere, because of the surface tension of the liquid. Repeating the melting process four times results in a better homogeneity of the sample. Melting the sample again in a high-frequency furnace, after the synthesis in the arc furnace, does not improve the sample quality. The X-ray powder-diffraction patterns are quite similar before HF melting and after (Fig. 3.21) and contain a couple of foreign phases.

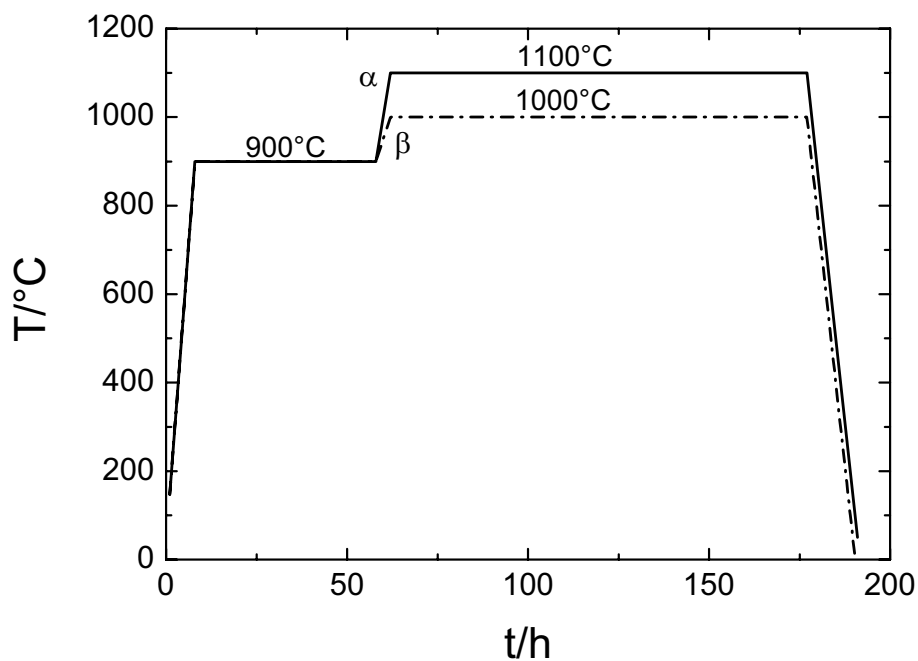


**Figure 3.20:** *Temperature profiles  $\alpha$  and  $\beta$  used for different parts of batch no. 55063.*

One part of batch 55063 was annealed according to the temperature-time profile  $\alpha$  and another part with profile  $\beta$  (Fig. 3.20) under vacuum in horizontal Heraeus furnaces. The samples were placed on a tungsten boat and wrapped into zirconium foil to bind remaining oxygen. After evacuating

and purging the sample chamber with argon several times the furnace was started. Annealing parts of the samples only reduces slightly the amount of foreign phases, as seen in the comparison of the powder diffraction pattern (Fig. 3.21). Some little peaks disappear, but others gain intensity.

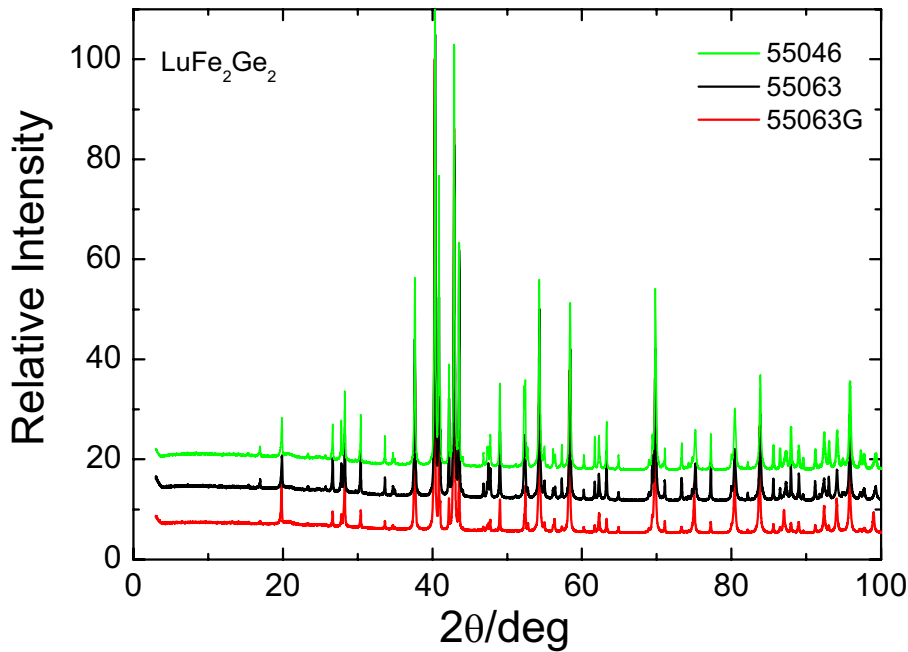
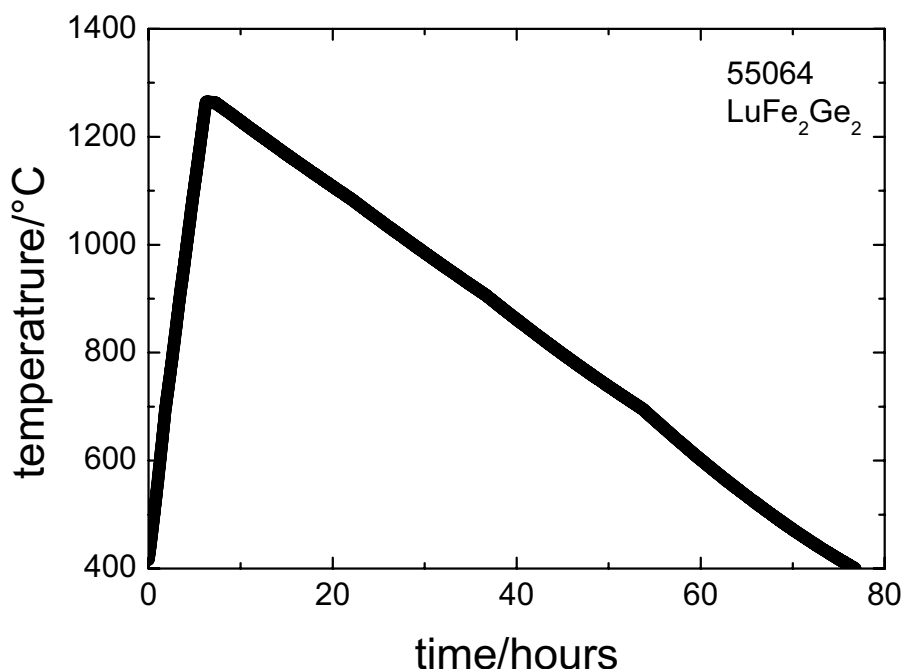


Figure 3.21: Comparison of X-ray powder-diffraction patterns of non-annealed and annealed polycrystalline samples of batch 55063. The black curve shows  $\text{LuFe}_2\text{Ge}_2$  after the melting in an arc and in a high-frequency furnace, while the red curve shows the annealed sample. The green data show sample 55046 (only arc furnace without high-frequency furnace). The data sets of 55063 (black) and 55046 (green) are shifted for clarity.

Preparing polycrystals with the mentioned methods does not result in high quality samples. A completely different approach was to grow single crystals using a flux method. For  $\text{LuFe}_2\text{Ge}_2$  we tried two different fluxes. A first attempt using indium flux failed, because the crystals did not form and the end product after etching the flux was black powder. The result of the



second attempt using tin flux gave high-quality single crystals. The better crystal-growth results with Sn flux is likely related to the higher solubility of Fe in Sn than in In. The LuFe<sub>2</sub>Ge<sub>2</sub> single crystals were grown in Sn flux using an Al<sub>2</sub>O<sub>3</sub> crucible. A mixture of 92% Sn and 8% of stoichiometric Lu and FeGe, where the binary FeGe was obtained by arc melting, was put into an Al<sub>2</sub>O<sub>3</sub> crucible which was then inserted in a Ta crucible. The mixture was dissolved in the Sn flux by holding the temperature at 1200°C for two hours (Fig. 3.22).



**Figure 3.22:** *Temperature-time profile for growing LuFe<sub>2</sub>Ge<sub>2</sub> single crystals from a Sn flux.*

After four days of slow cooling the crucible was taken out of the furnace and the flux was removed by first heating above the melting point of Sn, taking out solid parts containing the crystal and then etching these solid parts with diluted nitric acid. Tin flux is always more difficult to remove than indium flux. The melting temperature is much higher ( $T_{\text{Sn}} = 232.0^\circ\text{C}$ ) in contrast to

In ( $T_{\text{In}} = 156.6^\circ\text{C}$ ) and etching takes much longer. Diluting nitric acid with water in the ratio of 1:1 gives the perfect mixture for removing the tin flux which covers the single crystals. This takes a bit more than 35 hours at a temperature around  $40^\circ\text{C}$ . Shiny platelets with the  $c$  axis perpendicular to the plate were visible. These single crystals, with a size of roughly  $(3 \times 3 \times 0.1) \text{ mm}^3$  were characterised with the same technique as described for YbFe<sub>2</sub>Ge<sub>2</sub>. The X-ray analysis of the powder-diffraction pattern (Fig. 3.23) shows the ThCr<sub>2</sub>Si<sub>2</sub> crystal structure with the lattice constants of  $a = 3.9113(4) \text{ \AA}$ ,  $c = 10.3438(15) \text{ \AA}$  with a  $z$  parameter for the Ge position of 0.38023 [Cardoso 2005]. Foreign phases were not found, neither in the powder-diffraction pattern nor in microprobe analysis of the surface using energy-disperse X-ray analysis.

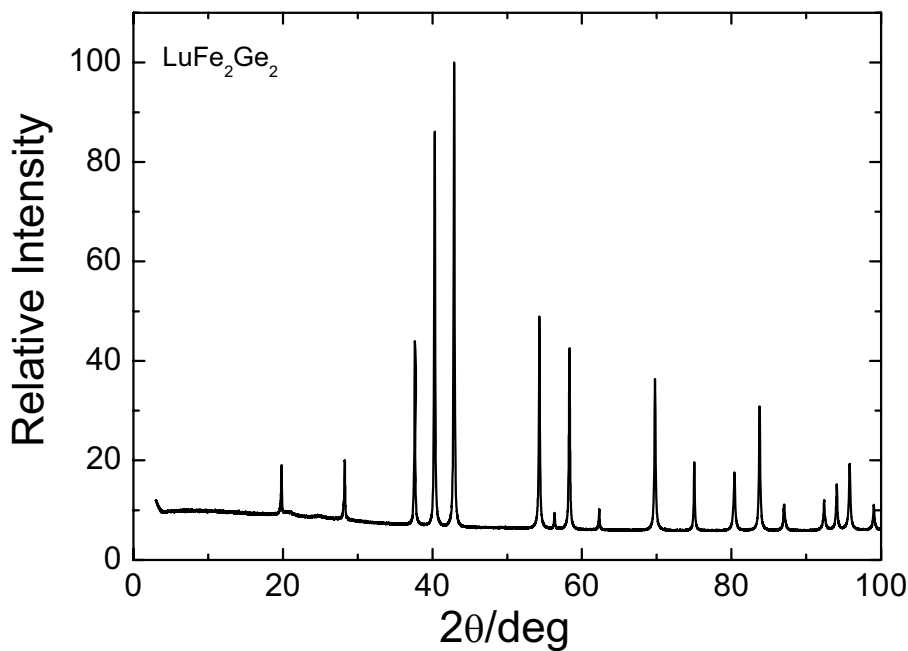


**Figure 3.23:** The powder diffraction pattern of LuFe<sub>2</sub>Ge<sub>2</sub> crystals shows a pure phase with ThCr<sub>2</sub>Si<sub>2</sub> crystal structure. No foreign phases are visible.

### 3.3.2 Physical properties of LuFe<sub>2</sub>Ge<sub>2</sub>

The resistivity and specific heat were measured with the same equipment, a commercial PPMS. The susceptibility was determined using a MPMS SQUID magnetometer.

#### 3.3.2.1 Resistivity

The resistivity (Fig. 3.24) of LuFe<sub>2</sub>Ge<sub>2</sub> was measured on two single crystals from batch 55064. Both data sets are very similar over the whole temperature region from 2 to 300 K.

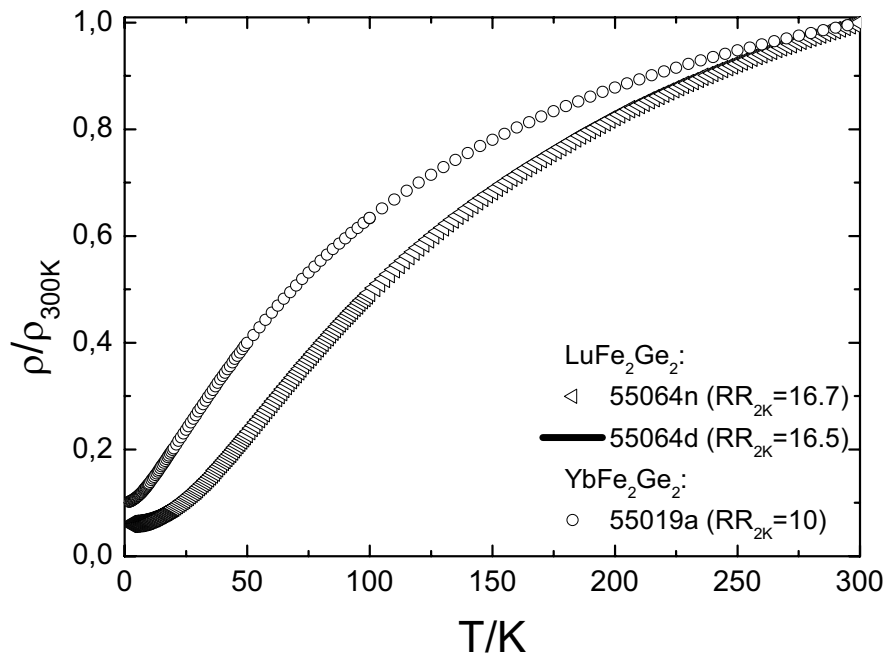


**Figure 3.24:** Resistivity of two different LuFe<sub>2</sub>Ge<sub>2</sub> single crystals and one YbFe<sub>2</sub>Ge<sub>2</sub> single crystal in the temperature range of 2 K to room temperature. The residual resistivity ratio at 2 K has a value of 16.5 and is a sign for the good quality of the single crystals,  $\rho_{300K}$  is approximately 200  $\mu\Omega\text{cm}$ .

The resistivity decreases upon cooling from room temperature with a weak constant negative curvature down to 100 K followed by a clear positive curvature below 30 K.

Eventually  $\rho(T)$  merges in the temperature independent residual resistivity. The residual resistivity ratio at 2 K of 16.5 is quite good, indicating a rather good quality of the single crystals. For comparison the data of YbFe<sub>2</sub>Ge<sub>2</sub> (sample 55019a) were added, which show a higher scattering rate than LuFe<sub>2</sub>Ge<sub>2</sub> at low temperatures.

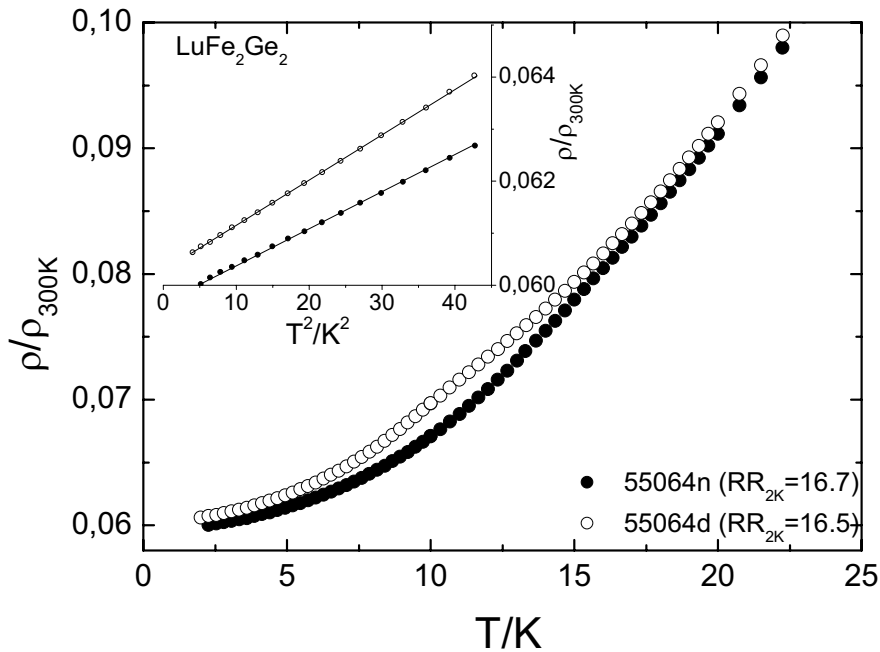


**Figure 3.25:** Resistivity for LuFe<sub>2</sub>Ge<sub>2</sub> in the temperature region between 2 and 25 K. The inset shows the data on a quadratic temperature scale below 7 K to demonstrate the  $T^2$  behaviour. The lines are only guides to the eyes.

A more detailed look at the low temperature part of the data (Fig. 3.25) shows that the two sets of data start to deviate from each other below 25 K, the difference being largest around 10 K. While sample 55064n shows a very smooth temperature dependence,  $\rho(T)$  of sample 55064d suggest the presence of a kink at this temperature. This kink is very likely related to the

anomalies observed in  $\chi(T)$  and  $C_p(T)$  which indicate the presence of a phase transition at  $T_0 = 9$  K. The comparison of both resistivity curves suggests that the transition is present in sample 55064d, but suppressed in sample 55064n. Independently of the behaviour around 10 K, both curves evidence a well behaved  $T^2$  power law  $\rho(T) = \rho_0 + AT^2$  below 6 K, as shown in the inset of Fig. 3.25, where  $\rho(T)$  is plotted versus  $T^2$ . These plots lead to coefficients of  $A = 0.014 \mu\Omega\text{cmK}^{-2}$  and  $A = 0.017 \mu\Omega\text{cmK}^{-2}$  for sample 55064d and 55064n, respectively. It is very surprising that  $\Delta\rho$  is dominated by electron-electron interaction, instead of electron-phonon interaction as expected here. This and the value of  $A$  shall be discussed more precisely later.

### 3.3.2.2 Specific heat

The specific data of LuFe<sub>2</sub>Ge<sub>2</sub> was measured on both polycrystalline and single-crystalline material in zero field in the temperature range of 2 to 100 K. Very interesting and unusual is the high  $C/T$  value at low temperatures. For non magnetic “reference” compounds based on Lu, Y or La one expects only a small value of  $\gamma_0$  (in the order of a couple of mJ/molK) related to the electronic contribution to the specific heat of a normal metal. Compared to other La, Lu or Y reference compounds the iron-germanium based ‘reference compounds’ show larger values with  $\gamma_0 = 60 \text{ mJmol}^{-1}\text{K}^{-2}$  for both YFe<sub>2</sub>Ge<sub>2</sub> and LuFe<sub>2</sub>Ge<sub>2</sub> [Avila 2004]. Furthermore, the data of the single crystals show a peak around 8.5 K, which is not visible in the polycrystalline samples. The specific heat of several polycrystalline samples from different batches is shown in Fig. 3.26. Sample 55041Gu (green circles) is a part of batch 55041 which was annealed to improve the sample quality. There is no visible difference between the annealed and the non-annealed samples. The inset of Fig. 3.26 shows  $C/T$  versus  $T^2$  in the temperature region between 2 and 20 K,  $C/T$  follows nicely a power law  $C = \gamma T + \beta T^3$ . A Debye

temperature of  $\Theta = 267$  K could be calculated from  $\beta$ . This value is comparable with the value of  $\Theta = 253$  K obtained for YbFe<sub>2</sub>Ge<sub>2</sub>.

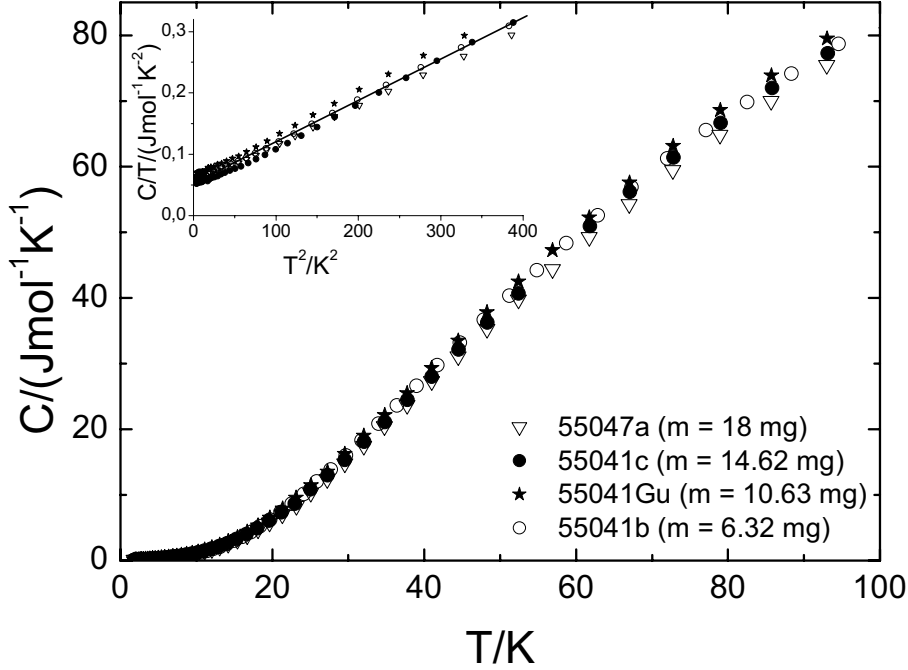


**Figure 3.26:** Comparison of the specific heat data of polycrystalline LuFe<sub>2</sub>Ge<sub>2</sub> samples from different batches in the temperature range of 2 to 100 K. The inset shows the quadratic temperature dependence of  $C/T$  at low temperatures. The anomaly around 8.5 K visible in the single-crystal data could not be resolved.

In comparison to the single-crystal data no anomaly around 8.5 K could be resolved. The data for the single-crystalline material is presented in Fig. 3.27, where a plot of  $C/T$  versus  $T^2$  (inset) shows this anomaly best. To have a comparison with the polycrystalline samples the data set of sample 55041c was added. We suspect that the difference in the absolute values between both sets of data is mainly due to the small value of the absolute specific heat of the sample in comparison to the specific heat of the addenda, resulting in a rather large error when doing the subtraction. The value of the

pure addenda at 2 K is 0.3  $\mu\text{J}/\text{K}$ , which is quite large compared to the contribution of the sample with 1.4  $\mu\text{J}/\text{K}$ . The overall temperature dependence of the specific heat of single and polycrystalline LuFe<sub>2</sub>Ge<sub>2</sub> are similar and in accordance to the data from Avila [Avila 2004]. Our absolute  $C_p$  values for both single crystals and polycrystals are slightly smaller.

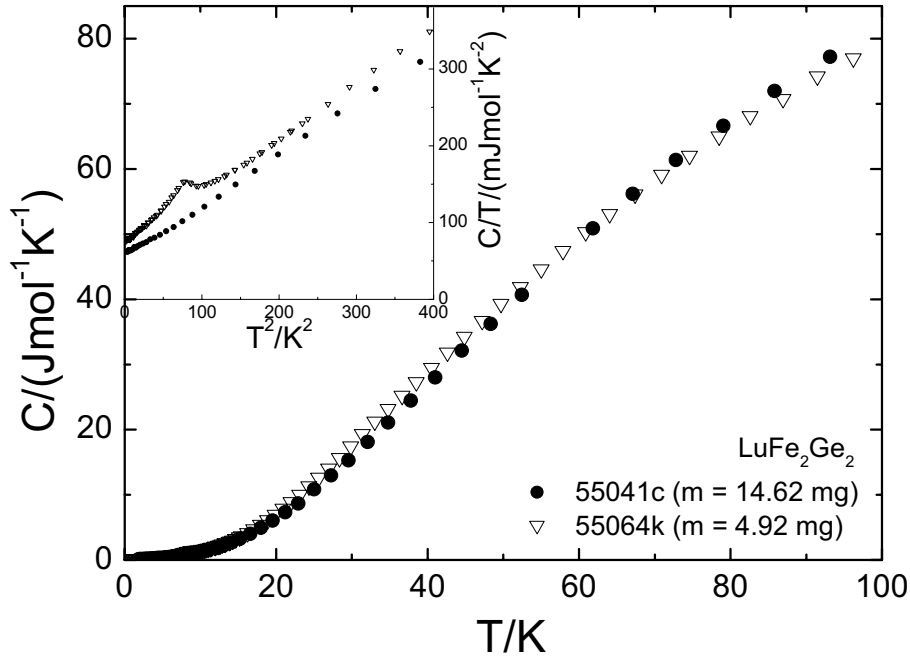


**Figure 3.27:** Specific-heat data of the LuFe<sub>2</sub>Ge<sub>2</sub> single crystal 55064k ( $m = 4.92$  mg) up to 100 K on a linear temperature scale in comparison with one of the polycrystalline samples 55041c ( $m = 14.62$  mg). The inset shows  $C/T$  versus a quadratic temperature scale. Around 8.5 K a small peak is visible in the single-crystal data indicating a phase transition.

The  $\gamma$  value we determine in our polycrystalline samples amounts to  $(60 \pm 10)$   $\text{mJmol}^{-1}\text{K}^{-2}$ , in good agreement with results obtained by Avila et al [Avila 2004]. At low temperatures  $C/T$  of the single crystal is slightly larger than for the polycrystals, resulting in a slightly larger  $\gamma$  value of  $\gamma = (77 \pm 3)$   $\text{mJmol}^{-1}\text{K}^{-2}$ . The peak visible in the specific heat of the single crystal was already observed by [Avila 2004]. The specific-heat data in the temperature

region between 5 and 14 K with different selected applied magnetic fields are shown in Fig. 3.28. For a better view the data sets are shifted parallel to the temperature axis proportional to the applied magnetic field, e.g. the 3 T data set is shifted by 30 mJmol<sup>-1</sup>K<sup>-2</sup>. Small oscillations visible around 4 and 2.3 K are due to problems with the temperature calibration, which will be discussed in the chapter La/YbRh<sub>2</sub>Si<sub>2</sub>. Applying magnetic fields ( $B \parallel c$ ) up to 13.5 T reduces the maximum and shifts it slightly to lower temperatures. This was graphically proved by a “Zwickelabgleich”, which evidences a  $T_c$  shift from 8.9 K (at 0 T) towards 8.5 K (at 13.5 T) with a reduction of  $\Delta C/T$  from 35 mJmol<sup>-1</sup>K<sup>-2</sup> to 27 mJmol<sup>-1</sup>K<sup>-2</sup>. Additional measurements on a different sample gave the same results. Above 14 K the data points overlap again until 100 K.

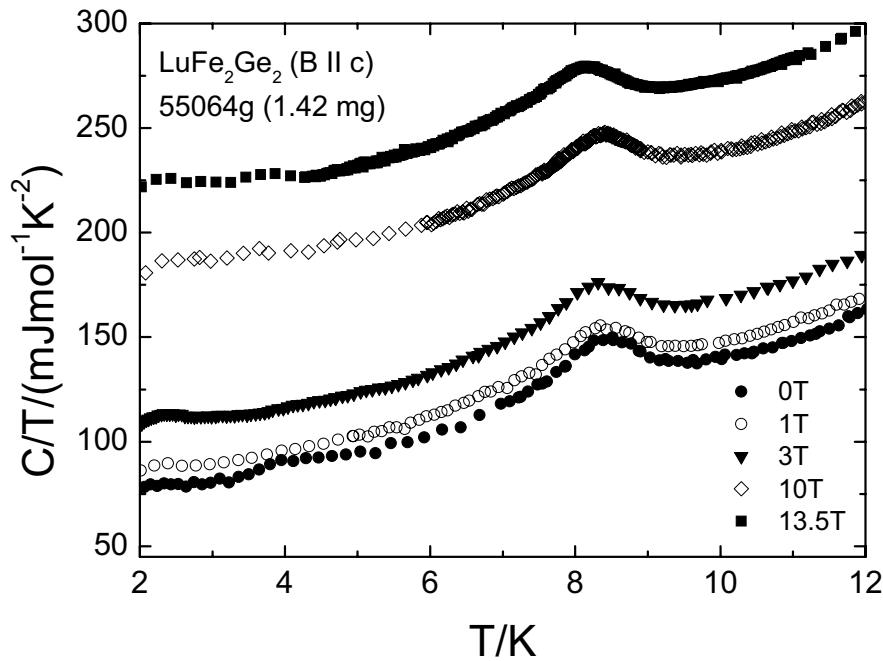


**Figure 3.28:** Specific heat of LuFe<sub>2</sub>Ge<sub>2</sub> single crystals with applied magnetic fields ( $\mu_0 H \parallel c$ ) up to 13.5 T. The plot shows  $C/T$  on a linear temperature scale between 2 K and 12 K. For a better view the data sets are shifted parallel to the temperature axis proportional to the applied magnetic field, e.g. the 3 T data set is shifted by 30 mJmol<sup>-1</sup>K<sup>-2</sup>.



### 3.3.2.3 Magnetic properties

All susceptibility and magnetisation measurements were performed in a commercial SQUID magnetometer. For measurements at higher temperatures a special oven for the SQUID magnetometer was used. The sample was fixed in a thin glass tube. The background of this glass tube was subtracted from the whole signal, to get the magnetisation of the sample only.

#### 3.3.2.3.1 Susceptibility

The susceptibility of LuFe<sub>2</sub>Ge<sub>2</sub> was measured on single crystals and powdered single crystals. Figure 3.29 shows measurements for several single crystals in an applied field of 5 T parallel and perpendicular to the c axis.

Figure 3.29 evidences three obvious results: i) The susceptibility of LuFe<sub>2</sub>Ge<sub>2</sub> presents a significant temperature dependence, in contradiction to the temperature-independent susceptibility expected for a nonmagnetic metal. ii) There is a weak anisotropy,  $\chi$  for field along the basal plane being slightly larger than for field along the c direction. iii) Although the temperature dependence is similar for all data sets, there is non-negligible scatter between the different measurements. This scattering was found to result from two different problems. On one hand, the weakness of the susceptibility of LuFe<sub>2</sub>Ge<sub>2</sub> combined with the smallness of the single crystals resulted in quite small values of the absolute moment, making the results very sensitive to background effects. But the main problem arises from the ferromagnetic contribution of a foreign phase. As already pointed out by Avilla et al. [Avila 2004], it is extremely difficult to prepare RFe<sub>2</sub>Ge<sub>2</sub> samples free of ferromagnetic foreign phases. The evidence for this ferromagnetic foreign phase and the way we deal with it shall be presented further below.

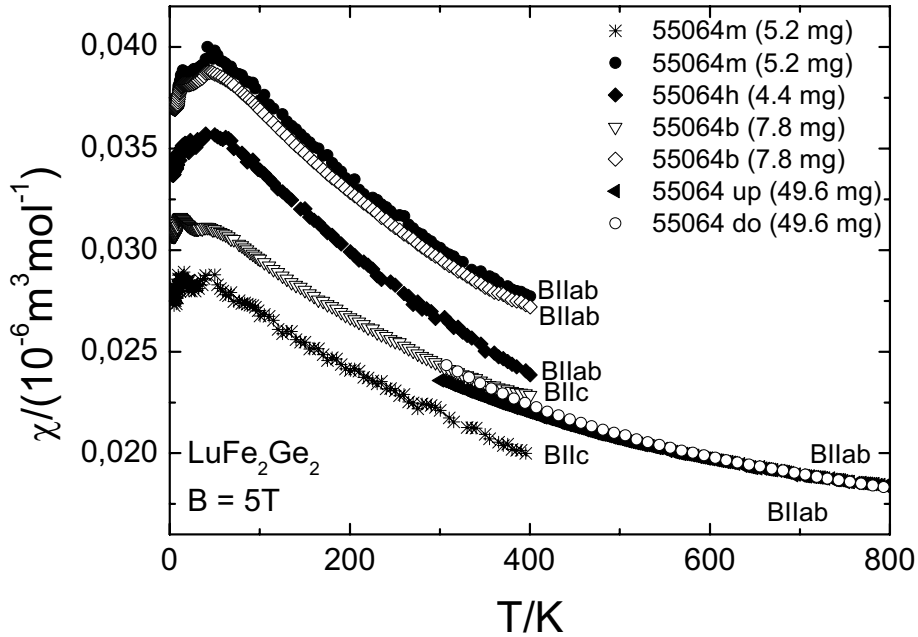


**Figure 3.29:** Susceptibility of several single crystals in an applied field of 5 T perpendicular and parallel to the *c* axis of the crystals. Additional measurements up to 800 K also show a temperature-dependent susceptibility. The peak at 30 K in some of the data sets is due to a technical problem with the equipment.

Despite the scatter between different measurements, a plot  $1/\chi$  versus  $T$  for all data (Fig. 3.30) demonstrates that the main feature we claim to be present in LuFe<sub>2</sub>Ge<sub>2</sub>, the presence of a Curie-Weiss susceptibility with a quite large effective moment, is clearly visible in all curves. The effective moment calculated from these plots varies between 3.9  $\mu_B$  per mole and 4.2  $\mu_B$  per mole for  $B \parallel c$  and between 3.9  $\mu_B$  per mole and 4.4  $\mu_B$  per mole for  $B \perp c$ , while the paramagnetic Weiss temperature scatters between -775 K and -875 K for  $B \parallel c$  and between -600 K and -800 K for  $B \perp c$ . The results of the measurements at higher temperatures seem to be shifted compared to those at low temperatures, but we had strong difficulties doing these high-temperature measurements because of reaction of the sample at higher

temperatures and because of a much larger background. An evidence for oxidation of the sample is the small discrepancy between the data obtained during heating (55064up) and the data obtained during cooling of the sample (55064down). Thus we suspect these data to be less reliable than the low-temperature data. Nevertheless, the slope (and thus  $\mu_{\text{eff}}$ ) at 400 K is very similar, while the slight negative curvature at higher temperatures is likely due to a temperature-independent contribution, e.g. a Pauli and a Van Vleck contribution.

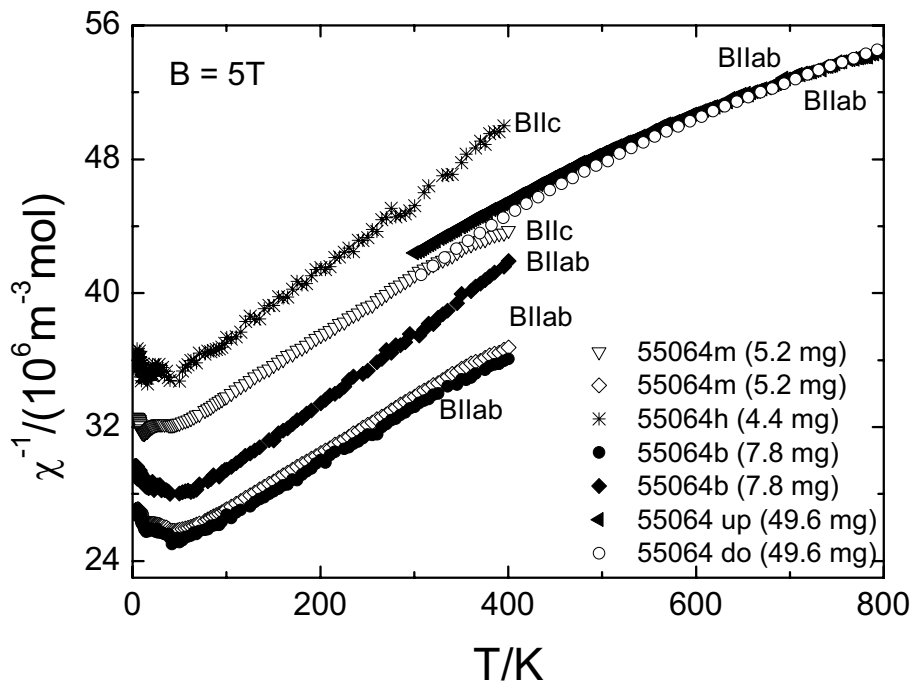


**Figure 3.30:** Inverse susceptibility versus temperature up to 800 K for several single crystals in an applied field of 5 T. All data show a dominant Curie-Weiss behaviour.

In order to get more precise information we picked up the measurement which we suspect to be the most reliable (55064b) and analyzed the results in more details. In Fig. 3.31 we plot  $\chi(T)$  for different fields. It is evident that all curves show the same temperature dependence, but that they are shifted

by an amount roughly proportional to  $1/\mu_0 H$ . This is a clear evidence for a ferromagnetic contribution with a  $T_C$  far above 400 K.

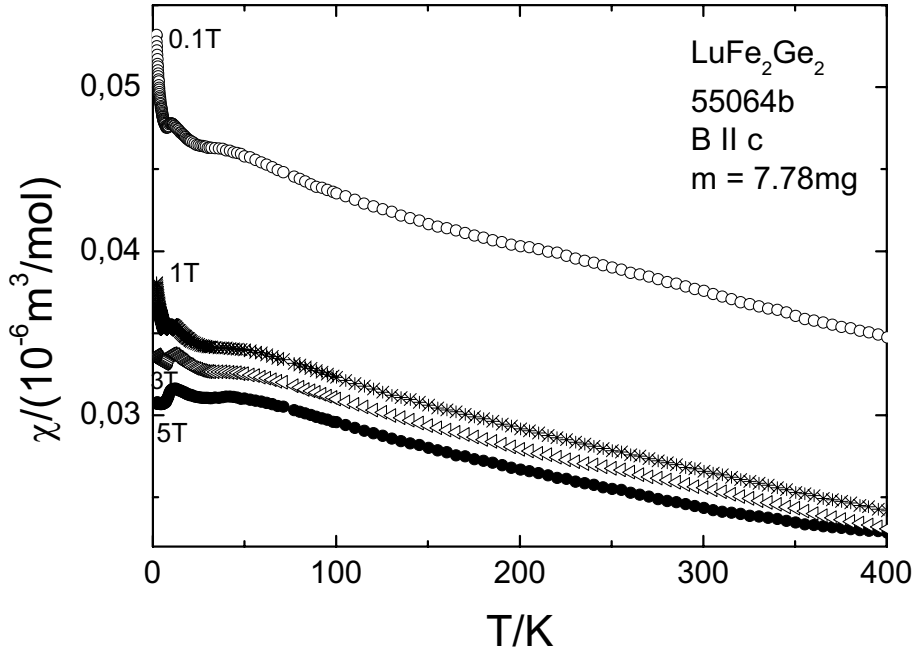


**Figure 3.31:** Susceptibility in different magnetic fields applied parallel to the  $c$  axis of the single crystal 55064b.

We performed a quantitative analysis by assuming that at each temperature the magnetization is the sum of a field-independent ferromagnetic contribution  $M_0(T)$  due to a foreign phase, and the intrinsic contribution of LuFe<sub>2</sub>Ge<sub>2</sub>, which is proportional to the susceptibility  $\chi(T)$  of LuFe<sub>2</sub>Ge<sub>2</sub> and the applied magnetic field  $H$ . The total moment  $M(T)$  is then given by:

$$M(T) = M_0 + \chi_I(T)H. \quad (1)$$

$M_0(T)$  and  $\chi_I(T)$  can then easily be calculated from the susceptibility  $\chi_1$  and  $\chi_2$  measured in two different fields  $H_1$  and  $H_2$ .

$$\chi_I(T) = (\chi_1 \cdot H_1 - \chi_2 \cdot H_2)/(H_1 - H_2) \quad (2)$$

$$M_0(T) = (\chi_1 - \chi_2) \cdot (1/H_1 - 1/H_2)^{-1} \quad (3)$$

In figure 3.32, we plot  $M_0(T)$  determined from the difference in  $\chi$  between 0.1 and 3 T, and between 1 and 3 T,  $\Delta\chi_{0.1}$  and  $\Delta\chi_1$ , respectively.

The 5 T data set was not used because the merging of the  $\chi(T)$  curves for 5 and 3 T at 400 K suggests that there the difference is mainly due to a reaction or a displacement of the sample at the beginning of the 5 T measurement.

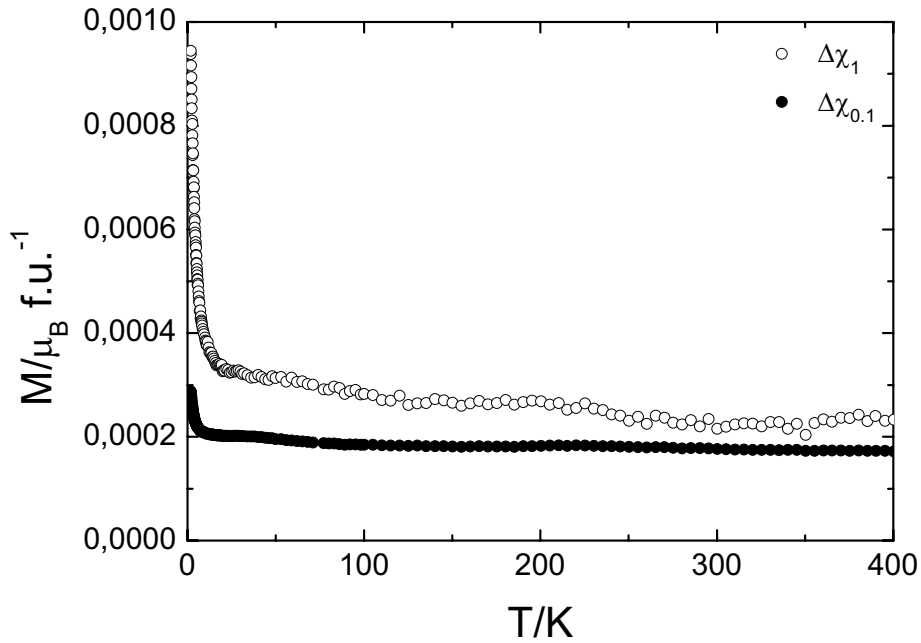


**Figure 3.32:** *The presence of a small amount of a ferromagnetic impurity phase with a saturation moment of approximately  $3 \cdot 10^{-4} \mu_B$  per formula unit is visible in a small temperature-independent difference between the  $\chi(T)$  data at 0.1 T (red data) or 1 T (blue data) and those at 3 T.*

Both data sets lead to a similar result: an almost temperature-independent  $M_0$  of the order of  $2 \cdot 10^{-4} \mu_B$  per formula unit. The scatter for  $M_0$  calculated from  $\Delta\chi_1$  is much larger because the difference  $\Delta\chi_1$  itself is much smaller than  $\Delta\chi_{0.1}$ . The value of  $M_0$  for magnetic field applied parallel to the ab plane was estimated to  $1.5 \cdot 10^{-4} \mu_B$  per formula unit and is almost constant over the whole temperature range. Thus figure 3.32 demonstrates the presence of

a ferromagnetic contribution with a saturated moment of  $2 \cdot 10^{-4} \mu_B$  per mole, and a Curie temperature far above 400 K. Such a small moment can be accounted for  $10^{-2}$  mol% of a foreign phase with ferromagnetic Fe. It is very difficult to prevent the formation of such small amount of foreign phase, and to detect it by standard structural and chemical-analysis methods.

We determined the effect of the ferromagnetic component on the measured susceptibility. While at low field it shifts  $\chi(T)$  significant upward to higher values, the effect at 5 T is smaller than the experimental accuracy of the data,  $\approx 1\%$ . Thus we shall in the following use the data measured at 5 T to discuss the magnetic properties of LuFe<sub>2</sub>Ge<sub>2</sub>. In figure 3.33, we plot  $\chi(T)$  as a function of T for both field directions.

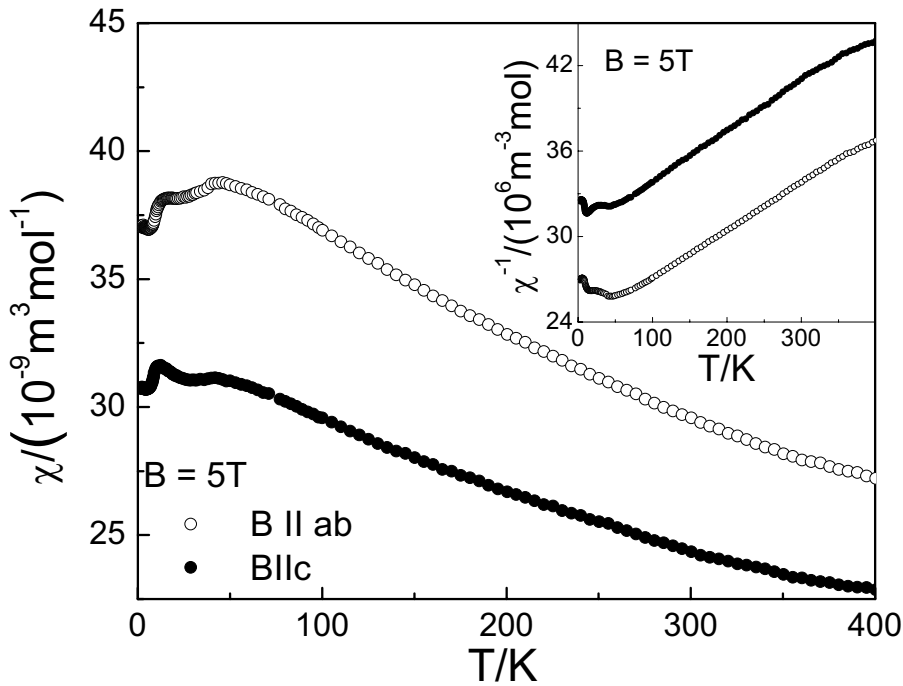


**Figure 3.33:** Temperature dependence of the susceptibility and (inset) inverse susceptibility of LuFe<sub>2</sub>Ge<sub>2</sub> single crystals along the two crystallographic directions.

Along both directions,  $\chi(T)$  increases with decreasing temperatures below 400 K, evidences a weak maximum around  $T \approx 50$  K, and shows at 9 K a small, but well-defined anomaly. This anomaly was already observed in the specific-heat data (see chapter 3.3.2.2). The susceptibility is slightly anisotropic, being 20% larger for fields along the basal plane than along the *c* direction. Those results are very similar to Ref. [Avila 2004]. The main difference is that our absolute values at higher fields are slightly smaller while those at lower fields are higher compared to the data of Avila et al. at  $H = 1$  kOe, while the temperature dependence and the anisotropy are almost identical.

The plot  $1/\chi$  versus  $T$  (inset of Fig. 3.33) reveals a well defined Curie-Weiss law, with almost the same slope for both field directions. A fit through the data between 80 and 400 K results in an effective moment of 4.15 (+/- 0.2)  $\mu_B$  per formula unit, which corresponds to an effective moment of 2.9  $\mu_B$  per Fe, almost the same value as our estimation in YbFe<sub>2</sub>Ge<sub>2</sub>. The Weiss temperatures are rather large,  $\theta \approx -800$  K. These results and analysis confirm the presence of a fluctuating paramagnetic Fe moment in the RFe<sub>2</sub>Ge<sub>2</sub> compounds.

Avila et al. already recognized in LuFe<sub>2</sub>Ge<sub>2</sub> the presence of a phase transition at  $T_0 = 9$  K evidenced by anomalies in  $\chi(T)$  and  $C(T)$ , but they left its nature open. In order to gain a deeper insight into this phase transition, we performed a more detailed analysis of  $\chi(T)$  and  $C(T)$  at low  $T$ . In figure 3.34 we compared the  $C(T)$  and  $\chi(T)$  data at low temperatures. Since we are interested in the intrinsic part of the susceptibility at low field, we plotted in figure 3.34 the susceptibility for  $\mu_0 H = 0.1$  T along both directions after subtracting the temperature-independent ferromagnetic contribution  $M_0$ ,  $\chi_{shift} = \chi - M_0/\mu_0 H$ .

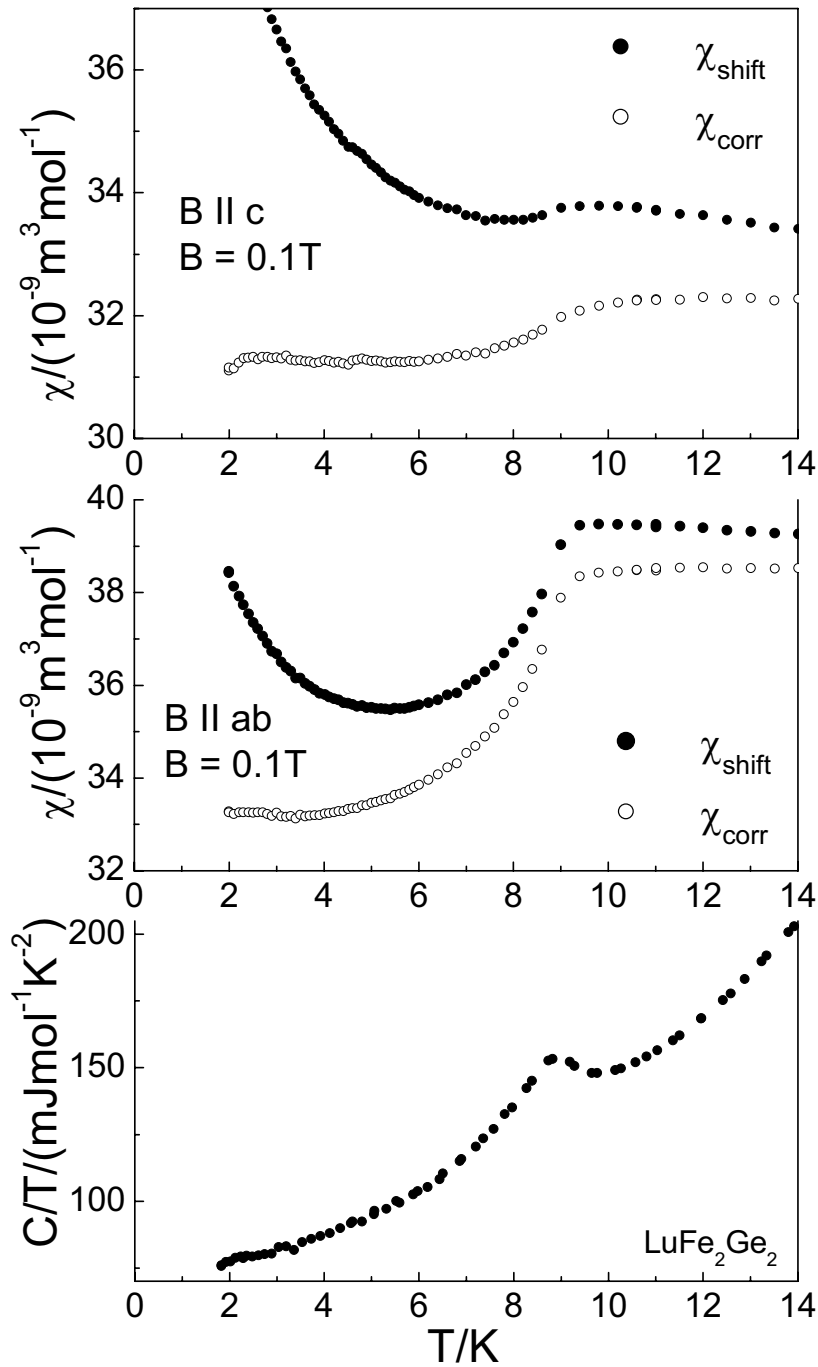


**Figure 3.34:** Anomalies in  $C(T)$  and  $\chi(T)$  at the phase transition at 9 K.  $\chi_{\text{shift}}$  was obtained by subtracting the  $T$ -independent ferromagnetic contribution  $M_0$  from the measured data. For  $\chi_{\text{corr}}$  a low-temperature Curie contribution was further subtracted.



Already these data evidence at  $T_0$  a rather strong decrease of  $\chi(T)$  for field along the basal plane, while for  $B \parallel c$  the anomaly looks much weaker. The upturn below 5 K down to 2 K can be attributed to a small amount of a paramagnetic impurity, since it is quite strong in the 0.1 T data set, but disappeared in the 5 T data set. This is confirmed by a plot  $\chi(T) \cdot T$  versus temperature for  $T < 6$  K, which shows for both directions a straight line (Fig. 3.35).

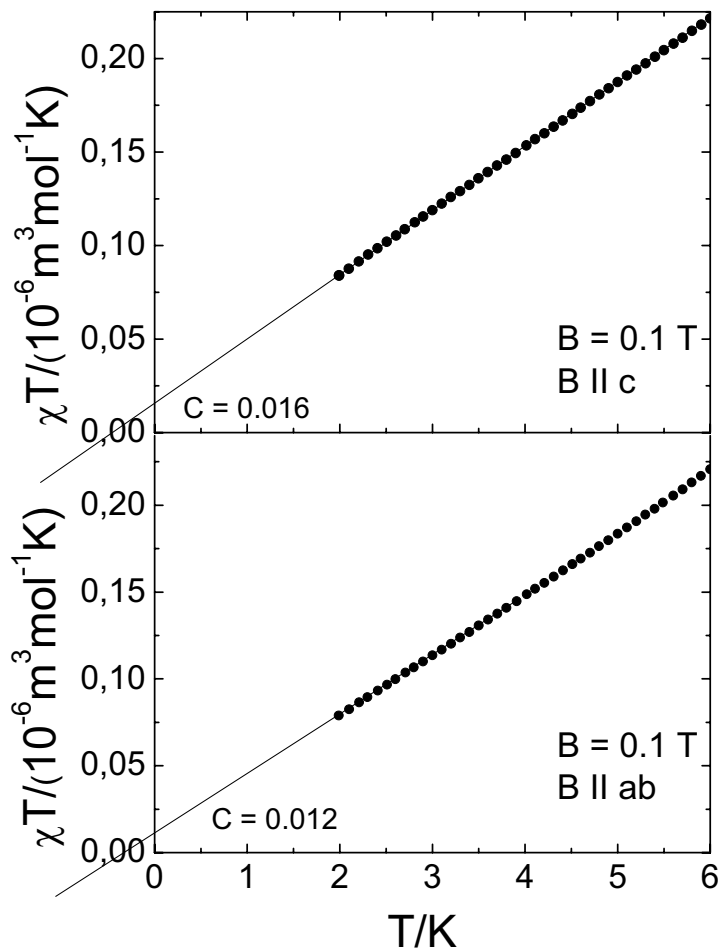


**Figure 3.35:** Estimation of Curie-like impurity contributions by plotting  $\chi T$  versus  $T$ . Linear fitting in the temperature range up to 6 K for  $B \parallel c$  and up to 4 K for  $B \parallel ab$  gives an intersection with the  $\chi T$  axis of  $C = 0.016 \cdot 10^{-6} \text{ m}^3 \text{ mol}^{-1} \text{ K}$  and  $C = 0.012 \cdot 10^{-6} \text{ m}^3 \text{ mol}^{-1} \text{ K}$ , respectively.

The Curie contribution calculated from the intercept in these plots was subtracted from  $\chi_{shift}$  resulting in the curve  $\chi_{corr}$ .

After this subtraction the anomaly is still much more pronounced for  $B \parallel ab$  than for  $B \parallel c$ . This analysis indicates that the transition at  $T_0$  is connected with an anisotropic decrease of the susceptibility of the order of 15 % for  $B \parallel ab$  and only 3 % for  $B \parallel c$ . Such an anisotropy, which is also visible in the data of [Avila 2004], suggests this phase transition to be an antiferromagnetic one.

The corresponding anomaly in the specific heat is rather small but well visible (see Fig. 3.34 and Fig. 3.27). The Sommerfeld coefficient estimated from an extrapolation of  $C(T)/T$  to  $T = 0$  amounts to  $\gamma = 74 \text{ mJ/K}^2\text{mol}$ . Using this  $\gamma$  value,  $\mu_{eff} = 2.9 \mu_B$  and an average low-temperature susceptibility  $\chi = 35 \cdot 10^{-9} \text{ m}^3/\text{mol}$ , the Sommerfeld-Wilson ratio estimates to  $R_W = \pi^2 k_B^2 / \mu_0 \mu_{eff}^2 \cdot (\chi_0/\gamma) = 1.1$ , which is not enhanced. This (as well as the large  $\theta$  value) indicates that LuFe<sub>2</sub>Ge<sub>2</sub> is not close to a ferromagnetic instability, but is consistent with the proximity of an antiferromagnetic instability.

### 3.3.2.3.2 Magnetisation

For the Lu compound magnetisation measurements were done up to 5 T in a commercial SQUID magnetometer.

Sample 55064b has a mass of  $m = 7.78 \text{ mg}$  and the field was applied perpendicular to the  $c$  axis of the single crystal. The data for selected constant temperatures (Fig. 3.36) show a linear field dependence above  $\mu_0 H = 1 \text{ T}$ , as expected for the intrinsic part of the magnetisation. Unfortunately no high-field magnetisation data are available for this compound, but nothing spectacular is expected here.

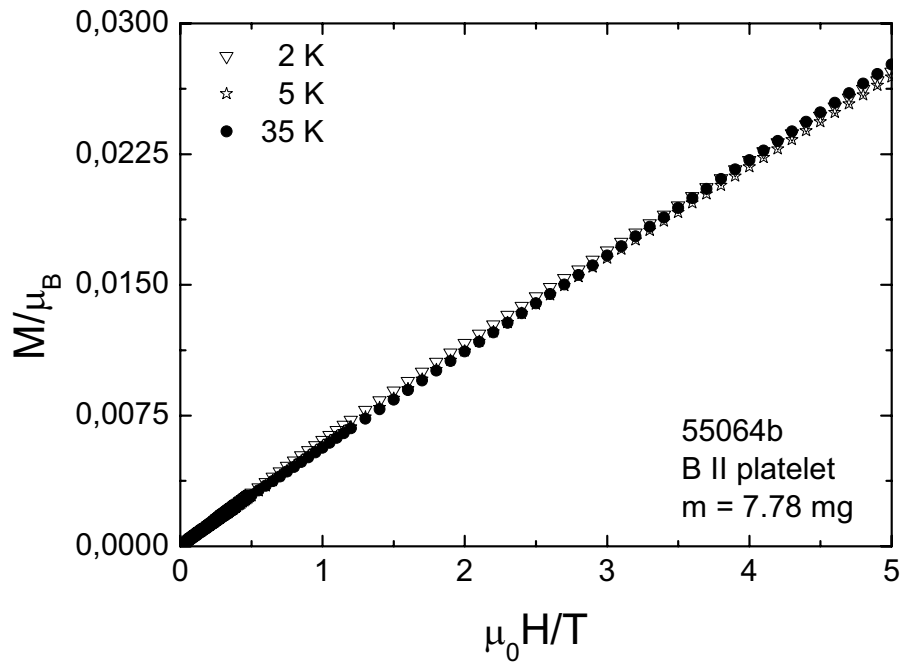


**Figure 3.36:** *Magnetisation of LuFe<sub>2</sub>Ge<sub>2</sub> up to 5 T at selected different temperatures shows in all cases a linear field dependence above 1 T as expected for the intrinsic part of the magnetisation. The direction of the magnetic field is perpendicular to the c axis of the single crystal.*

M/B versus the inverse magnetic field is shown in Fig. 3.37 to calculate the intrinsic susceptibility for comparison and to obtain  $M_0$ . The resulting susceptibility values are in agreement with susceptibility measurements in figure 3.33.

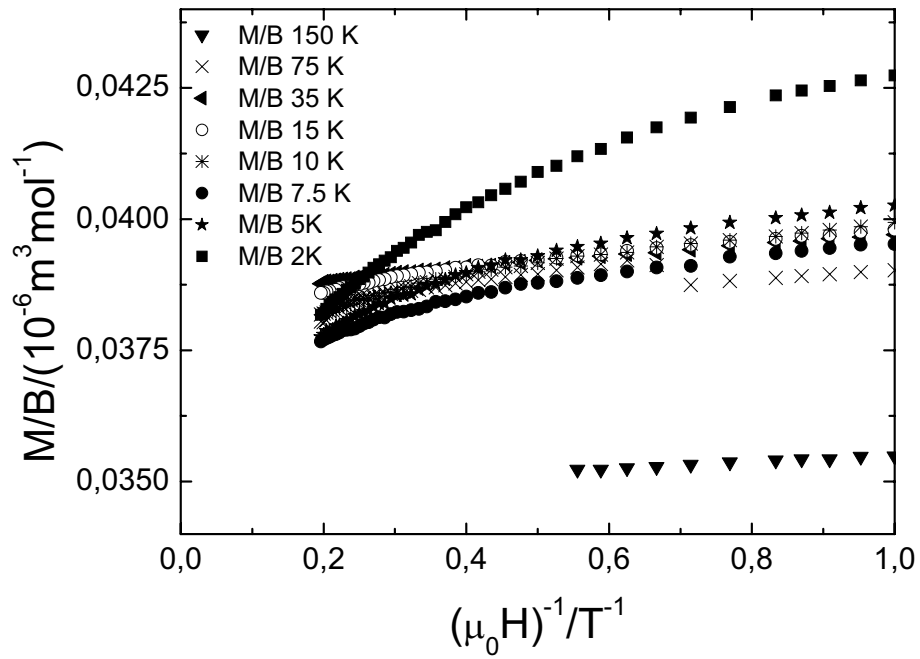


**Figure 3.37:**  $M/B$  versus  $1/B$  for  $B \perp c$ . The extrapolation to  $1/B \rightarrow 0$  corresponds to the intrinsic susceptibility, while the slope is proportional to  $M_0$ .

### 3.4 Neutron scattering

Inelastic neutron-scattering experiments on powdered YbFe<sub>2</sub>Ge<sub>2</sub> and LuFe<sub>2</sub>Ge<sub>2</sub> samples were performed at the *ISIS Facility (Rutherford Appleton Laboratory* in Didcot) to investigate the excitations of this system. E. Faulhaber and O. Stockert carried out the experiment, using the instrument HET (High Energy Transfer). Both samples were measured under the same conditions to separate the magnetic excitations of Yb in YbFe<sub>2</sub>Ge<sub>2</sub> from phononic contributions. Here LuFe<sub>2</sub>Ge<sub>2</sub> was expected to serve as a non-magnetic reference to determine the phonon background, since at the time of the experiment, the magnetic character of Fe was not established. Aluminium foil (with a thickness of 20  $\mu\text{m}$ ) was folded to form sachets in which the powdered samples (approximately 9 g each) were filled in. The sachets with a sample thickness of 2 to 3 mm were mounted in metal frames (covered with neutron-absorbing material) attached to the cold finger of a displax cryostat. The size of the sachets matched the incident neutron beam ( $\sim 40 \text{ mm} \times 45 \text{ mm}$ ). The incident neutron energies varied between 15 meV and 400 meV. Measurements were performed at 5 K, 50 K and 300 K with approximately 12 hours of counting time per incident energy and temperature. To obtain absolute values of the recording spectra the data were normalised using a vanadium standard. All data reduction, e.g. conversion from time of flight to energy, was performed by the data-reduction software HOMER supplied by ISIS. Figure 3.38 displays the inelastic neutron-scattering spectra of YbFe<sub>2</sub>Ge<sub>2</sub> and LuFe<sub>2</sub>Ge<sub>2</sub> at  $T = 5$  and 300 K for low scattering angle  $\langle\Phi\rangle = 4^\circ$ . Apart from incoherent elastic scattering (dotted lines) the response is dominated by a broad quasielastic contribution (solid lines) extending well beyond  $\hbar\omega = 50$  meV. No inelastic excitation, in particular no CEF excitation could be detected. It might be hidden below the strong quasielastic response. Two small peaks appear around 10 meV and 33 meV and can be attributed to phonons.

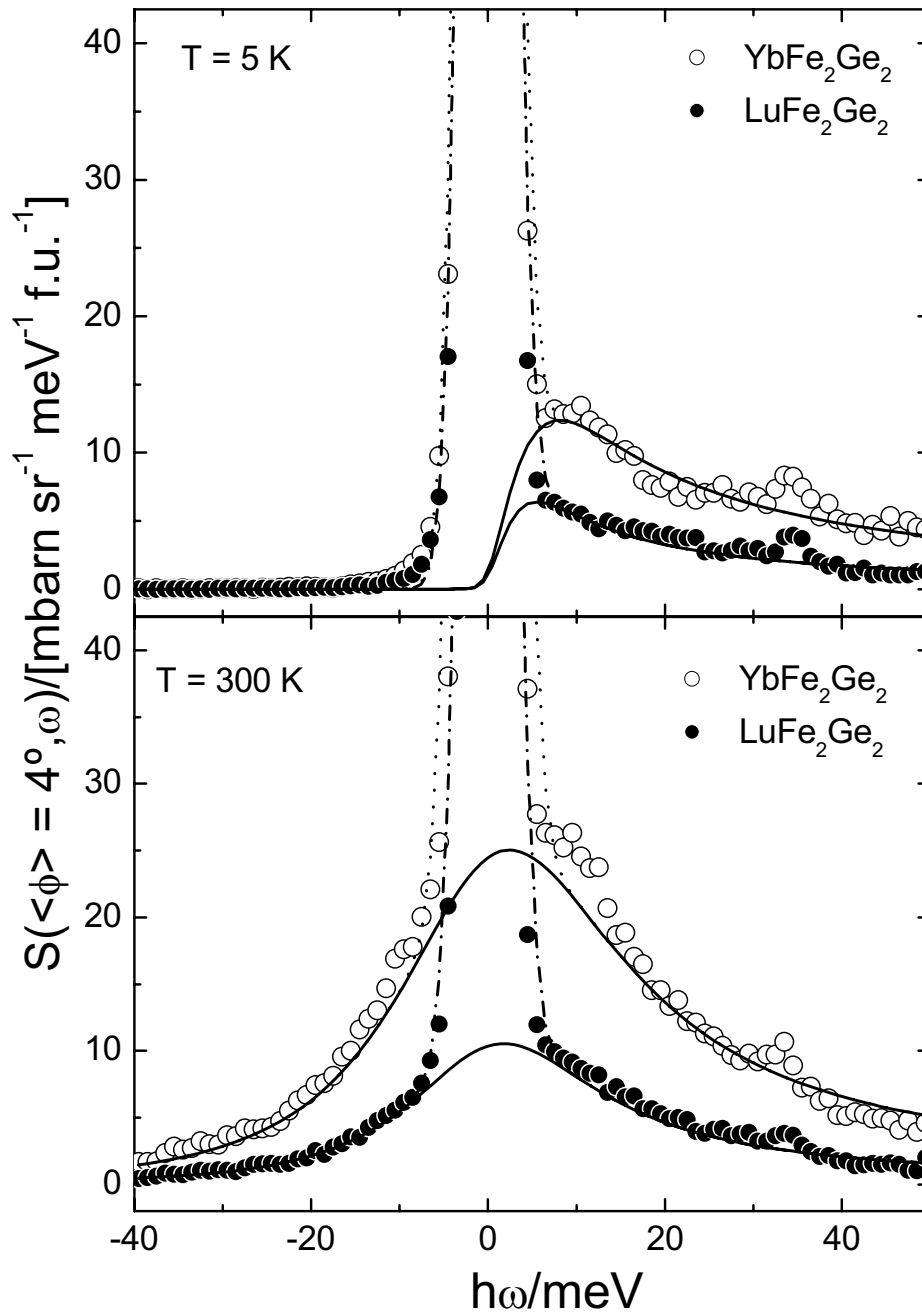


**Figure 3.38:** Inelastic neutron-scattering spectra of  $\text{YbFe}_2\text{Ge}_2$  and  $\text{LuFe}_2\text{Ge}_2$  at 5 K and 300 K. The data were taken on HET at low scattering angle  $\langle\Phi\rangle = 4^\circ$  with an incident neutron energy  $E_i = 60$  meV. Solid and dotted lines represent fits to the data (see text).

Surprisingly, LuFe<sub>2</sub>Ge<sub>2</sub> was found to be magnetic, too. Therefore, a determination of the phonon background for YbFe<sub>2</sub>Ge<sub>2</sub> was not possible. Hence, for a first crude analysis of the data the spectra at low scattering angle  $\langle \Phi \rangle = 4^\circ$  were used.

The analysis is based on the fact that for small scattering angles  $\Phi$  or equivalently for small momentum transfer  $q$  the phonon intensity is weak (remember that the phonon intensity follows roughly  $q^2$ ) while the magnetic contribution dominates (which falls off as a function of  $q$  according to the magnetic form factor). Neglecting the small phonon contribution should yield mainly the magnetic scattering at low  $q$ .

To analyse the data, the incoherent elastic part was fitted by a peak with Gaussian lineshape and the quasielastic magnetic response with a Lorentzian lineshape. The fluctuations are decaying exponentially in time with a lifetime  $\tau$  related to a quasielastic response with Lorentzian lineshape and the width in energy  $\Gamma/2 = 1/\tau$ . Hence the magnetic response has the form:

$$S_{magn.} = \Gamma/2\pi\chi_N / [\omega^2 + (\Gamma/2)^2] \hbar\omega / [1 - \exp(-\hbar\omega/k_B T)]$$

The fit of the magnetic response yields the integrated intensity  $\chi_N$  and the line width  $\Gamma$  (full width of half maximum). The first part of this equation after the prefactor is the Lorentzian and the second part is the Boltzmann factor. We obtained the following  $\Gamma$  and  $\chi_N$  values at the three different temperatures.

**Table 3.2:** Half width  $\Gamma$  and integrated intensity  $\chi_N$  of the quasielastic response in YbFe<sub>2</sub>Ge<sub>2</sub>.

T/K	$\Gamma$ /meV	$\chi_N$ / [mbarn·sr <sup>-1</sup> f.u. <sup>-1</sup> ]
5	16(2)	78(8)
50	21(5)	65(9)
300	32(4)	47(5)

Assuming that the magnetic excitations are local and therefore  $q$  independent, then  $\chi_N$  should scale with the bulk susceptibility. Figure 3.39

shows the comparison of the bulk susceptibility obtained in a SQUID magnetometer (see chapter 3.2.2.3) and that obtained from the integrated intensity  $\chi_N$  derived from the neutron data. The temperature dependence of  $\chi_N$  decreases with temperature as the bulk susceptibility. However, there is a quantitative discrepancy at high temperature, which might be due to a possible phonon contribution and insufficient background subtraction. That would affect mostly the high temperature value of  $\chi_N$ . But the good agreement at low temperatures supports the validity of the analysis of the neutron data, especially the assumption that most of the inelastic intensity at low  $q$  is due to magnetic scattering.

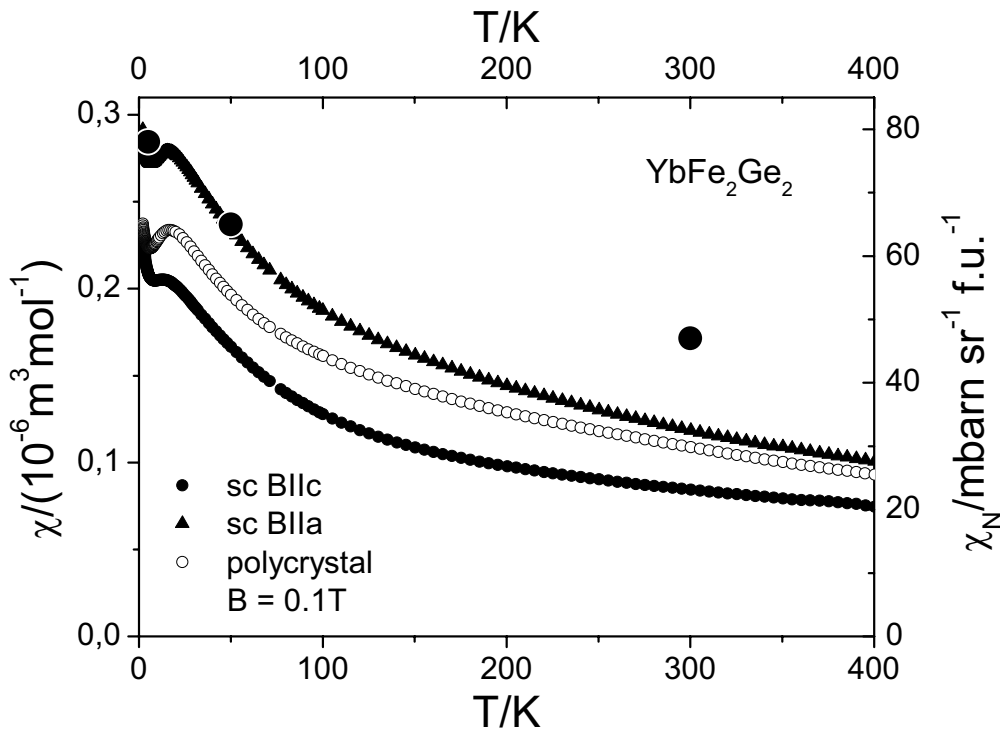


**Figure 3.39:** Comparison of the susceptibility derived from neutron-scattering data with the bulk susceptibility obtained in a SQUID magnetometer for YbFe<sub>2</sub>Ge<sub>2</sub>.



$\Gamma$  decreases slightly with temperature and levels off at a residual value of  $\Gamma_0 \approx 16$  meV. Within standard theories for single ion Kondo impurities,  $\Gamma_0$  is proportional to the Kondo temperature  $k_B T_K = \Gamma_0/2$ . Thus one can deduce from the neutron data a Kondo temperature  $T_K \approx 90$  K. This  $T_K$  value corresponds approximately to the values obtained from thermodynamic measurements.

It is noteworthy that  $\Gamma\chi_N \approx \text{constant}$ . Such a proportionality  $\Gamma \propto 1/\chi_N$  is predicted in Kondo systems for  $T < T_K$ , in certain circumstances [Shiba 1975, Kuramoto 1987]. These conditions seem to be fulfilled in YbFe<sub>2</sub>Ge<sub>2</sub>.

An analysis of the magnetic excitations for LuFe<sub>2</sub>Ge<sub>2</sub> was not carried out, because of the difficult separation of the magnetic contribution from the phonon background. It still remains an open issue to find a non-magnetic reference compound to determine the contribution to the excitations of magnetic Fe.

### 3.5 LDA calculations

The possibility of a fluctuating Fe moment was studied from a theoretical point of view using calculations of the electronic properties. The local density approximation (LDA) has nowadays reached a level where it allows a precise calculation of the ground-state energy for different magnetic configurations. Using the local spin density (LSDA) approach, H. Rosner calculated the ground-state energy of LaFe<sub>2</sub>Ge<sub>2</sub>, LuFe<sub>2</sub>Ge<sub>2</sub> and YFe<sub>2</sub>Ge<sub>2</sub> as a function of the ferromagnetic moment  $\mu_{\text{Fe}}$  imposed on the Fe atoms. The ferromagnetic configuration was chosen in a first approach as being the simplest one and because of the absence of any information on the antiferromagnetic structure. The evolution of the calculated total energy as a function of  $\mu_{\text{Fe}}$  is shown in Fig. 3.40. The energy of the paramagnetic state ( $\mu_{\text{Fe}} = 0$ ) was taken as reference. The same calculations were also performed for YbFe<sub>2</sub>Ge<sub>2</sub>, but these results are not reliable because it is presumably impossible to account properly for an intermediate-valent Yb state in the LDA calculations.

The results clearly evidence a minimum of the total energy for a finite moment on Fe of the order of  $\mu_{\text{Fe}} = (0.7-1.0) \mu_{\text{B}}$ . During the calculation, H. Rosner [Rosner 2005] observed that the result is very sensitive to the position parameter  $z$  of Ge. This is demonstrated by two calculations for YFe<sub>2</sub>Ge<sub>2</sub> with slightly different  $z$  parameters. The initial calculation was done using a standard value  $z = 0.375 \text{ \AA}$ . The second calculation using the larger experimental value  $z = 0.3789 \text{ \AA}$  reported in the literature [Venturini 1996] leads to a 30% stronger reduction of the total energy of the ferromagnetic state and to a slightly larger ferromagnetic moment at the minimum of the total energy. Thus a larger  $z$  value seems to stabilise the ferromagnetic state. The calculation for LaFe<sub>2</sub>Ge<sub>2</sub> and LuFe<sub>2</sub>Ge<sub>2</sub> were also performed with the experimental values  $z = 0.3719$  [Venturini 1996] and  $z = 0.38023$  [Cardoso 2005], respectively. Here, the much smaller  $z$  parameter of LaFe<sub>2</sub>Ge<sub>2</sub> correlates with a much weaker decrease of the

ferromagnetic total energy and a slightly smaller ferromagnetic moment at the minimum of the total energy.

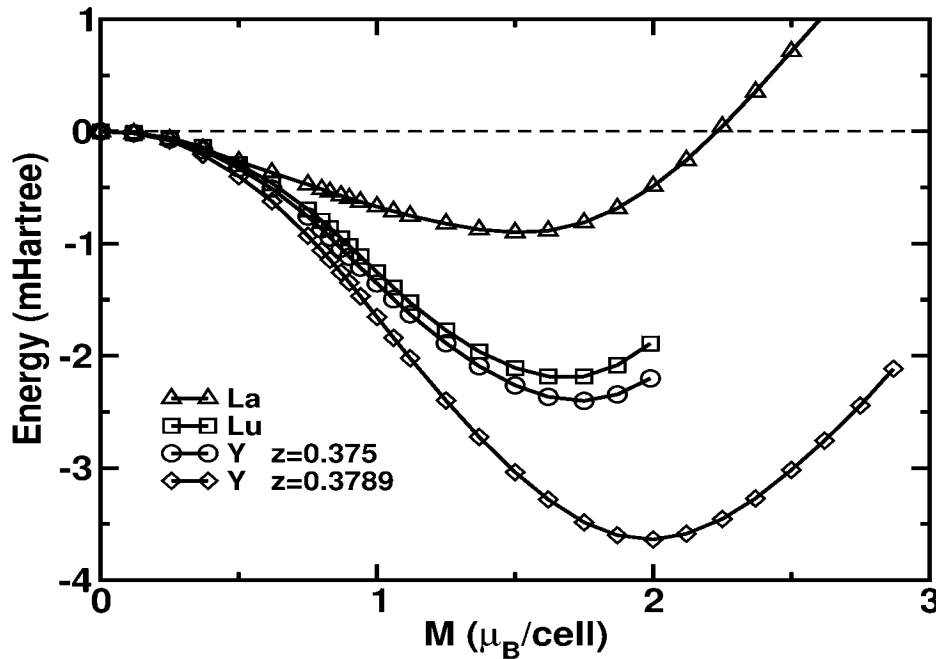


**Figure 3.40:** Total energy  $E_{tot}$  versus magnetic moment as obtained from a fixed spin-moment calculation for  $RFe_2Ge_2$  ( $R = La, Lu$  and  $Y$ ). The irreducible cell contains two Fe atoms.

Usually, the stability of itinerant ferromagnetism is expected to decrease with decreasing volume, since a reduction of the interatomic distances leads to an increase of the bandwidth. Thus the density of states (DOS) at the Fermi level,  $N(E_F)$ , and the Stoner product,  $N(E_F)I$  (when  $I$  is the exchange parameter), gets reduced and the system becomes less magnetic. Surprisingly, in the  $RFe_2Ge_2$  compounds, the decrease of the unit-cell volume from  $LaFe_2Ge_2$  to  $LuFe_2Ge_2$  is accompanied by a stabilisation of the magnetic state, in contrary to the usual expectations. Indeed the LSDA calculations result in a 30% larger  $N(E_F)$  in  $LuFe_2Ge_2$  than in  $LaFe_2Ge_2$ ,

explaining the stabilisation of the magnetically ordered state. Obviously, in these compounds the ferromagnetism is more sensitive to details of the band structure (as evidenced by the strong sensibility to the  $z$  parameter) than to the volume. A strict interpretation of the results of these calculations would lead to the conclusion that all these compounds should order at least ferromagnetically. However, it is well known that these LSDA calculations do not account correctly for fluctuations. Because of the small value of the calculated moment and the small value of the reduction in total energy, one would expect these fluctuations to be able to suppress magnetic order in the real material. Therefore, the results of these calculations are in good agreement with an observation of a fluctuating moment in LuFe<sub>2</sub>Ge<sub>2</sub> and YbFe<sub>2</sub>Ge<sub>2</sub> at higher temperatures. They give further support for the presence of this fluctuating moment.

## 3.6 Final discussion of YbFe<sub>2</sub>Ge<sub>2</sub> and LuFe<sub>2</sub>Ge<sub>2</sub>

### 3.6.1 Paramagnetic Fe moment

The most interesting result of our investigation of YbFe<sub>2</sub>Ge<sub>2</sub> and LuFe<sub>2</sub>Ge<sub>2</sub> is the observation of a paramagnetic Fe moment of the order of 3  $\mu_B$ /Fe at high temperatures. This is evidenced both by the Curie-Weiss behaviour of the susceptibility of LuFe<sub>2</sub>Ge<sub>2</sub> above 100 K as well as by the very large effective moment observed in YbFe<sub>2</sub>Ge<sub>2</sub> above 150 K, exceeding by a factor of two the value expected for a free Yb<sup>3+</sup> ion. A magnetic character of Fe in these compounds is also supported by LDA calculations, which show a reduction of the total ground-state energy if one assumes a ferromagnetic Fe moment. The effective moment on the Fe-site and the Curie-Weiss temperature deduced from the Curie-Weiss fit at high temperatures are close to the values observed in YCo<sub>2</sub> and LuCo<sub>2</sub>, which are two spin-fluctuating systems close to a magnetic instability.

According to the LDA calculations, the magnetic character of Fe seems to be more governed by the position parameter  $z$  of Ge within the unit cell, and not by the volume of the unit cell as usually assumed for itinerant magnets. In order to test this hypothesis, investigation of LaFe<sub>2</sub>Ge<sub>2</sub> would be very interesting, since LDA predicts a much weaker magnetic Fe character in this compound because of its smaller  $z$  parameter, despite a larger unit-cell volume. However, the preparation of pure samples of this compound turned out to be very difficult. Up to now only polycrystalline samples with a significant amount of ferromagnetic Fe-based foreign phases are available, precluding a detailed investigation of the magnetic properties.

### 3.6.2 Spin-fluctuations and magnetic order in LuFe<sub>2</sub>Ge<sub>2</sub>

In LuFe<sub>2</sub>Ge<sub>2</sub>, anomalies in  $C_p(T)$  and  $\chi(T)$  indicate a phase transition at  $T_0 = 9$  K. This transition is very likely related to an antiferromagnetic ordering of the paramagnetic Fe moment observed at high temperatures, since the anomalies in  $\chi(T)$  are quite anisotropic. However, the nature of the transition has to be confirmed by microscopic measurements in the future.

The temperature dependences of  $C(T)$  and  $\rho(T)$  at low temperatures evidence a Fermi-liquid with an enhanced effective mass. Below 6 K, the electronic contribution to the specific heat is linear in temperature, with a Sommerfeld coefficient  $\gamma_0 \approx 60$  mJmol<sup>-1</sup>K<sup>-2</sup>, which is at least a factor of 5 larger than in other LuT<sub>2</sub>X<sub>2</sub> compounds. The resistivity can be fitted with a power law,  $\rho(T) = \rho_0 + AT^2$ , with  $A \approx 0.015$   $\mu\Omega\text{cmK}^{-2}$ . This results in a Kadowaki-Woods ratio  $A/\gamma^2 = 4 \cdot 10^{-6}$   $\mu\Omega\text{cm}(\text{molK}^2/\text{mJ})^2$  well within the range expected for Fermi-liquid systems. This indicates that at low temperatures the electron-electron scattering is the dominant process. Using  $\mu_{\text{eff}} = 2.9$   $\mu_B/\text{Fe}$  as estimated from the high temperature susceptibility, the Sommerfeld-Wilson ratio  $R_W = k\chi_0/\gamma$  (where  $k = \pi^2 k_B^2 / (\mu_0 \mu_{\text{eff}}^2)$ ), of the temperature-independent susceptibility  $\chi_0$  at low temperatures and  $\gamma$ , amounts to  $R_W = 1.1$ , very close the value  $R_W = 1$  expected for a free-electron gas. Thus the temperature dependence of  $C(T)$ ,  $\rho(T)$  and  $\chi(T)$  as well as the value of the Kadowaki Woods ratio  $A/\gamma^2$  and of the Sommerfeld Wilson ratio  $k\chi_0/\gamma$  demonstrate the presence of a Fermi-liquid with an effective mass enhanced by a factor of  $\sim 5$  in LuFe<sub>2</sub>Ge<sub>2</sub>. Taking into account the paramagnetic Fe moment observed at high temperatures, this mass enhancement is very likely related to spin-fluctuations. Since the Sommerfeld-Wilson ratio is not enhanced, these spin-fluctuations are predominantly antiferromagnetic.

Neither  $\gamma$  nor  $\chi_0$  seems to be strongly affected by the phase transition at  $T_0$ , although one could expect a significant suppression of the spin fluctuations in a magnetically ordered phase. However, the size of the jump in  $C(T)$  at the phase transition is rather small (compared to  $\gamma$ ), indicating that only a

small part of the Fermi surface is affected by the transition. One could further suspect that because of the very small ordering temperature (compared to typical ordering temperatures of Fe-based compounds) LuFe<sub>2</sub>Ge<sub>2</sub> is close to the QCP associated with the disappearance of magnetic order. Then one expects that even below the ordering temperature a large part of the Fe moment is still fluctuating.

### 3.6.3 Intermediate valence and heavy-fermion behaviour in YbFe<sub>2</sub>Ge<sub>2</sub>

In YbFe<sub>2</sub>Ge<sub>2</sub>,  $\chi(T)$  increases below 150 K more strongly than expected for a Curie-Weiss law, passes through a broad peak centred around 15 K before ending in a temperature-independent susceptibility. This evidences a weakly intermediate valent Yb state, at the border to the Kondo regime with a rather low characteristic  $4f$  energy scale. In contrast to LuFe<sub>2</sub>Ge<sub>2</sub>, we did not observe any evidence for a phase transition in YbFe<sub>2</sub>Ge<sub>2</sub>. An Yb valence close to but smaller than 3+ is confirmed by the analysis of the susceptibility, magnetisation, specific-heat and neutron-scattering results. The large Sommerfeld coefficient,  $\gamma = 200 \text{ mJmol}^{-1}\text{K}^{-2}$ , we extract from the linear temperature dependence of  $C(T)$  at low temperatures, evidences YbFe<sub>2</sub>Ge<sub>2</sub> as a moderate heavy-fermion system. While  $\rho(T)$  shows at low temperatures in the absence of applied magnetic field a power law with an exponent lower than 2, whose origin is yet not clear, application of a magnetic field restores a Fermi-liquid behaviour,  $\rho(T) = \rho_0 + AT^2$ , with an almost field-independent coefficient  $A = 0.16 \text{ }\mu\Omega\text{cmK}^{-2}$ . The deduced Kadowaki-Woods ratio  $A/\gamma^2 = 4 \cdot 10^{-6} \text{ }\mu\Omega\text{cm}(\text{molK}^2/\text{mJ})^2$ , the same as in LuFe<sub>2</sub>Ge<sub>2</sub>, is also well within the range expected for Fermi-liquid systems. For the calculation of the Sommerfeld-Wilson ratio, we face the problem which  $\mu_{\text{eff}}$  has to be used. A lower limit  $R_W = 0.9$  is obtained with  $\mu_{\text{eff}} = 4.54 \text{ }\mu_B$  corresponding to the full effective moment of the free Yb<sup>3+</sup> ion. An upper bound  $R_W = 2.1$  results with  $\mu_{\text{eff}} = 3.0 \text{ }\mu_B$  corresponding to the estimated  $\mu_{\text{eff}}$

of Fe as well as to a mean value for a CEF-reduced  $\mu_{\text{eff}}$  for a typical CEF ground-state of Yb<sup>3+</sup>. Therefore, in any case  $R_W$  is close to 1. Thus, YbFe<sub>2</sub>Ge<sub>2</sub> is found to be a moderately heavy-fermion system with a mass-enhancement factor of the order of 20. Here the mass enhancement is predominantly connected with the interaction between 4*f* and conduction electrons.

Franziska Weickert performed a detailed analysis of the magnetization at low temperatures and of the temperature dependence of  $\chi(T)$  and  $C(T)$ . All these properties could nicely be fitted with the single-ion Kondo model assuming an effective  $J = 3/2$  and a characteristic energy  $T_K = (75 \pm 5)$  K [Weickert 2006]. This effective  $J = 3/2$  implies that the two lowest CEF doublets of Yb<sup>3+</sup> are involved in the physics at low temperatures. This can be understood by a comparison with the homologue compounds YbFe<sub>2</sub>Si<sub>2</sub> and YbRu<sub>2</sub>Ge<sub>2</sub>, where Ge and Fe were replaced by the isoelectronic elements Si and Ru, respectively. In both compounds Yb is in stable trivalent state leading to well resolved CEF levels. In YbRu<sub>2</sub>Ge<sub>2</sub>, it was recently found that the CEF ground-state doublet and the first excited doublet are almost degenerated, with an excitation energy of less than 10 K, while the next excited doublet is separated by 340 K. In YbFe<sub>2</sub>Si<sub>2</sub>, the first excited CEF doublet is separated from the ground-state by only 25 K, the exact position of the next doublet is not clear. Assuming a similar CEF in YbFe<sub>2</sub>Ge<sub>2</sub>, a Kondo-type interaction of the order of 75 K would lead to a strong mixing of the ground-state and the first excited doublet leading to an effective  $J = 3/2$  state, as deduced from the analysis of  $M(B)$ ,  $\chi(T)$  and  $C(T)$ .

A rather low characteristic 4*f* energy (for an intermediate-valent system) is also confirmed by the result of the inelastic neutron-scattering measurements. From the width of the quasielastic line, one can deduce  $T_K \approx 90$  K, very close to the value extracted from the analysis of  $M(B)$ ,  $\chi(T)$  and  $C(T)$ . We, therefore, now compare the properties of YbFe<sub>2</sub>Ge<sub>2</sub> with those of other compounds with an intermediate valent Yb state and a similar characteristic 4*f* energy. In Tab. 3.3 we have listed the  $\gamma$ - and the  $T_{\chi_{\text{max}}}$  values of these systems. YbFe<sub>2</sub>Ge<sub>2</sub> shows the lowest  $T_{\chi_{\text{max}}}$  (except for



YbCo<sub>2</sub>Ge<sub>2</sub>, where no maximum was observed) but its  $\gamma$  value is in between those of YbCuAl and YbCu<sub>2</sub>Si<sub>2</sub>. Thus, there seems to be no relation between  $T_{\chi_{\max}}$  and  $\gamma$ . This could be related to strong differences in the underlying CEF states. A first investigation of  $\rho(T)$  of YbFe<sub>2</sub>Ge<sub>2</sub> under pressure indicates the transition to a magnetic ground-state (presumably of Yb) at a critical pressure of  $\sim 9$  GPa. [Larrea 2006] A similar critical pressure has also been reported in other Yb-based intermediate valent systems with a low characteristic energy, as e.g. in YbCu<sub>2</sub>Si<sub>2</sub> or YbNi<sub>2</sub>Ge<sub>2</sub>. Thus, the presence of a fluctuating moment on the transition metal does not seem to strongly affect the behaviour of Yb in YbFe<sub>2</sub>Ge<sub>2</sub>.

**Table 3.3:** Comparing the Sommerfeld constant and  $T_{\chi_{\max}}$  of YbFe<sub>2</sub>Ge<sub>2</sub> with other intermediate valent Yb compounds with a comparatively low characteristic 4f energy.

compound	$\gamma/[\text{mJ/molYb-K}^2]$	$T_{\chi_{\max}}/\text{K}$	reference
YbCuAl	260	28	[Mattens 1977]
YbAgCu <sub>4</sub>	245	35	[Rossel 1987]
YbCo <sub>2</sub> Ge <sub>2</sub>	215	<1	[Trovarelli 1990]
YbFe <sub>2</sub> Ge <sub>2</sub>	200	15	this work
YbPd <sub>2</sub> Si <sub>2</sub>	203	30	[Sampath 1984]
YbNi <sub>2</sub> Ge <sub>2</sub>	136	45	[Oesterreicher 1977]
YbCu <sub>2</sub> Si <sub>2</sub>	135	50...5	[Sales 1976]

We tried to get more information on  $T_K$  and the energy of the CEF levels of YbFe<sub>2</sub>Ge<sub>2</sub> using the specific heat. In fig. 3.41, we plot  $C_p$  of YbFe<sub>2</sub>Ge<sub>2</sub> and LuFe<sub>2</sub>Ge<sub>2</sub> as well as the entropy estimated from the difference  $\Delta C$ . Since  $C_p$  of YbFe<sub>2</sub>Ge<sub>2</sub> is always larger than  $C_p$  of LuFe<sub>2</sub>Ge<sub>2</sub>, at a first glance this standard approach seems to be quite promising.

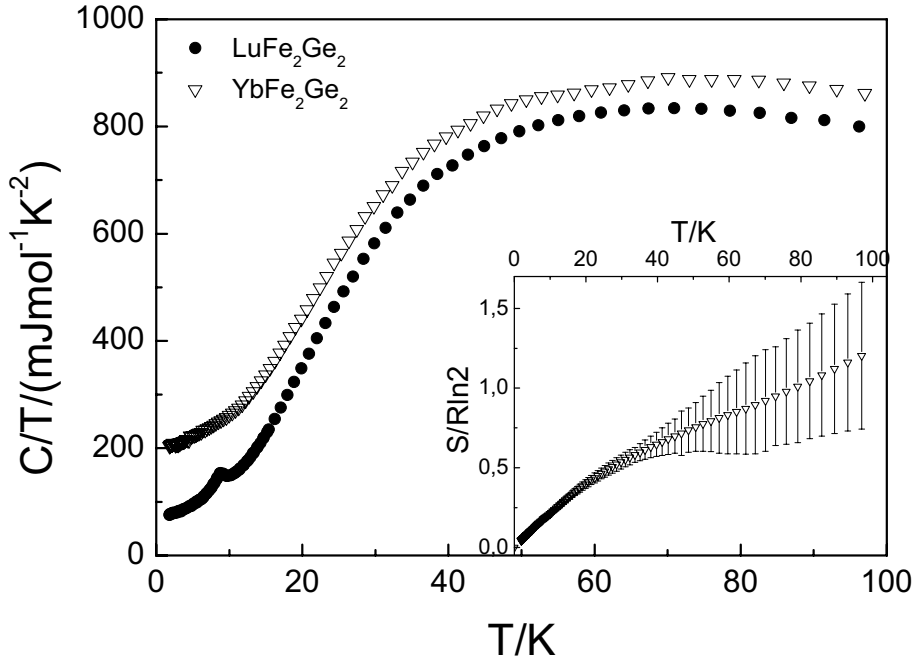


**Figure 3.41:** Comparison of the specific heat of LuFe<sub>2</sub>Ge<sub>2</sub> and YbFe<sub>2</sub>Ge<sub>2</sub>, shown by  $C/T$  on a linear temperature scale from 1.8 to 100 K. The inset shows the entropy estimated from the difference  $\Delta C$ .

However, it turned out that the entropy estimated from  $\Delta C$  increases much weaker above 20 K than the result expected from an effective  $J = 3/2$  model with  $T_K \approx 75$  K. However, for the RFe<sub>2</sub>Ge<sub>2</sub> compounds this standard procedure to estimate  $C_{4f}$  can be strongly questioned. Because of the Fe-spin fluctuations the electronic specific heat of LuFe<sub>2</sub>Ge<sub>2</sub> is strongly enhanced, but this enhancement is likely different in YbFe<sub>2</sub>Ge<sub>2</sub>. Then  $C_p$  of LuFe<sub>2</sub>Ge<sub>2</sub> is not anymore a reliable estimate for the non-f specific heat of YbFe<sub>2</sub>Ge<sub>2</sub>. Since it is impossible to account for the effect, we did not proceed with this analysis further.

## 3.7 Summary

We synthesized polycrystals and grew single crystals of YbFe<sub>2</sub>Ge<sub>2</sub> and LuFe<sub>2</sub>Ge<sub>2</sub>. The investigations of their physical properties revealed the presence of a paramagnetic Fe moment of  $\sim 3 \mu_B/\text{Fe}$  at high temperatures in both compounds. In LuFe<sub>2</sub>Ge<sub>2</sub>, we confirm a phase transition at  $T_0 \approx 9 \text{ K}$  which likely corresponds to antiferromagnetic ordering of the Fe moments. Nevertheless, strong antiferromagnetic spin fluctuations even below  $T_0$  lead to an enhancement of the effective mass by a factor of  $\sim 5$  in the Fermi-liquid state observed at low temperatures in this compound. In YbFe<sub>2</sub>Ge<sub>2</sub> our results indicate a weakly intermediate valent Yb state, at the border to the Kondo regime with a comparatively low characteristic  $4f$  energy of  $\sim 80 \text{ K}$ , corresponding to a valence close to but less than 3. Accordingly, we observe at low temperatures a heavy-fermion behaviour with a moderately enhanced Sommerfeld coefficient  $\gamma = 200 \text{ mJmol}^{-1}\text{K}^{-2}$ . The low-temperature properties can be well explained by an effective  $J = 3/2$  single-ion Kondo model.

# 4 Pure and doped $\text{YbRh}_2\text{Si}_2$ : Crossing the QCP

## 4.1 Introduction

### 4.1.1 Review

Within the class of intermetallic compounds, strong violations of Landau's Fermi-liquid theory were first reported and analysed in the Kondo alloy  $\text{Y}_{1-x}\text{U}_x\text{Pd}_3$  [Seaman 1991]. Since then quite a number of non-Fermi-liquid compounds were found, and this topic has gained increasing interest in the past years. Among the non-Fermi-liquid systems the heavy-fermion compound  $\text{YbRh}_2\text{Si}_2$  has attracted considerable attention because it is located very close to a quantum critical point (QCP) connected with the transition from a magnetically ordered ground state to a non-magnetic one [Gegenwart 2002]. At ambient pressure it orders antiferromagnetically at a very low temperature of  $T_N = 70$  mK.

First investigations on this system were performed by D. J. Thompson [Thomson 1987], which showed a heavy-fermion-like behaviour at high temperatures in the resistivity, but the sample had a quite large residual resistivity and therefore this compound was not studied in detail. Further investigations were not reported until O. Trovarelli [Trovarelli 2000a, Trovarelli 2000b, Trovarelli 2000c] got small  $\text{YbRh}_2\text{Si}_2$  single crystals in 1999. The following initial physical investigations confirmed the results of Thompson and showed that  $\text{YbRh}_2\text{Si}_2$  is a very interesting Yb-based heavy-

fermion system. At the beginning of my work the following properties of YbRh<sub>2</sub>Si<sub>2</sub> were known.

- i) The susceptibility shows strong single-ion anisotropy with  $\chi_{\parallel ab}$  twenty times larger than  $\chi_{\parallel c}$  at low temperatures (Fig. 4.1). For fields along the easy plane,  $\chi(T)$  follows a Curie-Weiss law below 400 K with an effective moment of  $\mu_{\text{eff}} = 4.4 \mu_B$  and  $\Theta_{\parallel ab} \approx -9$  K, indicating a trivalent Yb state and predominant antiferromagnetic interactions. Below 50 K,  $\chi$  increases with decreasing temperature faster than expected for a Curie-Weiss law. The low-temperature susceptibility shows an anomaly around 70 mK, which gives a first indication for antiferromagnetic ordering. In contrast  $\chi_{\parallel c}$  is temperature independent below 50 K, while above it decreases with increasing temperature. Above 200 K one can fit a Curie-Weiss law for  $\chi_{\parallel c}$  with  $\mu_{\text{eff}} = 4.3 \mu_B$  and  $\Theta_{\parallel c} \approx -180$  K [Trovarelli 2000a].

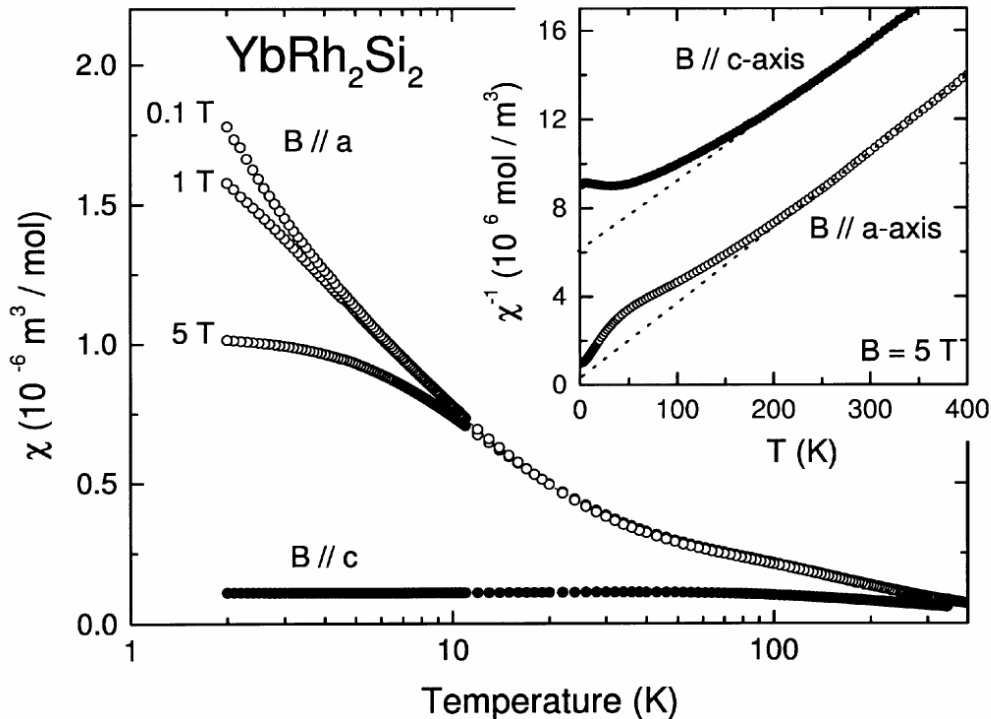


**Figure 4.1:** Susceptibility along the *a* and *c* axis for different fields *B*. Inset shows inverse susceptibility at  $B = 5$  T (Fig. taken from [Trovarelli 2000a]).

- ii) The high-temperature resistivity is typical for heavy-fermion systems. It shows a broad maximum around 120 K and a pronounced decrease with decreasing temperature below 80 K. The low-temperature resistivity shows a linear temperature dependence,  $\delta\rho(T) = \rho(T) - \rho_0$  is proportional to the temperature, indicative of a non-Fermi-liquid system (Fig. 4.2). An anomaly around 70 mK marks the magnetic ordering. Here the spin disorder scattering decreases.

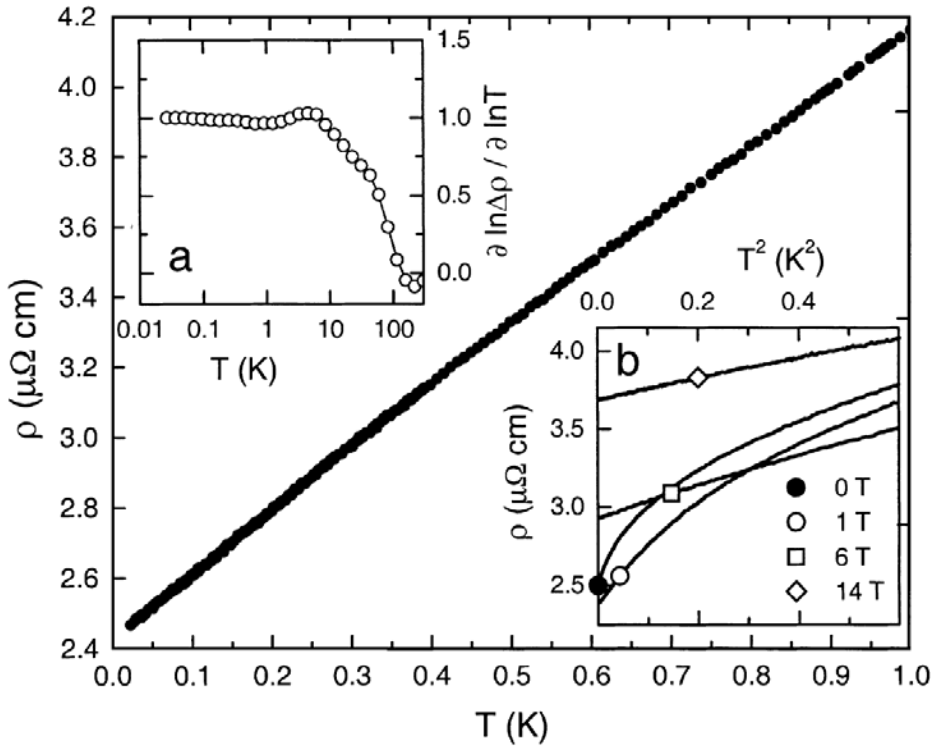


**Figure 4.2:** The low temperature resistivity of  $\text{YbRh}_2\text{Si}_2$  shows a linear temperature dependence below 1 K. Inset a: Temperature dependence of the resistivity exponent  $\varepsilon$ . Inset b: Resistivity on a quadratic temperature scale for  $B \leq 14$  T. (Fig. taken from [Steglich 2000])

- iii) Below 10 K,  $C/T$  increases logarithmically with decreasing temperature, another hallmark for the NFL behaviour in  $\text{YbRh}_2\text{Si}_2$  (Fig. 4.3). Below 0.4 K, the increase is stronger than logarithmic,

before a sharp anomaly marks the long-range antiferromagnetic ordering at 70 mK [Custers 2003].

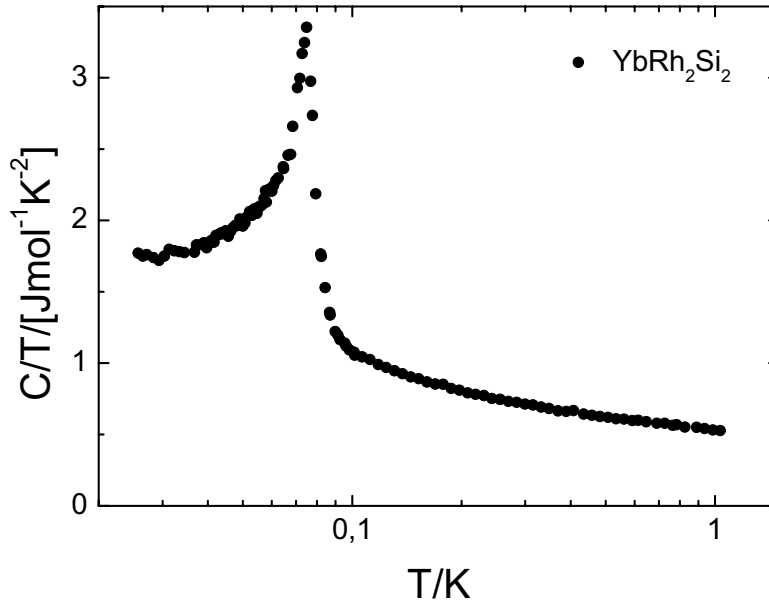


**Figure 4.3:** *Specific-heat data of  $\text{YbRh}_2\text{Si}_2$  plotted as  $C/T$  on a logarithmical temperature scale. (Fig. taken from [Custers 2003])*

- iv) By applying hydrostatic pressure  $T_N$  shifts to higher temperatures. At higher pressure ( $p \geq 1.5$  GPa) a second anomaly appears. With increasing pressure, the anomaly at  $T_N$  in the resistivity weakens, while that one at  $T_{ml}$  becomes more pronounced (Fig. 4.4). This behaviour indicates that the magnetically ordered state would disappear at a quantum critical point at a slightly negative pressure  $p_c \approx (-0.45 \pm 0.1)$  GPa [Mederle 2002b].

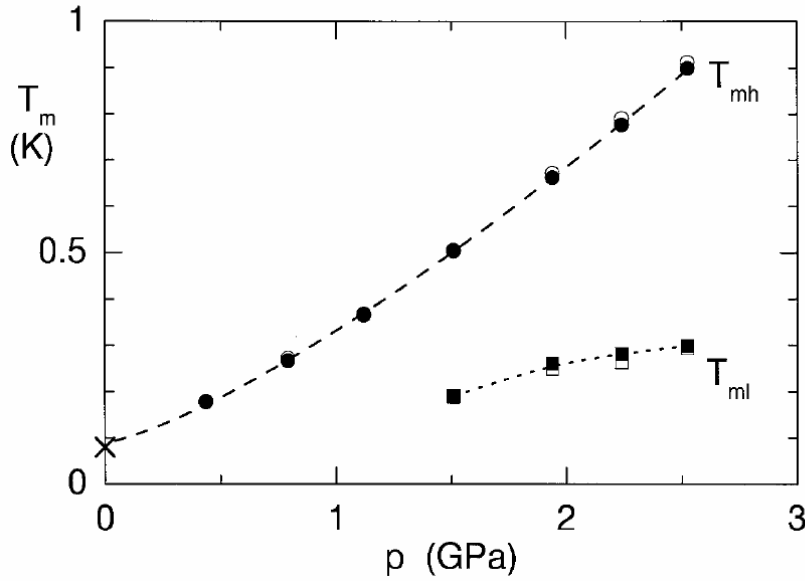


**Figure 4.4:** Pressure dependence of the two anomalies observed in electrical-resistivity measurements on two different samples (open and closed symbols) (taken from [Mederle 2001]).

- v) Low-temperature resistivity (Fig. 4.5), ac-susceptibility and specific-heat measurements (Fig. 4.6) show a shift of the antiferromagnetic transition to lower temperatures when applying a magnetic field. The critical field to suppress this antiferromagnetic order at a QCP is  $B_{\text{crit}} = 700$  G for field applied along the easy plane and a factor of 11 larger for field applied along the  $c$  axis [Gegenwart 2002]. At the field-induced QCP, one observes pronounced non-Fermi-liquid (NFL) behaviour in the resistivity,  $\rho(T)$ , and the specific heat,  $C(T)$ , down to the lowest investigated temperature even in pure YbRh<sub>2</sub>Si<sub>2</sub>.  $T_N$  disappears at a QCP where the effective mass of the quasiparticles seems to diverge, as deduced from a divergence of  $C/T$  [Küchler 2003, Küchler 2005], of the constant  $\chi_0$  observed in the ac susceptibility for  $B > B_{\text{crit}}$ , and of the coefficient  $A$  of the  $T^2$  term in the resistivity for  $B > B_{\text{crit}}$ .



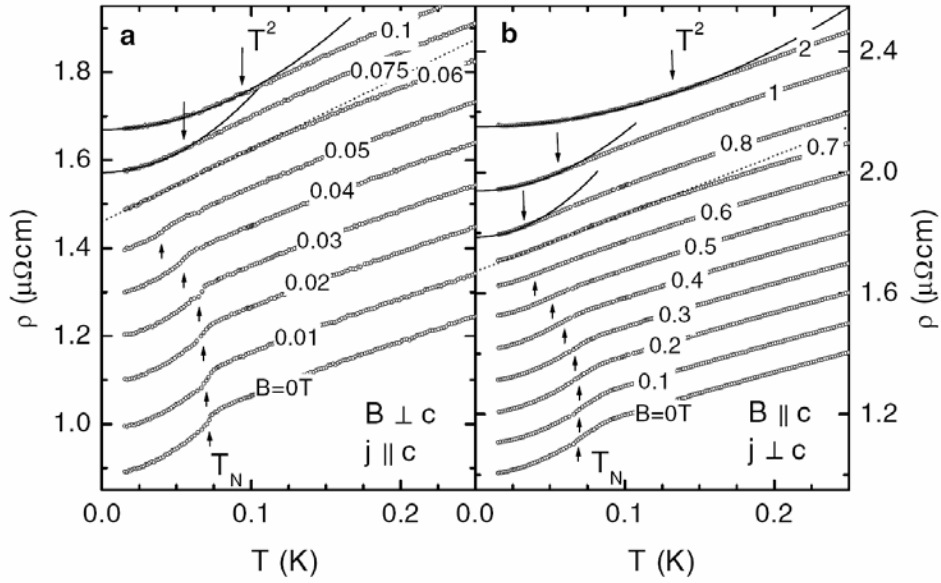


**Figure 4.5:** Low temperature resistivity of  $\text{YbRh}_2\text{Si}_2$  in different magnetic fields along the  $a$  axis (a) and along the  $c$ -axis (b). The curves for  $B > 0$  are shifted subsequently by  $0.1 \mu\Omega\text{cm}$ . The arrows indicate  $T_N$  and the upper limit of  $T^2$  behaviour, respectively. (Fig. taken from [Gegenwart 2002])

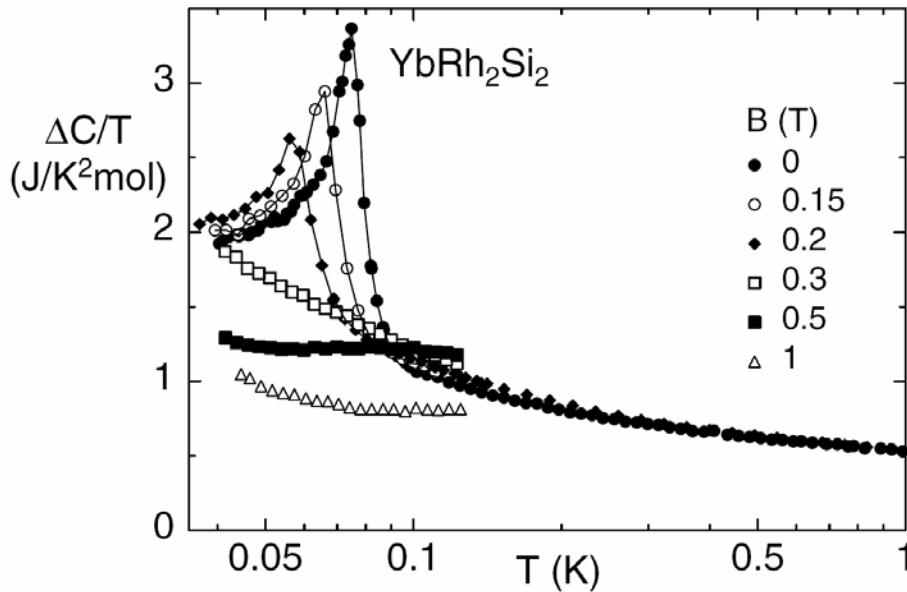


**Figure 4.6:** Specific heat  $\Delta C/T = (C - C_0)/T$  versus temperature on a logarithmic temperature scale in different magnetic fields applied parallel to the  $c$  axis. (Fig. taken from [Gegenwart 2002])

## 4.1.2 Aim of this work

The aim of this work was to reach and to cross the quantum critical point by using negative chemical pressure. Already slight negative chemical pressure using Ge doping [Custers 2003] leads to pronounced non-Fermi-liquid (NFL) behaviour in the resistivity  $\rho(T)$ . This Ge content was however not enough to cross the QCP. Since higher Ge contents could not be achieved, we tried to replace Yb by La, which should also lead to an increase of the unit-cell volume.

The value of the negative pressure required to push  $T_N$  to 0 in the pure system YbRh<sub>2</sub>Si<sub>2</sub> is  $p_c = (-0.45 \pm 0.1)$  GPa [Mederle 2002b]. Using the isotherm bulk modulus  $B_T = 189 \pm 15$  GPa for pure YbRh<sub>2</sub>Si<sub>2</sub> [Plessel 2002],

$$B_T = -V \cdot (dp/dV)_T, \quad (1)$$

and the volume of the unit cell of pure YbRh<sub>2</sub>Si<sub>2</sub> ( $V_{YRS} = 158.52 \text{ \AA}^3$ ) one can calculate the critical unit-cell volume  $V_c = 158.89 \text{ \AA}^3$  and the volume expansion  $dV_c = 0.377 \text{ \AA}^3$  required to reach the QCP. The unit-cell volume of YbRh<sub>2</sub>Ge<sub>2</sub> and LaRh<sub>2</sub>Si<sub>2</sub> are  $V_{YRG} = 166.07 \text{ \AA}^3$  [Francois 1985] and  $V_{LRS} = 173.41 \text{ \AA}^3$  [Caroca 2005], respectively. Assuming a linear concentration dependence of the alloy unit-cell volume, one can easily calculate the expected critical Ge and La concentrations:

$$x_{Ge} = 100\% \cdot dV_c / dV_{(YRG-YRS)} = 100\% \cdot 0.377 \text{ \AA}^3 / 7.55 \text{ \AA}^3 = 5.0\%, \quad (2)$$

$$x_{La} = 100\% \cdot dV_c / dV_{(LRS-YRS)} = 100\% \cdot 0.377 \text{ \AA}^3 / 4.63 \text{ \AA}^3 = 2.5\%. \quad (3)$$

This suggests critical compositions of YbRh<sub>2</sub>(Si<sub>0.95</sub>Ge<sub>0.05</sub>)<sub>2</sub> and Yb<sub>0.975</sub>La<sub>0.025</sub>Rh<sub>2</sub>Si<sub>2</sub>. It has to be pointed out that the volume of the unit cells of YbRh<sub>2</sub>Ge<sub>2</sub> and LaRh<sub>2</sub>Si<sub>2</sub> were taken from literature, while for the volume of the unit cell of pure YbRh<sub>2</sub>Si<sub>2</sub> we took our own X-ray results. Taking the volume of pure YbRh<sub>2</sub>Si<sub>2</sub> from the literature ( $V_{YRS} = 158.24 \text{ \AA}^3$ ) [Rossi 1979] gives, however, only slightly different values  $dV_c = 0.376 \text{ \AA}^3$ ,  $x_{Ge} = 4.8\%$  and  $x_{La} = 2.5\%$ , respectively. Both ways of doping were tried and the result compared with those obtained on the pure system.

Since the crystal-growth process of pure YbRh<sub>2</sub>Si<sub>2</sub> was still not well established, the growth parameters were changed until a reproducible crystal

quality was obtained. This quality was mainly evaluated using the residual resistivity ratio.

A lot of investigations were performed on YbRh<sub>2</sub>Si<sub>2</sub> in the low-temperature region, but some high-temperature properties, like e.g. the crystal electric field, were yet not settled. We, therefore, analyzed the high-temperature specific heat to fix this crystal field (CEF). The samples obtained from the reproducible crystal growth were further used for neutron scattering and ESR experiments. With inelastic neutron scattering we studied the magnetic excitations, i.e., the CEF excitations and the magnetic fluctuations. The ESR experiment gave a very surprising result, because for the first time the ESR signal of the Kondo ion was found in a dense Kondo system.

## 4.2 Crystal growth

### 4.2.1 Introduction

To get polycrystalline material, it is often sufficient to melt the elements together in an arc furnace. For the growth of single crystals, more sophisticated procedures are required, like e.g. crystal pulling, zone melting or Bridgman technique. Growing Yb-based single crystals is even more difficult, because of the low boiling point of Yb,  $T_B = 1196^\circ\text{C}$ . Thus, if temperatures above  $1200^\circ\text{C}$  are required, the melt has generally to be enclosed in a sealed tantalum container. This is especially true for the crystal growth of YbRh<sub>2</sub>Si<sub>2</sub>, because of the high melting temperature of Rh ( $T_S = 1966^\circ\text{C}$ ). At this temperature, direct melting of the elements shall generally lead to a reaction of the melt with the crucible needed to avoid Yb evaporation. An appropriate method to reduce the growth temperature is to use the flux technique [Fisk 1989, Canfield 1992], where the material to grow is dissolved in a low-melting liquid. Besides reducing the growth

temperature, this method has some further advantages. The main advantage is that this technique does not require sophisticated equipment. Further on, the growth at lower temperatures leads to less defects, less thermal strain, and sometimes to a lower impurity concentration, if the distribution coefficient of the impurity between melt and compound is below 1. This technique is widely used for compounds which otherwise present some growth problems, but it does not work for all systems. The disadvantages of this method are the presence of flux inclusions in the crystal (e.g. pure flux parts surrounded by the desired material) or incorporation of the flux elements into the structure of the desired compound. Sometimes reaction of the flux with the surrounding crucible can be a problem. The difficult part in this technique is choosing the right solvent for the growth. The best flux metals are those with relatively low melting points as aluminium, bismuth, gallium, indium, tin and zinc. In our case indium flux was found to be the best suitable solvent for growing pure and La-doped or Y-doped  $\text{YbRh}_2\text{Si}_2$ , because Zn and Bi are poor solvents for Si [Hansen 1958] while Ga and Al can incorporate into the crystal structure. Choosing between In and Sn puts the preference to In, because separating the single crystals from indium flux is much easier than from tin flux. The next problem arose in the choice of the right crucible, since tantalum reacts with indium and therefore we had to use a second  $\text{Al}_2\text{O}_3$  crucible inside the Ta crucible to contain the melt and prevent the reaction between melt and tantalum.

But also the  $\text{Al}_2\text{O}_3$  crucible is not the perfect one. When we started the crystal growth at a very high temperature ( $T > 1600^\circ\text{C}$ ) we observed AlRh cubes or pure aluminium clusters attached on the surface of the  $\text{YbRh}_2\text{Si}_2$  single crystals. We suspect that this is due to a reduction of the  $\text{Al}_2\text{O}_3$  by the Yb contained in the melt. Thus, all pure and La-, Y- and Ge- doped  $\text{YbRh}_2\text{Si}_2$  single crystals were grown using In flux and the sealed tantalum-crucible technique at slightly lower temperatures. The first step was to anneal the Ta and  $\text{Al}_2\text{O}_3$  crucibles and lids in vacuum for 20 hours and 17 hours at  $1250^\circ\text{C}$  and  $1200^\circ\text{C}$  respectively, in order to clean them.

The pure starting elements were cut into little pieces outside (Rh, Si, and Ge) or inside (Yb, La, and Y) the argon box. The required mass of the elements was mixed with the appropriate amount of indium and filled in the Al<sub>2</sub>O<sub>3</sub> crucible. The filling order of the elements does not play such an important role as long as rhodium is not in the upper part of the crucible and indium not the base layer. Indium melts first during heating the furnace before starting the crystal growth and flows in between the other (still solid) elements. The Al<sub>2</sub>O<sub>3</sub> crucible was covered with a lid and placed into the Ta crucible. The crucible was then sealed under argon atmosphere at a pressure of 300 mbar. Argon is an ideal gas and expands during the crystal growth. Sealing the crucible at ambient pressure would result in a deformation or even bursting of the sealed Ta crucible. Zirconium foil wrapped around the tantalum protects it against oxidation. This serves also as a leak test for the ceramic tube (Al<sub>2</sub>O<sub>3</sub>), which separates the Ta crucible from the air atmosphere during the crystal-growth process. The vertical furnaces from Xerion or Gero were used for the flux crystal growths. For the growth process itself, the crucible was cooled either by slowly reducing the furnace temperature, keeping the crucible inside the furnace (furnace cooling) or the crucible was slowly pulled out of the furnace which was then kept at a constant temperature (Bridgman technique).

Small differences and variations from the established standard procedure are explained in the following chapters.

## 4.2.2 Crystal growth of pure YbRh<sub>2</sub>Si<sub>2</sub>

Polycrystalline YbRh<sub>2</sub>Si<sub>2</sub> was first synthesised by [Rossi 1979]. They first melted the starting components Rh (4N), Si (4N) and Yb (3N) in an induction furnace under argon and then annealed the ingot at 773 K for one week. The resulting sample was heterogeneous. The lattice parameters were estimated on powder samples with X-ray Fe-radiation to  $a = 0.4010$  nm and  $c = 0.9841$  nm. Further investigations to improve the sample quality by the

same or other groups were not reported until O. Trovarelli [Trovarelli 2000a] after several tries got in 1999 small YbRh<sub>2</sub>Si<sub>2</sub> single crystals by using the sealed Ta-crucible technique and In flux. But the growth process was still not reproducible. The right starting temperature, the duration of growth and even the In-flux ratio were not settled. Preliminary attempts to determine an appropriate flux ratio indicated that a mixture of 96 mol% In and 4 mol% YbRh<sub>2</sub>Si<sub>2</sub> is a good starting composition. In the present work, quite a number of crystal-growth runs were dedicated to provide the experimental groups with a sufficient amount of single crystals for the further investigations of the physical properties of YbRh<sub>2</sub>Si<sub>2</sub>, but a few attempts could be dedicated to an improvement of the growth process. The parameters which were looked at were the melting temperature, the cooling process and the flux-ratio. Concerning the melting temperature, we found that a temperature well below 1480°C results in a very fine powder material, suggesting that the temperature was too low to dissolve all elements. Here we tried to start with the binary RhSi instead of the pure elements Rh and Si, with the expectation that RhSi might dissolve more easily than Rh, but we did not observe any improvement. On the other hand larger melting temperatures lead to an increase of the amount of Al impurities as described above, thus a melting temperature of 1480°C with a melting time of 3 hours seems to be optimal. A few attempts were made with a lower In-flux ratio of 90% or 80%, but they did not lead to larger single crystals. For the cooling procedure we used finally the standard process shown in Fig. 4.7, where the temperature of the furnace was lowered down to 930°C within 40 hours. The temperature of 930°C was kept for 75 hours to anneal the samples and then the temperature was reduced fast to room temperature. The temperature profile as well as the cooling speed for the Bridgman technique was changed several times, until the best reproducible result was obtained. Typical single-crystalline platelets are shown in Fig. 4.8.

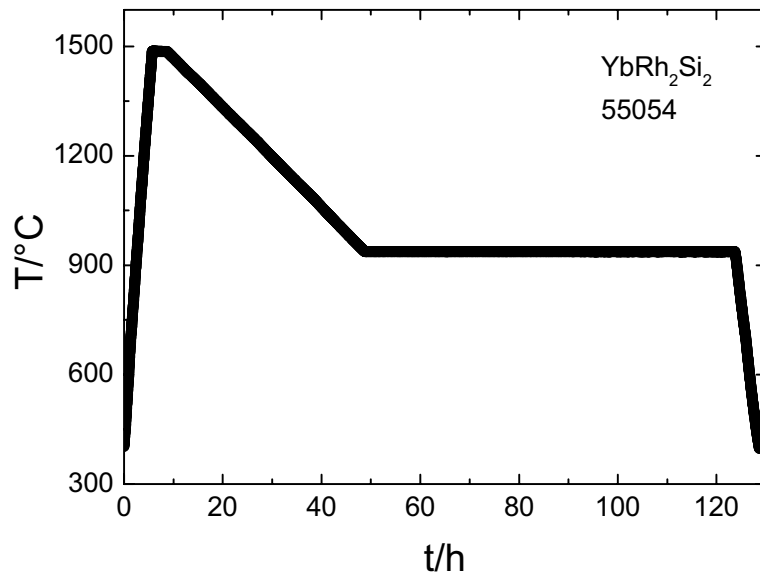


**Figure 4.7:** Standard temperature versus time profile used for the optimised  $\text{YbRh}_2\text{Si}_2$  crystal growth.

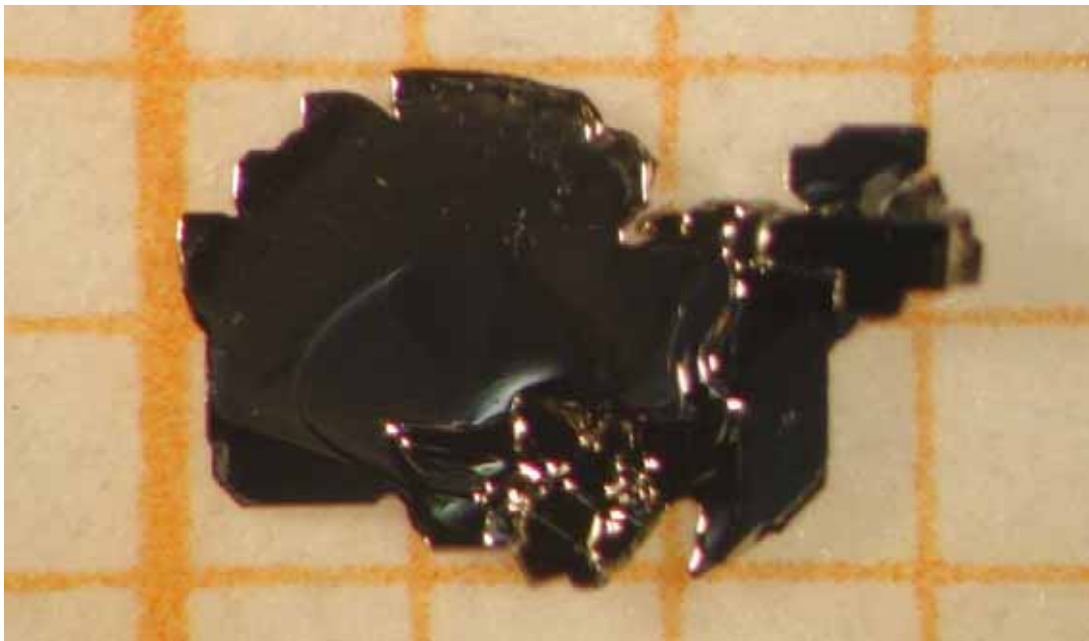


**Figure 4.8:** Single crystals of pure  $\text{YbRh}_2\text{Si}_2$  are platelet like.

Table 4.1 lists all performed crystal growth of pure  $\text{YbRh}_2\text{Si}_2$  including batch number, temperature profile, amount of In flux used, total mass of batch and furnace used.

**Table 4.1:** *Parameters of the different  $\text{YbRh}_2\text{Si}_2$  growth attempts.*

batch no.	furnace	flux-ratio	total mass of Yb, Rh, Si	melting temperature / time	details of cooling process	results
55008	GERO	96 % In	2	up to 1460°C with 300°C/h	Bridgman: Stroke: 135 (0.2 mm/h) power cut after 80 hrs	few SC + PC
55010	GERO	96 % In	2	up to 1000°C, holding 12h, up to 1460C, holding 2h	Bridgman: Stroke: 9 (3 mm/h), but movement is faster!	a lot of small SC
55031	GERO	90 % In	5	up to 1480°C, holding 1h, up to 1330C, holding for 20min	Bridgman: Stroke: 194 (0.14 mm/h)	only 2 SC
55034	Xerion	96 % In	2	up to 1480°C in 8 h, holding 3h	furnace cooling: intended: in 50h to 730°C (15C/h), but due to heater failure several hours at 930°C	a lot of SC
55054	Xerion	96 % In	2.5	up to 1480°C in 8h, holding for 180min,	furnace cooling: in 40h down to 930°C and annealing here for 75h	PC and SC in middle
55056	Xerion	80 % In	5.0	up to 1600°C in 10h, holding for 180min	furnace cooling: in 50h down to 930°C and annealing here for 20h	no SC
55059	Xerion	96 % In	2.5	up to 1480°C in 8h,	Bridgman: down to 1460°C, then Stroke 30 (0.9 mm/h)	a lot of SC
55071	Xerion	96 % In	2.5	up to 1480°C in 8h, holding 180 min,	furnace cooling: in 40h down to 930°C and annealing for 75h	a lot of small SC



### 4.2.3 Crystal growth of doped YbRh<sub>2</sub>Si<sub>2</sub>

To induce negative chemical pressure in YbRh<sub>2</sub>Si<sub>2</sub> several possibilities via doping with isoelectronic elements were tried. Isoelectronic dopands, e.g. elements within the same row of the periodic system, are known to induce much less disorder effects than non-isoelectronic dopands, which lead to a change of the total number of electrons. The first obvious choice was to replace Si by the larger Ge. Several Ce-T-Si/Ge alloys have been thoroughly investigated, resulting in a composition dependence of the magnetic properties very similar to that observed in the Ge compound under pressure. This proves that the main effect of Ge doping corresponds indeed to a negative chemical pressure with only minor disorder effects.

However, the crystal growth of Ge-doped YbRh<sub>2</sub>Si<sub>2</sub> turned out to be very difficult. Therefore, we tried another way, replacing Yb by the larger La or Y. This results in a depletion of the magnetic sublattice, but as long as this depletion is not too large (< 30%), the effect on collective phenomena should not be too strong. As an example, the alloy Ce<sub>1-x</sub>La<sub>x</sub>Ru<sub>2</sub>Si<sub>2</sub> has been thoroughly investigated and for  $x < 0.3$  the properties are quite similar to those observed in CeRu<sub>2</sub>(Ge<sub>x</sub>Si<sub>1-x</sub>)<sub>2</sub> [Haen 1996]. Since the growth of La-doped YbRh<sub>2</sub>Si<sub>2</sub> worked quite well from the beginning, we concentrated on this system and performed only one attempt with Y.

#### 4.2.3.1 Crystal growth of YbRh<sub>2</sub>(Si<sub>1-x</sub>Ge<sub>x</sub>)<sub>2</sub>

Table 4.2 lists all performed crystal growths of Ge-doped YbRh<sub>2</sub>Si<sub>2</sub> with the temperature profile used, batch number, furnace used and amount of In flux.

**Table 4.2:** Parameters of the different YbRh<sub>2</sub>(Si<sub>1-x</sub>Ge<sub>x</sub>)<sub>2</sub> growth attempts.

batch no. (Ge-content)	furnace	flux-ratio	total mass of elements	melting temperature / time	details of cooling process	results
55011 (10% Ge)	Xerion	96% In	2	up to 1100°C in 5h, holding 24h, up to 1475°C in 2h, holding 5h	furnace cooling: with 1.5K/h to 1000°	SC with only 2 % Ge
55013 (10% Ge)	GERO	96% In	2	up to 1100°C with 300K/h, holding 2h, up to 1460°C in 90min	Bridgman: Stroke 27 (1mm/h)	SC with only 2 % Ge
55028 (10% Ge)	GERO	92% In	4	up to 1380°C with 300K/h, holding 1.5h, to 1330°C in 20min,	Bridgman: Stroke: 194 (0.14 mm/h)	no SC
55030 (100 %Ge)	GERO	90% In	6	up to 1480°C with 300K/h, holding 1.3h, down to 1330°C, holding 20min	Bridgman: Stroke: 194 (0.14 mm/h)	no SC, PC of Yb <sub>4</sub> Rh <sub>7</sub> Ge <sub>6</sub>
55036 (100 %Ge)	Xerion	90% In	6	up to 930°C (in 6h), holding 100h (heater broken)	Bridgman: Stroke: 170 (0.16 mm/h)	no SC, PC of Yb <sub>4</sub> Rh <sub>7</sub> Ge <sub>6</sub>
55037 (100 %Ge)	Xerion	90% In	6	up to 1400°C (in 8h), holding 100h	Bridgman: Stroke: 170 (0.16 mm/h)	large SC, but Yb <sub>4</sub> Rh <sub>7</sub> Ge <sub>6</sub>
55039 (50% Ge)	Xerion	94% In	3	up to 1450°C (in 6h), holding 3h	furnace cooling: down to 700°C in 100h, annealing for 60min	large SC, but Yb <sub>4</sub> Rh <sub>7</sub> Ge <sub>6</sub>
55055 (75% Si + 75% Ge)	GERO	96% In	3.00	up to 1480°C with 300K/h, holding 300min	furnace cooling: down to 800°C with 10 K/h and annealing here for 1800min	pure Ge-SC + PC with the phases: YbRh <sub>2</sub> Si <sub>2</sub> , YbRh <sub>1.75</sub> Si <sub>2</sub> Ge <sub>0.25</sub> , YbRh <sub>2</sub> Si <sub>1.5</sub> Ge <sub>0.5</sub> , Yb <sub>2</sub> Rh <sub>1.5</sub> SiGe <sub>0.5</sub> , Ge <sub>2.5</sub> InRh <sub>1.5</sub> Si <sub>0.1</sub>
55070 (5% Ge)	GERO	30% In	6.78	up to 1600°C with 300°C/h	Bridgman: Stroke 27 (1mm/h)	black nuggets, no SC

Usually the preparation of samples of Ce-T-Si/Ge alloys is rather simple. The chemical properties of Si and Ge are quite similar and the melting temperatures,  $T_S = 1410^\circ\text{C}$  and  $T_S = 937.4^\circ\text{C}$  for Si and Ge, respectively, are not too much different. Thus, for the first attempts we just replaced a small part (5 % - 10 %) of Si by Ge and used the standard crystal-growth procedure developed for pure YbRh<sub>2</sub>Si<sub>2</sub>.

However, determination of the lattice parameters of the obtained single crystals using X-Ray powder diffraction did not reveal any significant increase of  $a$  or  $c$  (table 4.3). It seems that the effect of flux is much larger than the effect of Ge for the lattice constants. There is no evidence for the incorporation of Ge in the YbRh<sub>2</sub>Si<sub>2</sub> lattice.

**Table 4.3:** *Lattice parameters  $a$  and  $c$  of crystals with a nominal concentration of  $\text{YbRh}_2(\text{Si}_{0.95}\text{Ge}_{0.05})_2$  and  $\text{YbRh}_2(\text{Si}_{0.9}\text{Ge}_{0.1})_2$  do not show any significant difference from lattice constants of pure  $\text{YbRh}_2\text{Si}_2$ .*

Ge	% In	$a$	$c$	batch no.
0 %	96	4.010	9.860	55008
0 %	96	4.010	9.857	55010
0 %	33	4.008	9.853	37085
0 %	33	4.009	9.858	37091
0 %	96	4.010	9.861	37105
5 %	33	4.006	9.852	48002
10 %	96	4.011	9.862	37111
10 %	96	4.011	9.862	55011
10 %	96	4.010	9.855	55013

For flux growth there is no simple relation between starting composition and composition in crystals. To get the amount of Ge built into the crystal structure first an investigation of lattice parameters and than an investigation with EDAX (energy dispersive analysis of X-ray) was performed. The lattice parameters calculated from the X-ray powder diffraction pattern of the Ge-doped samples do not show any significant difference to those of the pure YbRh<sub>2</sub>Si<sub>2</sub>, the values vary within the estimated accuracy of  $10^{-3}$  Å. For a

10% Ge-doped-sample, one expects an expansion of the lattice parameters of  $\Delta a = 0.005 \text{ \AA}$  and  $\Delta c = 0.02 \text{ \AA}$ , five times larger than the accuracy of the measurement. Thus any Ge content larger than 2% should be detectable. But in Fig. 4.9, there is no significant difference in the powder-diffraction patterns of pure (red data, batch 55010), nominal 5% Ge-doped (blue data, batch 48002) and nominal 10% Ge doped  $\text{YbRh}_2\text{Si}_2$  (green data, batch no 55013) visible. No shift of the peaks is visible at higher angles. One expects that a larger lattice constant (which means a larger nominal Ge-content) shifts the peaks towards lower angles.

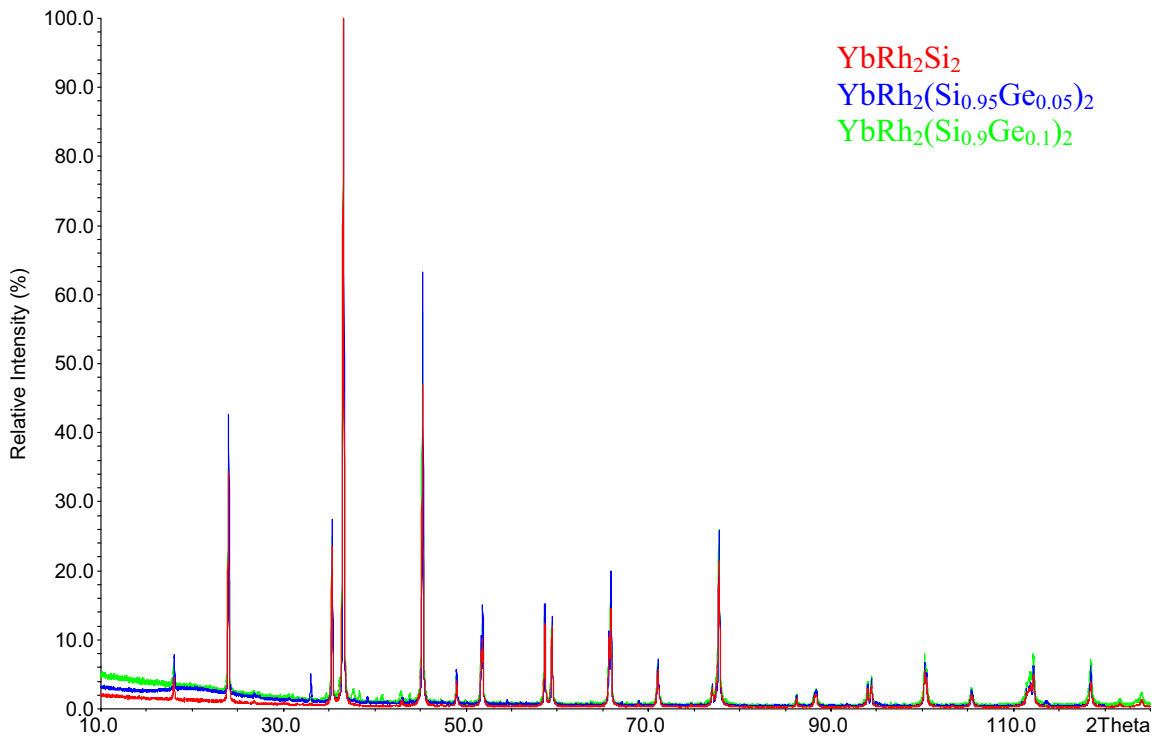


**Figure 4.9:** Comparison of X-ray powder diffraction pattern of pure, nominal 5% Ge-doped and 10% Ge-doped  $\text{YbRh}_2\text{Si}_2$ . All peaks of the  $\text{ThCr}_2\text{Si}_2$  structure are visible, but no shift to lower angles with larger Ge content is observable.

This put an upper limit of 2% to the Ge-substitution level achieved in the single crystals. A direct determination of the Ge content by microprobe analysis turned out to be impossible.

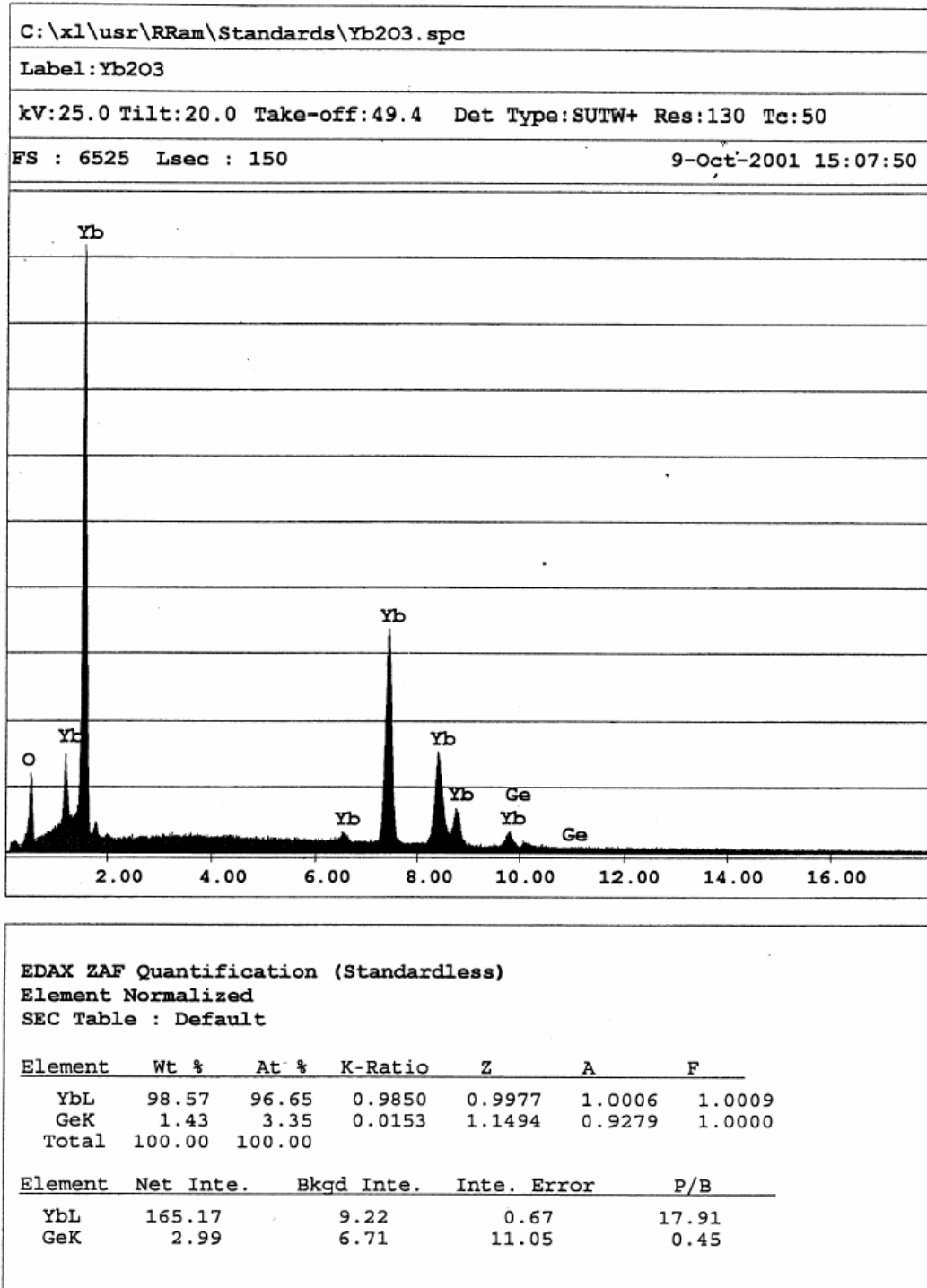


**Figure 4.10:** EDAX results of pure Yb<sub>2</sub>O<sub>3</sub> with an analysis allowing for the presence of Ge. The overlap of Yb and Ge lines leads to the wrong result with 3.3% Ge in the EPMA standard for Yb.

The position of the Ge-L and Ge-K lines matches perfectly with the M lines and L lines of Yb, respectively. Thus it is not possible to determine a small amount of Ge in presence of a large amount of Yb. Indeed a test analysis of pure  $\text{Yb}_2\text{O}_3$ , but allowing in the fit of the EPMA (electron probe microanalysis) spectra for the presence of Ge, led to a Ge content of 3.3% (Fig. 4.10).

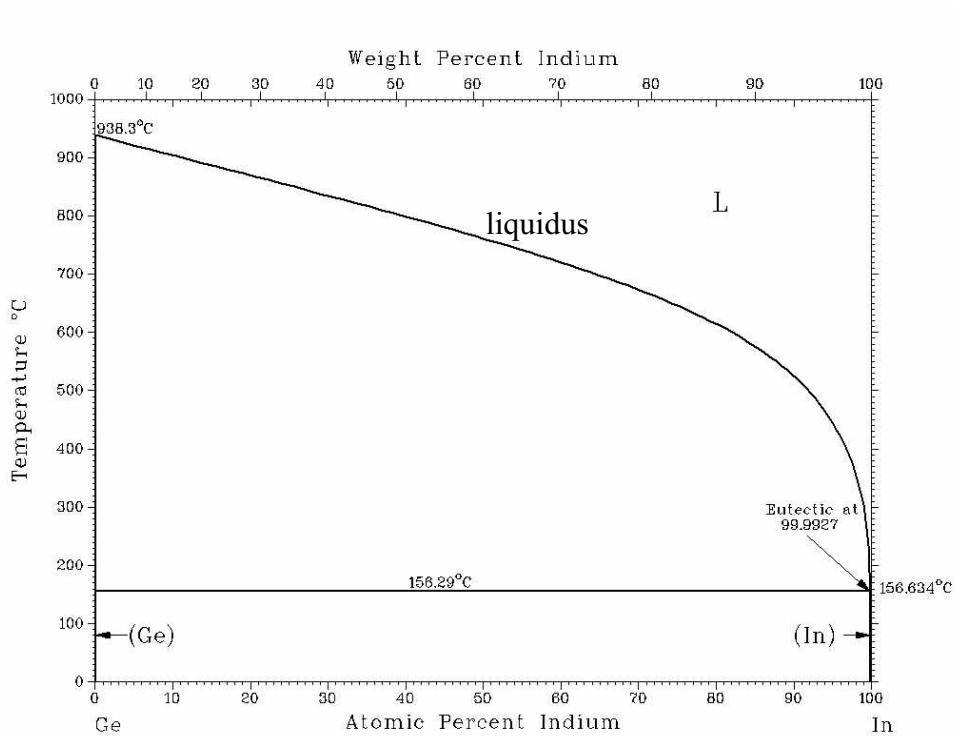


**Figure 4.11:** *Ge-In phase diagram [Massalski 1986a]. When cooling below the liquidus line, Ge separates from the homogenous liquid.*

We changed some of the growth parameters, like e.g. the In-flux content, the temperature-time profile, but without success. Then we tried the growth of 50 % Ge doped  $\text{YbRh}_2\text{Si}_2$  and of pure  $\text{YbRh}_2\text{Ge}_2$ . We obtained nice single crystals, but of  $\text{Yb}_4\text{Rh}_7\text{Ge}_6$ , not of the 1-2-2 phase. The  $\text{Yb}_4\text{Rh}_7\text{Ge}_6$  phase (see chapter 5) seems to be much more stable and seems to grow perfectly in

the In flux. A look at the binary Si-In and Ge-In phase diagrams give a hint for the problem of growing Ge-doped single crystals. At high temperatures (above  $1000^\circ\text{C}$ ), the solubility of Ge (100 at%) is much larger than that of Si ( $\sim 5$  at%). Thus, Ge prefers to stay in the flux than to be incorporated into the  $\text{YbRh}_2\text{Si}_2$  single crystal. Because of this difference in solubility, R-T-Ge compounds are usually better grown out of Sn, while R-T-Si compounds are better grown with In flux.

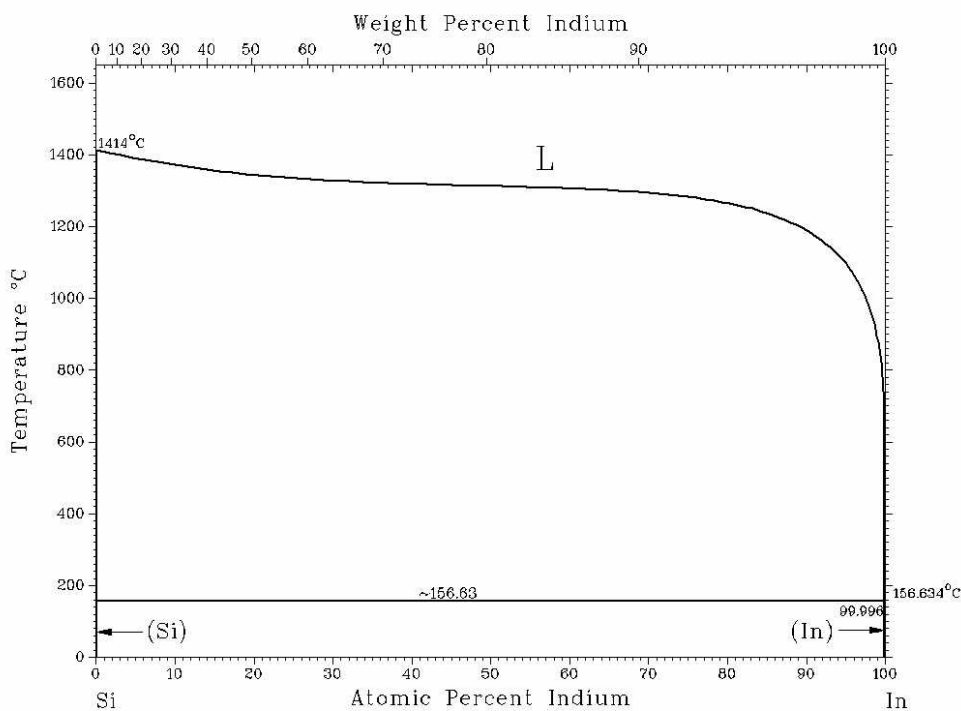


**Figure 4.12:** *Si-In phase diagram [Massalski 1986b].*

#### 4.2.3.2 Crystal growth of $\text{Yb}_{1-x}\text{La}_x\text{Rh}_2\text{Si}_2$ and $\text{Yb}_{0.95}\text{Y}_{0.05}\text{Rh}_2\text{Si}_2$

Table 4.4 lists all performed crystal growths of La- and Y-doped  $\text{YbRh}_2\text{Si}_2$  with the used temperature profile, batch number, used furnace and amount of In flux.

**Table 4.4:** Parameters of the different Yb<sub>1-x</sub>R<sub>x</sub>Rh<sub>2</sub>Si<sub>2</sub> (R = La and Y) growth attempts.

batch no.	furnace	flux-ratio	total mass of elements	melting temperature / time	details of cooling process	results
55053 (Yb <sub>0.95</sub> La <sub>0.05</sub> Rh <sub>2</sub> Si <sub>2</sub> )	Xerion	96% In	3.5	up to 1480°C (in 8h), holding 300min	furnace cooling down to 930°C (in 40h) and annealing here for 15h	SC: EDAX shows: Yb <sub>0.95</sub> La <sub>0.05</sub> Rh <sub>2</sub> Si <sub>2</sub>
55057 (Yb <sub>0.9</sub> La <sub>0.1</sub> Rh <sub>2</sub> Si <sub>2</sub> )	Xerion	96% In	2.5	up to 1480°C (in 8h), holding 300min	furnace cooling down to 930°C (in 40h) and annealing here for 15h	SC of Yb <sub>0.9</sub> La <sub>0.1</sub> Rh <sub>2</sub> Si <sub>2</sub> confirmed by EDAX
55060 (Yb <sub>0.95</sub> Y <sub>0.05</sub> Rh <sub>2</sub> Si <sub>2</sub> )	GERO	96% In-flux	2.5	up to 1480°C with 300°C/h, holding 2h	furnace cooling to 1000°C with 14°C/h	SC with a small amount of Y in YbRh <sub>2</sub> Si <sub>2</sub>
55069 (Yb <sub>0.8</sub> La <sub>0.2</sub> Rh <sub>2</sub> Si <sub>2</sub> )	Xerion	96% In-flux	2.5	up to 1480°C (in 8h), holding 300min	furnace cooling to 930°C (in 40h) and annealing here for 15h	single crystals with x = 0.2
55072 (Yb <sub>0.7</sub> La <sub>0.3</sub> Rh <sub>2</sub> Si <sub>2</sub> )	Xerion	96% In-flux	2.5	up to 1480°C (in 8h), holding 180min	furnace cooling to 930°C (in 40h) and annealing here for 25h	single crystals with x = 0.3
55075 (Yb <sub>0.95</sub> La <sub>0.05</sub> Rh <sub>2</sub> Si <sub>2</sub> )	Xerion	96% In-flux	2.5	up to 1480°C (in 8h), holding 120min	furnace cooling to 1150°C (in 40h) and then fast (8h) to 40°C	single crystals with x = 0.05
55076 (Yb <sub>0.95</sub> La <sub>0.05</sub> Rh <sub>2</sub> Si <sub>2</sub> )	Gero	96% In-flux	7.5	up to 1480°C with 300°C/h, holding 2h	furnace cooling to 1100°C with 10°C/h	single crystals with x = 0.05
55077 (Yb <sub>0.9</sub> La <sub>0.1</sub> Rh <sub>2</sub> Si <sub>2</sub> )	Xerion	96% In-flux	2.5	up to 1480°C (in 8h), holding 120min	furnace cooling to 1100°C (in 38h) and then fast (6h) to 40°C	single crystals with x = 0.1
55079 (Yb <sub>0.85</sub> La <sub>0.15</sub> Rh <sub>2</sub> Si <sub>2</sub> )	Xerion	96% In-flux	2.5	up to 1480°C (in 8h), holding 120min	furnace cooling to 1100°C (in 38h) and then fast (6h) to 40°C	single crystals with x = 0.15



In our study of the QCP we faced strong difficulties in growing single crystals with a larger Ge content. We therefore tried the growth of La-doped single crystals, because La doping provides a further possibility for inducing a negative chemical pressure. According to experience in La-doped Ce-Kondo lattices, the disorder induced in the periodicity of the rare-earth lattice does not seem to be detrimental as long as the La doping is not too large. We could successfully grow single crystals of La-doped  $\text{YbRh}_2\text{Si}_2$  up to a La concentration of 30% and investigated their properties in detail.  $\text{Yb}_{1-x}\text{La}_x\text{Rh}_2\text{Si}_2$  single crystals with  $x = 0.05, 0.1, 0.15, 0.2$  and  $0.3$  were grown from In flux, using the standard procedure developed for  $\text{YbRh}_2\text{Si}_2$ . The only change was to substitute Yb by the appropriate amount of La in the starting composition. In the following this La content shall be called nominal concentration. We did not experience a significant change in the size of the surface of the single crystals, but the thickness increases with larger La content from 0.1 mm (pure  $\text{YbRh}_2\text{Si}_2$ ) (Fig. 4.8) up to 0.3 mm ( $\text{Yb}_{0.7}\text{La}_{0.3}\text{Rh}_2\text{Si}_2$ ) (Fig. 4.13). The size (surface) of the platelets, grown perpendicular to the c-axis, varies from (3 mm x 3 mm) to (1 mm x 1 mm) randomly in all batches.

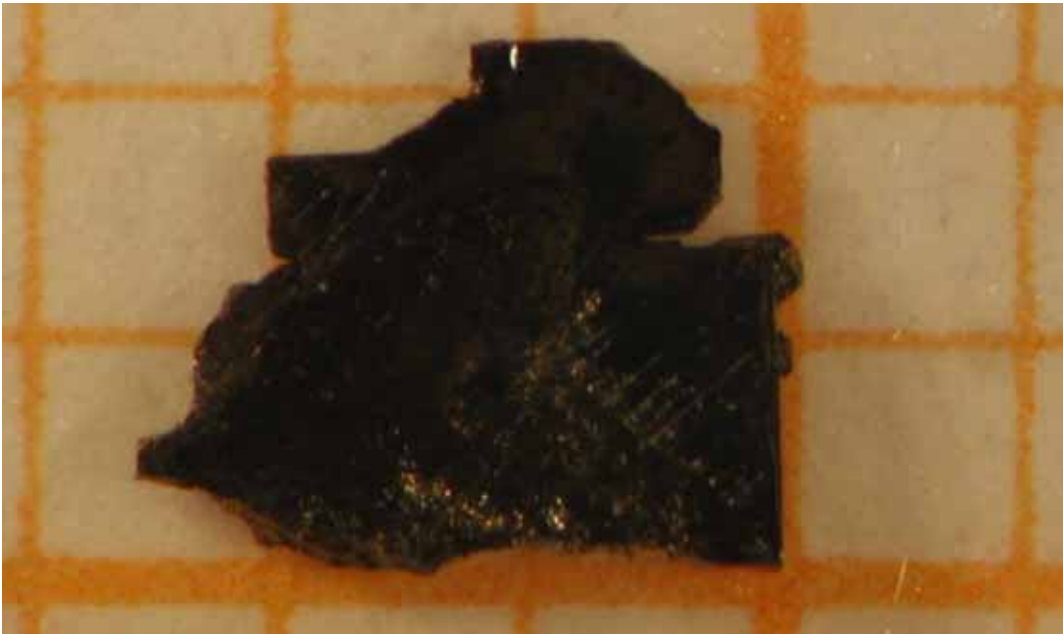


**Figure 4.13:** *Example for a 30% La-doped  $\text{YbRh}_2\text{Si}_2$  single crystal.*

We also performed a crystal growth of  $\text{YbRh}_2\text{Si}_2$  where 5% Yb was replaced by Y. Yttrium is also larger than Yb, but smaller than La. This could lead to a reduced disorder effect compared to La doping. We obtained single crystals of the usual size and EPMA confirmed an Y content of  $\approx 5\%$ .

### 4.3 Lattice constants

A small amount of the single crystals of each batch was powdered to perform the X-ray analysis. For all batches the X-ray powder diffraction patterns could be indexed with the  $\text{ThCr}_2\text{Si}_2$  crystal structure (see Fig. 3.4 – chapter 3.2.1). The lattice parameters were then calculated using the program “WinXPOW”.

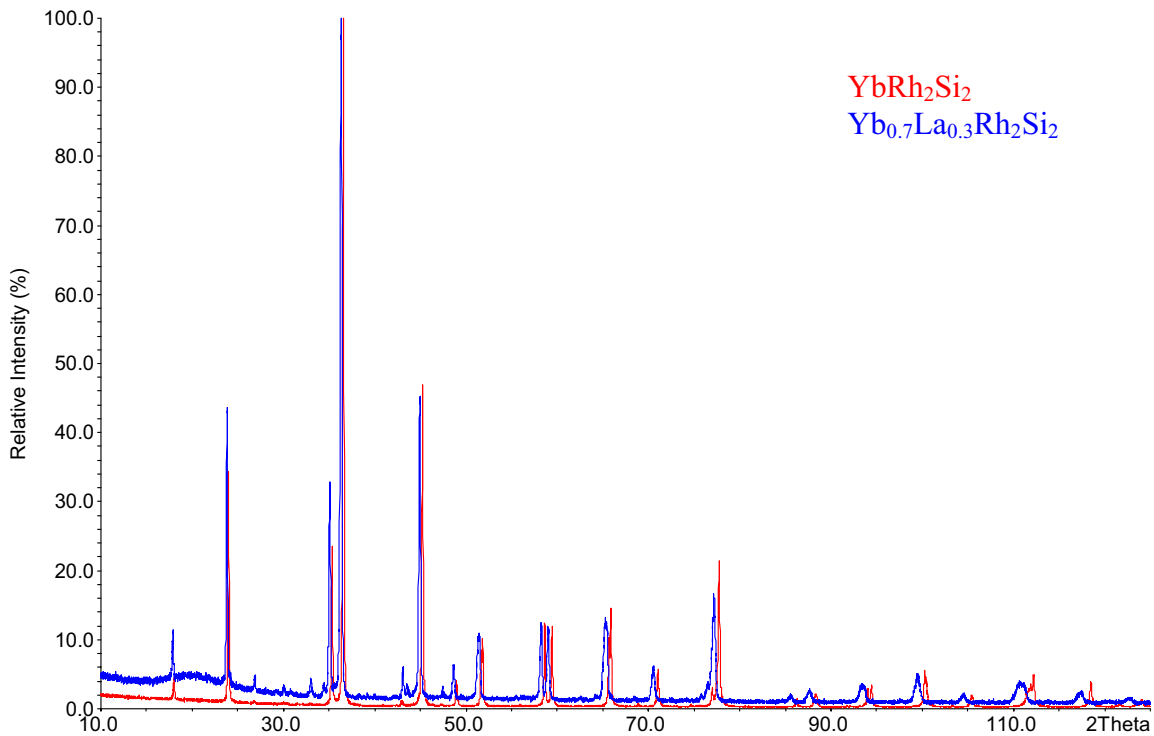


**Figure 4.14:** Comparison of the X-ray powder diffraction patterns of pure and 30% La-doped  $\text{YbRh}_2\text{Si}_2$ . The shift of peaks with increasing  $2\theta$  evidences the increase of the lattice parameter in the La-doped sample.

A comparison of the lattice constants of  $\text{Yb}_{1-x}\text{La}_x\text{Rh}_2\text{Si}_2$  with those of the pure system shows an increase of both lattice parameters with increasing La content. This is already visible by just comparing the powder-diffraction pattern of  $\text{Yb}_{0.7}\text{La}_{0.3}\text{Rh}_2\text{Si}_2$  with that of pure  $\text{YbRh}_2\text{Si}_2$  (Fig. 4.14). With increasing angle, the peaks of the La-doped samples are shifted to lower angle. This corresponds to an increase of the lattice parameters. One can also notice a broadening of the reflexes, which likely indicates some La distribution within the batch.

In Fig. 4.15 we have plotted the evolution of both lattice parameters as a function of the nominal La content. Within the accuracy of the experiment, both lattice parameters increase linearly with the La content. This increase is weaker than expected from a simple Vegard law, suggesting a reduced amount of La in the single crystals compared to the starting nominal concentration.

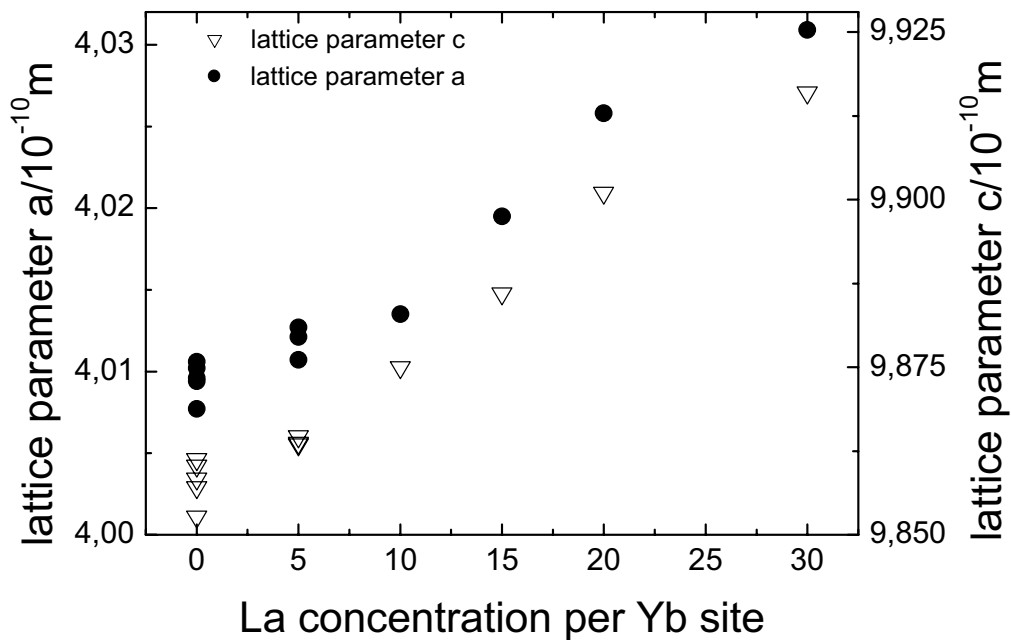


**Figure 4.15:** Evolution of the lattice parameters of all La-doped  $\text{YbRh}_2\text{Si}_2$  samples as a function of the nominal La content.

However, the La contents determined from microprobe measurements were even slightly larger than the (nominal) starting concentrations (Fig. 4.16). Since EPMA is a direct determination of the La content, while the estimation using the lattice parameters is an indirect one, and deviations from the simple Vegard law are not unusual, we shall from now on use the nominal La concentrations. The deviation between EPMA results and nominal starting concentrations is within the error bar of this method.

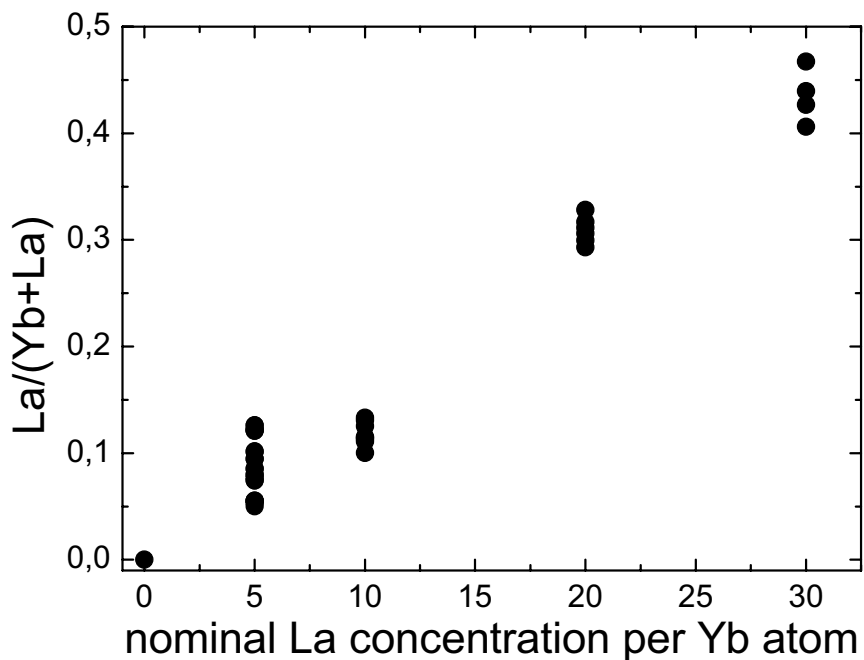


**Figure 4.16:** Evolution of the La-contents determined from microprobe measurements of all La-doped  $\text{YbRh}_2\text{Si}_2$  samples as a function of the nominal starting concentrations.

## 4.4 Physical properties

The electrical resistivity and the specific heat were determined in a commercial PPMS (Quantum Design) using an ac four-contact technique and a relaxation method, respectively.

### 4.4.1 Resistivity

#### 4.4.1.1 Resistivity of pure $\text{YbRh}_2\text{Si}_2$

A typical resistivity curve from room temperature down to 2 K for a pure  $\text{YbRh}_2\text{Si}_2$  sample looks like shown in Fig. 4.17. For the clarity only one data set is shown. All samples from the other batches show the same behaviour.

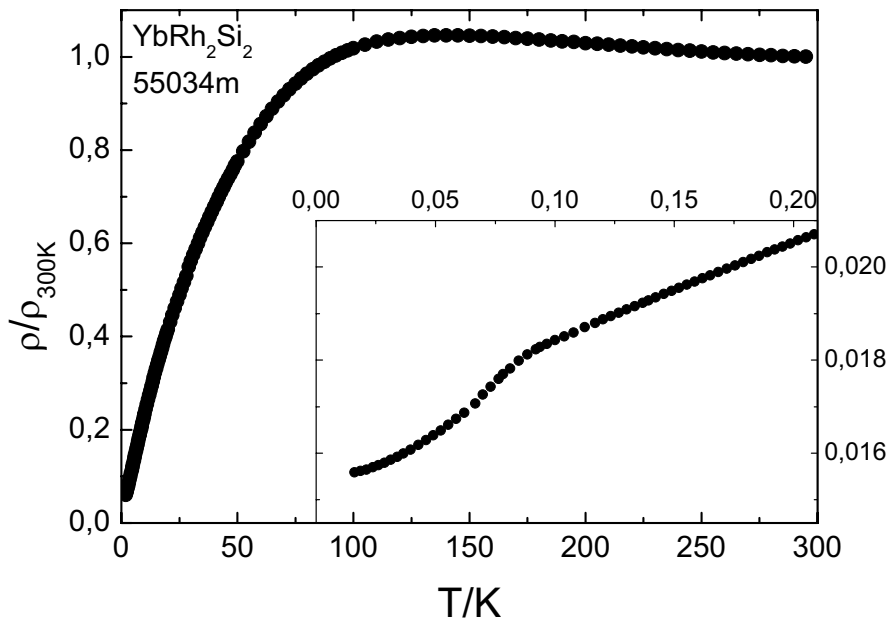


**Figure 4.17:** Resistivity data from 300 K down to 2 K on a linear temperature scale for pure  $\text{YbRh}_2\text{Si}_2$  (sample no 55034m). The inset shows the low-temperature data obtained in a dilution refrigerator by J. Custers.

Below room temperature the value of  $\rho(T)$  increases a little with decreasing temperature. Around 100 K a broad maximum, which can be related to Kondo scattering on both ground state and excited crystal field levels, is visible. Below this maximum the resistivity decreases with a change in the slope until 10K. Below this temperature a linear resistivity dependence is observed, indicating non-Fermi-liquid behaviour. A significant kink at  $T_N = 70$  mK as seen in the low-temperature resistivity measurements obtained in a dilution refrigerator by J. Custers points to the transition from a non-magnetic state to a magnetically ordered one (inset Fig. 4.17).

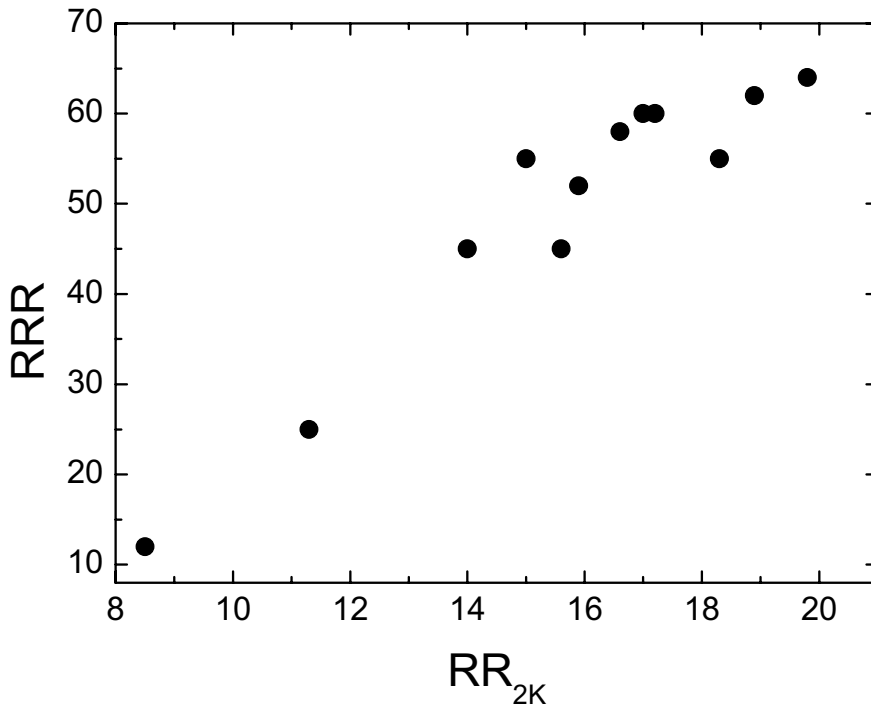


**Figure 4.18:** Comparison of the residual resistivity ratio (extrapolated to 0 K) of pure YbRh<sub>2</sub>Si<sub>2</sub> and the resistivity ratio at 2K (lowest temperature in the <sup>4</sup>He system).

The quality of the samples is often evaluated using the residual resistivity ratio, RRR, i.e., the ratio of  $\rho$  at 300 K to the value at low temperatures. However, in YbRh<sub>2</sub>Si<sub>2</sub>, only a few of our single crystals could be measured down to the mK range, allowing for a determination of RRR. Most of the single crystals were only measured down to 2 K. In order to be able to assess the quantity of these single crystals we studied the relation between the resistivity ratio at 2 K and RRR. In Fig. 4.18 the residual resistivity ratio extrapolated to 0 K is plotted versus the resistivity ratio at 2 K (lowest temperature reachable in the <sup>4</sup>He-system).

The RRR value extrapolated to 0 K is much larger than the RR<sub>2K</sub> value, because of the large linear temperature dependence of  $\rho(T)$  below 10 K. Figure 4.18 evidences a linear relation between RRR and RR<sub>2K</sub>. Therefore the value at RR<sub>2K</sub> is significant enough to predict the residual resistivity ratio and thus the sample quality. All crystals measured in resistivity, except for two samples, are showing a resistivity ratio at 2 K around  $17 \pm 3$  and a RRR between 45 and 65. The two exceptions are from the first crystal growths performed during this work (using the Bridgman technique). Therefore, the quality of the samples is quite good and reproducible. A residual resistivity ratio of  $60 \pm 5$  is a good value for high-quality samples without impurities. The absolute value for the residual resistivity is  $\rho \cong 1 \mu\Omega\text{cm}$  for pure YbRh<sub>2</sub>Si<sub>2</sub>.

But  $\rho(T)$  does not show an exactly linear behaviour below 10 K down to  $T_N$ . The resistivity measurement in the temperature range from 350 mK to 4.5 K for sample 55031a is shown in Fig. 4.19 as an example. Looking more closely to the data, an exactly linear dependence from 10 K down to 2.5 K and another linear dependence from 1 K down to the transition temperature  $T_N = 70 \text{ mK}$  is visible. In between a small curvature leads to a deviation from this linear dependence. This was observed for several measurements on different samples. This deviation from the linear behaviour is not only observed in the <sup>3</sup>He -measurements obtained in the PPMS, it is also visible in the measurements in a dilution refrigerator. Unfortunately only data sets from lowest temperature up to 1 K or data sets of the high-temperature range

above 2 K are shown in previous publications [Custers 2001, Custers 2004, Mederle 2002a, Trovarelli 2000b, Steglich 2000, Steglich 2003]. The very small curvature is the reason why in previous publications the dependence up to 10 K was called ‘quasilinear’ or ‘almost linear’ [Trovarelli 2000b].

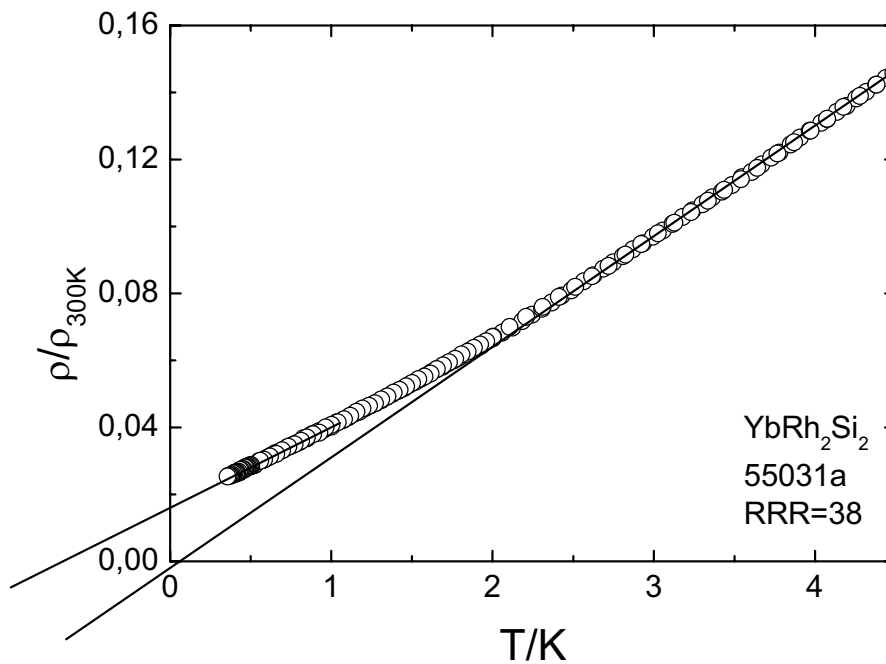


**Figure 4.19:** *The temperature dependence of the resistivity between 350 mK and 4.5 K shows a small deviation from a linear dependence and is therefore quasilinear.*

#### 4.4.1.2 Resistivity of Yb<sub>1-x</sub>La<sub>x</sub>Rh<sub>2</sub>Si<sub>2</sub>

In all La-doped samples, the resistivity (Fig. 4.20) keeps the typical Kondo lattice behaviour observed in pure YbRh<sub>2</sub>Si<sub>2</sub>, with a constant or slightly increasing value below room temperature, a broad maximum around 100 K and a pronounced decrease below this maximum. As expected the residual



resistivity increases continuously with increasing La-content, leading to a residual resistivity ratio of only 2.3 in the 30% La-doped sample. But even in that sample the onset of coherence, i.e., the pronounced decrease of  $\rho(T)$  below the temperature of the maximum, is still clearly visible.

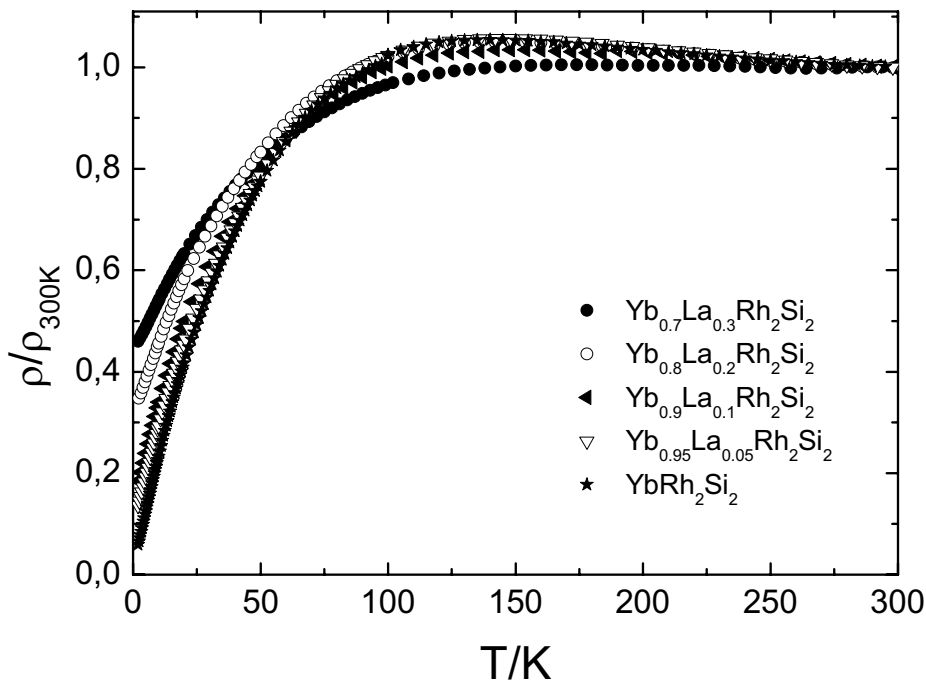


**Figure 4.20:** Comparison of the temperature dependence of the resistivity of all La-doped  $\text{YbRh}_2\text{Si}_2$  samples.

The dependence of the resistivity ratio at 0.4 K is displayed in Fig. 4.21. The almost linear increase with the La concentration is an indication for stochastic replacement of the Yb atoms by La atoms in the structure. Here the La acts as impurity atom. This imperfection increases the residual resistivity ratio.

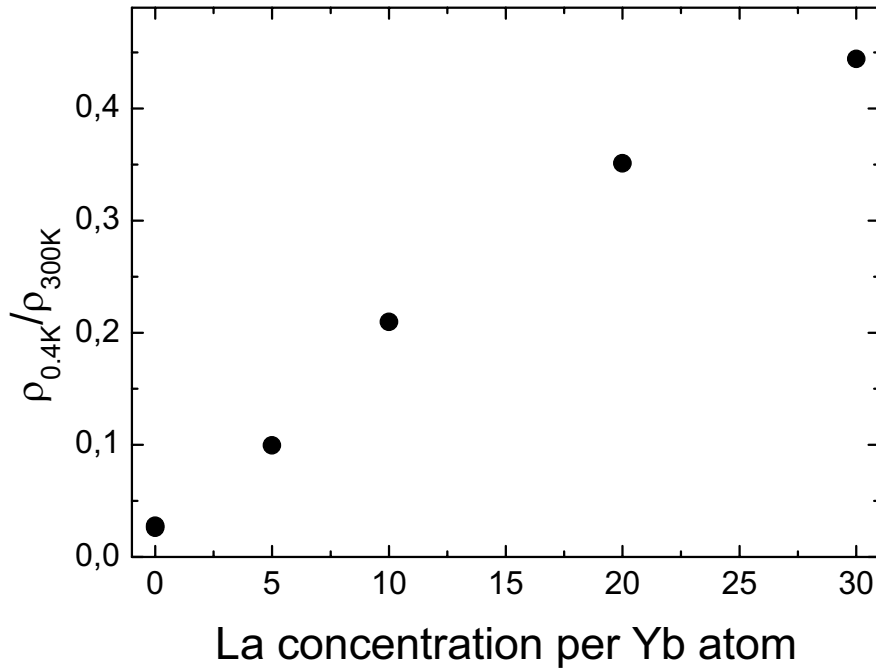


**Figure 4.21:** Resistivity ratio  $\rho_{300K}/\rho_{0.4K}$  for all La-doped  $\text{YbRh}_2\text{Si}_2$  samples measured with the  $^3\text{He}$  option of the PPMS.

One hallmark for the NFL behaviour in pure  $\text{YbRh}_2\text{Si}_2$  is a quasilinear decrease of  $\rho(T)$  with  $T$  below 10 K down to  $T_N = 70$  mK. In the La-doped samples, this quasilinear temperature dependence is also present, but with increasing La content an upward curvature becomes visible in  $\rho(T)$  at low temperatures, corresponding to an increase of the exponent  $n$  in a power law  $\rho(T) = \rho_0 + AT^n$ . Both  $n$  and the upper temperature limit of this positive curvature region increase with the La content, evidencing an evolution towards a Fermi liquid (Fig. 4.22).

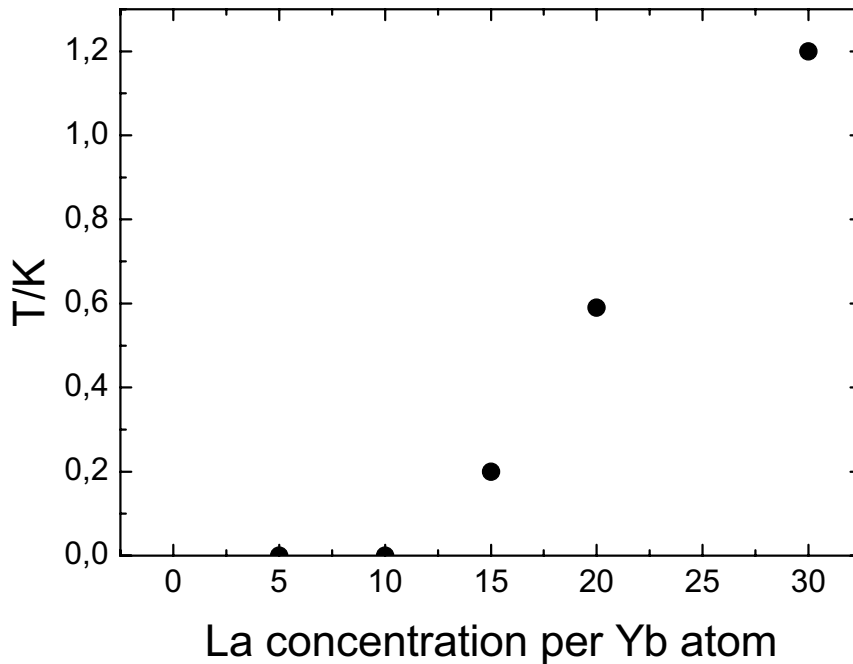


**Figure 4.22:** *The phase diagram of  $\text{Yb}_{1-x}\text{La}_x\text{Rh}_2\text{Si}_2$  ( $0 \leq x \leq 0.3$ ) shows the crossover temperature  $T^*$ , below which Fermi-liquid behaviour was observed.*

Measurements in the mK range for all La-concentrations were performed in a dilution refrigerator by F. Weickert to determine the behaviour for  $T \rightarrow 0$ . The data for zero-field resistivity from 4 K down to lowest temperatures is shown in Fig. 4.23, where up to 10% La concentration a quasilinear temperature dependence is observed. Unfortunately the latter samples contain some In-flux inclusions, where the resistivity data drop to lower values around 3 K due to superconductivity.  $\text{Yb}_{0.85}\text{La}_{0.15}\text{Rh}_2\text{Si}_2$  has an additional small In-containing phase, which gets superconducting around 100 mK.

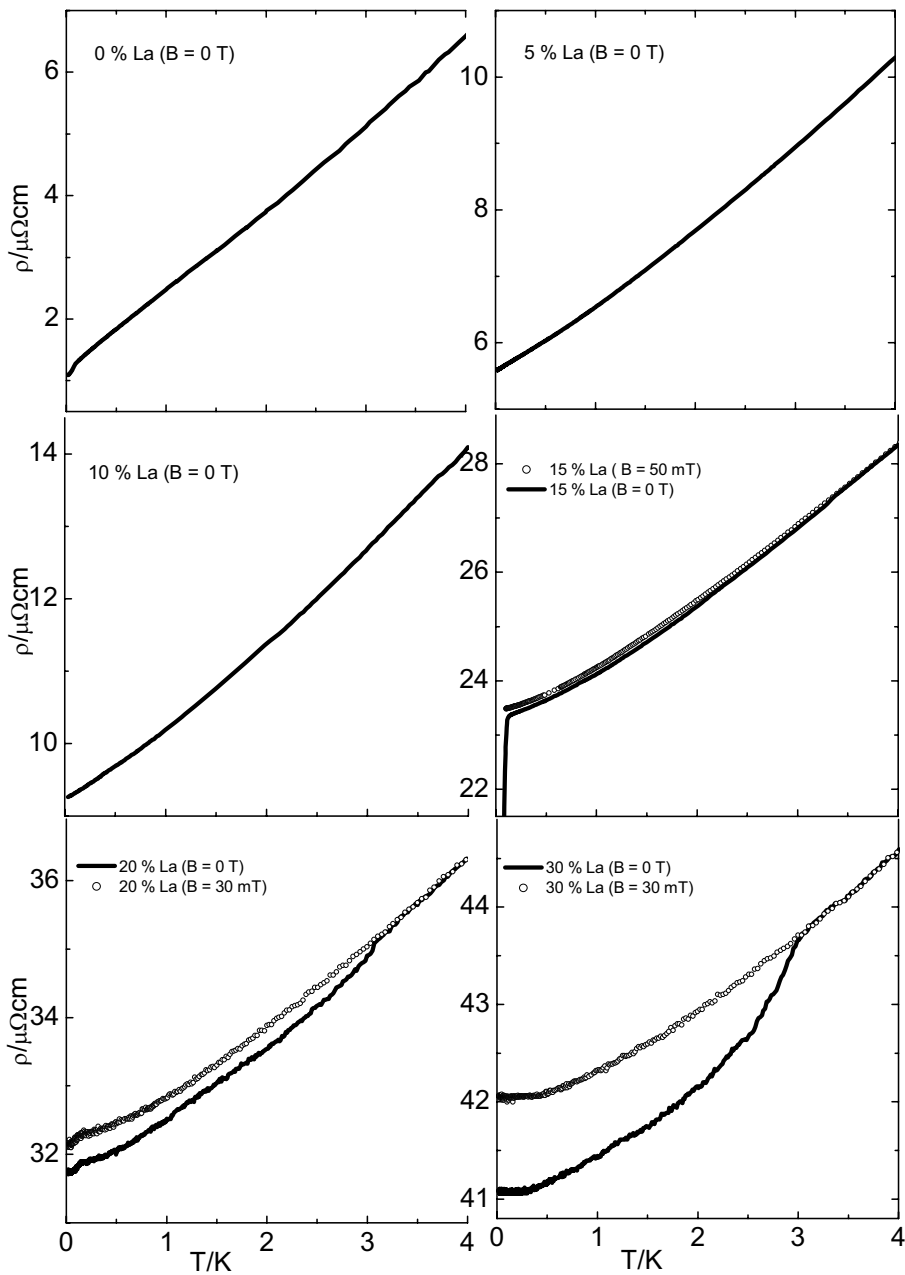


**Figure 4.23:** Low-temperature resistivity data of all  $\text{Yb}_{1-x}\text{La}_x\text{Rh}_2\text{Si}_2$  ( $x = 0, 0.05, 0.1, 0.15, 0.2$  and  $0.3$ ) samples measured by F. Weickert. Samples with superconducting foreign phase inclusions were remeasured in a small magnetic field.

All samples with superconducting foreign phases were remeasured by applying a small magnetic field, e.g. 30 mT for Yb<sub>0.7</sub>La<sub>0.3</sub>Rh<sub>2</sub>Si<sub>2</sub> and Yb<sub>0.8</sub>La<sub>0.2</sub>Rh<sub>2</sub>Si<sub>2</sub> and 50 mT for the Yb<sub>0.85</sub>La<sub>0.15</sub>Rh<sub>2</sub>Si<sub>2</sub> sample to suppress the superconductivity. For higher La concentrations a T<sup>2</sup> behaviour is visible, already below 200 mK for the 15% doped sample.  $\rho(T)$  could be fitted with a quadratic dependence below 600 mK for Yb<sub>0.8</sub>La<sub>0.2</sub>Rh<sub>2</sub>Si<sub>2</sub> and below 1.5 K for Yb<sub>0.7</sub>La<sub>0.3</sub>Rh<sub>2</sub>Si<sub>2</sub>.

The analysis of the low-temperature electrical-resistivity data suggests a QCP in La-doped YbRh<sub>2</sub>Si<sub>2</sub> between 5% and 10% of La. This main conclusion is taken from the field dependence of the upper limit of the T<sup>2</sup> behaviour as seen in the temperature-field diagram [Weickert 2006]. In Yb<sub>0.95</sub>La<sub>0.05</sub>Rh<sub>2</sub>Si<sub>2</sub> no anomaly could be resolved in the temperature dependence of the resistivity, indicating that the antiferromagnetic transition has been shifted below 50 mK or even been completely suppressed. The analysis of the field dependence of the electrical resistivity of the Yb<sub>0.9</sub>La<sub>0.1</sub>Rh<sub>2</sub>Si<sub>2</sub> system indicates that this compound is just at the limit of the formation of a Fermi liquid at T = 0 [Weickert 2006].

## 4.4.2 Specific heat

### 4.4.2.1 Specific heat of pure YbRh<sub>2</sub>Si<sub>2</sub>

A lot of investigations of the specific heat were devoted to the low-temperature region, but much less to the behaviour at high temperatures. However, the data and the analysis of the high-temperature specific heat are essential to settle the crystal field (CEF), which was not fixed until now and for the determination of the Kondo-energy scale. The results will be analysed in view of crystal field effects and the single-ion Kondo model and will be discussed in comparison with results from inelastic neutron scattering. The estimation of the magnetic contribution of the specific heat is very difficult at higher temperatures, because of the very large phonon

contribution. Therefore very accurate measurements are necessary. The specific-heat data of the pure system  $\text{YbRh}_2\text{Si}_2$  was measured on several samples in the temperature range from room temperature down to 2 K. Fig. 4.24 shows the data of two different samples (55054c and 55054i). The inset shows the relative error of the measurement,  $\Delta C/C$ , with  $\Delta C = C_{55054c} - C_{55054i}$ , which varies between 0 and 5 %.

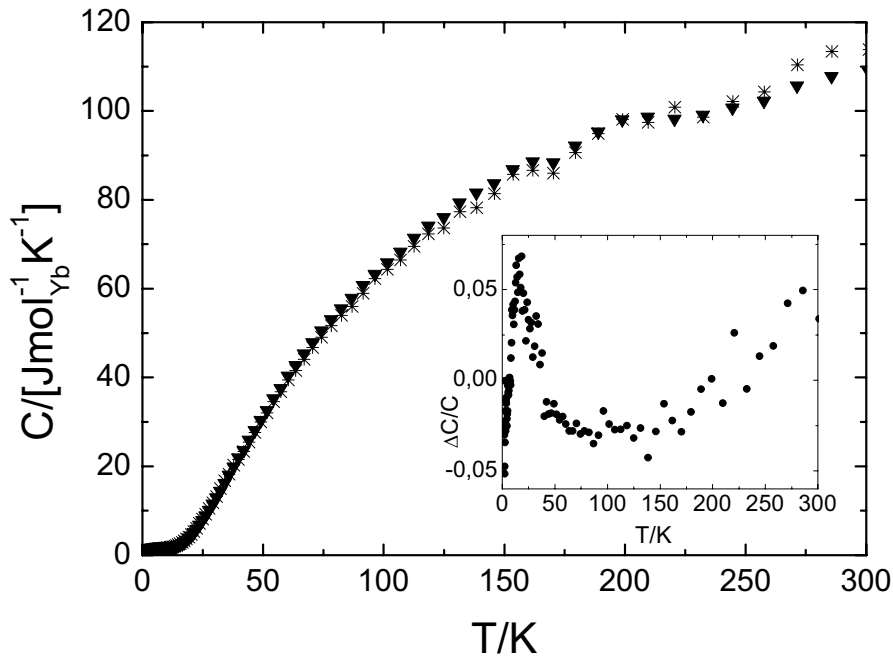


**Figure 4.24:** Specific-heat data of two samples of  $\text{YbRh}_2\text{Si}_2$  measured from room temperature down to 2 K. The inset shows the relative difference  $\Delta C/C$  between both measurements.

Additional measurements on the reference compound  $\text{LuRh}_2\text{Si}_2$  were performed (Fig. 4.25) to obtain the lattice contribution and the contribution of the non-f conduction electrons.

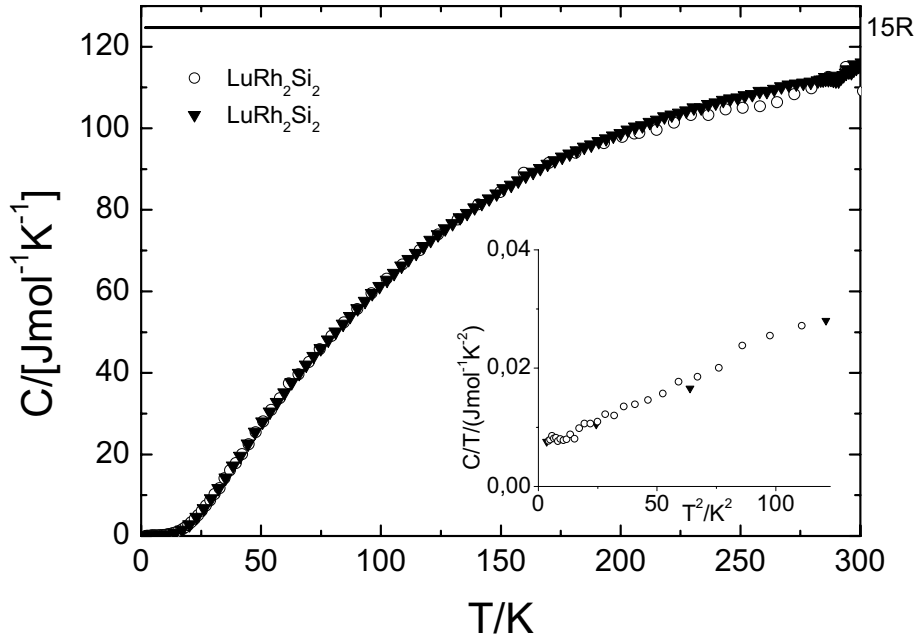


**Figure 4.25:** Specific-heat data of two different samples of the reference compound  $\text{LuRh}_2\text{Si}_2$  on a linear temperature scale. At high temperature the data reach the expected classical value of  $C = 5 \cdot 3 N k_B \approx 125 \text{ J} \cdot \text{mol}^{-1} \text{K}^{-1}$ . The inset shows the lower temperature region of  $C/T$  on a quadratic temperature scale.

The high temperature specific heat data for the reference compound  $\text{LuRh}_2\text{Si}_2$  levels out at the experimental value of  $3R$  per atom (Fig. 4.25) as expected. Having 5 atoms per unit cell of  $\text{LuRh}_2\text{Si}_2$  gives:

$$C_{\text{high}} = 3 N_A \cdot k_B \cdot 5 \approx 125 \text{ J} \cdot \text{mol}^{-1} \text{K}^{-1} \quad (4)$$

Below 12 K, a plot  $C/T$  versus  $T^2$  (inset of Fig. 4.17) shows a straight line demonstrating that the specific heat of  $\text{LuRh}_2\text{Si}_2$  at these temperatures is described quite well by the sum of a linear-in- $T$  electronic contribution  $\gamma T$  and a  $\beta T^3$  phonon contribution. From  $\beta$  one can calculate a Debye temperature of  $\Theta = 379 \text{ K}$ , while the Sommerfeld coefficient  $\gamma$  is roughly  $8 \text{ mJmol}^{-1} \text{K}^{-2}$ . This small value is very typical for non-magnetic reference compounds based on Lu, La or Y.

The absolute values of  $C$  for YbRh<sub>2</sub>Si<sub>2</sub> at 50 K and at 60 K range from 29.5 J/molK to 31 J/molK and from 37 to 40 J/molK, respectively. For a comparison with the reference compound LuRh<sub>2</sub>Si<sub>2</sub> the absolute values range here between 26.5 and 28 J/molK at 50 K and 35.3 and 35.5 J/molK at 60 K. It is clearly visible, that the absolute values for the reference compound (for all measured samples) are always below the absolute values for all samples of pure YbRh<sub>2</sub>Si<sub>2</sub> (from different batches). The magnetic contribution  $C_{4f}$  of the Yb 4f electrons of YbRh<sub>2</sub>Si<sub>2</sub> was deduced from the difference of both measurements, which corresponds to subtracting the phonon and the electronic contribution from the specific heat data of the pure YbRh<sub>2</sub>Si<sub>2</sub>. The result for three different samples is shown in Fig. 4.26 for the temperature range up to 120 K.

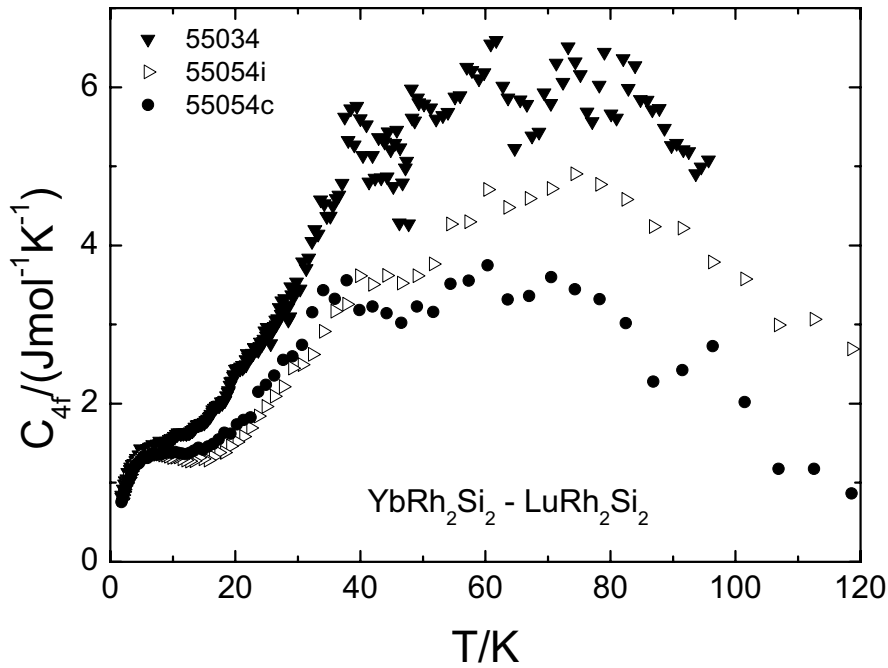


**Figure 4.26:** *The magnetic specific-heat contribution, obtained after subtracting the phonon contribution, shows a broad maximum around 60 K.*



The temperature dependence of  $C_{4f}(T)$  is very similar for all three YbRh<sub>2</sub>Si<sub>2</sub> samples (Fig. 4.26), only the absolute values differ. A broad maximum between 40 and 80 K is clearly visible which places the first excited CEF level in the energy range from 10 to 17 meV. According to the neutron data, this level is located around 17 meV. The  $J = 7/2$  multiplet of Yb is expected to split into four Kramers doublets in a tetragonal environment. While  $C_{4f}$  is more conclusive than neutron data for the lowest excited CEF level,  $C_{4f}(T)$  is less conclusive for the higher levels, for which neutron data give rather precise excitation energies of 25 and 43 meV. Thus the combination of specific heat at higher temperatures and neutron data allows a more reliable determination of the whole CEF scheme.

To analyse those data in more detail, the magnetic specific-heat contribution of sample 55054i was selected and plotted separately (Fig. 4.27) including the error bar in the temperature range up to 120 K. (The error bars of the specific-heat data of pure YbRh<sub>2</sub>Si<sub>2</sub> and LuRh<sub>2</sub>Si<sub>2</sub> sum up and result in much larger values at higher temperatures.) The higher the temperature the larger the inaccuracy of the data points. This sample was selected, because its data are in between the data of the two extreme cases 55034 and 55054c and are therefore likely more representative for the intrinsic behaviour. Beside the maximum around 60 K a second maximum around 5 K is also visible, which can be explained by using the single Kondo-impurity model. Since both maxima are well separated analysing them with two completely different models is possible.

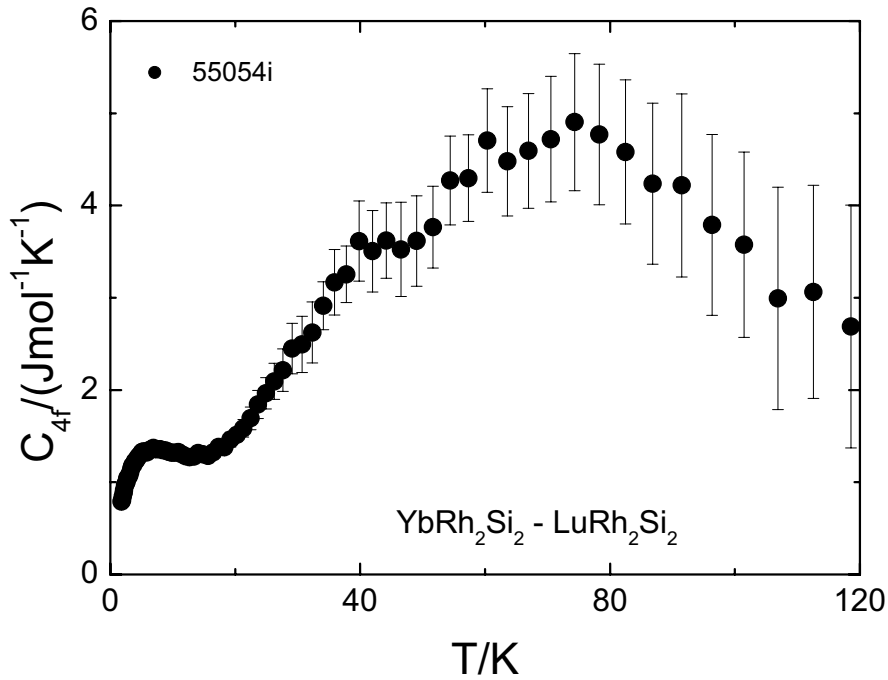


**Figure 4.27:** *Magnetic specific-heat contribution of sample 55054i after subtracting the phonon contribution including the error bar for the resulting data.*

The Schottky-like anomaly between 40 and 80 K can be described by a simple CEF-model, where we assume well-defined delta-like CEF doublets occupied according to Boltzmann statistics. Fig. 4.28 shows the magnetic specific-heat contribution of sample 55054i including two curves obtained with this simple CEF-model. The first curve (red dots) was calculated by using the CEF level scheme as obtained by inelastic neutron-scattering experiments (0, 17 meV, 25 meV and 43 meV) while the second curve (black dots) was calculated by using the following level scheme: 0, 12 meV, 25 meV and 43 meV. For this second level scheme only the first excited level was shifted to lower temperatures. The higher levels, for which neutron data gave rather precise excitation energies, were kept fixed. This second level scheme shows a much better overlap with the experimental data of the

magnetic specific heat, but this simple model does not account for the broadening of the CEF levels due to the Kondo interaction. Comparing with results of Desgranges and Rasul [Desgranges 1985] for a more exact treatment of CEF in the presence of Kondo interaction, one expects for the case  $T_K < 10 \Delta$  a broadening of the CEF-related Schottky anomaly and a reduction of its maximum. Then the second model gives a lower bound for the energy of the first excited level. Therefore, the specific-heat results confirm that the first excited CEF level is above 150 K, in contrast to very preliminary estimation which suggested it to be around 100 K, but in good agreement with the neutron data.

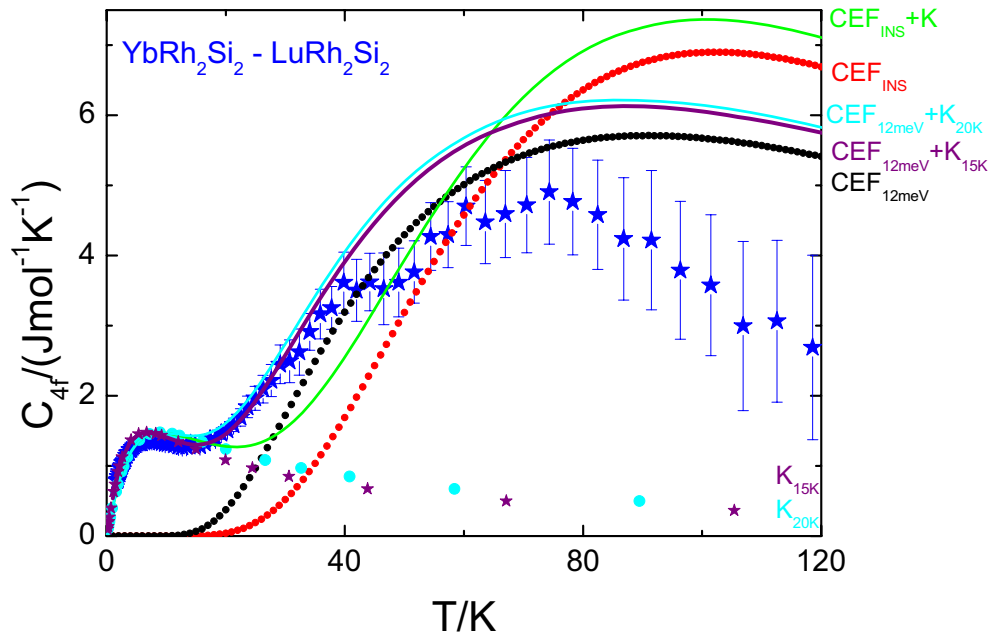


**Figure 4.28:** *Magnetic specific-heat contribution of sample 55054i including results of calculations using a simple CEF model for the contribution of the excited CEF levels and a single Kondo-ion model for the low-temperature maximum.*

To analyse the maximum at lower temperatures, the single-impurity Kondo model was used. We just scaled the theoretical results of Desgranges and

Schotte [Desgranges 1982] for the specific heat of the single Kondo-ion impurity model with different estimations for  $T_K$ . The light-blue dotted curve was obtained by using a Kondo temperature of  $T_K = 20$  K and the curve with purple stars with  $T_K = 15$  K. For a deeper insight Fig. 4.29 shows  $C_{\text{mag}}$  in the temperature range from 0 to 22 K, including the measured and all calculated data. The calculations reproduce the experimental data quite well, suggesting that a Kondo model is quite appropriate for describing the properties of YbRh<sub>2</sub>Si<sub>2</sub>, at least above 2 K. The value at the maximum is slightly lower, which might be accounted by a transfer of entropy to the region of the critical fluctuations at very low temperature. The value of this maximum implies that only the CEF ground-state doublet is involved, else it would have to be almost a factor of three higher if the state involved would correspond to a quartet [Rajan 1983].

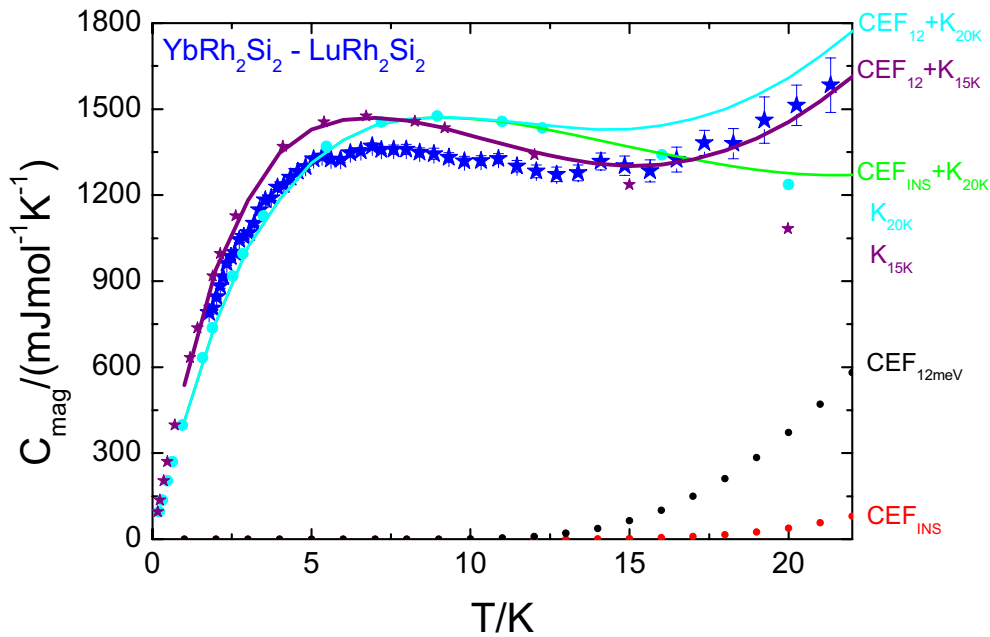


**Figure 4.29:** Magnetic specific-heat contribution of sample 55054i and calculations (using the single-impurity Kondo model) in the temperature range from 0 to 22 K.

$T_K$  is defined by the region at low temperatures, where  $C(T)$  shows a large positive slope. From the comparison with the two theoretical curves one can deduce that  $T_K$  should be around 17-18 K. To combine both analyses the theoretical data of the CEF and of the Kondo model were just added. This is possible, because the CEF and the Kondo maxima are well separated [see Desgranges 1985]. Using the Kondo temperature of  $T_K = 20$  K and the CEF scheme obtained by inelastic neutron-scattering experiments results in the green curve. Using the same Kondo temperature, but the level scheme of 0, 12 meV, 25 meV and 43 meV the light blue curve was obtained. A better result is given with the level scheme of 0, 12 meV, 25 meV and 43 meV and a lower Kondo temperature, here  $T_K = 15$  K (purple curve), but as stated before, neglecting the Kondo interaction for the CEF excitation leads to an underestimation of the excitation energies. While below 50 K the agreement is quite good, at higher temperatures the theoretical curves are far above the experimental results. The increasing difference between calculations and experimental results indicates that the subtracted phonon part is too large at higher temperatures. This could be due to slight changes between the phonon spectra of LuRh<sub>2</sub>Si<sub>2</sub> and YbRh<sub>2</sub>Si<sub>2</sub>. A more detailed discussion is given later in this chapter.

The magnetic specific-heat data of YbRh<sub>2</sub>Si<sub>2</sub> over the whole investigated temperature range up to 120 K are plotted in Fig. 4.30 as  $C/T$  on a logarithmic scale to estimate the magnetic entropy of the system (inset).

The value  $0.5R\ln 2$  is reached around 8.5 K (see Fig. 4.32). The entropy value of  $0.5R\ln 2$  is important for systems with a doublet ground state since it allows to estimate the characteristic Kondo temperature. The Kondo temperature (twice the temperature at which  $S = 0.5R\ln 2$ ) estimates here to  $T_K = 17$  K.

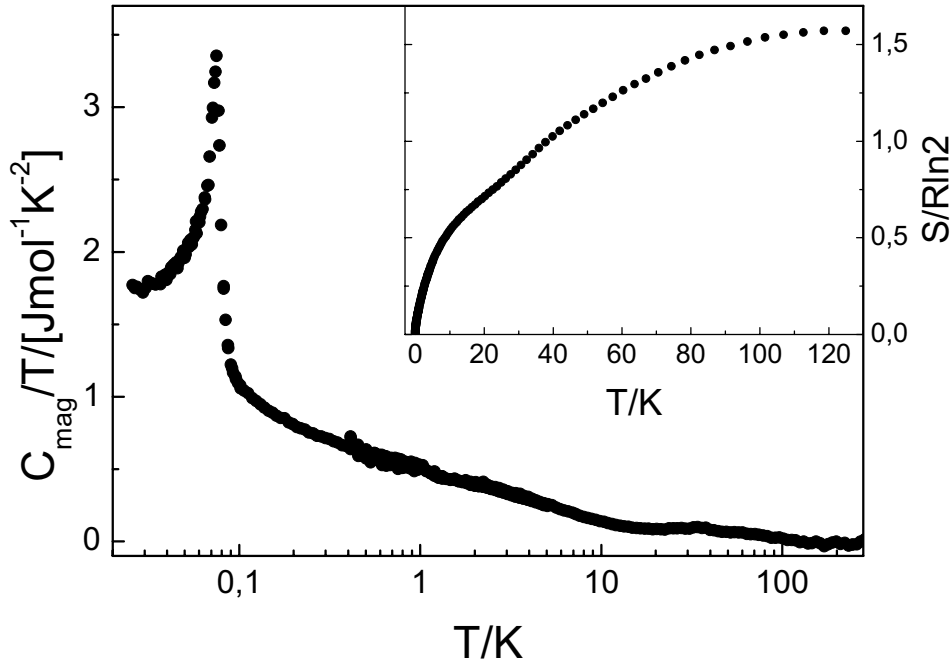


**Figure 4.30:** *Magnetic specific heat data of  $\text{YbRh}_2\text{Si}_2$  in the temperature range up to 120 K as  $C/T$  on a logarithmic temperature scale. The inset shows the entropy of the system up to 120 K.*

The value  $T_K = 17$  K obtained from the entropy is below the literature value for the characteristic spin-fluctuation temperature  $T_0 = 24$  K given by Trovarelli [Trovarelli 2000c], the difference being larger than expected from the accuracy of the determination of the magnetic specific heat. However, Trovarelli et al. determined the characteristic energy  $T_0$  in a different way, by extrapolating the  $C/T = \ln T$  fit to  $C = 0$ . It is not unusual that for systems with a  $T_K > 10$  K,  $T_0$  is larger than  $T_K$  determined from the entropy [Sereni 1997]. A comparison of the entropy and the Kondo temperature with the La-doped system will be given in the next section.

#### 4.4.2.2 Specific heat of Yb<sub>1-x</sub>La<sub>x</sub>Rh<sub>2</sub>Si<sub>2</sub>

In Fig. 4.31,  $C(T)/T$  of the La-doped samples, normalized to Yb moles, is shown on a logarithmic T scale. The  $\ln(T)$  behaviour is kept until 10%La, with only a minor decrease of the normalized values at low T.

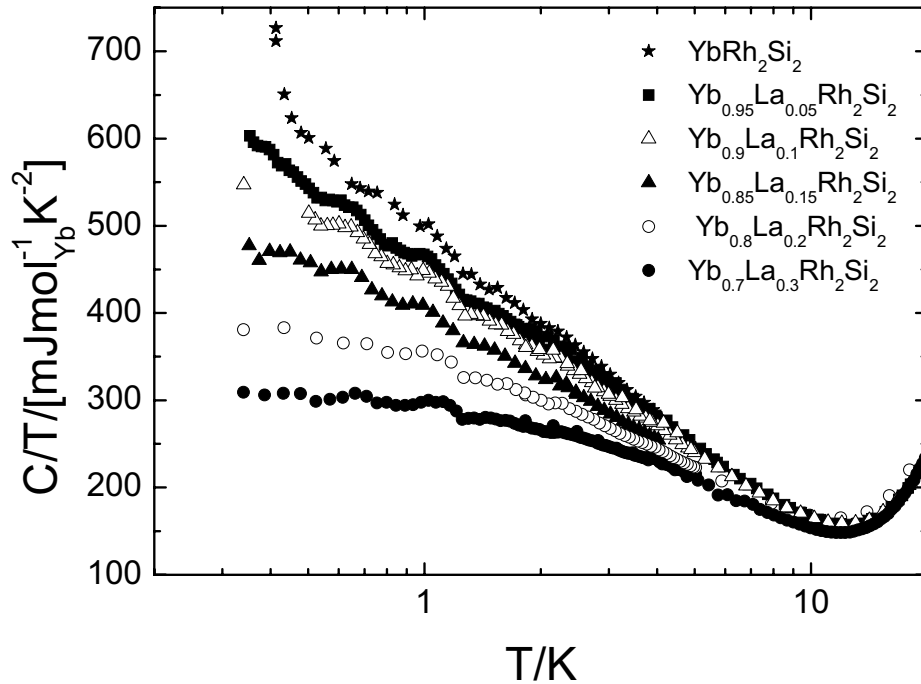


**Figure 4.31:** Low-temperature specific-heat data  $C/T$  of all La-doped samples on a logarithmic temperature scale down to 350 mK.

For the 20% and 30% La-doped samples  $C(T)/T$  saturates upon cooling below 1 K to rather large values of  $\gamma = 380 \text{ mJ/K}^2\text{mol}$  and  $\gamma = 300 \text{ mJ/K}^2\text{mol}$  for  $x = 0.2$  and  $x = 0.3$ , respectively, indicating the transition to a heavy Fermi-liquid behaviour in the specific heat at these concentrations. The overall decrease of the specific heat at low temperatures with increasing La content implies that the recovery of the entropy contribution ( $R\ln 2$ ) related to the doublet ground state is shifted towards larger temperature (Fig. 4.32).

Thus the Kondo temperature  $T_K$  (or characteristic 4f temperature) increases as expected since the increase of the volume should lead to an evolution of the Yb from a trivalent towards a valence-fluctuating state.

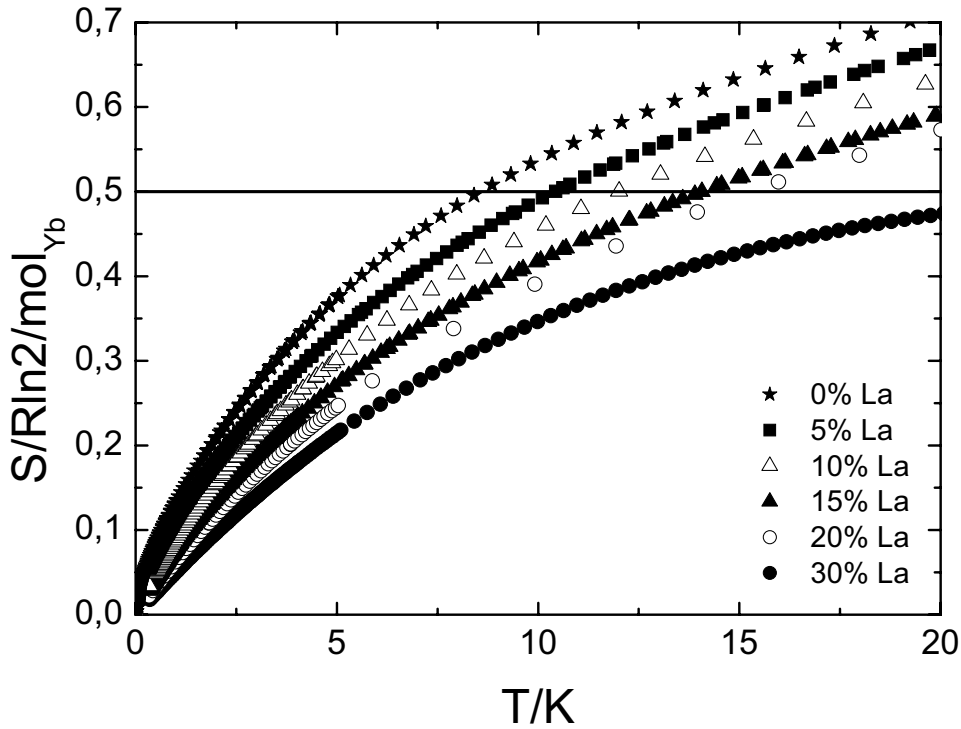


**Figure 4.32:** *The magnetic entropy of La-doped  $\text{YbRh}_2\text{Si}_2$  decreases with increasing La content. The Kondo temperature (twice the temperature at which  $S = 0.5R\ln 2$ ) increases with La concentration.*

To determine the entropy, first a subtraction of the  $\text{LuRh}_2\text{Si}_2$  specific heat from the  $\text{Yb}_{1-x}\text{La}_x\text{Rh}_2\text{Si}_2$  specific heat and then the integration of  $C_{\text{mag}}/T$  over the whole temperature range was performed. The phononic contribution obtained from specific-heat data of  $\text{LaRh}_2\text{Si}_2$  [Sereni 2005, Berisso 2002] is very similar to that of  $\text{LuRh}_2\text{Si}_2$  (Fig. 4.33). Therefore, an exact subtraction of  $\text{Lu}_{1-x}\text{La}_x\text{Rh}_2\text{Si}_2$  was not necessary.



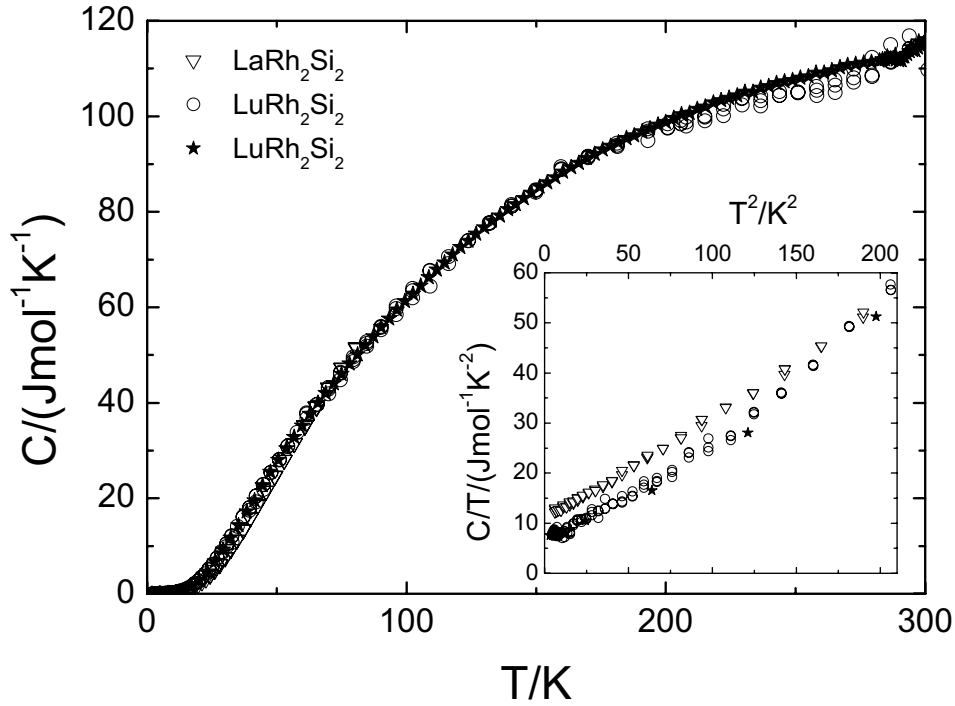


**Figure 4.33:** Comparison of specific-heat data of pure  $\text{LuRh}_2\text{Si}_2$  with pure  $\text{LaRh}_2\text{Si}_2$  in the temperature range from 300 K down to 2 K. The inset shows the low-temperature region with  $C/T$  versus a quadratic temperature scale.

The Kondo temperature could also be determined using  $\gamma_0$  from specific-heat data [Desgranges 1982] using:

$$\gamma_0 = R\pi/(3T_K). \quad (5)$$

A comparison of both ways to estimate the Kondo temperature is shown in Fig. 4.34 (red data: determination from  $0.5R\ln 2$ , blue data: determination from  $\gamma_0$ ). The difference can be attributed to the presence of the critical fluctuations at low temperatures, which enhance  $\gamma_0$ , but have only a weak effect on the entropy at higher temperatures. Additionally, the evolution of the Weiss temperature  $\Theta_W$  obtained from the low-temperature susceptibility (see chapter 4.4.1.2) is plotted on the right axis. The Weiss temperature is also increasing with increasing La content. The similarity with the evolution

of  $T_K$  suggests that in this temperature range,  $\Theta_W$  is related to the Kondo scale.

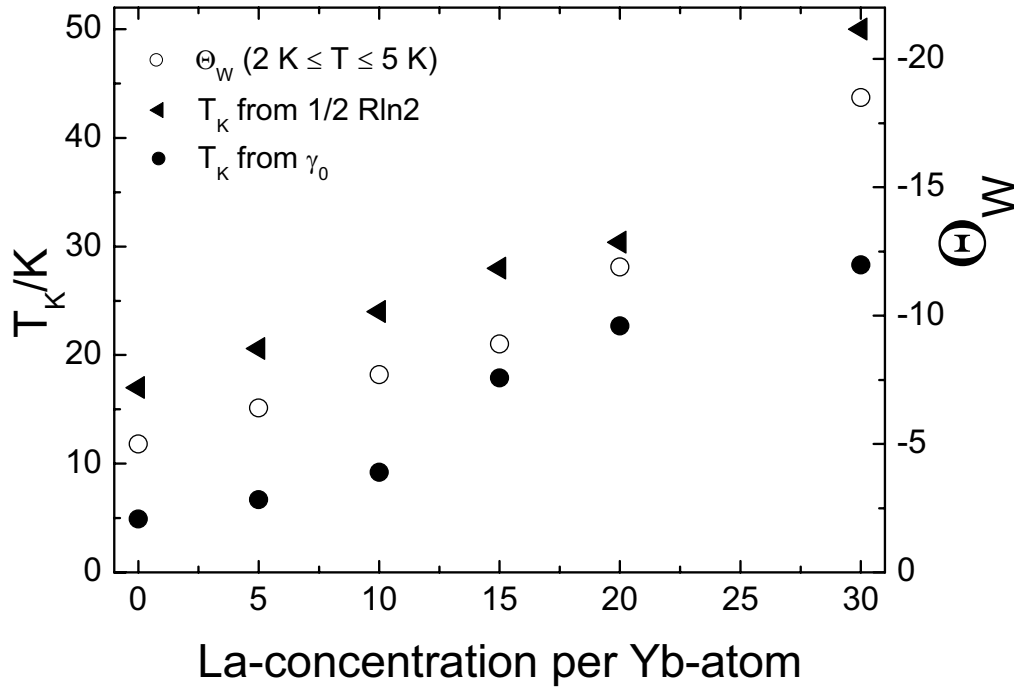


**Figure 4.34:** Evolution of the Kondo temperature as determined from the entropy and from the low-temperature Sommerfeld coefficient. Left axis: evolution of the low-temperature (around 3 K) Weiss temperature.

Low temperature specific-heat data (Fig. 4.35) for the 5 %La-doped sample [Radu 2005] down to 40 mK evidence the disappearance of the peak observed in pure YbRh<sub>2</sub>Si<sub>2</sub> which is connected with the antiferromagnetic ordering, while the increase of  $C(T)/T$  to low temperatures is similar to that observed in a nominal 5%-Ge-doped [Custers 2003] sample. This suggests that the QCP related to the disappearance of the AF state is located around 5% La doping.

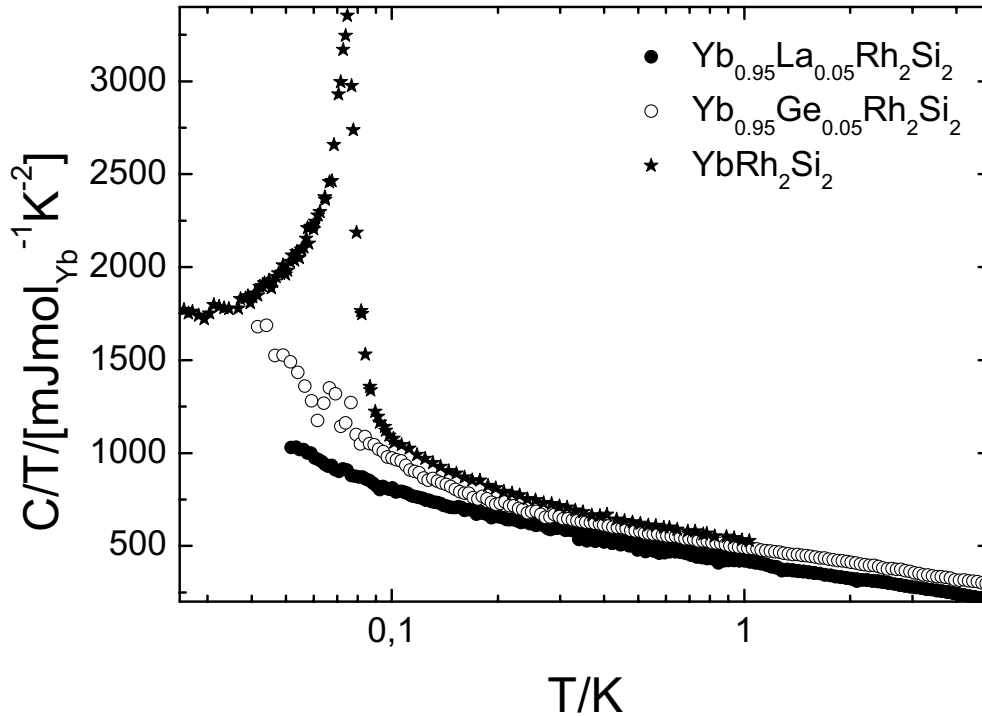


**Figure 4.35:** Comparison of low-temperature specific-heat data,  $C/T$ , of pure, 5% La- and 5% Ge-doped YbRh<sub>2</sub>Si<sub>2</sub>, normalised to Yb moles, on a logarithmic temperature scale (data from [Radu 2005] and [Custers 2003]).

## 4.5 Magnetic properties

Susceptibility and magnetisation measurements were performed on a commercial SQUID magnetometer using fields up to 5T. After orientating the sample with Laue technique it was fixed in the middle of the plastic straw. Measurements were done with field parallel and perpendicular to the platelet (a-b plane).

## 4.5.1 Susceptibility

Susceptibility measurements were performed at constant fields of 5, 3, 1 and 0.1 T in general. Additional measurements with fields at 4, 2 and 0.8 T were obtained for special samples. The samples, always platelets, were fixed in the middle of the sample holder either with the ab plane perpendicular or parallel to the applied magnetic field. In the latter case (sample parallel to field) because of its easy magnetic plane the sample is in a stable orientation and does not move. If the sample is fixed with its hard magnetic direction (c axis) along the field direction it likes to flip by 90° to get into the stable orientation in the applied field. Therefore, the sample was wrapped tightly with a piece of plastic straw, which forms a spiral around the sample, and fixed in the middle of the sample tube by cutting opposite parts of the tube walls into an L shape. Additional electrical tape was fixed on the outside of this cylindrical shell for further stabilisation. The signal for the measurements with  $B \parallel c$  is very small and, therefore, the diamagnetic background had to be subtracted, but it was very difficult to detect. To measure the straw with the empty spiral of plastic straw is impossible, because the centring could not be performed in a trustable way. Therefore, we put a very small piece of paper inside the spiral (where the sample is placed in general) and tried the centring process, which was still quite difficult, and then performed the measurement. The background subtraction with 65% of this signal works quite well for the susceptibility data obtained with magnetic field in the hard plane. An appropriate correction was done also for the susceptibility data obtained in the easy direction.

### 4.5.1.1 Susceptibility of pure YbRh<sub>2</sub>Si<sub>2</sub> in both directions

Susceptibility data for pure YbRh<sub>2</sub>Si<sub>2</sub> were obtained for both crystallographic directions to compare the magnetic properties in the easy

and hard magnetic directions. Fig. 4.36 shows selected data of pure YbRh<sub>2</sub>Si<sub>2</sub> in both directions. The inset shows the inverse susceptibility without any background subtraction.

The susceptibility of YbRh<sub>2</sub>Si<sub>2</sub> presents a significant temperature dependence. This temperature dependence is similar for all data sets. There is a large anisotropy;  $\chi$  for field along the basal plane is much larger than for field along the c direction. The ratio of  $\chi_{ab}/\chi_c$  at 2 K is roughly 5.

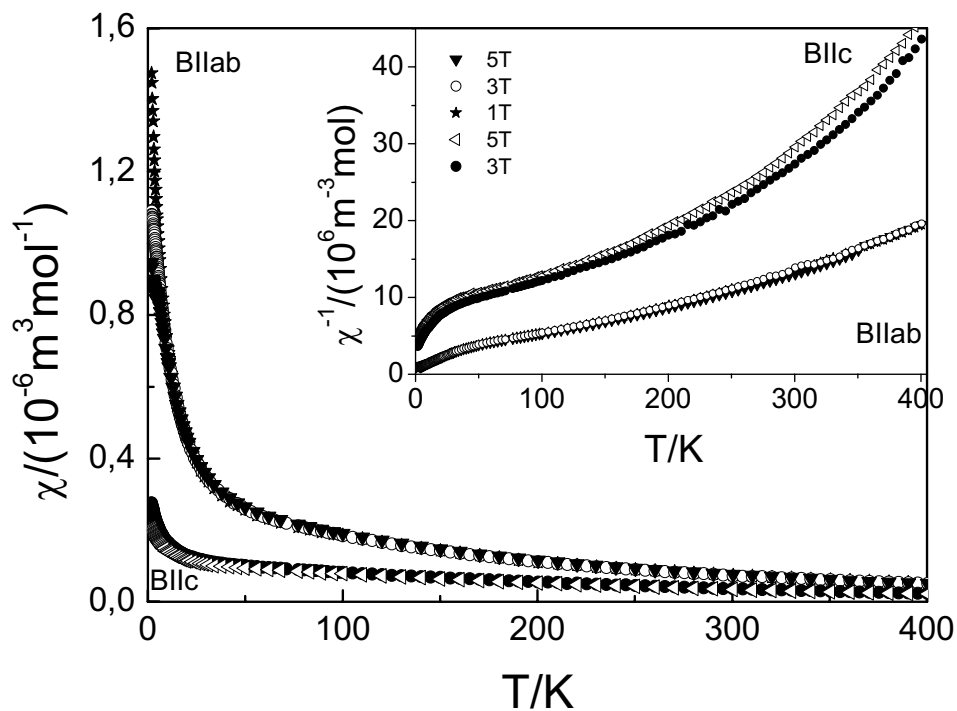


**Figure 4.36:** Temperature dependence of the magnetic susceptibility (raw data) for pure YbRh<sub>2</sub>Si<sub>2</sub> in both directions for selected magnetic fields to compare the behaviour in the easy ab plane and along the c direction.

At high temperatures we did not observe a significant field dependence of the susceptibility. But below 12 K, the field dependence of the susceptibility in the ab plane is clearly visible; the lower the field the higher the value of  $\chi(T)$  towards lower temperatures. This can be related to the suppression of

critical fluctuations with increasing magnetic field. This field dependence is not so drastic for the susceptibility along the *c* axis.

For  $B \parallel c$ , the large diamagnetic background leads to a strong upturn in the raw data of the inverse susceptibility as a function of temperature. As an example the data set at 3 T is shown in Fig. 4.37 (blue data set). After subtracting the background data the curve becomes linear for  $T > 200$  K (black data set in Fig. 4.37). This background subtraction was performed for all data sets with field parallel to the *c* axis. Afterwards a Curie-Weiss fit can be done between 200 K and 400 K (red line), which results in an effective moment of  $\mu_{\text{eff}} = 4.49 \mu_{\text{B}}$ , in close agreement with the value  $4.54 \mu_{\text{B}}$  expected for  $\text{Yb}^{3+}$ , and a Weiss constant of  $\theta_{\text{CW}} = -150$  K.

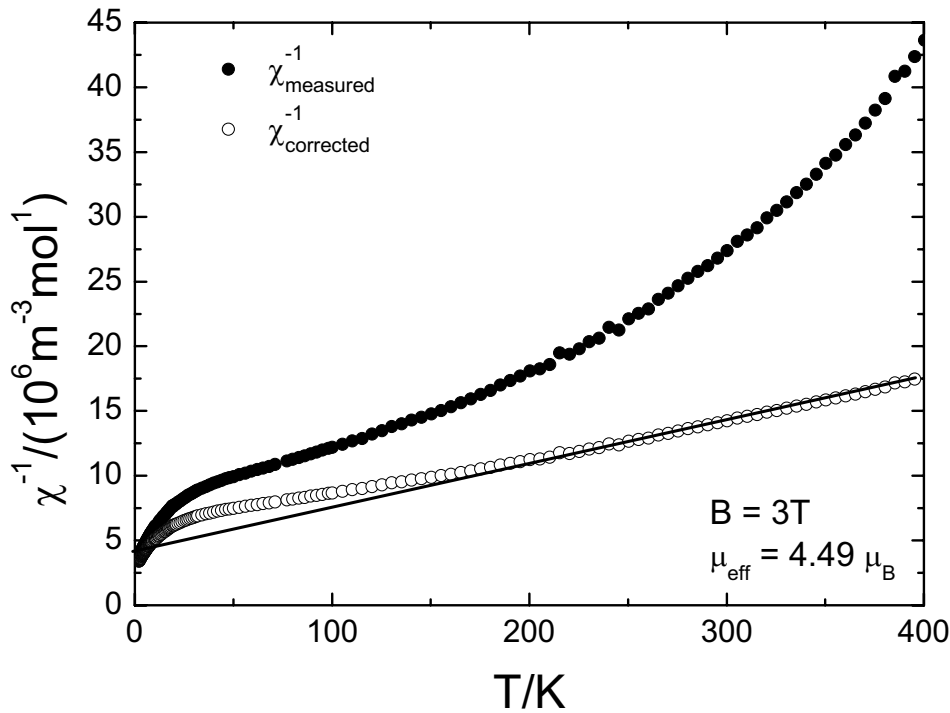


**Figure 4.37:** Comparison of the inverse susceptibility of raw data (blue dots) and background-subtracted (corrected) data of pure YbRh<sub>2</sub>Si<sub>2</sub> for magnetic field applied along the hard direction.

This background subtraction was optimised on the critical  $c$  direction and, therefore, the background was scaled in the same way for the susceptibility along the easy plane. Fig. 4.38 shows one representative example for the inverse susceptibility of YbRh<sub>2</sub>Si<sub>2</sub> for fields in the basal plane. All other data sets were very similar. A Curie-Weiss fit between 200 and 400 K gives an effective moment of  $\mu_{\text{eff}} = 4.48 \mu_{\text{B}}$ , also very close to the value for the free Yb<sup>3+</sup> ion, and a paramagnetic Weiss temperature of  $\theta_{\text{CW}} = -34$  K. This background subtraction results in a Weiss temperature larger than the value obtained by Trovarelli [Trovarelli 2000a]. Taking a smaller background would give a smaller  $\theta_{\text{CW}}$ , but also a smaller value of the effective moment. The large difference between the  $\theta_{\text{CW}}$  along the  $c$  axis and  $ab$  plane can be related to a large CEF splitting, as confirmed e.g. by the excitation energy of 43 meV for the highest CEF level.

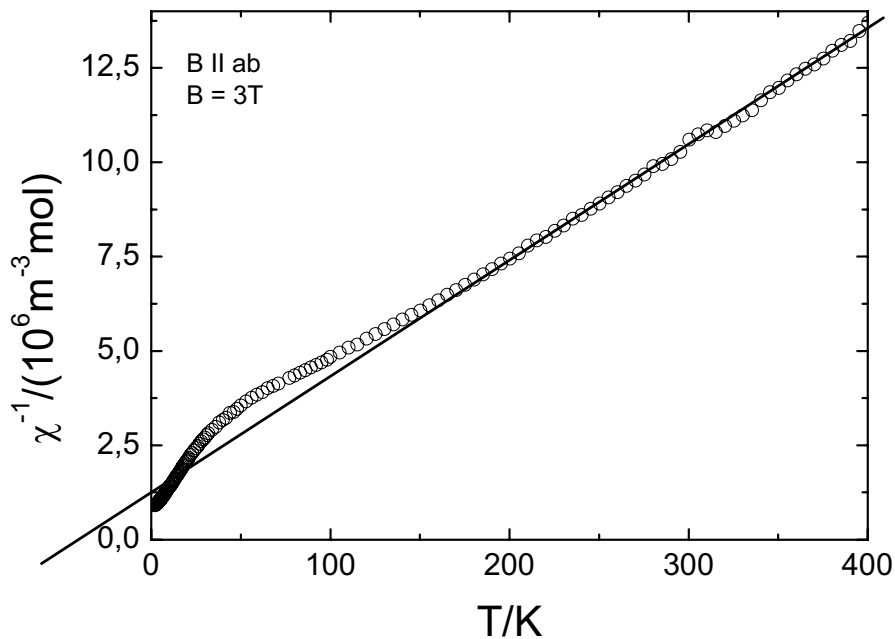


**Figure 4.38:** Temperature dependence of the inverse susceptibility for pure YbRh<sub>2</sub>Si<sub>2</sub> with magnetic field of  $B = 3$  T applied along the  $ab$  plane. The line is the Curie-Weiss fit between 200 and 400 K.

### 4.5.1.2 Comparison of susceptibility of La-doped $\text{YbRh}_2\text{Si}_2$

The susceptibility for  $B \parallel ab$  and the corresponding inverse susceptibility (inset) of pure and La-doped  $\text{YbRh}_2\text{Si}_2$  are shown in Fig. 4.39 for comparison. A background was subtracted for all data sets. The susceptibility normalised to Yb moles nearly overlaps in the temperature region from 100 to 400 K. Below 80 K the difference increases. The higher the La concentration the lower the value for the absolute susceptibility. The comparison of the inverse susceptibility shows only minor changes at high temperatures. No difference is visible in the magnetic moments between pure and La-doped samples. The Curie-Weiss fit between 200 and 400 K or 250 and 400 K, respectively, does not show any significant change of the slope.

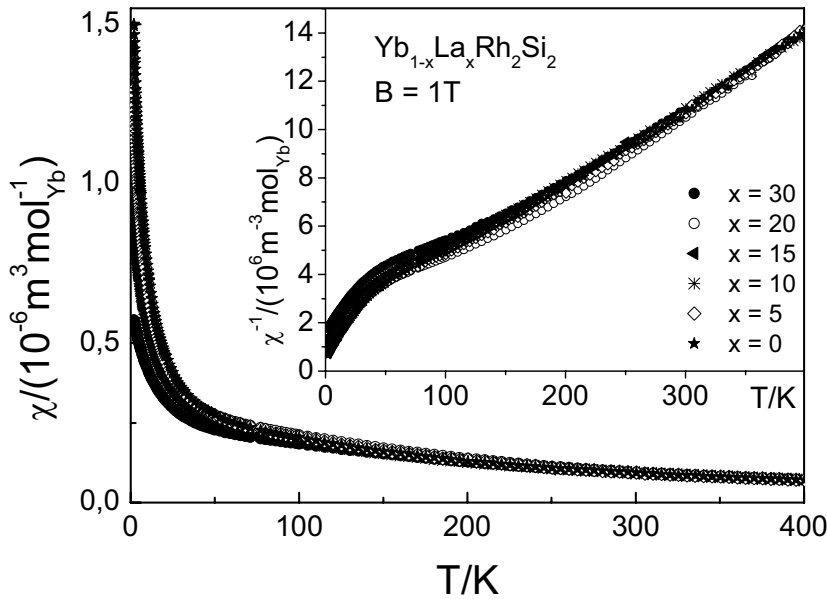


**Figure 4.39:** Comparison of susceptibility of La-doped  $\text{YbRh}_2\text{Si}_2$  for  $B \parallel ab$  plane after background subtraction: only minor changes are visible at high temperatures, while at low temperatures  $\chi$  decreases with increasing La content. The inset shows the inverse susceptibility.



To get a closer look at the major difference of the susceptibility at low temperature, Fig. 4.40 shows the inverse susceptibility below 40 K. The Weiss temperature, obtained from a Curie-Weiss fit below 3 K, increases with the La content. In Fig. 4.34 (page 120) we compare the evolution of the Kondo temperature as determined from the entropy and the low-temperature  $C/T$  value with the evolution of the low-temperature Weiss temperature. The similarity suggests that in this temperature range the evolution of  $\theta_{\text{CW}}$  is strongly related to that of the Kondo exchange. However, the effective moment does not change with La concentration as can be deduced from the similarity of the slopes of  $1/\chi$  versus temperature at low temperatures for all concentrations. One would expect that the increase of the Kondo scale lead to a reduction of the effective moment with increasing La content, but this is not the case.

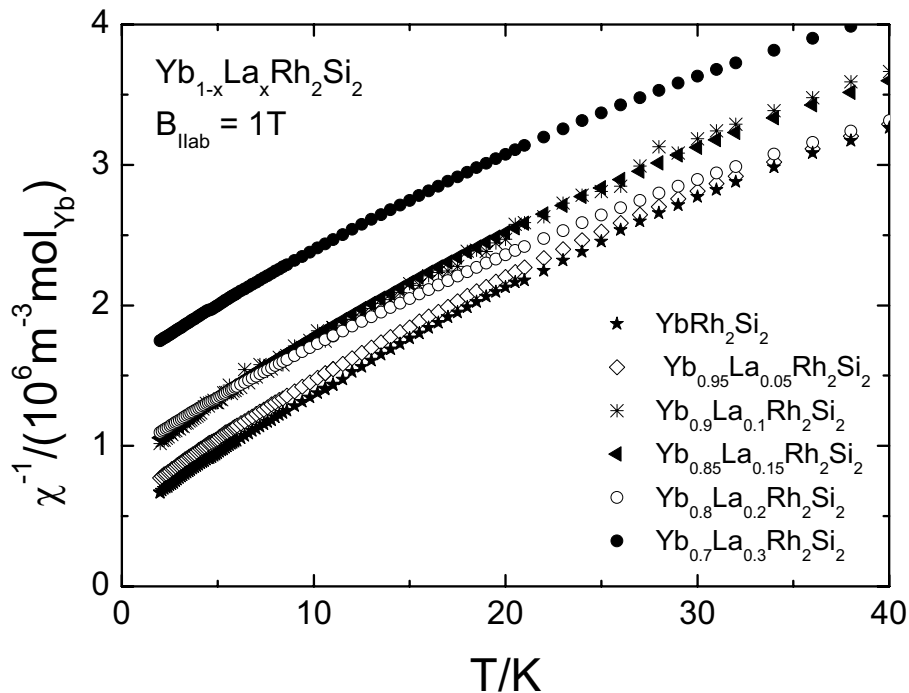


**Figure 4.40:** Comparison of inverse susceptibility of La-doped  $\text{YbRh}_2\text{Si}_2$  below 40 K: The Curie-Weiss temperature is increasing with increasing La content.

## 4.5.2 Magnetisation

The magnetisation data of the La-doped YbRh<sub>2</sub>Si<sub>2</sub> samples at 2 K and up to  $\mu_0 H = 5$  T are shown in Fig. 4.41 for all concentrations. The magnetic field was applied along the ab plane ( $\mu_0 H \parallel ab$ ). The curvature is clearly visible in the pure YbRh<sub>2</sub>Si<sub>2</sub> but decreases with larger La content until it disappears in Yb<sub>0.7</sub>La<sub>0.3</sub>Rh<sub>2</sub>Si<sub>2</sub>. The large symbols at  $\mu_0 H = 1$  T are extracted from susceptibility measurements (see Fig. 4.39) and demonstrate a good agreement between magnetisation and susceptibility measurements. Small deviations from the curvature for Yb<sub>0.9</sub>La<sub>0.1</sub>Rh<sub>2</sub>Si<sub>2</sub> at 3.75 T and for YbRh<sub>2</sub>Si<sub>2</sub> at 4.5 T are due to repositioning of the sample and therefore a slight displacement of the sample during the measuring process.

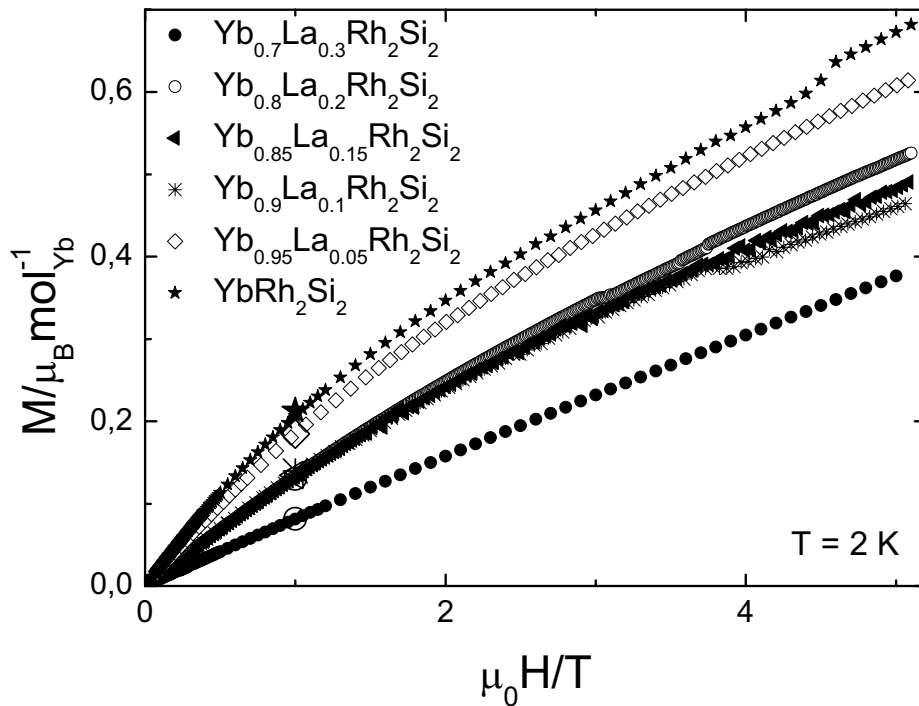


**Figure 4.41:** Isothermal magnetisation with magnetic field applied along the ab plane for Yb<sub>1-x</sub>La<sub>x</sub>Rh<sub>2</sub>Si<sub>2</sub>. The large symbols at  $\mu_0 H = 1$  T are extracted from susceptibility data.

## 4.6 Neutron scattering

Neutron-scattering experiments on the system YbRh<sub>2</sub>Si<sub>2</sub> only started recently. So far neutron diffraction failed in detecting any magnetic Bragg peaks below  $T_N$  [Stockert 2006]. However, inelastic neutron scattering already revealed important results. Inelastic neutron experiments on YbRh<sub>2</sub>Si<sub>2</sub> were performed for the following purposes: first to determine the crystalline-electric-field excitations and second to investigate the quasielastic fluctuations and their temperature dependence. To study the CEF excitations inelastic neutron scattering has been carried out on the time-of-flight spectrometer IN4 at the Institut Laue-Langevin (ILL) in Grenoble, while the latter point, the fluctuations, was addressed by an experiment on IN6, again a time-of-flight spectrometer at the ILL. The experiments were performed by O. Stockert, while A. Murani and M. Koza were the local contacts at the ILL.

The time-of-flight spectrometer IN4 is generally used for the study of excitations in condensed matter and works in the thermal neutron energy range from 10 to 100 meV. The spectrometer consists of a crystal monochromator to get a monochromatic neutron beam and a fast-rotating Fermi chopper to define short monochromatic neutron pulses. Most of the fast neutrons and gamma rays that would give background noise in the spectra are eliminated from the beam by additional choppers, so called background choppers. The sample environment allows accommodating standard cryostats or furnaces. A radial collimator around the sample position suppresses the scattering from the sample environment. <sup>3</sup>He tubes are used as detectors covering scattering angles up to 120°. In each detector the arrival time of the neutrons is recorded in relation to the time when the neutrons hit the sample. To obtain the scattering function  $S(Q,\omega)$  it is necessary to measure the time-of-flight spectra at various angles.

For the experiment on IN4 powdered samples of YbRh<sub>2</sub>Si<sub>2</sub> and LuRh<sub>2</sub>Si<sub>2</sub> (~ 12 g each) were measured. LuRh<sub>2</sub>Si<sub>2</sub> served as the non-magnetic reference substance. The experiments were performed with an incident

neutron energy of  $E_i = 68$  meV at the following temperatures:  $T_1 = 1.5$  K,  $T_2 = 30$  K,  $T_3 = 70$  K,  $T_4 = 125$  K,  $T_5 = 200$  K and  $T_6 = 300$  K. Due to the high absorption of neutrons by rhodium the powdered sample was filled between two concentric aluminium cylinders yielding a hollow cylinder with a thickness of approximately 0.6 mm as sample space. From the measured neutron spectra the electronic background was subtracted and the data normalised to vanadium. After this a conversion from the time-of-flight to energy, a correction for self-absorption and the sample can, and finally a conversion into  $(q, \omega)$  space were done. The self-absorption correction is very important due to the strong absorption of rhodium in YbRh<sub>2</sub>Si<sub>2</sub> and has the largest effect at large positive energy transfers ( $\hbar\omega > 0$ ).

The raw neutron spectra of YbRh<sub>2</sub>Si<sub>2</sub> and LuRh<sub>2</sub>Si<sub>2</sub> at  $T = 1.5$  K for small momentum transfers  $q = 3 \pm 0.5 \text{ \AA}^{-1}$  after detector normalisation, subtraction of the electronic background and correction for absorption (but still including the contribution of the aluminium sample container) are shown in Fig. 4.42. Several peaks are visible. The peak at 10 meV turned out to be of phononic origin.

The separation of the spectra to get only the magnetic response was done as follows: the high- $q$  response (high angles) was scaled down by the ratio of the high  $q$  versus low  $q$  of phonon intensity in LuRh<sub>2</sub>Si<sub>2</sub> and then subtracted from the low- $q$  data in YbRh<sub>2</sub>Si<sub>2</sub>. This is necessary because the nuclear scattering lengths of Yb and Lu differ and the phonons are slightly shifted between both compounds. Thus a direct subtraction of the nonmagnetic LuRh<sub>2</sub>Si<sub>2</sub> does not work satisfactorily. This scaling method [Murani 1983] works since the magnetic contribution at high  $q$  is negligible.

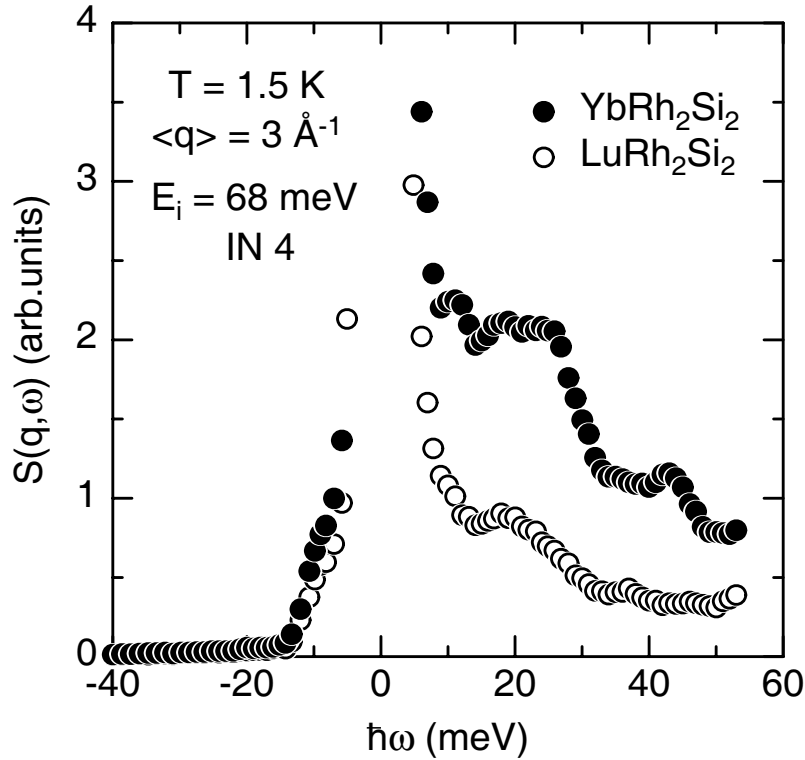


**Figure 4.42:** Neutron spectra of YbRh<sub>2</sub>Si<sub>2</sub> and LuRh<sub>2</sub>Si<sub>2</sub> at  $T = 1.5$  K with  $E_i = 68$  meV for small momentum transfer  $q = 3 \pm 0.5 \text{ \AA}^{-1}$  (taken from [Stockert 2006]).

The dynamic magnetic response at  $T = 1.5$  and 300 K for  $q = (3 \pm 0.5) \text{ \AA}^{-1}$  obtained after subtraction of the phonon part are displayed in Fig. 4.43. The magnetic signal is broad in energy, but well structured and extends beyond 60 meV. For a more quantitative description of the magnetic response at  $T = 1.5$  K, the data have been fitted by a sum of three peaks with a Lorentzian lineshape. The solid line indicates the fit and describes the data quite well. The analysis yields for the excitation energies:  $\hbar\omega \approx 17, 25$  and 42 meV. Those excitations are magnetic in origin and can be attributed to CEF excitations, because they decrease in intensity with  $q$ . For a tetragonal unit cell with Yb<sup>3+</sup> ions ( $J = 7/2$ ) surrounded by a tetragonal environment a ground-state doublet and three excited doublets are expected. All three excited CEF doublet states have therefore been detected. The  $J = 7/2$  Yb<sup>3+</sup>

multiplet splits into four doublets with the CEF level scheme 0-17-25-43 meV, which corresponds to 0-200-290-500 K. The ground-state doublet determines in connection with the Kondo and RKKY exchange the low temperature thermodynamic and transport properties. The first excited doublet at 17 meV is within its error range in agreement with the maximum observed in the specific heat  $C_{\text{mag}}$  between 40 and 80 K.

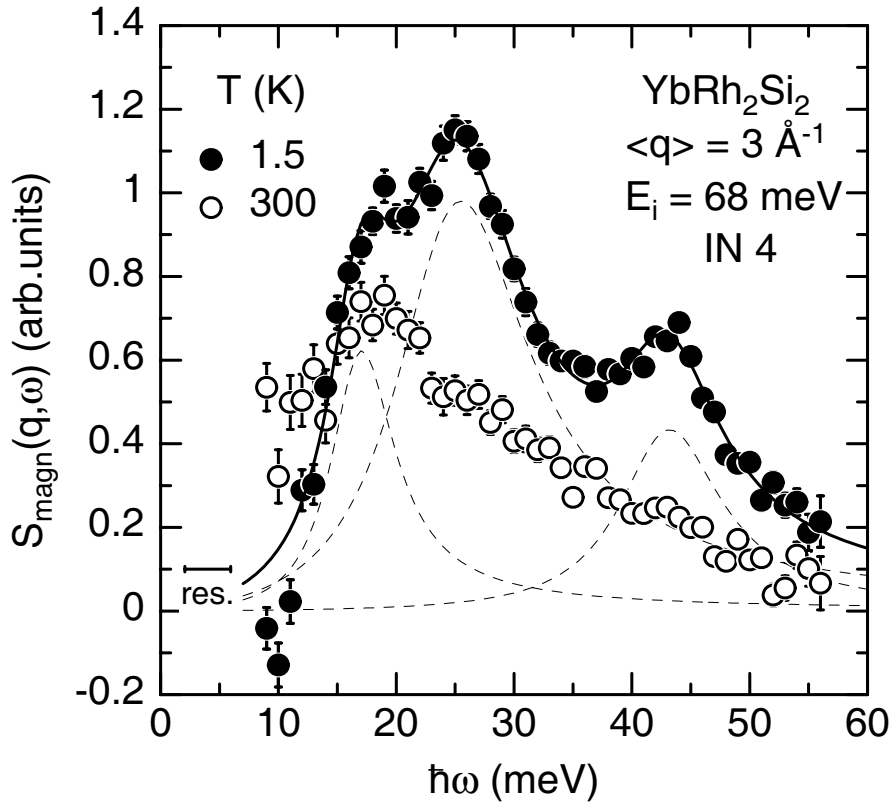


**Figure 4.43:** Magnetic part of the excitation spectra of YbRh<sub>2</sub>Si<sub>2</sub> for two temperatures  $T = 1.5$  and  $300$  K at an average momentum transfer of  $q = (3 \pm 0.5) \text{ \AA}^{-1}$ . The solid line indicates a fit with three Lorentzians (dashed lines) to the  $T = 1.5$  K data (taken from [Stockert 2006]).

A second experiment on IN6 with the same sample was performed to investigate the magnetic response at low energy transfers at three selected temperatures  $T_1 = 1.6$  K,  $T_2 = 12$  K and  $T_3 = 33$  K with an incident neutron energy  $E_0 = 3.12$  meV.

IN6 is again a time-of-flight spectrometer with a crystal monochromator, but in contrast to IN4 which is located on a thermal beam, IN6 is a cold-neutron spectrometer for energies below 5 meV.

The low-energy response of  $\text{YbRh}_2\text{Si}_2$  for all three temperatures is plotted in Fig. 4.44.

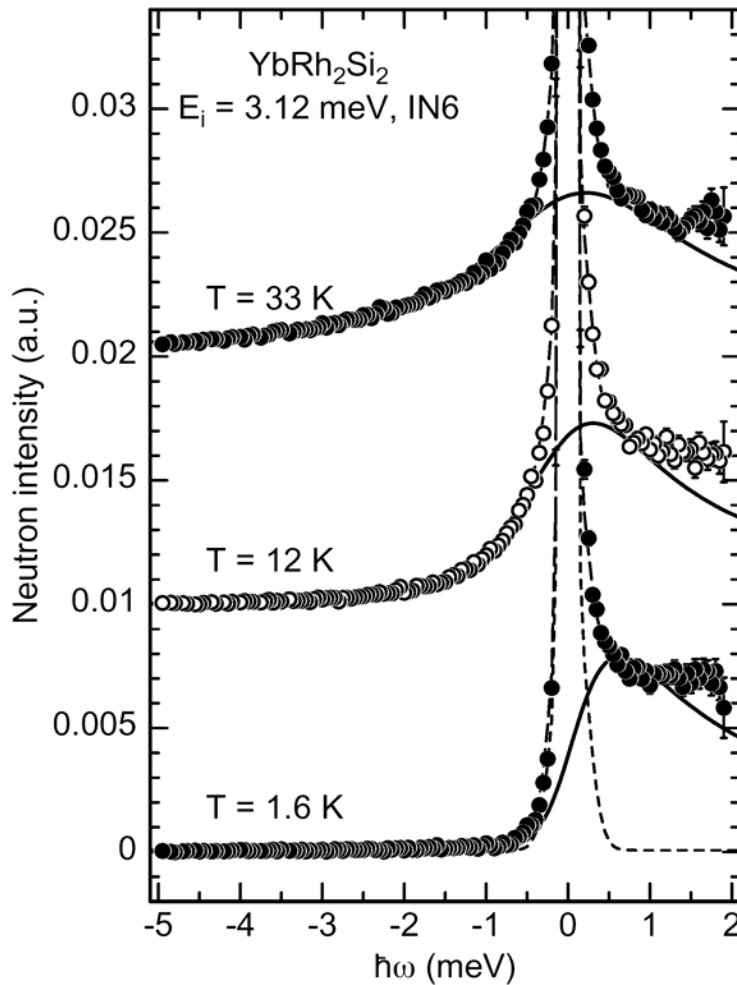


**Figure 4.44:** Neutron spectra of  $\text{YbRh}_2\text{Si}_2$  taken at three different temperatures  $T_1 = 1.6$  K,  $T_2 = 12$  K and  $T_3 = 33$  K. The dashed line is a fit to the data with an incoherent elastic line (Gaussian) (dashed line) and a quasielastic Lorentzian (solid line), to model the magnetic part of the response.

The spectra were fitted by a sum of a Gaussian centred at  $\omega = 0$  to describe the incoherent elastic signal, and a quasielastic Lorentzian line to model the magnetic response, i.e., the spin fluctuations. From the Lorentzian fits two important parameters can be deduced: the width  $\Gamma$  of the response and the static susceptibility  $\chi(\langle q \rangle)$ . The linewidth  $\Gamma$  (**F**ull **W**idth at **H**alf **M**aximum) of the Lorentzian response decreases with temperature, which is a sign for a slowing down of the magnetic response. This is expected for systems above the ordering temperature, like YbRh<sub>2</sub>Si<sub>2</sub> ( $T_N = 65$  mK), showing a phase transition at lower temperatures or even at  $T = 0$ . The temperature dependence of the linewidth  $\Gamma$  of the quasielastic response and of the determined static susceptibility are shown in Fig. 4.45. The static susceptibility is compared to the bulk susceptibility measured with a SQUID. The static susceptibility  $\chi$ , determined from the fit of the quasielastic response, behaves in a similar way as the bulk susceptibility and increases with decreasing temperature.



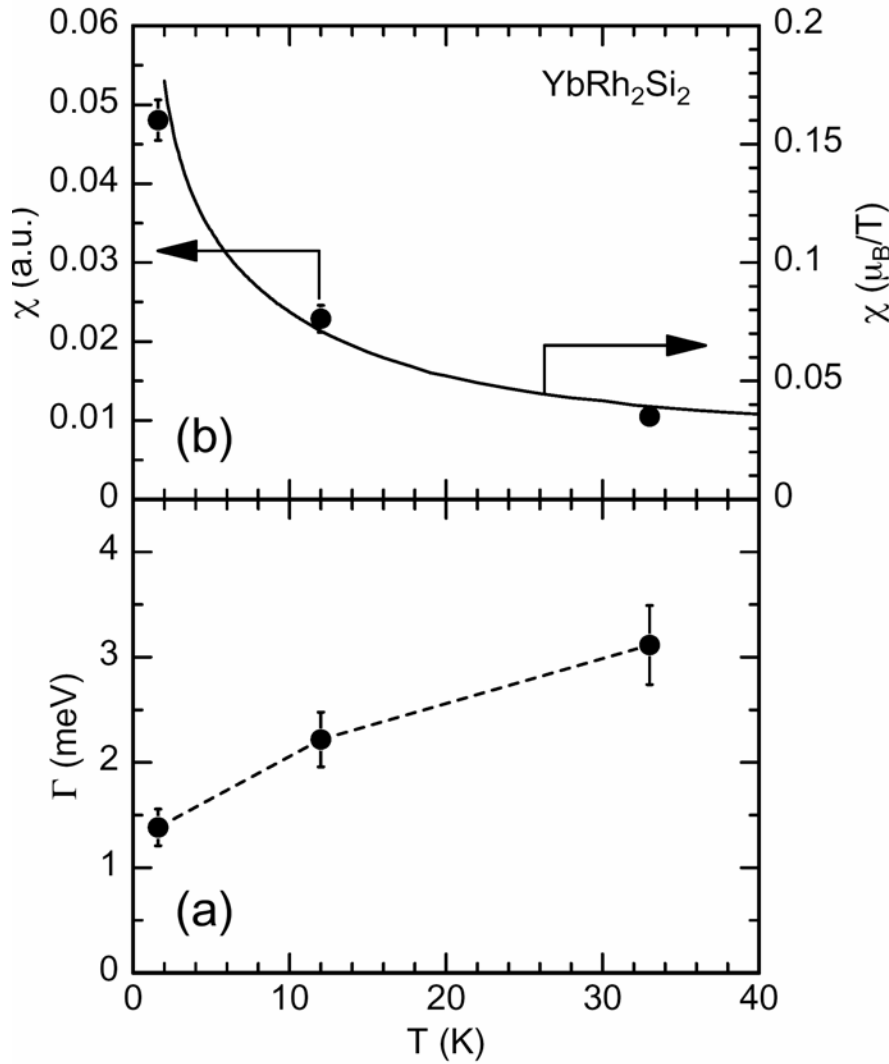


**Figure 4.45:** *a: Temperature dependence of the linewidth  $\Gamma$  (FWHM) of the quasielastic response.*  
*b: Static susceptibility determined from the quasielastic response and comparison with bulk susceptibility.*

A small comment should be given to the deviation of the data from the fit at higher positive energy transfers ( $\hbar\omega > 1$  meV), where a long tail is visible. This is an indication of an additional fast relaxing part in addition to the slowly relaxing part of the response. Measuring the magnetic response at the ordering vector (which would only be possible on large single-crystalline samples) should show a narrowing of  $\Gamma$  down to 0 around 65 mK with

decreasing temperature. This is not the case, because of the averaging in  $k$  space. A different way to analyse those data is to use a phenomenological model introduced by Bernhoeft [Bernhoeft 2001]. It assumes a distribution of relaxation times and gives a non-Lorentzian-like magnetic response with a  $T$ -dependent narrow part and a broad  $T$ -independent tail. This calculation is still under discussion, but it shows a linear temperature dependence of  $\Gamma$  down to 0. It would be very interesting to extend the experiments on the magnetic response of YbRh<sub>2</sub>Si<sub>2</sub> to lower temperatures in order to observe the critical slowing down, and also to extend the measurement to lower  $q$  transfer to check if the response is showing a small maximum at finite  $q$ , as expected for an antiferromagnet.

## 4.7 ESR

The electron spin resonance (ESR) probes the excitation of the spin of the electrons. In general Kondo systems are not appropriate for this technique since the typical spin-fluctuation rate of the Kondo ions lead to a very large ESR linewidth. This large ESR linewidth makes the ESR signal undetectable. A direct observation of the Kondo ions by ESR measurements has only been reported in dilute Kondo systems like Yb diluted in Au [Baberschke 1980] with a very small  $T_K$  of 10  $\mu$ K. In the last years a lot of work has been done on dense Kondo-lattice systems with an additional ESR probe ion, like Gadolinium, substituted for the Kondo ions [Elschner 1997, Krug von Nidda 1998, Mair 1999].

The signal of the Kondo ion itself was never observed in these experiments. Therefore, we did not expect to see an ESR signal in YbRh<sub>2</sub>Si<sub>2</sub>. To our surprise, a strong and sharp ESR signal appeared in the first ESR measurement on YbRh<sub>2</sub>Si<sub>2</sub>. From the analysis of the spectra it turned out that the ESR is probing the local Yb<sup>3+</sup>  $4f$  spins.

### 4.7.1 ESR signal in pure YbRh<sub>2</sub>Si<sub>2</sub>

The experiments were performed at two frequencies: 9.4 and 43.1 GHz to explore the X band as well as the Q band. ESR probes the absorbed power,  $P$ , of a transversal magnetic microwave field as function of a longitudinal external static magnetic field. Two typical spectra are shown in Fig. 4.46.

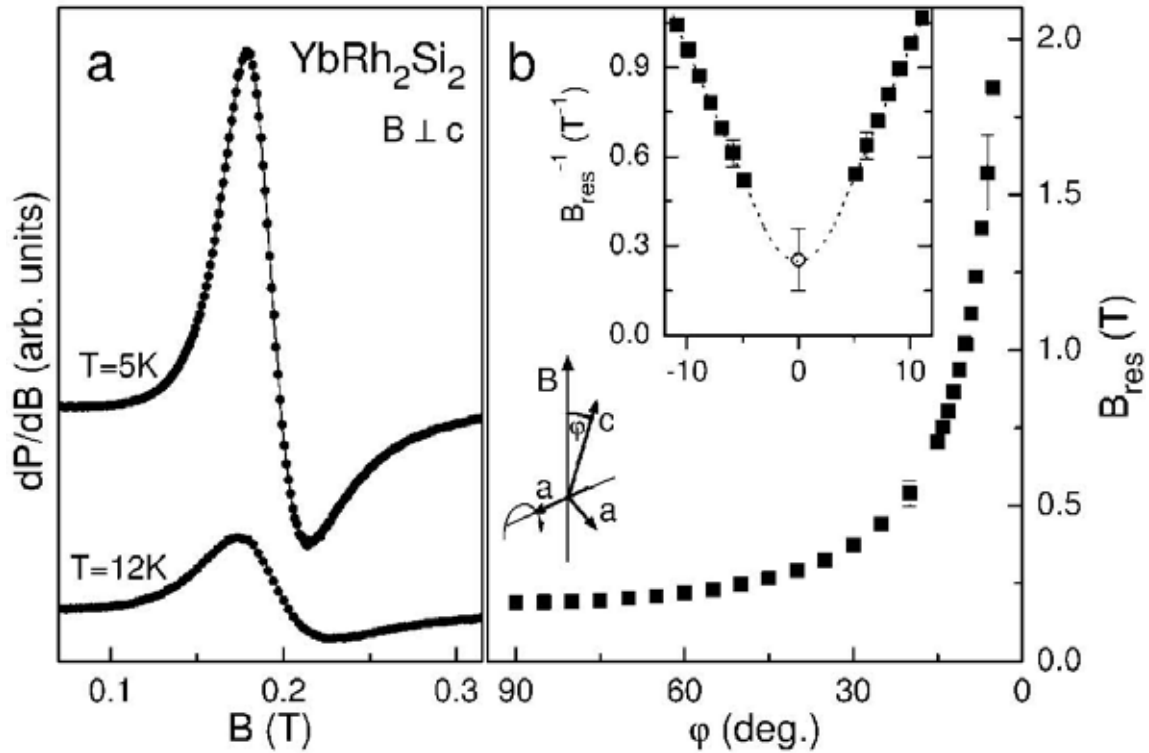


**Figure 4.46:** (a) ESR spectra at 9.4 GHz (X band) at 5 and 12 K. (b) angle dependence of the resonance field  $B_{res}$  at 5 K. Inset: reciprocal  $B_{res}$  for  $|\phi| < 12^\circ$  (taken from [Sichelschmidt 2003]).

Solid lines represent fits of the data with a Lorentzian line shape. The asymmetry of this line shape is typical for metals with a penetration depth smaller than the sample size [Barnes 1981] and occurs due to a non-vanishing dispersive contribution to the line. The ESR intensities of YbRh<sub>2</sub>Si<sub>2</sub> were compared with the results in the intermetallic compound Y<sub>0.99</sub>Yb<sub>0.01</sub>Pd<sub>3</sub> to estimate the amount of Yb<sup>3+</sup> ions contributing to the ESR

spectra. This amount was estimated to be at least 60%, which shows that the observed ESR resonance is a bulk property and cannot be ascribed to foreign Yb<sup>3+</sup> phases. The ESR intensity  $I_{ESR}$  reflects the uniform static susceptibility  $\chi(q=0)$  of the Yb<sup>3+</sup> spins. It is proportional to the area under the absorption signal. A linear relation  $I_{ESR} \propto (\chi - \chi_0)$  with  $\chi_0 = 0.3 \cdot 10^{-6} \text{ m}^3 \text{ mol}^{-1}$  was found, which indicates a small temperature independent contribution to the bulk susceptibility.

The effective  $g$  value of the spin is determined by  $B_{res}$  via the resonance relation  $\hbar\omega = g\mu_B B_{res}$ . The XY behaviour of the Yb<sup>3+</sup> moment is visible in the magnetic susceptibility, where  $\chi_{BIIab} \approx 100 \cdot \chi_{BIIc}$  at 100 mK. Fig. 4.46(b) shows that this strong magnetocrystalline anisotropy is reflected in a strong anisotropy of the resonance field. The single crystal is rotated in the magnetic field  $B$  as illustrated in the drawing.  $B_{res}$  increases strongly up to a non detectable value when the orientation of the field gets close to the  $c$  axis. This anisotropy also supports the bulk origin of the ESR signal. From the observed  $g$ -factors  $g_{\perp} = 3.56$  and  $g_{\parallel} = 0.17$ , one can deduce the wave function of the CEF ground-state doublet. Best agreement for both  $g_{\perp} = 3.56$  and  $g_{\parallel} = 0.17$  is reached assuming a  $\Gamma_7$  doublet [Sichelschmidt 2003].

It is presently not clear why the ESR signal of the Kondo ion can be observed in YbRh<sub>2</sub>Si<sub>2</sub>. One of the present hypotheses is that it is due to the local character of the QCP in YbRh<sub>2</sub>Si<sub>2</sub>. Another suggestion is that it is due to strong ferromagnetic fluctuations, as evidenced e.g. by NMR measurements [Ishida 2002]. Interestingly, the relaxation behaviour of the ESR signal can be scaled to the relaxation behaviour of the NMR signal (Fig. 4.47). Thus the observation of the ESR signal deserves further investigations.

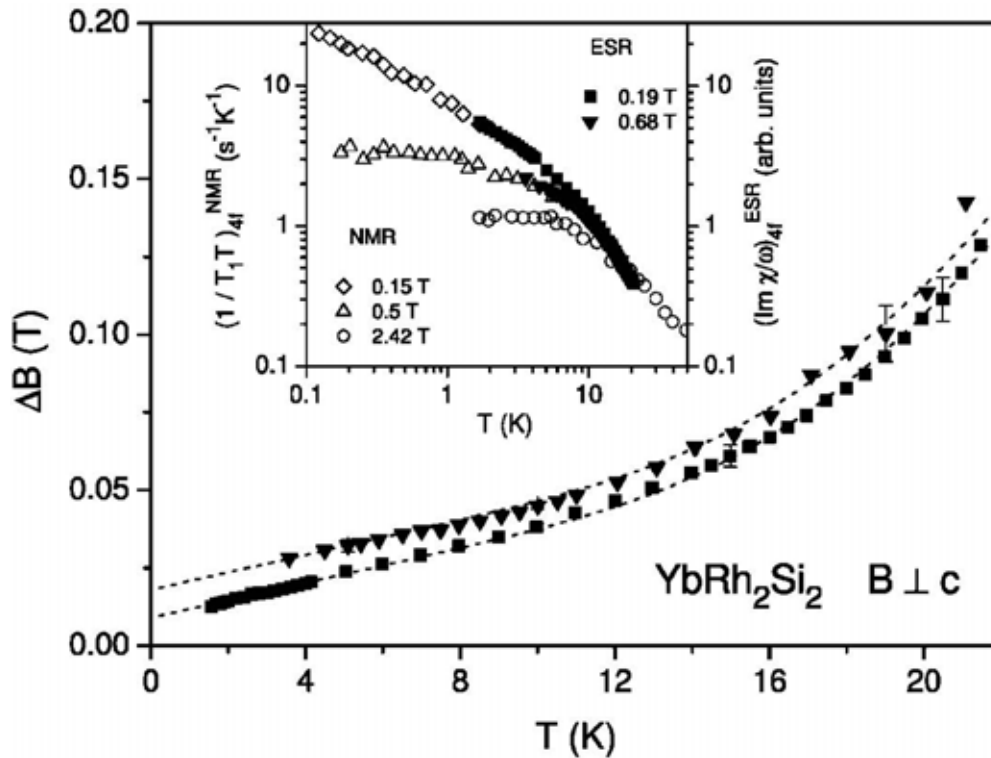


**Figure 4.47:** Temperature dependence of the ESR linewidth  $\Delta B$  at 9.4 GHz (squares) and 34.1 GHz (triangles). Inset: Comparison of the temperature dependence of  $(\text{Im } \chi''/\omega)$  from the ESR data with  $^{29}\text{Si}$  NMR data (taken from [Sichelschmidt 2003]).

## 4.7.2 ESR signal in Yb<sub>1-x</sub>La<sub>x</sub>Rh<sub>2</sub>Si<sub>2</sub>

ESR investigations were also performed on La<sub>x</sub>Yb<sub>1-x</sub>Rh<sub>2</sub>Si<sub>2</sub> by J. Wykhoff [Wykhoff 2005]. A clear ESR signal was detected in the 5% (55076) and 10% (55057) La-doped samples. In the samples with higher La concentration the linewidth was smeared out and no clear result could be taken from the obtained signal. The main result of those measurements is that the linewidth scales with the residual resistivity as seen in Fig. 4.48. The linewidth of the ESR signal at a constant temperature depends exponentially on the resistivity ratio.

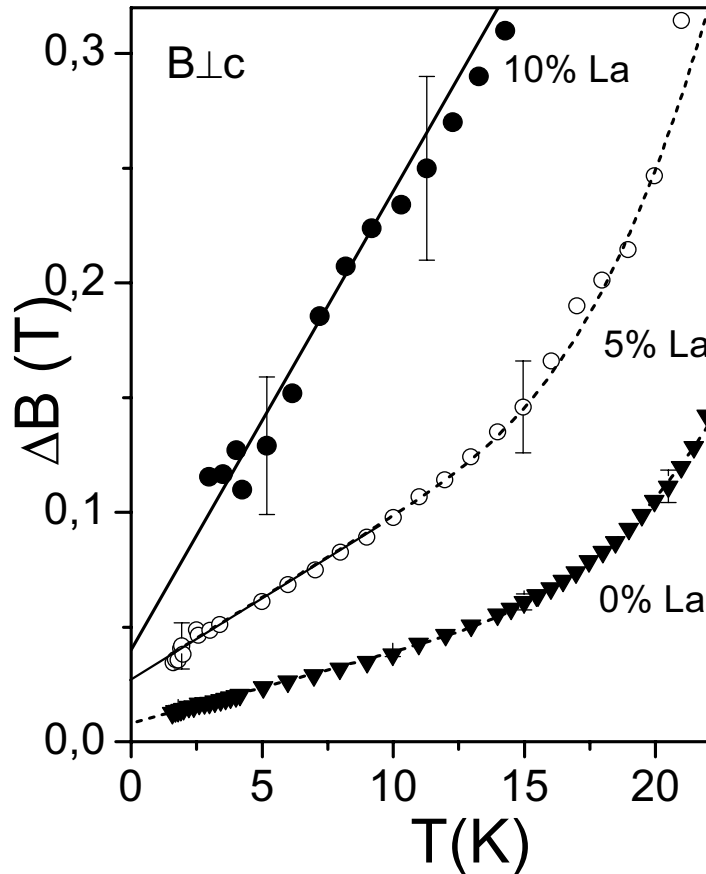


**Figure 4.48:** Temperature dependence of linewidth for  $\text{La}_x\text{Yb}_{1-x}\text{Rh}_2\text{Si}_2$  ( $x = 0, 0.05, 0.10$ ). The residual linewidth of the ESR signal depends exponentially on the resistivity ratio.

Since the direct observation of an ESR signal in Kondo systems is very rare, measurements on the system  $\text{Yb}_4\text{Rh}_7\text{Ge}_6$  (chapter 5) were performed to search for the possibility of the existence of an ESR signal there. But no ESR signal could be detected and therefore the sharp signal obtained in the system  $\text{YbRh}_2\text{Si}_2$  is very unique.

## 4.8 Muon spin relaxations in $\text{Yb}_{0.95}\text{La}_{0.05}\text{Rh}_2\text{Si}_2$

The investigation of the magnetic ground state in the 5% La-doped  $\text{YbRh}_2\text{Si}_2$  using  $\mu\text{SR}$  measurements were performed at the  $\pi\text{A}$ -port of the Meson Science Laboratory (KEK-MSL) by K. Ishida [Ishida 2003a]. The powdered single-crystalline sample was cooled down to the base temperature of about 17 mK after fixing it to a “cold plate” of the top-loading dilution refrigerator. The time dependence of the  $\mu\text{SR}$  decay at 900 and 17 mK is shown in Fig. 4.49. At both temperatures the same relaxation behaviour is found, which means that no evidence for magnetic order is observed down to 17 mK.

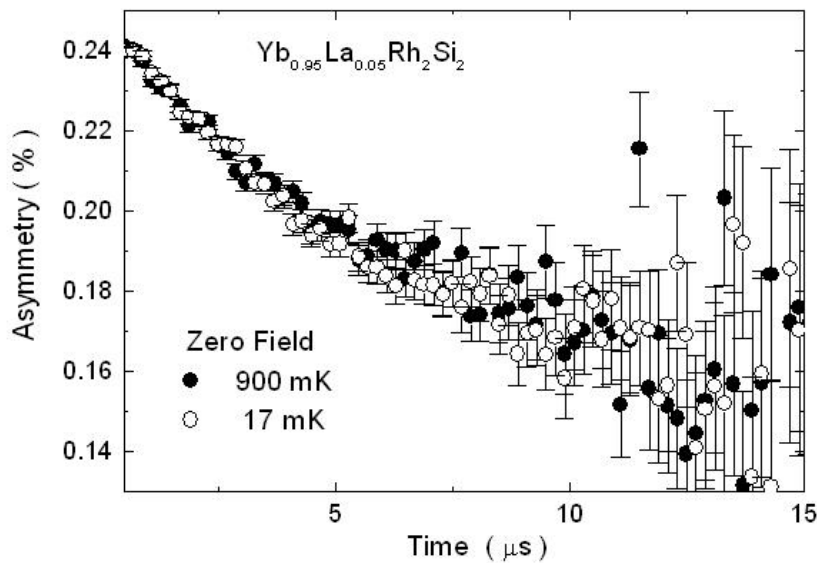


**Figure 4.49:** Time dependence of the zero field  $\mu\text{SR}$  asymmetry relaxation in  $\text{Yb}_{0.95}\text{La}_{0.05}\text{Rh}_2\text{Si}_2$  at 900 mK and 17 mK.

The faster relaxation in  $\text{Yb}_{0.95}\text{La}_{0.05}\text{Rh}_2\text{Si}_2$  than in pure  $\text{YbRh}_2\text{Si}_2$  [Ishida 2003b, Ishida 2003c, Ishida 2003d] is due to the nuclear contribution from the doped La.

The disorder effect of La doping is considered to be very small since the magnetic fluctuations are determined almost by a single component of  $T_1$ . Stretched exponential behaviour in relaxation was reported in disordered systems like spin-glass compounds, but this behaviour is absent or very weak in Yb<sub>0.95</sub>La<sub>0.05</sub>Rh<sub>2</sub>Si<sub>2</sub>.

## 4.9 Summary

In summary, the crystal growth process was modified to improve the quality and size of YbRh<sub>2</sub>Si<sub>2</sub> single crystals. We developed a growth procedure which resulted in YbRh<sub>2</sub>Si<sub>2</sub> with a reproducible high quality, as evidenced by a residual resistivity ratio in between 55 and 65 for most of the single crystals. These single crystals were used for a large number of investigation in our institute as well as by other research groups. My own investigations were focussed on two different problems: the determination of the main energy scales of the 4*f* electrons and the study of the behaviour across the QCP using Yb<sub>1-x</sub>La<sub>x</sub>Rh<sub>2</sub>Si<sub>2</sub>.

For the determination of the main energy scale of the 4*f* electrons, i.e. of the Kondo temperature and of the excitation energies of the crystal field levels, we estimated and analysed the contribution  $C_{4f}$  of the 4*f* electrons to the specific heat. For this purpose, we carefully measured the specific heat of YbRh<sub>2</sub>Si<sub>2</sub> and LuRh<sub>2</sub>Si<sub>2</sub> and estimated  $C_{4f}$  from the difference. We confirm the presence of a local maximum in  $C_{4f}$  between 40 and 80 K. Inelastic neutron data allow to fix quite precisely the two upper CEF levels at 25 meV and 42 meV, while the position  $E_1 = 17$  meV obtained for the first excited CEF level is not very reliable and is far above the first estimation  $E_1 = 100$  K ( $\approx 8$  meV) from earlier specific-heat measurements. We therefore analysed  $C_{4f}$  more precisely using the combination of a simple CEF model and the theoretical prediction for the single-ion Kondo model. This analysis places the first excited CEF level at an energy  $(12 \pm 2)$  meV, in good agreement with the neutron data. Therefore, the combination of the



present analysis of the specific-heat data and neutron-scattering results allows to fix the energies of the CEF levels.

Further on, this analysis showed that the magnetic specific heat can be well described above 2 K by the single-ion Kondo model with  $15 \text{ K} < T_K < 20 \text{ K}$ . A complementary analysis of the temperature dependence of the entropy gives  $T_K = 17 \text{ K}$ . This result is also in agreement with the width of the quasielastic line observed in inelastic neutron scattering. Thus the present data allow to fix the Kondo energy scale to  $T_K = (17 \pm 1) \text{ K}$ . The observation that  $C_{4f}$  follows the Kondo behaviour above 2 K and the determination of a reliable value of  $T_K$  are important in the context of the present discussion of YbRh<sub>2</sub>Si<sub>2</sub>, since some of its properties, such as the observation of the Yb ESR line and the increase of  $\chi_{ab}$  down to low temperatures, are at odd with standard expectations for Kondo systems.

For the investigation of the behaviour across the QCP using doped YbRh<sub>2</sub>Si<sub>2</sub>, the initial approach with Ge-doped single crystals was unsuccessful because of the impossibility to grow single crystals with a Ge amount larger than 2%. In contrast, the attempt to substitute Yb by La was very successful. Yb<sub>1-x</sub>La<sub>x</sub>Rh<sub>2</sub>Si<sub>2</sub> single crystals with  $x = 0.05, 0.1, 0.15, 0.2$  and  $0.3$  were grown from In flux, using the sealed Ta-crucible technique. Their resistivity, specific heat and susceptibility were investigated and analysed. While the La content determined by EPMA was larger than the nominal one, the increase of the lattice parameters was weaker than expected from Vegard's law. The residual resistivity increases linearly with the La content, indicating a statistical replacement of Yb by La. But even in the  $x = 0.3$  sample, despite a RRR of only 2, the resistivity strongly decreases below its maximum at around 125 K, indicating the formation of a coherent state.

From the analysis of the temperature dependence of the  $4f$  entropy, we deduce a monotonous increase of the Kondo temperature  $T_K$  from  $T_K = 17 \text{ K}$  in YbRh<sub>2</sub>Si<sub>2</sub> to  $T_K = 50 \text{ K}$  for  $x = 0.3$ , as expected from the chemical negative pressure due to the lattice expansion. Accordingly, the antiferromagnetic order gets suppressed. Already in the  $x = 0.05$  sample, we

did not observe any evidence for magnetic order, neither in the specific heat, nor in the resistivity, nor in the  $\mu$ SR experiment. The latter one implies an upper bound of 17 mK for  $T_N$ .  $C/T$  of the  $x = 0.05$  and  $x = 0.1$  samples increases logarithmically down to the lowest measured temperature,  $T = 50$  mK. In contrast, in the samples with  $x \geq 0.15$ ,  $C/T$  levels at a temperature independent value at low  $T$ , evidencing the formation of a heavy Fermi-liquid ground state with an enhanced Sommerfeld coefficient decreasing from  $\gamma = 470$  mJ/K<sup>2</sup>mol for  $x = 0.15$  to  $\gamma = 300$  mJ/K<sup>2</sup>mol for  $x = 0.3$ . The temperature dependence of the resistivity at low temperatures evolves from a linear one in pure YbRh<sub>2</sub>Si<sub>2</sub> to a power law with an exponent  $n$  in between 1 and 2 and increasing with  $x$  for  $0 < x < 0.15$ , while for  $x \geq 0.15$  one observes  $n = 2$  as expected for a Fermi liquid. Thus, all the investigations of the Yb<sub>1-x</sub>La<sub>x</sub>Rh<sub>2</sub>Si<sub>2</sub> samples indicate an increase of  $T_K$  with  $x$  due to the lattice expansion. This increase of  $T_K$  lead to a suppression of the antiferromagnetic state at a QCP located in the region  $0.05 < x < 0.10$ . Accordingly, the NFL behaviour extends down to the lowest investigated temperature for  $0.05 \leq x \leq 0.10$ , but for  $x \geq 0.15$  it is replaced by a heavy Fermi-liquid state.

Very surprising is the Yb ESR signal observed for the first time in the present sample. It was the first case where the ESR line of the Kondo ion has been seen in a dense Kondo system. The very strong anisotropy of the  $g$ -factor reflects the anisotropy of the bulk susceptibility, allowing for a precise determination of the wave function of the CEF ground state. It further proves that the ESR signal stems from (almost) localised  $4f$  electrons. In the La-doped samples, the ESR linewidth scales with the residual resistivity, suggesting that the bottleneck effect plays an important role for the observability of the ESR line. It is presently not clear, whether the observation of the ESR line is related to the local nature of the QCP or whether it is related to ferromagnetic fluctuations.



## 5 Magnetic order of well localised Yb<sup>3+</sup> moments in Yb<sub>4</sub>Rh<sub>7</sub>Ge<sub>6</sub>

YbRh<sub>2</sub>Si<sub>2</sub> is a very interesting compound, lying quite close to the transition from a magnetically ordered ground state to a non-magnetic one [Gegenwart 2002]. The ordering temperature of  $T_N = 70$  mK disappears at a quantum critical point where the effective mass of the quasi particles diverges upon applying a small magnetic field (700 G) or a slight negative chemical pressure (0.3 GPa). In an attempt to prepare the isoelectronic compound YbRh<sub>2</sub>Ge<sub>2</sub>, single crystals of Yb<sub>4</sub>Rh<sub>7</sub>Ge<sub>6</sub> were obtained. An investigation of the physical properties (susceptibility, resistivity and specific heat) of this compound was performed, since up to now only its structure has been reported [Francois 1985]. The results evidence a stable Yb<sup>3+</sup> state, which orders presumably antiferromagnetically at 0.49 K. The CEF ground-state doublet is well separated from the excited states. The stable Yb<sup>3+</sup> state likely results from the very short Ytterbium-Rhodium and Ytterbium-Germanium nearest-neighbour distances in the Yb<sub>4</sub>Rh<sub>7</sub>Ge<sub>6</sub> structure.

### 5.1 Crystal growth

Our attempt to grow YbRh<sub>2</sub>Ge<sub>2</sub> single crystals from an In flux resulted in a mixture of several phases. The pure elements (germanium pieces, rhodium powder, and small pieces of ytterbium) were carefully placed into an Al<sub>2</sub>O<sub>3</sub>-crucible and mixed with the required amount of indium. We usually use a ratio of 90% In-flux and 10% YbRh<sub>2</sub>Ge<sub>2</sub>, resulting typically in a starting mass of 6 g Yb + Rh + Ge and 12 g In. The filled Al<sub>2</sub>O<sub>3</sub> crucible was covered with an Al<sub>2</sub>O<sub>3</sub> lid and placed into an annealed Ta-crucible, which had to be sealed under argon atmosphere in an arc furnace, because of the high vapour pressure of ytterbium. With zirconium foil covering the outside

of the Ta crucible to bind residual oxygen, it was set into the sample chamber of a furnace (generally the Xerion furnace). This chamber was evacuated and flooded several times with argon to clean the atmosphere. The crystals were either grown by Bridgman technique (pulling down the sample crucible with a defined speed of 0.138 for 55030 and with 0.007 mm/h for 55037) or by furnace cooling (reducing the furnace temperature with  $7.5^\circ\text{C}/\text{h}$  for 55039 without moving the crucible). Both ways gave the same result. The temperature versus time profiles are shown in fig. 5.1.

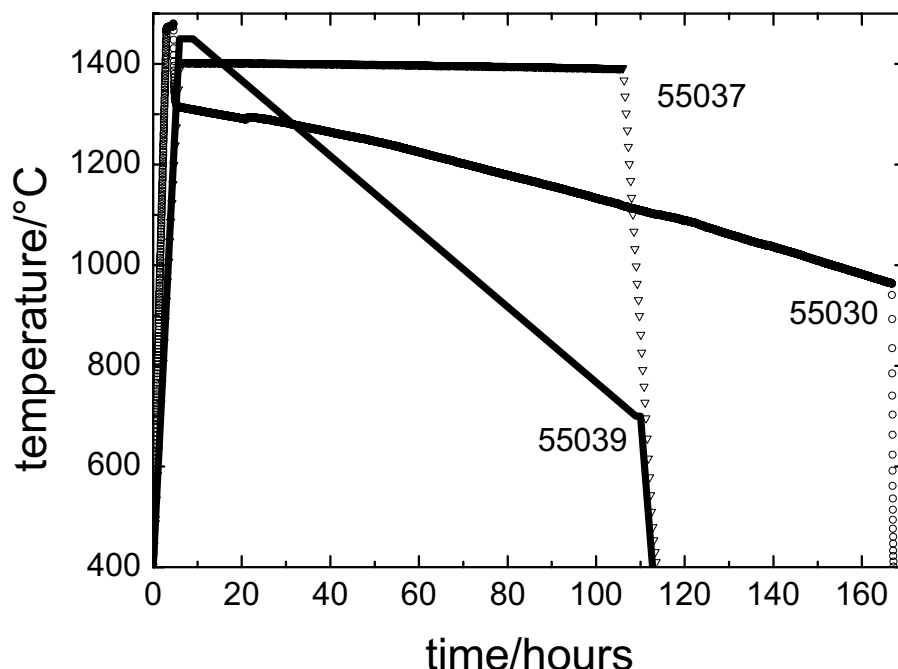


**Figure 5.1:** *Temperature versus time profiles of three different batches which resulted in  $\text{Yb}_4\text{Rh}_7\text{Ge}_6$  crystals.*

After the crystal growth the Ta crucible was opened and the In flux was removed using diluted hydrochloric acid in the ratio 1:1. After one to two days of etching the resulting crystals were washed with pure water to remove the acid. The cleaning process was finished with ethanol. Several pieces of different shape, some single- and some polycrystalline-like were

visible. Several crystals of similar shape (mostly rectangular), hardness and shiny appearance were selected for powdering for the X-ray analysis. The size of the crystals with cube-like shape was roughly  $10 \text{ mm}^3$  and one example is shown in Figure 5.2. The X-ray powder-diffraction pattern of powdered rectangular crystals of batch 55037 is shown in figure 5.3.

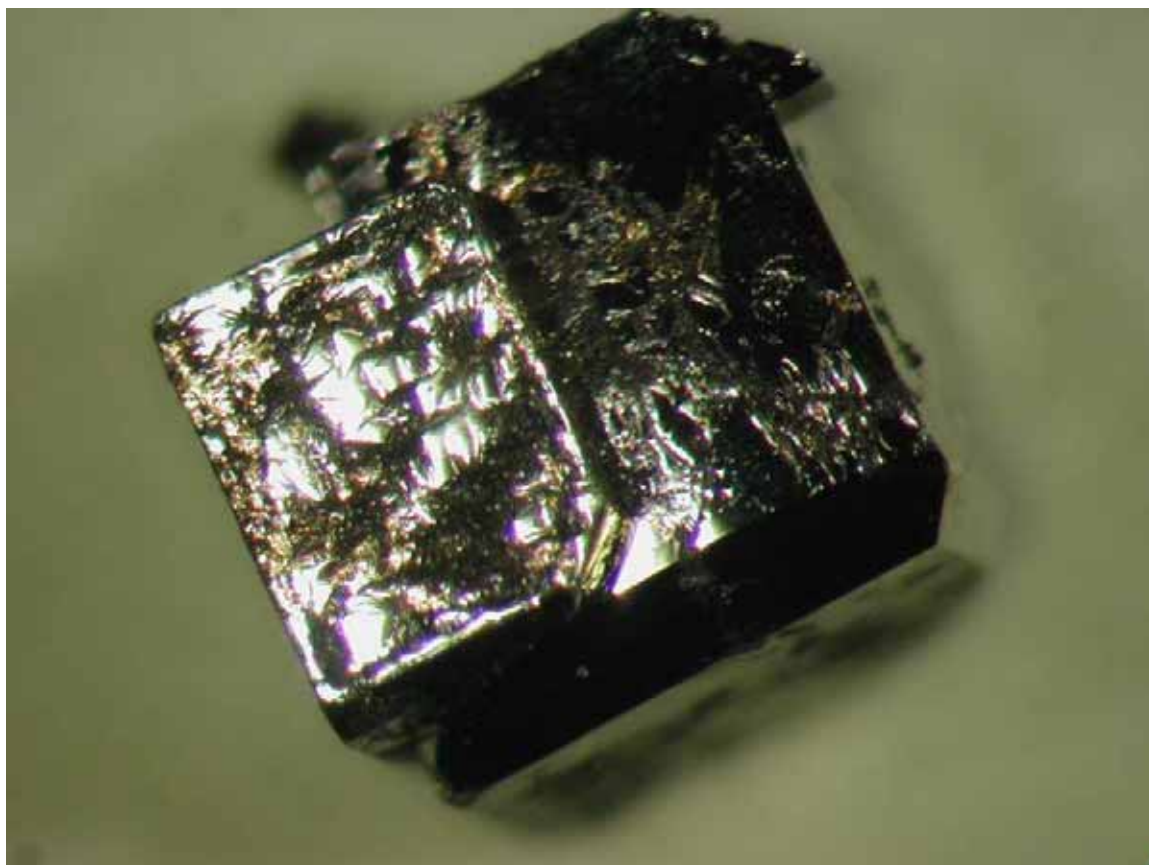


**Figure 5.2:** *The largest single crystals extracted from batch 55037 show a rectangular shape in accordance with the cubic structure of  $\text{Yb}_4\text{Rh}_7\text{Ge}_6$ .*

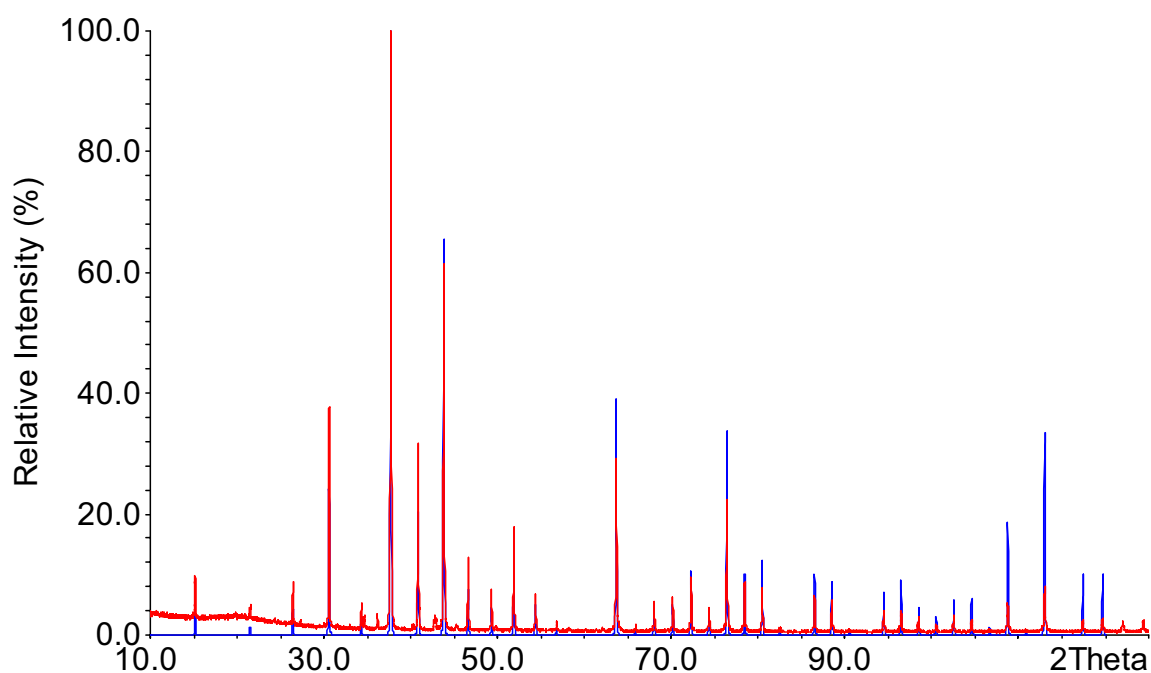


**Figure 5.3:** *The X-ray powder-diffraction pattern of the largest single crystals of batch 55037 (red data set) shows the cubic phase of Yb<sub>4</sub>Rh<sub>7</sub>Ge<sub>6</sub> and a negligible amount of another foreign phase. The theoretical diffraction pattern calculated for Yb<sub>4</sub>Rh<sub>7</sub>Ge<sub>6</sub> is shown for comparison (blue curve).*

From the regular spacing between the peaks one can conclude the existence of a cubic structure even before starting to analyse this pattern. After analysing the powder X-ray diffraction pattern, it could be indexed with the cubic structure of U<sub>4</sub>Re<sub>7</sub>Si<sub>6</sub> (fig.5.4). A theoretical pattern of this structure with the elements Yb, Rh and Ge is included in figure 5.3 (blue curve). This calculated pattern is in good agreement with the obtained powder diffraction pattern of the single crystals. The lattice parameter was estimated to  $a = 8.262 \text{ \AA}$ , very close to the value  $a = 8.254 \text{ \AA}$  reported in the literature [Francois 1985]. The amount of foreign phases is very small and can be neglected. Thus the structure and phase of the cubic-shaped crystals was found to be Yb<sub>4</sub>Rh<sub>7</sub>Ge<sub>6</sub>.

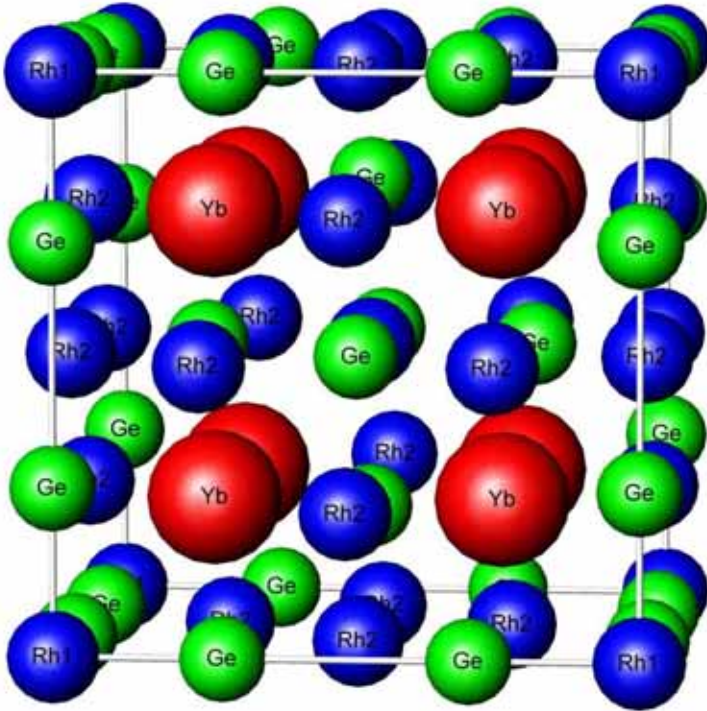


**Figure 5.4:** *The crystal structure of Yb<sub>4</sub>Rh<sub>7</sub>Ge<sub>6</sub> belongs to the structure type U<sub>4</sub>Re<sub>7</sub>Si<sub>6</sub> and space group Im-3m (229). The calculated lattice parameter of the cubic unit cell is quite large with  $a = 8.262 \text{ \AA}$ .*

Dr. Raul Cardoso [Cardoso 2001] performed a structure refinement on those single crystals. The atomic coordinates and displacement parameters ( $U_{eq}$ ,  $U_{ij}$  in pm<sup>2</sup>) for Yb<sub>4</sub>Rh<sub>7</sub>Ge<sub>6</sub> are shown in table 5.1. It is the first investigation of the crystal structure of this compound.

The same analysis was performed with the other crystals with different shape and hardness (softer than the cubes). Those crystals were much smaller in size and did not shine so much. Unfortunately those single crystals, found in the upper part of the crucible swimming in the indium flux, seem to consist of pure germanium. At the bottom and in the middle of the crucible even smaller crystals of undefined shape were found, consisting mostly of ternary Yb-Rh-Ge and binary Rh-Ge phases.



**Table 5.1:** Atomic coordinates and displacement parameter ( $U_{eq}$ ,  $U_{ij}$  in  $\text{pm}^2$ ) for Yb<sub>4</sub>Rh<sub>7</sub>Ge<sub>6</sub> [Cardoso 2001].

atom	site	$x$	$y$	$z$	$U_{11}$	$U_{22}=U_{33}$	$U_{23}$	$U_{13}$ = $U_{12}$	$U_{eq}$
Yb	8c	1/4	1/4	1/4	46.7(2)	$U_{11}$	16.4(6)	$U_{23}$	46.7(2)
Rh1	2a	0	0	0	35.3(3)	$U_{11}$	0	0	35.3(3)
Rh2	12d	1/4	0	1/2	22.4(3)	29.2(2)	0	0	26.9(2)
Ge	12e	0.31769(9)	0	0	43.6(4)	38.7(2)	0	0	40.3(2)

Batch no. 55039 was dedicated to grow the alloy YbRh<sub>2</sub>GeSi, corresponding to a 50% substitution of Si by Ge in YbRh<sub>2</sub>Si<sub>2</sub>. Also this attempt to grow the 1-2-2 phase failed and instead single crystals of Yb<sub>4</sub>Rh<sub>7</sub>Ge<sub>6</sub> were obtained. This batch had several crystals of similar shape as the other batches and additional some needle-shaped crystals which contained Si as well. EDAX analysis showed the main phase (largest crystals) to be again Yb<sub>4</sub>Rh<sub>7</sub>Ge<sub>6</sub>. The foreign phases are small single crystals of germanium or silicon and ternary Yb-Rh-Ge phases with a very small amount of the desired, but partially oxidised, YbRh<sub>2</sub>GeSi phase, which sits on the surface of some crystals.

## 5.2 Physical properties

An investigation of the physical properties of Yb<sub>4</sub>Rh<sub>7</sub>Ge<sub>6</sub> was performed by means of susceptibility, resistivity and specific-heat measurements. The susceptibility was measured in an MPMS-SQUID magnetometer, whereas the resistivity and the specific heat were determined in a commercial PPMS equipment using an ac four-contact technique and a relaxation method, respectively. Additional resistivity and susceptibility data down to 20 mK were obtained in a dilution refrigerator.

## 5.2.1 Magnetic properties: susceptibility and magnetisation

For the susceptibility measurement a sample of  $m_s = 102$  mg was introduced and fixed into the non-coloured-plastic straw of the SQUID. A field of 0.01 T was applied to check the SQUID response and to perform the centring of the sample. The complete measurement was performed with applied fields of 1 T and 0.1 T. Below room temperature, the susceptibility  $\chi(T)$  (fig. 5.5) follows nicely a Curie-Weiss law with an effective moment  $\mu_{\text{eff}} = 4.5 \mu_B/\text{Yb}$  very close to the value expected for Yb<sup>3+</sup>.

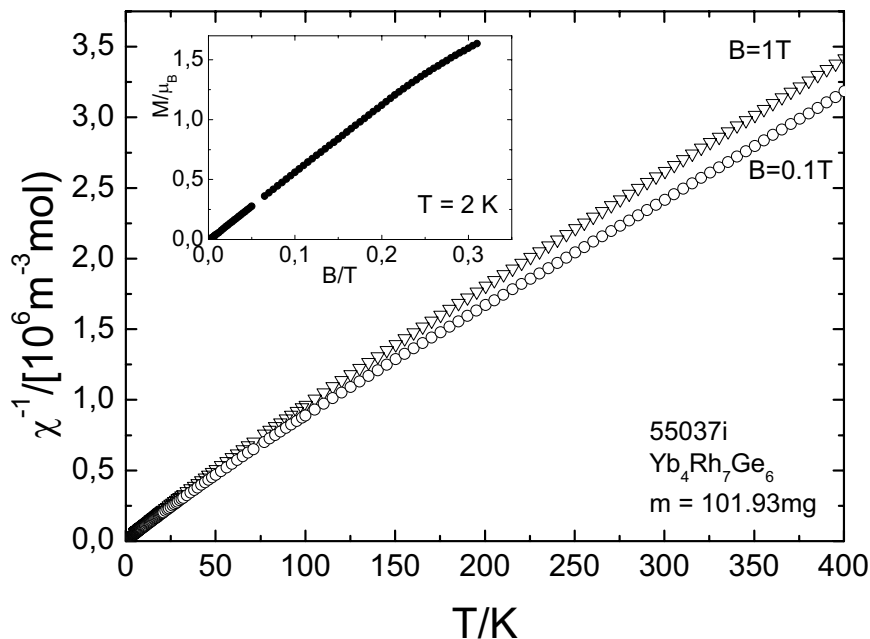


**Figure 5.5:** Inverse susceptibility of Yb<sub>4</sub>Rh<sub>7</sub>Ge<sub>6</sub> versus temperature for two different fields of  $B = 1$  T and  $B = 0.1$  T. The slope gives an effective moment of  $\mu_{\text{eff}} = 4.5 \mu_B/\text{Yb}$ . The slight difference between the results at  $B = 1$  T and  $B = 0.1$  T is likely due to the effect of very weak ferromagnetic impurities in the sample or the sample holder. The inset shows the magnetization curve at  $T = 2$  K.

The Weiss temperature is rather small with a value of  $\theta = -25$  K. Below 50 K,  $1/\chi(T)$  shows a slight curvature to a smaller effective moment  $\mu_{\text{eff}}$  and a smaller Weiss temperature  $\theta$ . While the curvature is very likely due to CEF effects, the low-temperature Weiss temperature  $\theta$  being almost zero indicates a very weak intersite magnetic exchange.

Magnetisation measurements (inset fig. 5.5) at constant temperatures revealed at 2 K a slight negative curvature above 0.2 T indicating the beginning of a saturation, while measurements at higher temperatures did not show a deviation from a linear field dependence.

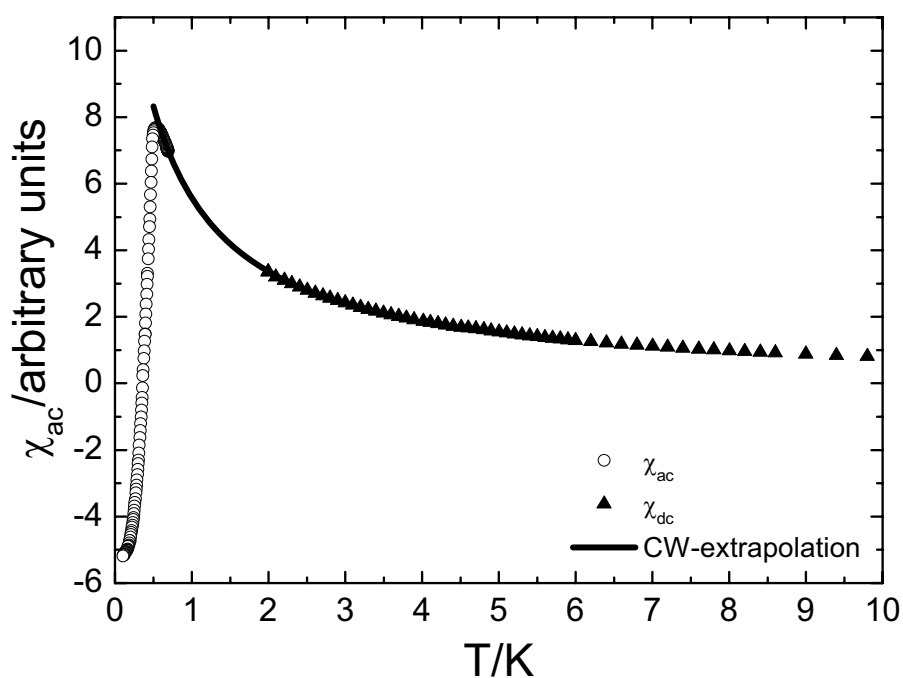


**Figure 5.6:** Low temperature susceptibility down to 100 mK. The low-temperature ( $< 0.6$  K) data were tentatively connected to the high-temperature ( $> 2$  K) data using a simple Curie-Weiss extrapolation. The negative  $\chi_{\text{ac}}$  values below the ordering temperature are an artifact of this very crude extrapolation.

We used the possibility to perform additional low-temperature ac-susceptibility measurements from 600 mK down to 100 mK (fig. 5.6) in the group of Prof. M. Lang (physical institute at the University of Frankfurt) by Katarina Removic-Langer for testing her cryostat. Because of technical problems measurements up to higher temperatures were not possible. A sharp maximum is visible around 500 mK, which evidences magnetic ordering. Below this transition temperature a clear decrease of the susceptibility evidences this phase transition to be an antiferromagnetic one. This temperature is equivalent with the temperature of the anomaly seen in specific-heat data (see 5.2.3) and low-temperature resistivity (fig. 5.8).

## 5.2.2 Resistivity

For resistivity measurements the sample was glued on the resistivity puck and the contacts were placed in such a way, that the current flows in [100] direction. The temperature dependence of the resistivity  $\rho(T)$  shows the behaviour of a classical metal, with a linear  $T$  dependence at high temperatures merging in a constant value at low temperatures (fig. 5.7). The absence of Kondo behaviour in  $\rho(T)$ , in connection with the observed  $\mu_{\text{eff}}$ , proves that the Yb ion is in a stable trivalent state. The resistivity ratio is rather small, of the order of 2, indicating some lattice defects. These defects are probably due to a non-stoichiometric Rh:Ge ratio, since the Rh:Ge ratio in the melt used for the crystal growth was certainly far from the optimal value.

Low-temperature resistivity data down to 20 mK are shown in fig. 5.8 in zero field and applied magnetic field up to 3 T. This measurement was performed in a dilution refrigerator by Franziska Weickert.

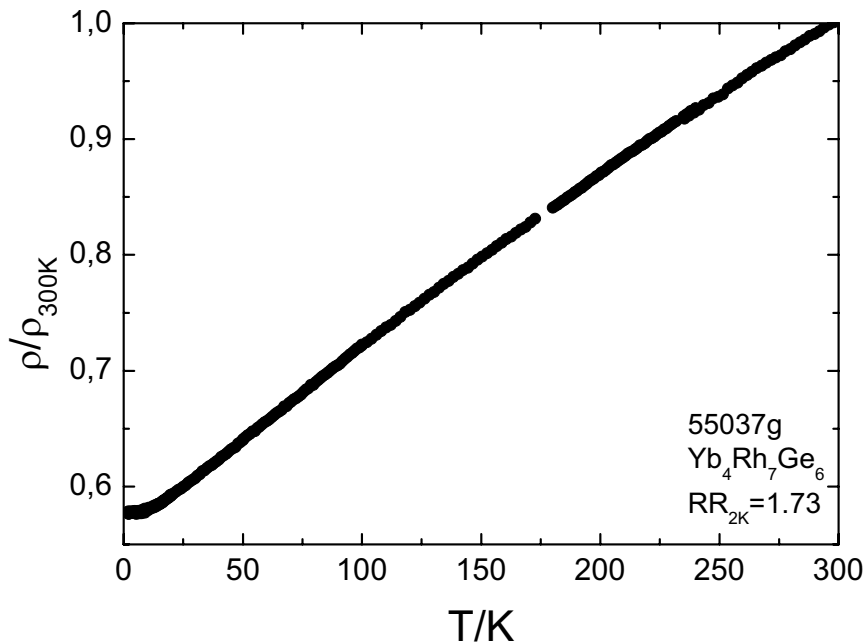


**Figure 5.7:** Normalized resistivity of Yb<sub>4</sub>Rh<sub>7</sub>Ge<sub>6</sub> versus temperature in the temperature range between 2 and 300 K.

The current flows here parallel to the *a* axis and the magnetic field was applied parallel to [011]. The temperature dependence of the resistivity shows a kink at  $T_m = 0.5$  K with a decrease of  $\rho(T)$  below  $T_m$ , as expected for a magnetic transition. Further on, the field dependence of  $\rho(T)$  reveals a decrease of  $T_m$  with increasing magnetic field as expected for an antiferromagnetic transition. The kink has disappeared at  $B = 0.75$  T, suggesting a change from an antiferromagnetic state to the field-aligned state between 0.5 T and 0.75 T. This is also evidenced by the magnetoresistance (fig. 5.9), where the  $\rho(B)$  curve for  $T < T_m$  merges with the  $\rho(B)$  curves for  $T = 0.55$  K and  $T = 0.7$  K above 0.7 T, while they lie significantly below for  $B < 0.7$  T. The positive magnetoresistance observed in the investigated B-T range corresponds to the behaviour expected for a normal metal.

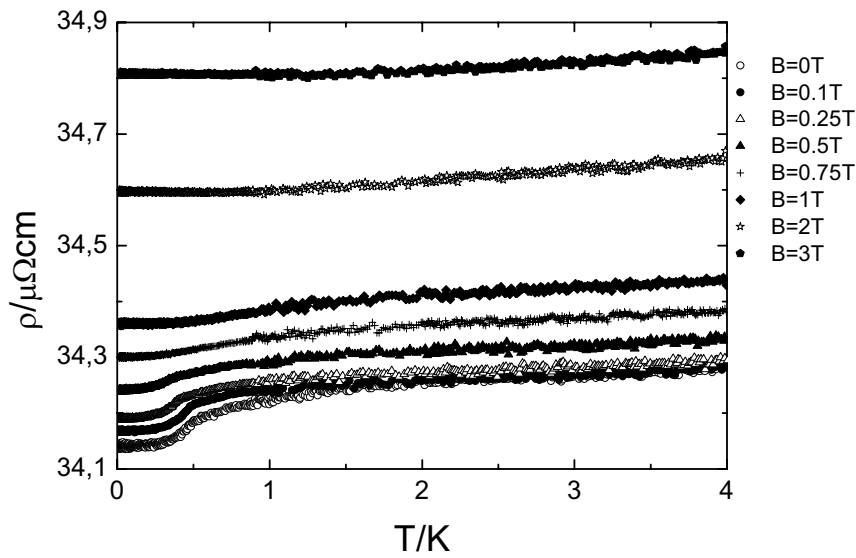


**Figure 5.8:** Temperature dependence of the resistivity down to 20 mK for several magnetic fields applied parallel to  $[011]$  obtained in a dilution refrigerator by F. Weickert.

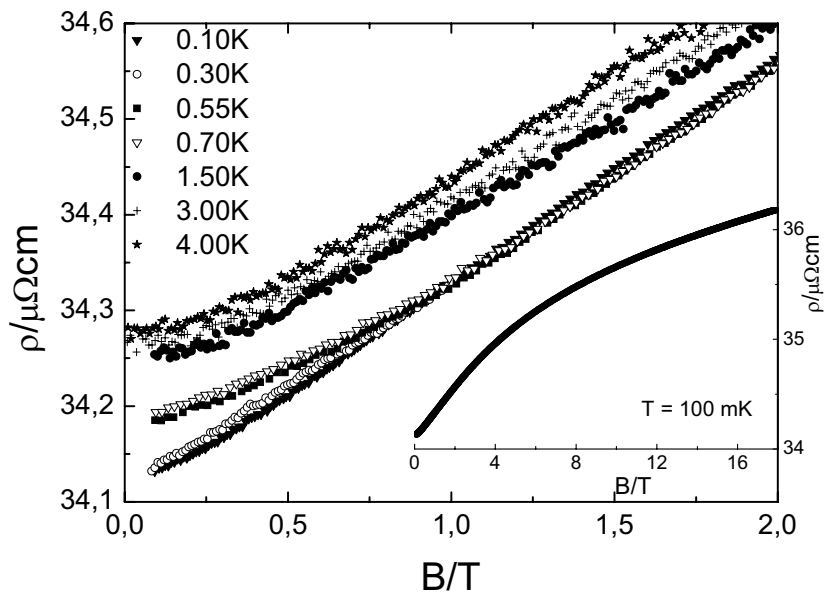


**Figure 5.9:** Magneto-resistance at temperatures between 0.1 and 4 K.

From those measurements a B-T phase diagram can be drawn as shown in fig. 5.10. It corresponds to that expected for a simple antiferromagnetic state.

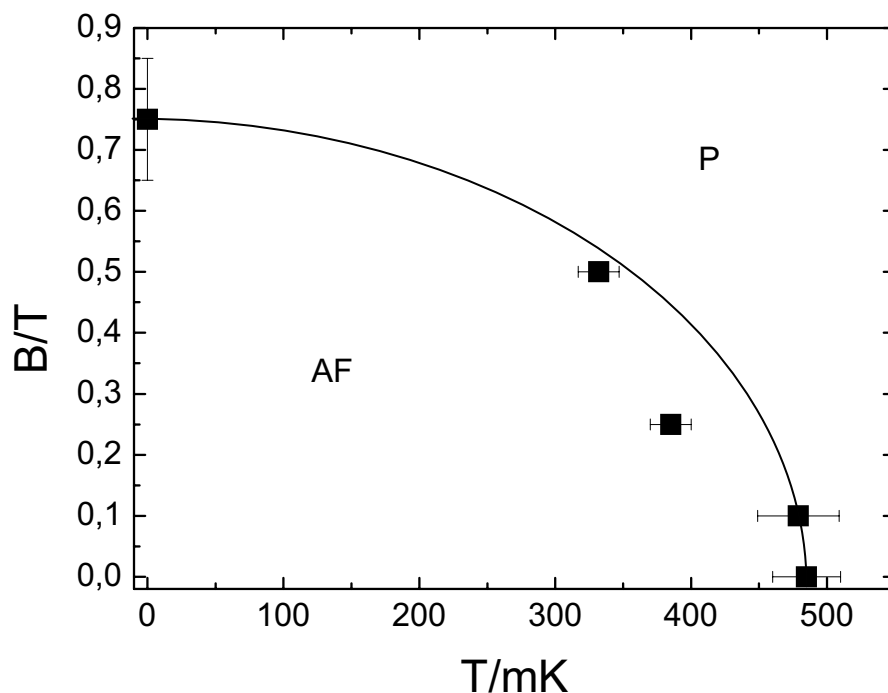


**Figure 5.10:** *B-T phase diagram obtained from low-temperature resistivity measurements in applied magnetic field parallel to [011]. The line is a guide to the eye.*

### 5.2.3 Anomalous specific heat and entropy

The mass of the single-crystalline sample for the specific-heat measurement was  $m = 5.76$  mg. Before starting the measurement, only the sample holder with grease was measured to allow an exact subtraction of the addenda.

The specific-heat data were measured in the temperature range from 50 down to 2 K with the  $^4\text{He}$ -system of the PPMS and from 4 K down to 350 mK with the  $^3\text{He}$ -system. Between 4 and 2 K both data sets overlap. At higher temperature (inset of figure 5.11) the specific heat decreases

continuously with decreasing temperature as expected, because  $C_p$  is dominated by the phonon contribution. The dominant feature in the low temperature specific heat (main part of figure 5.11) is a pronounced and sharp anomaly at  $T_m = 0.49$  K (fig. 5.11). The peak value of  $C$  at  $T_m$ ,  $C_{T_m} = 12$  J/(molYb)K is very close to the value expected for a magnetic mean-field transition for a CEF doublet ground state [Besnus 1992].

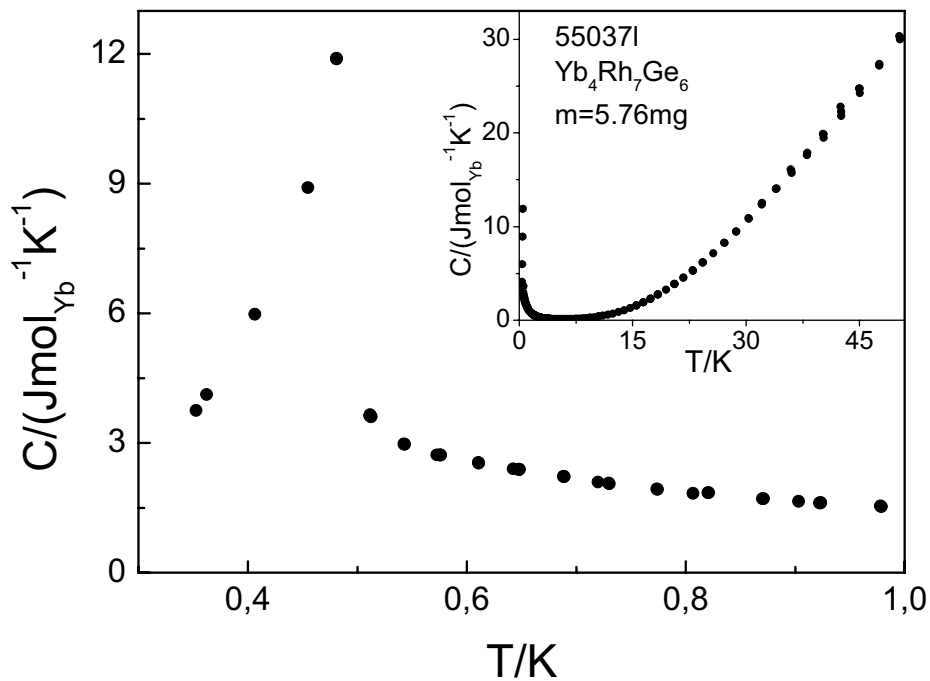


**Figure 5.11:** *Specific-heat data of  $\text{Yb}_4\text{Rh}_7\text{Ge}_6$  in the temperature range from 50 K down to 350 mK (inset). A sharp anomaly around 490 mK is visible in the low-temperature region.*

The power law of  $C(T)$  below  $T_m$  as well as the value of the Sommerfeld coefficient could not be determined, because the lowest temperature limit of the  $C(T)$  data are too close to  $T_m$ . Because of the low  $T_m$  value, the tail in  $C(T)$  above  $T_m$  due to short-range magnetic correlations can be observed very clearly up to  $T \cong 5$  K, one order of magnitude larger than  $T_m$ .  $C(T)$



decreases as  $T^{-1.7}$  in the range  $1 \text{ K} < T < 5 \text{ K}$ , while close to  $T_m$  the exponent for a power law  $(T-T_m)^n$  is much smaller,  $n \cong 0.35$ .

By integrating  $C(T)/T$  it is possible to determine the temperature dependence of the entropy  $S(T)$  (fig. 5.12). The data were not corrected for the phonon contribution since this contribution is negligible for  $T < 5 \text{ K}$ . The entropy  $S(T)$  at the lowest temperature of the measurements was estimated by extrapolating  $C/T$  smoothly to  $T = 0$ . Above  $1 \text{ K}$ ,  $S(T)$  levels off at a value very close to  $R\ln 2$ , indicating that the CEF ground state is a doublet well separated from the first excited state. This is in accordance with the local symmetry of ytterbium in this structure. Although the structure is cubic, the local symmetry of the ytterbium site is lower (hexagonal) ( $m3m$ ). Thus one expects a splitting of the  $J = 7/2$  state into 4 doublets.

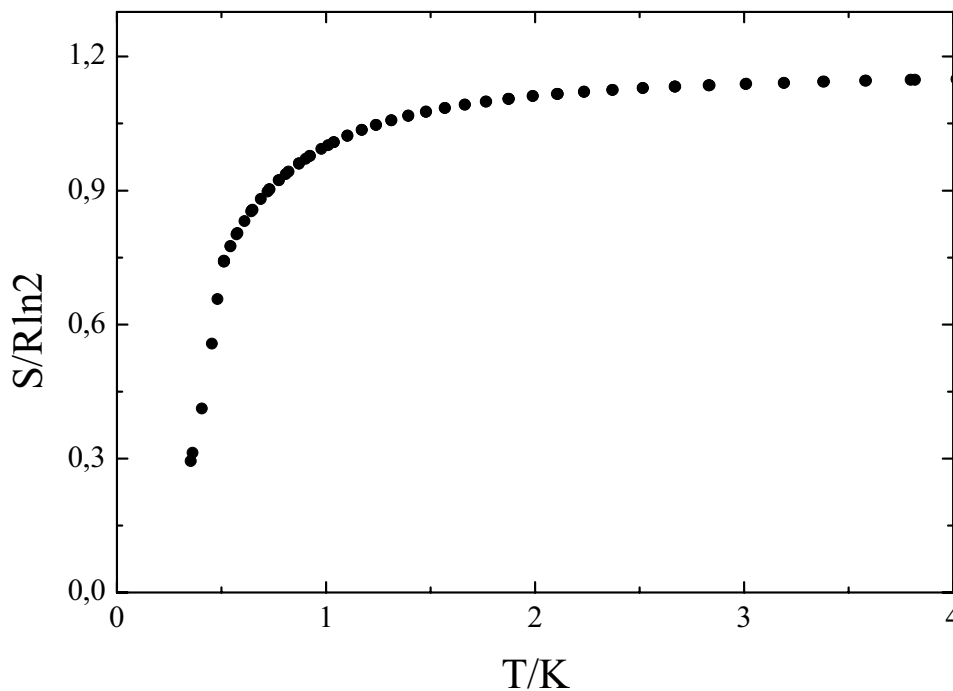


**Figure 5.12:** *The entropy calculated from specific-heat data of  $\text{Yb}_4\text{Rh}_7\text{Ge}_6$ , gets close to the value of  $R\ln 2$ , which indicates a doublet ground state.*

## 5.3 Discussion and comparison with other Yb-based compounds

The result of the susceptibility, the low-temperature resistivity and the specific-heat data point to a transition into an antiferromagnetic state at  $T_m$ . The observation of a stable Yb<sup>3+</sup> state in Yb<sub>4</sub>Rh<sub>7</sub>Ge<sub>6</sub> is a little bit surprising. The trivalent Yb has a smaller volume compared to divalent Yb. Pressure favours the trivalent state, whereas negative (chemical) pressure favours the divalent state. Since YbRh<sub>2</sub>Si<sub>2</sub> shows evidence for a quite strong Kondo type interaction and thus for an instability of the Yb<sup>3+</sup> state, one expects the Yb<sup>3+</sup> state to be even more unstable in the larger YbRh<sub>2</sub>Ge<sub>2</sub>, and thus in Yb<sub>4</sub>Rh<sub>7</sub>Ge<sub>6</sub> too, as the chemical composition of both compounds is similar. Instead, the results point to a very stable Yb<sup>3+</sup> state in Yb<sub>4</sub>Rh<sub>7</sub>Ge<sub>6</sub>. This can be explained by comparing the distances from Yb to its nearest ligands in both compounds (fig. 5.13). The hybridisation between the f ion and the ligand ions is known to be the dominant factor which determines the valence state of the f ion [Koelling 1985, Schank 1994]. The number of rhodium or germanium nearest neighbours is smaller in the Yb<sub>4</sub>Rh<sub>7</sub>Ge<sub>6</sub> (fig. 5.4 or inset fig. 5.13) structure than in the YbRh<sub>2</sub>Ge<sub>2</sub> (inset fig. 5.13) structure (6 against 8). However, the distances are significantly smaller, 2.918 Å compared to 3.234 Å for the ytterbium-rhodium distance and 2.937 Å compared to 3.121 Å for the Ytterbium-Germanium-distance. This strong reduction of the ytterbium ligand distances should lead to a much stronger hybridisation of the Yb states with the ligand states in Yb<sub>4</sub>Rh<sub>7</sub>Ge<sub>6</sub>, which support the transfer of an electron from the f shell to the d shell upon going from the free Yb<sup>2+</sup> ion to the Yb<sup>3+</sup> ion in the compound [Johansson 1987].

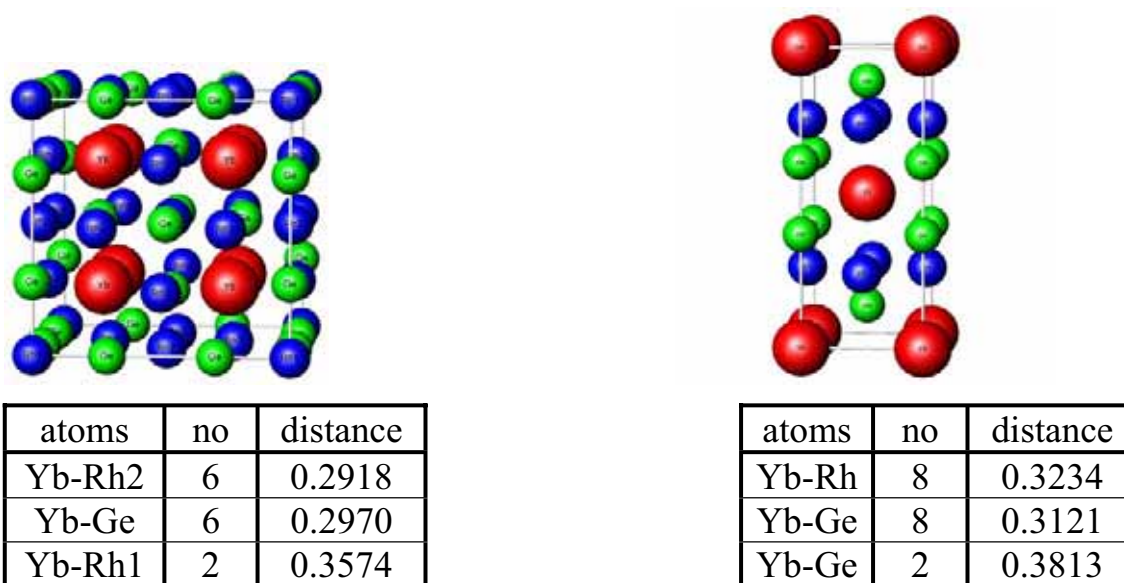


**Figure 5.13:** Comparison of the distance from Yb to its nearest ligands in the structure of  $\text{Yb}_4\text{Rh}_7\text{Ge}_6$  (cubic) and  $\text{YbRh}_2\text{Ge}_2$  (tetragonal).

## 5.4 Summary

In summary, preparation of  $\text{YbRh}_2\text{Ge}_2$  single crystals failed and instead single crystals of  $\text{Yb}_4\text{Rh}_7\text{Ge}_6$  were obtained. The investigation of their susceptibility, resistivity and specific heat was shown and discussed here. The results evidence a normal metal with a phase transition around  $T = 0.49$  K. Susceptibility evidences a stable  $\text{Yb}^{3+}$  state, which orders presumably antiferromagnetically at 0.49 K. Specific heat measurements and the resulting entropy show that the CEF ground-state doublet is well separated from the excited states. The stable  $\text{Yb}^{3+}$  state likely results from the very short ytterbium-rhodium and ytterbium-germanium nearest-neighbour distances within the  $\text{Yb}_4\text{Rh}_7\text{Ge}_6$  structure.

## 6 Summary

In this thesis we present and discuss the crystal growth and investigation of the physical properties of three different Yb-based compounds.

First we synthesised polycrystals and then grew single crystals of  $\text{YbFe}_2\text{Ge}_2$  and  $\text{LuFe}_2\text{Ge}_2$ . The analysis of their physical properties revealed the presence of a paramagnetic Fe moment of  $\sim 3 \mu_B/\text{Fe}$  at high temperatures in both compounds, which strongly contrasts the well-established non-magnetic behavior of Co and Fe in the  $\text{RCO}_2\text{Si}_2$ ,  $\text{RCO}_2\text{Ge}_2$  and  $\text{RFe}_2\text{Si}_2$  compound series. Additionally, a phase transition at  $T_0 \approx 9 \text{ K}$  appears in  $\text{LuFe}_2\text{Ge}_2$ , which likely corresponds to antiferromagnetic ordering of the Fe moments. The observation of a paramagnetic Fe moment is discussed in the context of results from LDA calculations. Our results in  $\text{YbFe}_2\text{Ge}_2$  further indicate a weakly intermediate-valent Yb state, at the border to the Kondo regime with a comparatively low characteristic  $4f$  energy of  $\sim 80 \text{ K}$ . This corresponds to a valence close to but less than 3. At low temperatures we observe a heavy-fermion behaviour with a moderately enhanced Sommerfeld coefficient,  $\gamma = 200 \text{ mJmol}^{-1}\text{K}^{-2}$ .

For  $\text{YbRh}_2\text{Si}_2$  we developed a growth procedure which resulted in reproducible high-quality single crystals, as evidenced by a residual resistivity ratio in between 55 and 65. Our present investigations were focussed on the determination of the main energy scales of the  $4f$  electrons and the study of the behaviour across the QCP using  $\text{Yb}_{1-x}\text{La}_x\text{Rh}_2\text{Si}_2$ . For the determination of the Kondo temperature and of the excitation energies of the crystal-field levels, the contribution  $C_{4f}$  of the  $4f$  electrons to the specific heat was estimated and analysed. The presence of a local maximum in  $C_{4f}$  between 40 and 80 K was confirmed. Inelastic neutron data give precise results for the two upper CEF levels at 25 and 42 meV, but the position obtained for the first excited CEF level at  $E_1 = 17 \text{ meV}$  is not very reliable. We analysed  $C_{4f}$  more precisely using the combination of a simple CEF model and the theoretical prediction for the single-ion Kondo model. This

analysis places the first excited CEF level at an energy  $(15 \pm 2)$  meV, in good agreement with the neutron data, and therefore allows to settle the CEF energy scheme. By using the single-ion Kondo model and a complementary analysis of the temperature dependence of the entropy we thoroughly determined the Kondo energy scale to  $T_K = 17$  K, which is also in agreement with the width of the quasielastic line observed in inelastic neutron scattering.

A second important part of this thesis was the investigation of the behaviour across the QCP in  $\text{Yb}_{1-x}\text{La}_x\text{Rh}_2\text{Si}_2$ . Single crystals with  $x = 0.05, 0.1, 0.2$  and  $0.3$  were grown from In flux, using the sealed Ta-crucible technique. Their resistivity, specific heat and susceptibility were investigated and analysed. The residual resistivity increases linearly with the La content, indicating a statistical replacement of Yb by La. From the analysis of the temperature dependence of the  $4f$  entropy, we deduce a monotonous increase of the Kondo temperature,  $T_K$ , from  $T_K = 17$  K in  $\text{YbRh}_2\text{Si}_2$  to  $T_K = 50$  K in  $\text{Yb}_{0.7}\text{La}_{0.3}\text{Rh}_2\text{Si}_2$ , as expected from the chemical negative pressure due to the lattice expansion. The antiferromagnetic order gets suppressed, and we did not observe any evidence for the magnetic order even in the  $x = 0.05$  sample down to 17 mK. In contrast  $C/T$  of the  $x = 0.05$  and  $x = 0.1$  samples increases logarithmically down to 50 mK, while in the samples with  $x \geq 0.15$ ,  $C/T$  levels off at a temperature-independent value at low  $T$ , evidencing the formation of a heavy Fermi-liquid ground state. The temperature dependence of the resistivity at low temperatures shows a power law with an exponent increasing with  $x$  for  $0 \leq x \leq 0.15$  from  $n = 1$  in pure  $\text{YbRh}_2\text{Si}_2$  (above  $T_N$ ) to  $n = 2$  for  $x \geq 0.15$ , as expected for a Fermi liquid. All the investigations of the  $\text{Yb}_{1-x}\text{La}_x\text{Rh}_2\text{Si}_2$  samples indicate an increase of  $T_K$  with  $x$  due to the lattice expansion, which leads to a suppression of the antiferromagnetic state at a QCP located in the region  $0.05 < x < 0.10$ . Accordingly the NFL behaviour extends down to the lowest investigated temperature for  $0.05 \leq x \leq 0.10$ , but for  $x \geq 0.15$  it is replaced by a heavy Fermi-liquid state.

Very surprising is the Yb ESR signal observed in  $\text{YbRh}_2\text{Si}_2$ , which was the first case where the ESR-line of the Kondo ion has been seen in a dense Kondo system. In the La-doped samples, the ESR line width scales with the residual resistivity, suggesting that the bottle neck effect plays an important role for the observability of the ESR line.

The preparation of  $\text{YbRh}_2\text{Ge}_2$  single crystals failed and instead single crystals of  $\text{Yb}_4\text{Rh}_7\text{Ge}_6$  were obtained. The Curie-Weiss behaviour of the susceptibility with an effective moment corresponding to that expected for free  $\text{Yb}^{3+}$  and a small Curie-Weiss temperature indicate a stable trivalent  $\text{Yb}^{3+}$  state. A large anomaly in the specific heat at  $T_m = 0.49$  K marks a transition to an ordered state. The field dependence of the associated weak anomaly in  $\rho(T)$  as well as the strong decrease of  $\chi_{ac}$  below  $T_m$  show that this ordering is of antiferromagnetic type. From the temperature dependence of the entropy a CEF ground-state doublet well separated from the excited states is deduced. The stable  $\text{Yb}^{3+}$  state likely results from the very short ytterbium-rhodium and ytterbium-germanium nearest-neighbour distances in the  $\text{Yb}_4\text{Rh}_7\text{Ge}_6$  structure.



# Bibliography

- [Alami-Yadri 1997] K. Alami-Yadri, Ph.D. Thesis, University of Geneva, 1997
- [Ashcroft 1976] N. W. Ashcroft and N. D. Mermin *Solid State Physics*. Harcourt College Publisher, Orlando 1976
- [Aviani 1997] I. Aviani, M. Miljak, V. Zlatic, D. Finsterbusch, W. Assmus, B. Lüthi, *Physica B* **230-232** (1997) 275-278
- [Avila 2004] M. A. Avila, S. L. Bud'ko, P. C. Canfield, *Journal of Magnetism and Magnetic Materials* **270**, (2004), p. 51-76
- [Baberschke 1980] K. Baberschke and E. Tsang, *Physical Review Letters* **45** (1980), 1512
- [Bara 1990] J. J. Bara, H. U. Hryniewicz, A. Mylos, A. Szytula, *Journal of the less common metals*, **161** (1990), p. 185-192
- [Barnes 1981] S. E. Barnes, *Advances in Physics* **30** (1981), no. 6, p. 801-938
- [Berisso 2002] M. Gómez, P. Pedrazzini, J. G. Sereni, O. Trovarelli, C. Geibel, F. Steglich, *The European Physical Journal B* **30** (2002), p. 343-349
- [Bernhoeft 2001] N. Bernhoeft, *Journal of Physics: Condensed Matter* **13** (2001), p. R771-R816
- [Besnus 1992] M. J. Besnus, A. Braghta, N. Hamdaoui, A. Meyer, *Journal of Magnetism and Magnetic Materials* **104-107** (1992), p. 1385-1386
- [Bonville 1985] P. Bonville and J. A. Hodges, *Journal of Magnetism and Magnetic Materials* **47-48** (1985), p. 152-154



- [Canfield 1992] P. C. Canfield and Z. Fisk, *Philosophical Magazine B* **65** (1992), no. 6, p. 1117-1123
- [Cardoso 2001] R. Cardoso, private communication (2001)
- [Cardoso 2005] R. Cardoso, private communication (2005)
- [Caroca 2005] N. Caroca-Canales, private communication (2005)
- [Chefki1998] M. Chefki, M. M. Abd-Elmeguid, H. Micklitz, C. Huhnt, W. Schlabit, *Physical Review Letters* **80** (1998), no 4, p. 802-805
- [Coleman 1999] P. Coleman, *Physica B* **259-261** (1999), p. 353-358
- [Coleman 2002] P. Coleman and C. Pepin, *Physica B* **312-313** (2002), p. 383-389
- [Custers 2001] J. Custers, P. Gegenwart, C. Geibel, F. Steglich, T. Tayama, O. Trovarelli, N. Harrison, *Acta Physica Polonica B* **32** (2001), 10, p. 3211-3217
- [Custers 2003] J. Custers, P. Gegenwart, H. Wilhelm, K. Neumaier, Y. Tokiwa, O. Trovarelli, C. Geibel, F. Steglich, C. Pepin, P. Coleman, *Nature* **424** (2003), p. 524-527
- [Custers 2003] private communication
- [Custers 2004] J. Custers, *Quantum-Critical Behavior in the Heavy-Fermion Compounds YbRh<sub>2</sub>Si<sub>2</sub> and CeIn<sub>3-x</sub>Sn<sub>x</sub>* Technische Universität Dresden, Dissertation 2004
- [Desgranges 1982] H.-U. Desgranges and K. D. Schotte, *Physics Letters* **91A** (1982), no. 5, p. 240-242
- [Desgranges 1985] H.-U. Desgranges and J. W. Rasul, *Physical Review B* **32** (1985), no. 9, p. 6100-6103 Rapid Communications
- [Dhar 1987] S. K. Dhar and E. V. Sampathkumaran, *Physics Letters A* **121** (1987), no 8, 9, p. 454-456

- [Dionicio 2005] G. Dionicio, H. Wilhelm, G. Sparn, J. Ferstl, C. Geibel, F. Steglich, *Physica B* **359-361** (2005), p. 50-52
- [Doniach 1977] S. Doniach, *Physica B* **91** (1977), 07, p. 231-234
- [Elschner 1997] B. Elschner and A. Loidl, in *Handbook on the Physics and Chemistry of Rare Earths*, vol. 24, edited by K. A. Gschneider, Jr. and L. Eyring (Elsevier Science B. V., Amsterdam, 1997), chapter 162
- [Felner1975]: I. Felner, I. Mayer, A. Grill, M. Schieber, *Solid State Communications* **16** (1975), p. 1005
- [Felner 1986] I. Felner and I. Nowik *Physical Review B* **33** (1986), no. 1, p. 617-619
- [Ferstl 2003] J. Ferstl et al., Poster at the SCES 2003, Krakov, to be published
- [Fulde 1997] P. Fulde *Physica B* **230-232** (1997), p. 1-8
- [Fisk 1989] Z. Fisk and J. P. Remeika, *Handbook on the Physics and Chemistry of Rare Earths*, vol. 12 edited by K. A. Gschneider, Jr. and L. Eyring, Elsevier Science Publishers B. V. (1989)
- [Francois 1985] M. Francois, G. Venturini, J. F. Marêché, B. Malaman, B. Roques, *Journal of the less common metals* **113** (1985), p. 231-237
- [Gegenwart 2002] P. Gegenwart, J. Custers, C. Geibel, K. Neumaier, T. Tayama, K. Kenya, O. Trovarelli, F. Steglich, *Physical Review Letters* **89** (2002), no. 5, p. 056402-1-4
- [Haen 1996] P. Haen, F. Mallmann, M.-J. Besnus, J.-P. Kappler, F. Bourdarot, P. Burlet, T. Fukuhara, *Journal of the Physical Society Japan* **65** (1996), suppl. B, p. 16-26

- [Hansen 1958] M. Hansen, *Constitution of Binary Alloys* (McGraw-Hill, New York) (1958)
- [Hertz 1976] J. A. Hertz, *Physical Review B* **14** (1976), 08, no. 3, p. 1165-1184
- [Hlubina 1995] A. R. Hlubina, T. M. Rice, *Physical Review B* **51** (1995), 04, no. 14, p. 9253-9260
- [Huhnt 1998] C. Huhnt, W. Schlabitz, A. Wurth, A. Mewis, M. Reehuis, *Physica B* **252** (1998), p. 44-54
- [Ishida 2002] K. Ishida, K. Okamoto, Y. Kawasaki, Y. Kitaoka, O. Trovarelli, C. Geibel, F. Steglich, *Physical Review Letters* **89** (2002), 09, no. 10, p. 107202-1-4
- [Ishida 2003a] K. Ishida, O.O. Bernal, D. E. MacLaughlin, W. Higemoto, A. Koda, K. Onishi, R. Kadono, J. Ferstl, C. Geibel, F. Steglich, *KEK annual report* (2003), p. S02-16
- [Ishida 2003b] K. Ishida, D. E. MacLaughlin, K. Okamoto, Y. Kawasaki, Y. Kitaoka, G. J. Nieuwenhuys, O. O. Bernal, A. Koda, W. Higemoto, R. Kadono, C. Geibel, F. Steglich, *Physica B* **329-333** (2003), 05, p. 589-590
- [Ishida 2003c] K. Ishida, D. E. MacLaughlin, O.O. Bernal, R. H. Hefner, G. J. Nieuwenhuys, O. Trovarelli, C. Geibel, F. Steglich, *Physica B* **326** (2003), 02, no. 1-4, p. 403-405
- [Ishida 2003d] K. Ishida, D. E. MacLaughlin, Ben-Li Young, K. Okamoto, Y. Kawasaki, Y. Kitaoka, G. J. Nieuwenhuys, R. H. Hefner, O.O. Bernal, W. Higemoto, A. Koda, R. Kadono, O. Trovarelli, C. Geibel, F. Steglich, *Physical Review B* **68** (2003) p. 184401-1-14

- [Johansson 1987] B. Johansson, N. Mårtensson, in *Handbook on the Physics and Chemistry of Rare Earth*, vol. 10, edited by K. A. Gschneider, L. Eyring, S. Hufner, (1987), p. 361
- [Julian 1996] S. R. Julian, C. Pfleiderer, F. M. Grosche, N. D. Mathur, G. J. McMullan, A. J. Diver, I. R. Walker, G. G. Lonzarich, *Journal of Physics: Condensed Matter* **8** (1996), p. 9675-9688
- [Knebel 2001] G. Knebel, E. Hassinger, G. Lapertot, P. G. Niklowitz, J. P. Sanchez, J. Flouquet, *Journal of Physics: Condensed Matter* **13** (2001), p. 10935-10946
- [Kimura 1997] Shin-ichi Kimura, A. Ochiai, T. Suzuki, *Physica B* **230-232** (1997) p. 705-707
- [Koelling 1985] D.D. Koelling, B.D. Dunlap, G.W. Crabtree, *Physical Review B* **31** (1985), no. 8, p. 4966-4971
- [Kojima 1990] K. Kojima, Y. Nakai, T. Suzuki, H. Asano, F. Izumi, T. Fujita, T. Hihara, *Journal of the Physical Society Japan* **59** (1990), p. 792-795
- [Kondo 1964] J. Kondo, *Theoretical Physics* **32** (1964), 07, no. 1, p. 37-49
- [Kuramoto 1987] Y. Kuramoto, *Solid State Communication* **63** (1987), p. 467
- [K. v. Nidda 1998] H.-A. Krug von Nidda, A. Schütz, M. Heil, B. Elschner, *Physical Review B* **57** (1998), no. 22, p. 14344-14351
- [Küchler 2003] R. Küchler, N. Oeschler, P. Gegenwart, T. Chichorek, K. Neumaier, O. Tegus, C. Geibel, J. A. Mydosh, F. Steglich, L. Zhu, Q. Si, *Physical Review Letters* **91** (2003) 08, no.6, p. 066405-1-4
- [Küchler 2005] Robert Küchler, *Thermische Ausdehnung und divergierendes Grüneisenverhältnis in Schwere*

- Fermionen-Systemen*, Technische Universität Dresden, Dissertation 2005. – ISBN 3-86537-658-4
- [Landau 1957] L. D. Landau, Soviet Physics JETP **3** (1957), p. 920
- [Larrea 2006] J. Larrea J., M. B. Fontes, E. M. Baggio-Saitovitch, J. Plessel, M. M. Abd-Elmeguid, J. Ferstl, C. Geibel, A. Pereira, A. Jornada, M. A. Continentino, *Physical Review B* **74** (2006), p. 140406(R)-1-4
- [Löhneysen 1996] H. v. Löhneysen, M. Sieck, O. Stockert, M. Waffenschmidt, *Physica B* **223-224** (1996), p. 471-474
- [Löhneysen 1999] H. v. Löhneysen, *Journal of Magnetism and Magnetic Materials* **200** (1999) p. 532-551
- [Mair 1999] S. Mair, H.-A. Krug von Nidda, M. Lohmann, A. Loidl, *Physical Review B* **60** (1999), no. 24, p. 16409-16414
- [Massalski 1986a] *Binary Alloy Phase Diagrams*, vol. 2, edited by T. B. Massalski, J. L. Murray, L. H. Bennett, H. Baker (American Society for Metals, Metals Park, Ohio, 1986), p. 1219 – ISBN 0-87170-263-0
- [Massalski 1986b] *Binary Alloy Phase Diagrams*, vol. 2, edited by T. B. Massalski, J. L. Murray, L. H. Bennett, H. Baker (American Society for Metals, Metals Park, Ohio, 1986), p. 1399 – ISBN 0-87170-263-0
- [Massalski 1986c] *Binary Alloy Phase Diagrams*, vol. 2, edited by T. B. Massalski, J. L. Murray, L. H. Bennett, H. Baker (American Society for Metals, Metals Park, Ohio, 1986), p. 1127 – ISBN 0-87170-263-0

- [Mathur 1998] N. D. Mathur, F. M. Grosche, S. R. Julian, I. R. Walker, D. M. Freye, R. K. W. Haselwimmer, G. G. Lonzarich, *Nature* **394** (1998), p. 39-43
- [Mattens 1977] W.C.M. Mattens, *Communications on Physics* **2** (1977), p. 147-150
- [Mederle 2001] S. Mederle, R. Borth, C. Geibel, F. M. Grosche, G. Sparn, O. Trovarelli, F. Steglich, *Journal of Magnetism and Magnetic Materials*, **226-230** (2001), p. 254-255
- [Mederle 2002a] S. Mederle, R. Borth, C. Geibel, F. M. Grosche, G. Sparn, O. Trovarelli, F. Steglich, *Journal of Physics: Condensed Matter* **14** (2002), p. 10731-10736
- [Mederle 2002b] S. Mederle *Der Einfluß von Druck und Substitution auf die Physik der Schwere-Fermionen-Systeme (UTh)Be<sub>13</sub> und YbRh<sub>2</sub>(SiGe)<sub>2</sub>*, Technische Universität Dresden, Dissertation 2002. – ISBN 3-8322-1335-X
- [Millis 1993] A. J. Millis, *Physical Review B* **48** (1993), 09, no. 10, p. 7183-7196
- [Moriya 1979] T. Moriya, *Journal of Magnetism and Magnetic Materials* **14** (1979), p. 1-46
- [Moriya 1995] T. Moriya, T. Takimoto, *Journal of the Physical Society of Japan* **64** (1995), 03, no. 3, p. 960-969
- [Moriya 2000] T. Moriya, K. Ueda, *Advances in Physics* **49** (2000), no. 5, p. 555-606
- [Morozkin 1997] A. V. Morozkin, Y. D. Seropegin, A.V. Griбанov, J. M. Barakatova, *Journal of Alloys and Compounds* **256** (1997), p. 175
- [Morozkin 1998] A. V. Morozkin, Y. D. Seropegin, A.V. Griбанov, I. A. Sviridov, J. M. Kurenbaeva, A. L.

- Kurenbaeva, *Journal of Alloys and Compounds* **264** (1998), p. 190
- [Murani 1983] A. P. Murani, *Physical Review B* **28** (1983) p. 2308-2311
- [Mushnikov 2003] N. V. Mushnikov, T. Goto, K. Yoshimura, W. Zhang, *Physica B* **334** (2003) 54-59
- [Nowik 1988] I. Nowik, I. Felner, J. Voiron, J. Beille, A. Najib, E. du Tremolet de Lacheisserie, G. Gratz, *Physical Review B* **37** (1988), no. 10, p. 5633-5638
- [Nowik 1997] I. Nowik, I. Felner, E.R. Bauminger, *Physical Review B* **55** (1997), p. 3033
- [Nowik 1995] I. Nowik, Y. Levy, I. Felner, E.R. Bauminger, *Journal of Magnetism and Magnetic Materials* **147** (1995), p. 373
- [Ochiai 1987] A. Ochiai, K. Takeuchi, N. Niitsuda, T. Suzuki, T. Kasuya, *Journal of Magnetism and Magnetic Materials* **63&64** (1987) p. 618-620
- [Oesterreicher 1977] H. Oesterreicher and F. T. Parker, *Physical Review B* **16** (1977), no. 11, p. 5009-5011
- [Palstra 1986] T.T. M. Palstra, G. Lu, A. A. Menovsky, G. J. Nieuwenhuya, P. H. Kess, J. A. Mydosh, *Physical Review Section B: Condensed Matter* **34** (7), 4566-4570 (1986)
- [Plessel 2002] J. Plessel, *Hochdruckuntersuchungen an Yb-Kondo-Gitter-Systemen in der Nähe einer magnetischen Instabilität*, Universität Köln, Dissertation 2002. – ISBN 3-89820-377-8
- [Plessel 2003] J. Plessel, M. M. Abd-Elmeguid, J. P. Sanchez, G. Knebel, O. Trovarelli, F. Steglich, *Physical Review B* **67** (2003), 05, p. 1800403(R)-1-4, - Rapid Communications

- [Radu 2005] M. T. Radu, *Thermodynamic Characterisation of Heavy Fermion Systems and Low Dimensional Quantum Magnets Near a Quantum Critical Point*, Technische Universität Dresden, Dissertation 2005
- [Rajan 1983] V. T. Rajan, *Physical Review Letters* **51** (1983), 07, no. 4, p. 308-311
- [Rams 1997] M. Rams, K. Krolas, P. Bonville, E. Alleno, C. Godart, D. Kaczorowski, F. Canepa, *Physical Review B* **56** (1997), no. 7, pp. 3690-6
- [Rosch 2000] A. Rosch, *Physica B* **280** (2000), p. 341-346
- [Rosner 2005] H. Rosner, private communication
- [Rossel 1987] C. Rossel, K. N. Yang, M. B. Maple, Z. Fisk, E. Zirnbiehl, J. D. Thompson *Physical Review B*, **35** (1987), no 4, p. 1914-1918
- [Rossi 1978] D. Rossi, R. Marazza, R. Ferro, *Journal of the Less Common Metals*, **58** (1978), p. 203-207
- [Rossi 1979] D. Rossi, R. Marazza, R. Ferro *Journal of the Less Common Metals*, vol. **66**, Issue 2, (1979) p. P17-P25
- [Sales 1976] B. C. Sales and R. Viswanathan, *Journal of Low Temperature Physics*, **23** (1976), p. 449-467
- [Sampath 1984] E. V. Sampathkumaran, K. H. Frank, G. Kalkowski, G. Kaindl *Physical Review B* **29** (1984), no 10, p. 5702-5707
- [Santa Barbara 1996] Proceedings of the International Conference on Non-Fermi Liquid Behaviour in Metals in Santa Barbara, USA (1996), *Journal of Physics: Condensed Matter* **8** (1996)
- [Sarraf 1998] J. L. Sarraf, A. P. Ramirez, T. W. Darling, F. Freibert, A. Migliori, C. D. Immer, Z. Fisk, Y. Uwatoko *Physical Review B* **58** (1998), no. 1, p. 409-413



- [Sarrazo 1999] J. L. Sarrazo, *Physica B* **259-261** (1999), p. 128-133
- [Schank 1994] C. Schank, U. Tegel, R. Henseleit, A. Grauel, G. Olesch, C. Geibel, G. Gordier, R. Kniep, F. Steglich, *Journal of Alloys and Compounds* **207&208** (1994), p. 333-336
- [Schlottmann 1993] P. Schlottmann, *Journal of Applied Physics* **73** (1993), p. 5412-5414
- [Schmidt 1997] B. Schmidt, P. Thalmeier, P. Fulde, *Physica B* **237-238** (1997) p. 221-223
- [Schröder 2000] A. Schröder, G. Aeppli, R. Coldea, M. Adams, O. Stockert, H. v. Löhneysen, E. Bucher, R. Ramazashvili, P. Coleman, *Nature* **407** (2000), p. 351-355
- [Seaman 1991] C. L. Seaman, M. B. Maple, B. W. Lee, S. Ghamaty, *Physical Review Letters* **67** (1991), no 20, p. 2882-2885
- [Sereni 1997] J. G. Sereni, C. Geibel, M. G.-Berisso, P. Hellmann, O. Trovarelli, F. Steglich, *Physica B*, **230-232** (1997), p. 580-582
- [Sereni 2005] J. G. Sereni, private communication (2005)
- [Shiba 1975] H. Shiba, *Progress of Theoretical Physics* **54** (1975), no. 4, p. 967- 981
- [Si 2004] Q. Si, cond-mat/0404303 (2004)
- [Si 2001] Q. Si, S. Rabello, K. Ingersent, J. L. Smith, *Nature* **413** (2000), 10, no. 6858, p. 804-808
- [Sichelschmidt 2003] J. Sichelschmidt, V. A. Ivanshin, J. Ferstl, C. Geibel, F. Steglich, *Physical Review Letters* **91** (2003), 10, no. 15, p. 156401-1-4
- [Steglich 1996] F. Steglich, P. Gegenwart, C. Geibel, R. Helfrich, P. Hellmann, M. Lang, A. Link, R. Modler, G. Sparn, N. Büttgen, A. Loidl, *Physica B* **223&224** (1996), p. 1-8

- [Steglich 2000] F. Steglich, P. Gegenwart, C. Geibel, P. Hinze, M. Lang, C. Langhammer, G. Sparn, O. Trovarelli, *Physica B* **280** (2000), p. 349-353
- [Steglich 2003] F. Steglich, N. K. Sato, N. Aso, P. Gegenwart, J. Custers, K. Neumaier, H. Wilhelm, C. Geibel, O. Trovarelli, *Physica B* **329-333** (2003), p. 441-445
- [Stewart 2001] G. R. Stewart, *Review of Modern Physics* **73** (2001), p. 797-855
- [Stockert 2005] O. Stockert, private communication (2005)
- [Stockert 2006] O. Stockert, M. M. Koza, J. Ferstl, A. P. Murani, C. Geibel, F. Steglich, *Physica B: Condensed Matter* **378-380** (2006), p. 157-158
- [Szytula 1989] A. Szytula, J. Leciejewicz, in *Handbook on Physics and Chemistry of Rare Earth*, vol. 12, edited by K. A. Gschneidner, Jr. and L. Eyring, Elsevier Science Publishers B. V. (1989) p. 133
- [Thomson 1987] J. D. Thompson in *Theoretical and Experimental aspects of Valence Fluctuations and Heavy Fermions*, edited by L. C. Gupta and S. K. Malik (Plenum Press, New York) **151** (1987)
- [Trovarelli 1990] O. Trovarelli, *Physica B*, **259-261** (1990), p. 140-141
- [Trovarelli 2000a] O. Trovarelli, C. Geibel, F. Steglich, *Physica B* **284-288** (2000) 1507-1508
- [Trovarelli 2000b] O. Trovarelli, C. Geibel, S. Mederle, C. Langhammer, F. M. Grosche, P. Gegenwart, M. Lang, G. Sparn, F. Steglich *Physical Review Letters* **85** (2000), 06, no 3, p. 626-629
- [Trovarelli 2000c] O. Trovarelli, C. Geibel, C. Langhammer, S. Mederle, P. Gegenwart, F. M. Grosche, M. Lang, G. Sparn, F. Steglich, *Physica B* **281 - 282** (2000), 06, p. 372-373

- [Venturini 1996] G. Venturini and B. Malaman, *Journal of Alloys and Compounds* **235** (1996), 03, no. 2, p. 201-209
- [Wada 1999] H. Wada, M. F. Hundley, R. Movshovich, J. D. Thomson, *Physical Review B* **59** (1999) no. 2, p. 1141-1144
- [Weickert2006] Franziska Weickert, *Quantenkritisches Verhalten in hochkorrelierten Elektronensystemen*, Technische Universität Dresden, Dissertation 2006. – ISBN 10-86727-030-9
- [Wykhoff 2005] J. Wykhoff, private communication 2005

## List of publications

- O. Stockert, M. M. Koza, J. Ferstl, C. Geibel, F. Steglich, *Science and Technology of Advanced Materials* (2007), doi:101016/j.stam2007.05.005 (article in press)
- J. Wykhoff, J. Sichelschmidt, J. Ferstl, C. Krellner, C. Geibel, F. Steglich, I. Fazlishanov, H.-A. Krug von Nidda, *Physica C* **460-462** (2007), p. 686-687
- J. Sichelschmidt, J. Wykhoff, H-A. Krug von Nidda, J. Ferstl, C. Geibel, F. Steglich, *Journal of Physics: Condensed Matter* **19** (2007), pp. 6
- J. Ferstl, H. Rosner, C. Geibel, *Physica B* **378-380** (2006), p. 744-745
- P. Gegenwart, Y. Tokiwa, T. Westerkamp, F. Weickert, J. Custers, J. Ferstl, C. Krellner, C. Geibel, P. Kersch, K.-H. Müller, F. Steglich, *New Journal of Physics* **8** (2006)
- S. Kimura, J. Sichelschmidt, J. Ferstl, C. Krellner, C. Geibel, F. Steglich, *Physical Review B* **74** (2006), p. 132408-1-4
- J. Larrea J., M. B. Fontes, E. M. Baggio-Saitovitch, J. Plessel, M. M. Abd-Elmeguid, J. Ferstl, C. Geibel, A. Pereira, A. Jornada and M. A. Continentino, *Physical Review B* **74** (2006), p. 140406(R)-1-4
- J. Larrea J., M. Fontes, E. Baggio-Saitovitch, M. M. Abd-Elmeguid, J. Plessel, J. Ferstl, C. Geibel, M. A. Continentino, *Journal of Magnetism and Magnetic Materials* (2006), in press.
- M. Nicklas, J. Ferstl, C. Geibel, F. Steglich, *Physica B* **378-380** (2006), p. 159-160
- O. Stockert, M. M. Koza, J. Ferstl, A. P. Murani, C. Geibel, F. Steglich, *Physica B* **378-380** (2006), p. 157-158
- Y. Tokiwa, P. Gegenwart, Z. Hossain, J. Ferstl, G. Sparn, C. Geibel and F. Steglich, *Physica B* **378-380** (2006), p.746-747

- F. Weickert, P. Gegenwart, J. Ferstl, C. Geibel, F. Steglich, *Physica B* **378-380** (2006), p. 72-73
- J. Ferstl, C. Geibel, F. Weickert, P. Gegenwart, T. Radu, T. Lühmann, F. Steglich, *Physica B* **359-361** (2005), p. 26-28
- G. Dionicio, H. Wilhelm, G. Sparn, J. Ferstl, C. Geibel, F. Steglich, *Physica B* **359-361** (2005), p. 50-52
- J. Sichelschmidt, J. Ferstl, C. Geibel, F. Steglich, *Physica B* **359-361** (2005), p.17-19
- Y. Tokiwa, P. Gegenwart, G. Sparn, J. Ferstl, C. Geibel and F. Steglich, *Physica B* **359-361** (2005), p. 29-31
- Y. Tokiwa, P. Gegenwart, T. Radu, J. Ferstl, G. Sparn, C. Geibel and F. Steglich, *Physical Review Letters* **94** (2005), 06, no. 22, p. 226402-1-4
- J. Ferstl, F. Weickert, C. Geibel, *Journal of Magnetism and Magnetic Materials* **272-276** (2004), p. e71-e73
- S. Kimura, T. Nishi, J. Sichelschmidt, V. Voevodin, J. Ferstl, C. Geibel, F. Steglich, *Journal of Magnetism and Magnetic Materials* **272-276** (2004), p. 36-37
- R. Küchler, F. Weickert, P. Gegenwart, N. Oeschler, J. Ferstl, C. Geibel, F. Steglich, *Journal of Magnetism and Magnetic Materials*, **272-276** (2004), 05, p. 229-230
- J. Sichelschmidt, V. A. Ivanshin, J. Ferstl, C. Geibel, F. Steglich, *Journal of Magnetism and Magnetic Materials* **272-276** (2004), p.42-43
- Y. Tokiwa, P. Gegenwart, F. Weickert, R. Küchler, J. Custers, J. Ferstl, C. Geibel and F. Steglich, *Journal of Magnetism and Magnetic Materials*, vol. **272-276** (2004), p. e87-e88
- K. Ishida, O.O. Bernal, D. E. MacLaughlin, W. Higemoto, A. Koda, K. Onishi, R. Kadono, J. Ferstl, C. Geibel, F. Steglich, *KEK annual report* (2003), p. S02-16

- V. A. Ivan'shin, L. K. Aminov, I. N. Kurkin, J. Sichelschmidt, O. Stockert, J. Ferstl and C. Geibel, *JETP Letters* **77** (2003), no. 9, p. 526-529
- J. Sichelschmidt, V. A. Ivanshin, J. Ferstl, C. Geibel, F. Steglich, *Physical Review Letters* **91** (2003), no. 15, p. 156401-1-4

## List of publications

---

# Acknowledgement

Over the last few years, I have benefited from a lot of people for their help, support, advice and encourage. It is my appreciation to acknowledge them here.

First of all, I would like to express my gratitude to Professor Frank Steglich for valuable suggestions, especially for the suggestion to investigate the La-doped  $\text{YbRh}_2\text{Si}_2$  and for providing me the opportunity to work for my dissertation in the Max-Planck-Institute for Chemical Physics of Solids.

Special thanks are given to Dr. Christoph Geibel for supervising my PhD thesis and his unending help and support during my work. As a group leader, he is always enthusiastic to solve all kinds of problems and to carefully arrange all the activities. Frequent discussions with him helped me to gain knowledge on both, the physics and crystal growth technique.

I would like to thank Dr. Octavio Trovarelli for his supervision during my first months. He introduced me into the flux crystal growth technique and equipment in our laboratories. I am grateful to work together with the enjoyable people in our materials development group, Dr. Zakir Hossain, Dr. Micha Deppe, Dr. Chandra Ramesh Nath, Dr. Enrique Kaul, Hirale S. Jeevan, Cornelius Krellner and Ralf Weise. For technical support in all kinds I am very thankful to our former group member Holger Diem. My office mate Nubia Caroca-Canales are specially thanked for her help in analysing X-Ray powder diffraction pattern and further support and motivation during my work. I am also grateful to Dr. Raul Cardoso for fruitful discussions from the crystallographic point of view.

A special tribute must go to the members of the low temperature group under the leadership of Dr. Philipp Gegenwart, especially Dr. Jeroen Custers and Dr. Franziska Weickert for low temperature resistivity and ac-susceptibility measurements and Dr. Robert K uchler for the thermal expansion and Dr. Teodora Radu and Dr. Thomas L uhmann for the low temperature specific heat measurements and their fruitful discussions.



Special thanks go to Dr. Michael Nicklas and Gabriel Dionicio for performing pressure experiments on pure and doped  $\text{YbRh}_2\text{Si}_2$ .

I would like to thank Dr. Walter Schnelle and Ralf Koban for the high temperature susceptibility measurements on  $\text{RFe}_2\text{Ge}_2$  and their valuable comments and discussions.

Very special thanks go to Dr. Jörg Sichelschmidt, Dr. Vladimir Ivan'shin and Jan Wykhoff for performing the ESR measurements on pure and doped  $\text{YbRh}_2\text{Si}_2$ .

A special acknowledge for performing the neutron scattering experiments and valuable discussions therein is made to Dr. Oliver Stockert, Dr. Amir Murani and Enrico Faulhaber.

I also give my thanks to Dr. Helge Rosner for performing the LDA-calculations and very fruitful discussions on  $\text{RFe}_2\text{Ge}_2$ .

I wish to give my thanks to Petra Scheppan and Katja Schulze for all EDAX analysis on my single crystals. For technical support needed for electronic problems in our PPMS I thank Torsten Breitenborn, Peter Krause and Wolfgang Geier from the electronic workshop. I also thank Kay Pollex, Thomas Engel and Jens Gerlach for solving computer problems immediately.

My colleagues and friends Dr. Adriana Sanchez, Edit Lengyel, Ulrike Köhler, Stefanie Hartmann, Dr. Corneliu Miclea, Dr. Niels Oeschler, Dr. Ivica Zerec and Vladimir Vovoedin are specially thanked for the nice working atmosphere at the institute.

I am very happy to thank Prof. Julian Sereni and Dr. Pablo Pedrazzini for stimulating discussions during my stay in San Carlos de Bariloche (Argentinien) and to make this trip to one of the highlights during my PhD thesis.

I am very thankful to my parents and my brother for their constant support, motivation and understanding.

Special thanks to Micha for his infinite patience and invaluable help, understanding and support during the difficult moments of my PhD work.

# **Author's declaration**

I declare that the work in this dissertation was carried out in accordance with the regulations of the Technische Universität Dresden. No part of this work has been submitted previously for a degree or other qualification at this or any other university. The research reported herein is original, except where specific reference is acknowledged to the work of others. All the research was carried out under the supervision of Prof. Frank Steglich and Dr. Christoph Geibel in Max-Planck-Institute for Chemical Physics of Solids.

Dresden, 15<sup>th</sup> of December.



# Versicherung

Hiermit versichere ich, dass ich die vorliegende Arbeit ohne unzulässige Hilfe Dritter und ohne Benutzung anderer als der angegebenen Hilfsmittel angefertigt habe; die aus fremden Quellen direkt oder indirekt übernommenen Gedanken sind als solche kenntlich gemacht. Die Arbeit wurde bisher weder im Inland noch im Ausland in gleicher oder ähnlicher Form einer anderen Prüfungsbehörde vorgelegt.

Die vorliegende Dissertation wurde am Max-Planck-Institut für Chemische Physik fester Stoffe in Dresden unter der wissenschaftlichen Betreuung von Herrn Prof. Dr. Frank Steglich und Herrn PD Dr. Christoph Geibel angefertigt.

Ich erkenne die Promotionsordnung der Technischen Universität Dresden an.

Dresden, den 15. Dezember 2006





